

FLOW OF MAGNETIZABLE PARTICLES IN TURBULENT AIR STREAMS

by

Kent Ritter Davey

B.S.-E.E., Tulane University
(1974)

M.S.-E.E., Carnegie Mellon University
(1976)

M.S.-Physics, University of Pittsburgh
(1976)

(NASA-CR-162418) FLOW ON MAGNETIZABLE
PARTICLES IN TURBULENT AIR STREAMS Ph.D.
Thesis (Massachusetts Inst. of Tech.) 265 p
HC A12/MF A01 CSCL 20D



N80-10461

G3/34 Unclas
45986

SUBMITTED IN PARTIAL FULFILLMENT
OF THE REQUIREMENTS FOR THE
DEGREE OF

DOCTOR OF PHILOSOPHY

at the

MASSACHUSETTS INSTITUTE OF TECHNOLOGY

August, 1979

© Kent R. Davey 1979

Signature of Author..... *Kent R. Davey*
Department of Electrical Engineering and Computer Science, August 1, 1979

Certified by..... *James R. Melcher*.....
Thesis Supervisor

Accepted by.....
Chairman, Departmental Committee on Graduate Students

REPRODUCTION OF THIS DOCUMENT IS UNRESTRICTED
NASA Scientific and Technical Information Facility

FLOW OF MAGNETIZABLE PARTICLES IN TURBULENT AIR STREAMS

by

Kent Ritter Davey

Submitted to the Department of Electrical Engineering on July 27, 1979 in partial fulfillment of the requirements for the Doctors of Science.

ABSTRACT

The requirement of particulate removal from turbulent flows arises in coal desulfurization, mineral beneficiation, water purification, particle research where particle loss is undesirable, and aerodynamic drag reduction, where the containment of particulate in a quasi-stationary manner within a turbulent boundary layer is desired followed by precipitation after a given length.

Special consideration will be given to particle precipitation. Light particle (diameter $< 20\mu$) and heavy particle models (diameter $> 20\mu$) are developed. The first involves the numerical solution of a diffusion equation in which boundary conditions are imposed only where particles enter the volume of interest. Inertial effects are unimportant. The second model involves a momentum balance in Lagrangian coordinates augmented by a diffusion force. The diffusion term is added so that the theory is consistent with inertia and diffusion dominated limits, and accounts for the effects of turbulent eddies in spreading particles in flight. Both models lump the effects of turbulent eddies into a measurable diffusivity constant.

Precipitation experiments with light and heavy iron powders acted on by a stationary permanent magnet structure are correlated with the numerical model predictions. A useful degree of accuracy in predicting particle precipitation, as compared to existing analytical models, is demonstrated for light and heavy particles.

Positive correlations with data encouraged the use of the heavy particle analysis in examining particle flight in an aerodynamic boundary layer over a flat plate. The model predicted that with conventional permanent magnets, 90% of the injected particulate is collected in 5 meters and 4% would be lost. An alternative is described in which a travelling wave structure is used to contain and shuttle particles along in the boundary layer. In this mode, in which particles continually interact with the wall, it appears that particle loss can be greatly reduced.

Thesis Supervisor: James R. Melcher
Professor of
Electrical Engineering
and Computer Science

ACKNOWLEDGEMENTS

I wish to express first and foremost the warmest thanks to my wife Lana who supplied a wealth of support, encouragement, and assistance in almost every endeavor of this project. Second, a deep appreciation is offered for my advisor and friend Jim Melcher, whose insights, knowledge, resources, inspiration, and prodding kept me and the project on its feet. Thanks are also in order to my readers Lou Smullin, Ain Sonin, and David Kelland, who provided many helpful suggestions and discussions. Joe Cairns was an invaluable aid in the construction of the experiment. Thanks also go to Paul Warren for advice in the laboratory and photographic help. The patience and attention of my typists, especially Terry Brown, is greatly appreciated.

Finally, I wish to thank my relatives for their support and help. No doubt my earliest interests in electrical engineering were planted and nurtured by my father Jack Davey and my mother's encouragement of those interests.

The project was initiated and funded under the auspices of the National Aeronautics and Space Administration by NSG 1453. Their support is gratefully acknowledged.

TABLE OF CONTENTS

	<u>Page No.</u>
ABSTRACT	1
ACKNOWLEDGEMENT	2
LIST OF FIGURES	7
LIST OF SYMBOLS	14
CHAPTER I. INTRODUCTION	17
Bibliography.....	23
CHAPTER II. MAGNETIC THEORY BACKGROUND	25
A. Magnetic Force	25
B. General Precipitation Remarks	30
C. Electric Versus Magnetic Precipitation	33
CHAPTER III. TURBULENCE PHENOMENA	44
A. Parameter Introduction and Interrelationships	44
B. Flux Conservation	53
C. Momentum Equation Attack	57
D. Statistical Approach	65
Bibliography	70
CHAPTER IV. TURBULENT PRECIPITATION THEORY	72
A. Introduction	72
B. Characteristic Times	73
C. Diffusion Model - 4μ Particles	78
1. Non-Causal Diffusion Model	80
2. Causal Perfunctory Model	93
3. Causal Fundamental Diffusion Model	98
D. Heavy Particle Analysis	99

	<u>Page No.</u>
1. Inertial Model ($r_p \geq 50\mu$)	99
2. Hybrid Inertial-Diffusion Model ($10\mu < r_p < 50\mu$)	106
Bibliography	116
CHAPTER V. DOCUMENTATION OF FIELDS AND FLOWS	117
A. Introduction	117
B. Inducement of Turbulent and the Velocity Profile Grid	118
C. Turbulent Diffusion Coefficient Determination	126
D. Magnetic Field Distribution	140
Bibliography	145
CHAPTER VI. EXPERIMENTAL RESULTS AND CONDITIONS WITH THEORETICAL MODELS	146
A. Small Particle Dynamics	146
1. Correlation of Measured Parameters with Numerical Models	146
2. Correlation of Measured Parameters from Deutsch Model ...	149
3. Observation of Theoretical Deposition Predictions	149
4. Numerical Density Profiles	158
5. Particle Size	165
6. Theoretical Predictions Compared to Experimental Deposition Data	167
7. Refinement of Causal Theory	172
B. Large Particle (50-100 μ) Analysis-Inertial Hybrid Model	174
1. Diffusion-free Model Results	174
2. Hybrid Inertial-Diffusion Results	177
3. Particle Size Considerations	177
4. Boundary Layer Thickness Sensitivity	188

	<u>Page No.</u>
5. Non-Isokinetic Injection	188
6. Field Harmonics	192
7. Conclusion	192
CHAPTER VII. PARTICLE FLIGHT OVER JET FUSELAGE	193
A. Introduction	193
B. Fluid Mechanics and Diffusivity	193
C. Typical Injected Density Profiles	197
D. Possibility of Quasi-Stationary Profiles	199
CHAPTER VIII. CONCLUDING REMARKS	205
A. Particle Entrainment over Jet Fuselage	205
B. Travelling Wave Interaction with Particulate	205
C. Synopsis and Current Research	212
APPENDIX A. Spherical Magnetizable Particle Field Analysis	215
APPENDIX B. Refinement of Basic Precipitation Models	219
APPENDIX C. KDDTRAG - Particle Trajectory Program - No Inertia	223
APPENDIX D. Analytical Diffusion Analysis	224
APPENDIX E. KDDI4, KDDI9 - Programs to Solve Non-Causal Density Problem	229
APPENDIX F. KDDFZ - Perfunctory Causal Computer Program	235
APPENDIX G. KDDF1 - Fundamental Causal Computer Program	239
APPENDIX H. KDIN4 - Computer Program to Solve Particle Trajectories- Considers Inertia but no Diffusion	243
APPENDIX I. KDIN7 - Hybrid Inertial-Diffusion Model Computer Program	245
APPENDIX J. Fourie - Basic Discrete Fourier Analysis Program	250

APPENDIX K. KD747G - Hybrid Inertial-Diffusion Program for Analyzing Particle Flight in an Aerodynamic Boundary Layer - No Gravity	251
APPENDIX L. Refinement of Causal Fundamental Light Particle Model	256
APPENDIX M. KDFF1 Refined Fundamental Causal Model FORTRAN Program ..	259
BIOGRAPHICAL NOTE	264

LIST OF FIGURES

<u>Chapter I</u>	<u>Page No.</u>
Figure 1-1. Applications.....	18
Figure 1-2. Experimental Appartus.....	21
<u>Chapter II</u>	
Figure 2-1. Field Structures Used.....	26
Figure 2-2. Normal Surface Force Density 1/4" Above Permanent Structure of Fig. (2-2 (b)).....	28
Figure 2-3. Fully Mixed Turbulent Flow Electrostatic Precip- itator.....	34
Figure 2-4. Laminar Flow Electrostatic Precipitator Trajectory Model.....	36
Figure 2-5. Fully Mixed Magnetic Precipitation.....	38
Figure 2-6. Laminar Flow Magnetic Precipitation Flow Trajec- tories.....	40
<u>Chapter III</u>	
Figure 3-1. Different Regions in Turbulent Duct Flow.....	48
Figure 3-2. Momentum Transfer in Turbulent Flow.....	51
Figure 3-3. Pipe Diffusivity.....	64
<u>Chapter IV</u>	
Table 4-1. Model Applicability Given Particle Size and Fluid Flow.....	74
Table 4-2. Chapter 4 Synopsis.....	75
Figure 4-1. Small Particle Diffusivity Assumptions-Non Causal Model.....	83

	<u>Page No.</u>
Figure 4-2. Normal Particle Density Dependence.....	85
Figure 4-3. Non-Causal Model Small Particle System Representation and Boundary Conditions.....	87
Figure 4-4. Numerical Solution of Diffusion Region.....	90
Figure 4-5. Stability of Diffusion Analysis.....	92
Figure 4-6. Turbulent Diffusivity Vertical Dependence.....	95
Figure 4-7. Perfunctory Causal Finite Difference Solution.....	96
Figure 4-8. Particle Inertial Trajectories.....	103
Figure 4-9. Particle Injection System.....	105
Figure 4-10. Langrangian Representation of Incremental Volume Element.....	109
Figure 4-11. Particle Trajectories from Injection Tube.....	112

Chapter V

Figure 5-1. Turbulent Intensity Variation.....	120
Figure 5-2. Velocity Profile Grid.....	122
Figure 5-3. Profile Grid Construction.....	123
Figure 5-4. Profiles of Axial Duct Velocity.....	125
Figure 5-5. Diffusion Coefficient Measurement Scheme.....	128
Figure 5-6. Anemometer Voltage-Velocity Curve.....	130
Figure 5-7. Turbulent Intensity Versus Position in Duct.....	131
Figure 5-8. Turbulent Intensity for 20 Hz Frequency Bands.....	132
Figure 5-9. Turbulent Intensity for 4 Hz Frequency Bands.....	134
Figure 5-10. Diffusivity vs. Position for a Main Stream Flow of 4.32 m/sec.....	135

Figure 5-11. Diffusivity vs. Position for a Main Stream
Flow of 2.28 m/sec..... 136

Figure 5-12. Turbulent Diffusivity vs. Axial Position..... 139

Figure 5-13. 5.08 cm Wavelength Field Pattern..... 142

Figure 5-14. 8 cm Wavelength Field Pattern..... 143

Figure 5-15. 12 cm Wavelength Field Pattern..... 144

Chapter VI

Figure 6-1. Small Particle Test Setup..... 147

Figure 6-2. Comparison of Theories, $\lambda=8\text{cm}, 4\frac{1}{2}\mu$ Particles..... 151

Figure 6-3. Deutsch and Causal Theories, $\lambda=8\text{cm}, 8\mu$ Particles... 153

Figure 6-4 Causal Fundamental Precipitation Results;
Magnetic vs. Gravitational Migration..... 156

Figure 6-5. Fundamental Causal Theory Sensitivity to
Diffusivity, $\lambda=8\text{cm}, 7\mu$ Particles..... 157

Figure 6-6. Transverse Density Profiles Along Duct with
Corresponding Diffusivity and Magnetic Force
Decay; $\lambda=5.08\text{cm}, 7\mu$ Particles..... 159

Figure 6-7. Transverse Density Profiles Along Duct with Cor-
responding Diffusivity and Magnetic Force Decay;
 $\lambda=8\text{cm}, 7\mu$ Particles..... 160

Figure 6-8. Transverse Density Profiles Along Duct with
Corresponding Diffusivity and Magnetic Force
Decay; $\lambda=12\text{cm}, 7\mu$ Particles..... 161

Figure 6-9. Traverse Density Profiles with Corresponding Diffusivity; No Magnetic Force; $\lambda = 8$ cm, 7μ particles.....	163
Figure 6-10. Traverse Density Profiles with Corresponding Magnetic Decay, No Diffusivity; $\lambda = 8$ cm; $4 \frac{1}{2} \mu$ Particles.....	164
Figure 6-11. Particle Sizing Spread for Light Particle Tests- Microscope Results.....	166
Figure 6-12. Anderson Impactor Particle Size Results.....	168
Figure 6-13. Deutsch and Fundamental Causal Precipitation with Particles; $\lambda = 5.08$ cm.....	169
Figure 6-14. Deutsch and Fundamental Causal Precipitation Correlations with Experiments, $\lambda = 8$ cm.....	170
Figure 6-15. Deutsch and Fundamental Causal Precipitation Correlations with Experiment, $\lambda = 12$ cm.....	171
Figure 6-16. Large Particle ($50-70\mu$) Experimental Set-up.....	175
Figure 6-17. 60 Micron, 12 cm Wavelength, 1500 ft./min injection- Trajectory Models with Experimental Collection.....	176
Figure 6-18. 100-180 Micron, 12 cm wavelength, 1300 ft./min. Injection- Trajectory Models with Experimental Collection.....	178
Figure 6-19. 70 Micron, 12 cm. Wavelength, 1300 ft./min.	

Injection- Hybrid Model with Experimental Collections, 76% Particulate Collected in Experiment.....	179
Figure 6-20. 5.08 cm Wavelength, 1000 ft./min. Injection, 70 μ Hybrid Model Versus Experimental Data- 51% Particulate Collected in Experiment.....	180
Figure 6-21. 8 cm Wavelength, 1400 ft./min. Injection, 60 μ Hybrid Model Versus Experimental Data- 46% Particulate Collected in Experiment.....	181
Figure 6-22. 12 cm Wavelength, 1500 ft./min. Injection, 60 μ Hybrid Model Versus Experimental Data- 64% Particulate Collected in Experiment.....	182
Figure 6-23. Hybrid Theory Particle Size Sensitivity, $\lambda = 8$ cm, 8mm tube, 1400 ft./min. Injection.....	184
Figure 6-24. 38-45 Micron Batch, 12 cm Wavelength, 1500 ft./min. Injected, Hybrid Model Representative 40 μ Spherical Prediction,.....	185
Figure 6-25. 45-53 Micron Batch, Comparison of 50 and 70 μ Computer Precipitations, 5.08 cm Wavelength, $Y_0=.37m$, 1000 ft./min. injection.....	186
Figure 6-26. 38-45 Micron Batch, Comparison of 60 and 40 μ Theory Predictions, $\lambda = 8cm$	187
Figure 6-27. Hybrid Model Boundary Layer Thickness Sensitivity	

8 cm Wavelength, 60 μ Particle, 1400
ft./min. injection.....189

Figure 6-28. Non-isokinetic Particle Injection,
8 cm Wavelength, 2300 ft./min. inject-
ion, 45-53 μ Batch, Hybrid Theory and
Data; 39% Collected, 70 μ190

Figure 6-29. Growth of Turbulent Interchange Region
for Non-Isokinetic Jet Injection.....191

Chapter VII

Figure 7-1. Turbulent Diffusivity Distribution Across
Boundary Layer.....195

Figure 7-2. Determination of Maximum D_t196

Figure 7-3. Particle Trajectories Over Jet Fuselage.....198

Figure 7-4. Density Profile for Particle Equilibrium.....201

Figure 7-5. Trajectories and Densities in Boundary Layer;
Typical Tube Profile Initially.....203

Figure 7-6. Trajectories and Densities in Boundary Layer;
Skewed Profile at Time $t=0$204

Chapter VIII

Figure 8-1. Circulating Field Above Travelling Wave
Structure.....207

Figure 8-2. Instantaneous Picture of Agglomerate Under
Traveling Wave Structure in Duct.....208

Figure 8-3. Particle Interaction with Travelling
Wave Structure.....209

Figure 8-4. Cylindrical Wave Structure for Studying
Particle Motion Without End Effects.....211

Appendix A

Figure A-1. Particle Magnetic Force.....215

Figure A-2. Permeable Sphere in External Field.....216

Appendix B

Figure B-1. Particle Trajectories with Upward
Magnetic Migration.....222

Appendix D

Figure D-1. Analytical Diffusion Study Model.....225

Figure D-2. Typical Density Profile.....228

LIST OF SYMBOLS

- a = duct half height
- \bar{B} = magnetic flux density
- D = diffusivity
- D_m = molecular diffusivity
- D_t = turbulent diffusivity
- \bar{E} = electric field
- \bar{F} = force
- \bar{F}_{mag} = magnetic particle force
- f = subscript for fluid; frequency
- g = gravitational acceleration
- \bar{H} = magnetic field intensity
- \bar{J} = current density
- k = wave number, $2\pi/\lambda$
- K = Von Karman constant
- L = normalized axial length; turbulent Lagrangian length scale
- ℓ = Prandtl mixing length
- ℓ_p = precipitation length
- m = particle mass
- \bar{M} = magnetization
- n = particle density
- n_0 = initial particle density
- P = pole pitch; subscript for particle
- P_x = x directed momentum
- q = charge

r = particle radius

R = velocity correlation $\frac{v_y'(\xi)v_y'(y)}{\overline{v_y'^2}}$

t = time

Th = thickness of particle flux tube

U = mean axial flow velocity

U_{avg} = average axial mean velocity (average transversely across the duct)

$U_* = \frac{\tau_o}{\rho}$ = shear velocity

$V_m(y)$ = magnetic migration velocity = $\frac{4\pi r^3 k \frac{1}{\mu_o}}{\beta} \sum_{m=1}^{\infty} \beta_n^2 e^{-2ky}$

$V_n'(y) = \left(\frac{d(V_m(y))}{dy} \right)$

v = velocity

v' = perturbation velocity

$\overline{v'^2}$ = perturbation velocity squared and then averaged on time

w_y = vertical fall velocity

x = axial direction

y = transverse direction

α = magnetic force constant = $\frac{4}{3} \pi r^3 \left(\frac{\mu}{\mu_o} - 1 \right) \left(\frac{3}{2 + \frac{\mu}{\mu_o}} \right) \mu_o H_o^2$

β = Stokes drag coefficient = $6\pi\eta r$

δ = boundary layer thickness

ϵ = small displacement; eddy viscosity

η = viscosity

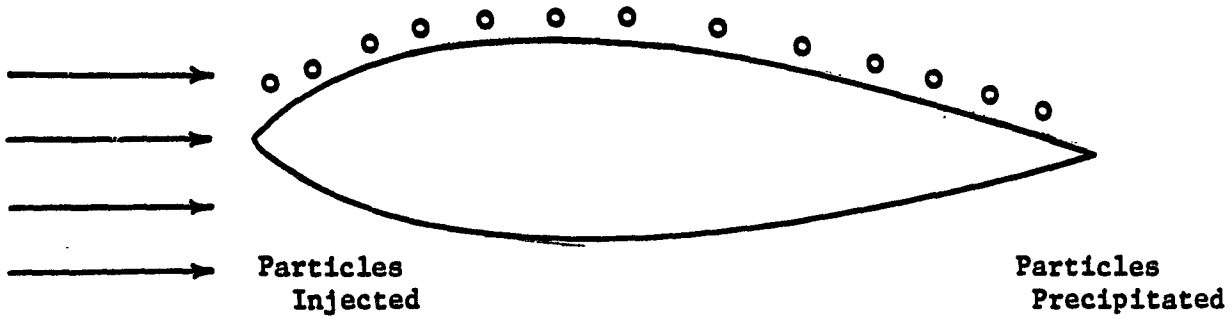
- λ = wavelength
- μ = permeability
- μ_0 = permeability-free space
- ν = kinematic viscosity
- ν_t = eddy viscosity
- γ = turbulent Lagrangian time scale
- ρ = particle mass density
- σ = variance
- τ = time scale; particle flux
- τ_{xy} = shear stress, directed
- ξ = dummy variable; Lagrangian displacement vector
- ω = $2\pi/\text{frequency}$

I. Introduction

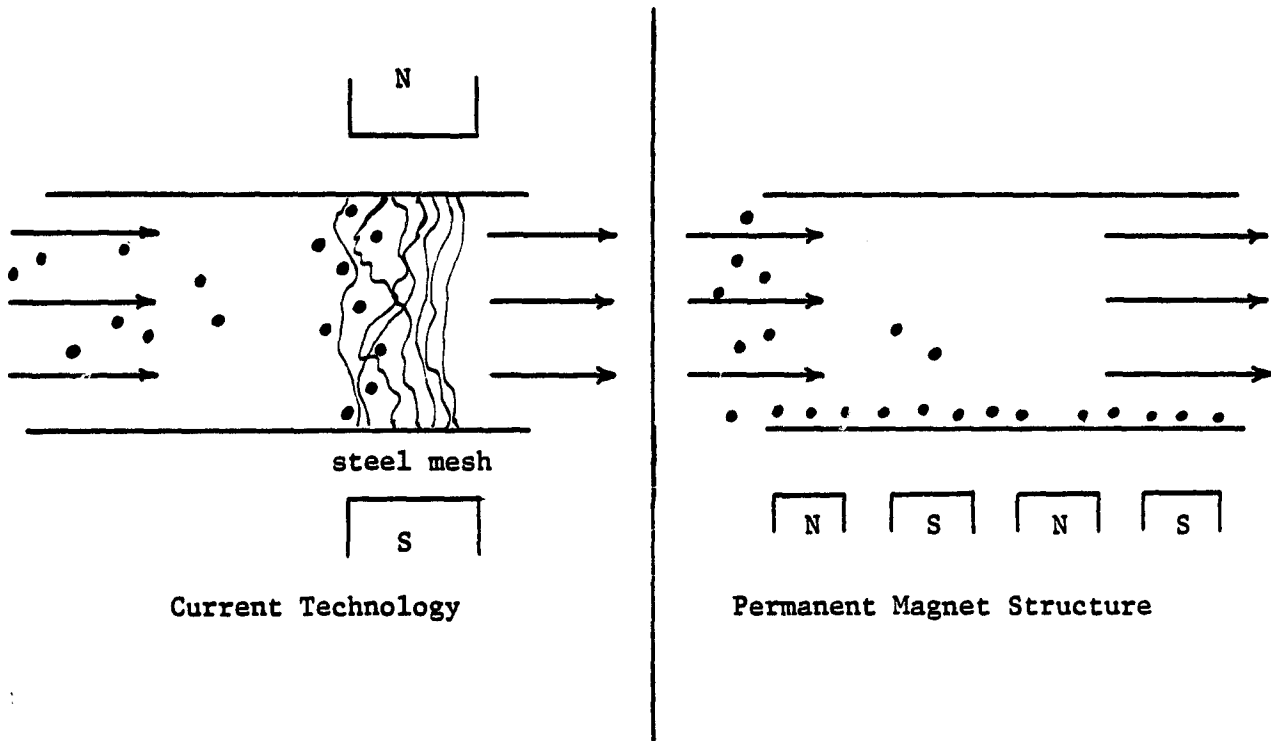
The flow of magnetizable particles in a turbulent air stream in the presence of an imposed magnetic field is of interest to NASA (National Aeronautics and Space Administration) in utilizing the experimentally observed phenomenon of drag reduction produced by the introduction of particles in a turbulent boundary layer. The earliest observation of this effect were in the 1940's [1, 2, 3] and have recently been expounded on by Landahl [4, 5], Boothroyd, and Rosetti, and Pfeffer [6, 7]. According to Landahl, the particles dissipate energy in the small scale boundary layer eddies. Long, thin particles are most effective in reducing drag. Other investigators believe that stabilization of small scale motion leads to a reduction in turbulent stresses near the wall, and to an associated thickening of the wall layer. In gas-solid suspensions, 10-60 micron particles yield significant drag reduction with a maximum reduction observed using 30 micron particles. Particles larger than 100 micron however, increase the drag [7]. NASA is interested in whether particles can be introduced into a turbulent boundary layer, ducted along the skin of a fuselage, and then precipitated. Figure 1-1(a) illustrates an hypothesized configuration over an airplane wing.

The interest in particle convection migration is widely ranging. Soo [8, 9] has been working with multiphase flows for some time. The applications of and interest in such flows are quite varied. Some examples are as follows:

- (1) Determination of the proximity of the particle flow to stream motion in order to use solid particles as tracers in studying the flow of fluids [10].
- (2) Determination of the diffusivity of the particles with respect to the continuous phase [11].



(a) Drag Reduction



(b) Precipitation

Figure 1-1 Applications

- (3) Determination of the diffusion of fuel and air as influenced by the relative motion of the fuel particles and air stream in order to optimize the combustion of solid field particles [12].
- (4) Determination of the relation of the motion of solid particles and the field stream in sedimentation studies and pneumatic conveyance applications [13, 14].

More germane to this investigation is work being done in the area of magnetic precipitation [15, 16, 17]. Liu and Lin give an excellent overview of work in this area. It is now clear that the use of magnetic fields in removing pyrite (desulfurization) and other inorganic contaminants from coal will be important in the next few decades. An IEEE Magnetics conference this past summer (1978) [18], as well as in 1975 [19], summarized the current work in this area. Currently, most magnetic precipitators use steel wool or a similar magnetizable mesh to enhance the magnetic gradient and precipitate particles (Fig. 1-1(b)). The first major contribution to this area where the effect of particle inertia was considered appeared in a thesis by Clarkson [22].

The central theme of this thesis is the flow of particles in turbulent air streams, and particularly in the boundary layer interaction. Towards this end, two practical avenues of research emerge. A detailed study of the precipitation of particles from an aerodynamic air stream is considered. Precipitation is required for removing particles from the boundary layer. It is also a measure of the turbulent diffusion magnetic migration processes at work in the flow. This thesis will focus on precipitation because of both its basic implications and its practical application to drag reduction and particle management.

- (1) Small particle theory (< 10 micron)

Inertial effects are small but turbulent diffusion must be considered. The determination of particulate density is accomplished by solving a two-dimensional diffusion equation.

(2) Large particle theory (> 40 micron)

Turbulent diffusion is less dominant, and inertial forces are significant. Particulate distribution is analyzed through a numerical integration of the momentum equation, i.e. of determining the particle trajectories modified by the inclusion of a diffusion-type force.

The principle contribution of this study is the incorporation of turbulent diffusion theory with an imposed magnetic migration process both with and without inertia effects. In this work, the imposed migration is magnetostatic; the nature of this magnetic force to particle interaction will be explored in depth.

This thesis begins with a review of the pertinent background information on turbulent flows and the prediction of particulate diffusion. The nature of the particle magnetic force will be discussed and the inherent difference between electric and magnetic precipitation considered. Small and large particle concentration theories will be developed and followed by a presentation of the experimental apparatus, procedures, and theory correlation. Finally, the computer model will be used to simulate the flight of particulate in an air stream over a flat plate. The objective in this final study will be to understand the controllability of particle confinement in the boundary layer by altering the density profile. A steady density in the layer is desirable to obtain the drag reduction benefits. A brief consideration is given in the concluding chapter to using a traveling wave structure for

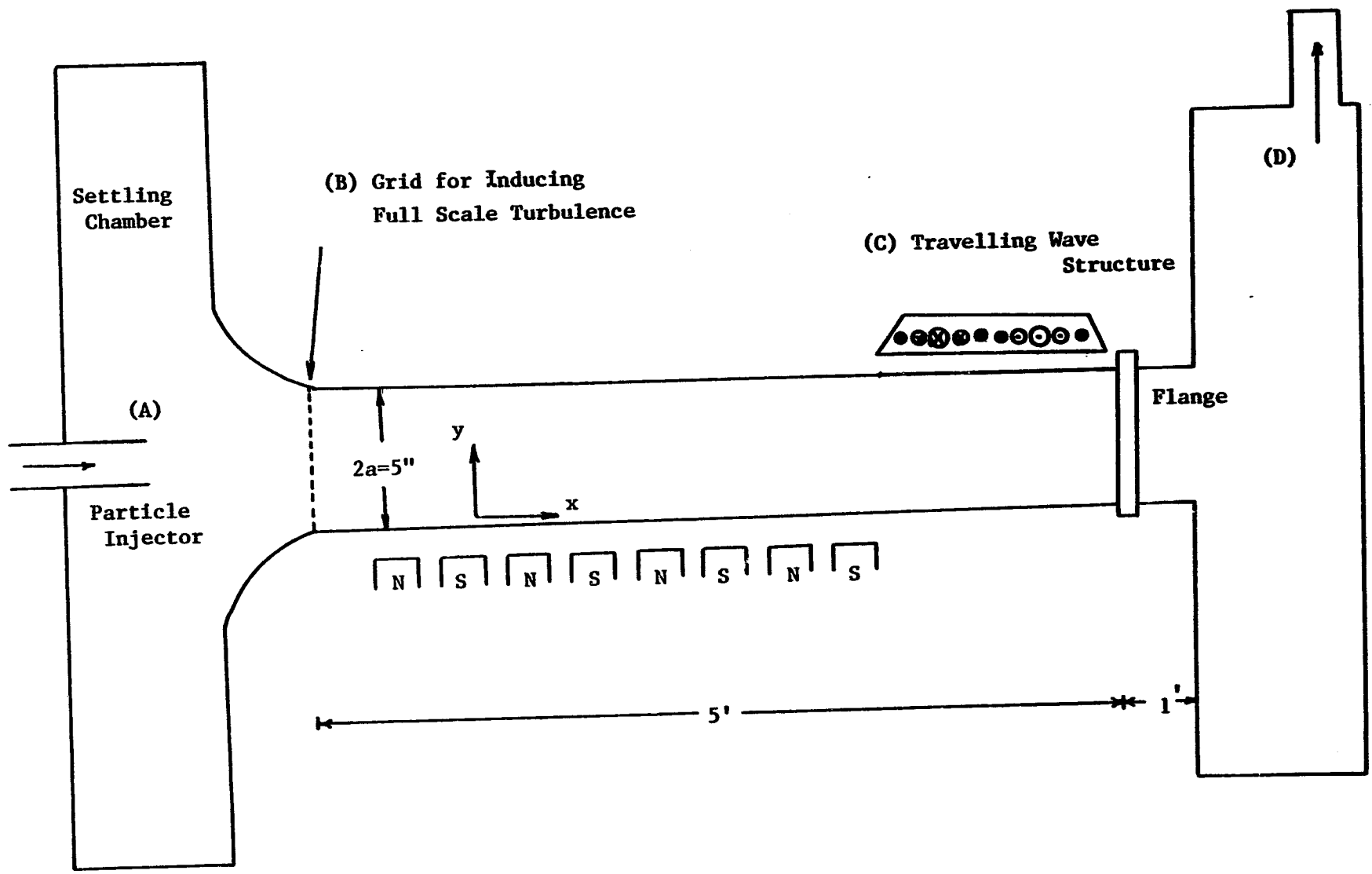


Figure 1-2 Experimental Apparatus

walking particles along a wall in a boundary layer. Figure (1-2) shows such a structure mounted on the top of the duct.

Before beginning turbulent diffusion theory review, a cursory examination of the basic experiment is in order. The apparatus used in studying both the precipitation and ducting of magnetizable particles is shown in Fig. 1-2. Particles are injected through a copper tube at A and blown down a six-foot duct. In the precipitation experiments, a permanent magnet structure serves as the source of a periodic static magnetic field source. The magnets along the bottom of the duct enhance the precipitation of magnetizable particulate on the lower plate. Particles not collected by this field leave the duct at D. A velocity profile grid at B is used to promote and control turbulent air flow.

Chapter 1 - Bibliography

1. Toms, B. A., Proc. 1st INT. Congr. Rhedl. Vol. 2 (1948) 135, Amsterdam: North Holland.
2. Oldroyd, J. E., Proc Roy. Soc. (London) A, 245 (1958) p. 278.
3. Mysels, K. H., U.S. Pat. No. 2, 492, 173 (1949).
4. Landahl, Marten T., "Drag Reduction by Polymer Addition", Applied Mechanics Proceedings of the 13th International Congress of Theoretical and Applied Mechanics, Moscow, August 1972.
5. Landahl, Marten T., "On Dynamics of Boundary Layer Turbulence and Mechanics of Drag Reduction", I.U.T.A.M. Symposium on Structure and Drag Reduction, 1977.
6. Boothroyd, R. "Pressure Drop in Duct Flow of Gaseous Suspensions of Fine Particles", Trans Inst. Chem. Engrs., Vol. 44, 1966, T 306-T313.
7. Rosetti, S. and Pfeffer, R., "Drag Reduction in Dilute Flowing Gas Solid Suspensions," AIChE Journal, Vol. 18, No. 1, Jan. 1972, pp. 31-39.
8. Soo, S., Fluid Dynamics of Polyphase Systems, Blaisdell Publishing Co., Waltham, 1967.
9. Soo, S., "Statistical Properties of Momentum Transfer in Two-Phase Flow", Chemical Engineering Science, Vol. 3, No. 2, April, 1956, p. 57.
10. Nicholson, H. M. and Field, J. P., "Some experimental techniques for the investigation of the mechanism of flame stabilization in the wakes of bluff bodies" Third Symposium on Combustion, Flame, and Explosive Phenomena, 1949, p. 45.
11. Latinen, G. A., Mechanisms of fluid-phase mixing in fixed and fluidized beds of uniformly sized spherical particles, Ph.D. Thesis Chemical Engr. Princeton University, 1951.
12. Longwell, J. P., "High Speed Aerodynamics and Jet Propulsion, Vol. 2, Combustion Processor, Princeton University Press, 1956.
13. Vanoni, V. A., et.al., "Dynamics of Particulate Matter in Fluid Suspension" Rept. No. N-71.1, Hydrodynamic Laboratory, California Institute of Technology, Nov. 1950.
14. Pinkus, O., "Pressure Drops in Pneumatic Conveyance of Solids", J. Appl. Mech. 1952, Dec., p. 425.
15. Oberteuffer, J., "Magnetic Separation, a Review of Principles, Devices, Applications," IEEE Transactions on Magnetics, Vol. MAG. 10 No. 2, June 1974, pp. 223-232.

16. Luborsky, F. E., and Drummond, B. J., "High Gradient Magnetic Separation: 'Theory vs. Experiment'", Report- General Electric Corporate Research and Development, Schenectady, New York, March, 1975.
17. Cummings, D., Hemmenblau, D., Oterteuffer, J., Powers, G., "Capture of Small Magnetic Particles by Magnetic Forces from Low Speed Fluid Flows", AIChE Journal, Vol. 22, No. 3, May, 1976, pp. 569-575.
18. International Conference on Industrial Application of Magnetic Separation. IEEE Magnetics Symposium, summer 1978.
19. IEEE Magnetics Conference, 1975, Transactions on Magnetics, Vol. Mag. 12, No. 5, September, 1976.
20. Chadam, J., M. S. Thesis, Math Dept., M.I.T., 1961.
21. Barfield, B., Smerdon, E., and Hiler, E., "Prediction of Sediment Profiles in Open Channel Flow by Turbulent Diffusion Theory", Water Resources Research, Vol. 5., No. 1, February 1969, pp. 292-299.
22. Clarkson, Chris, "Modelling of High Gradient Magnetic Separation and its Application to Cold Rolling Mill Lubricants," Ph.D. Thesis, Mat. Science, M.I.T., 1977.
23. Liu, Y. A., and Lin, C. J., "Research Needs and Opportunities in High Gradient Magnetic Separation of Particulate Gas Systems", Magnetochemical Engr. Laboratory, Dept. of Chem. Engr., Auburn University.

II. MAGNETIC THEORY BACKGROUND

A. Magnetic Force

The first question that must be considered whether considering particle precipitation or ducting is "what is the nature of the particle magnetic force?" A ferromagnetic particle of radius a , permeability μ , in a field of intensity \bar{H} , experiences a total force

$$\bar{F} = \frac{4}{3} \pi a^3 \left(\frac{3}{2 + \frac{\mu}{\mu_0}} \right) \left(\frac{\mu}{\mu_0} - 1 \right) \frac{\mu_0}{2} \nabla(\bar{H} \cdot \bar{H}) \quad (2-1)$$

The reader is referred to Appendix A for a derivation of the Eqn. (2-1).

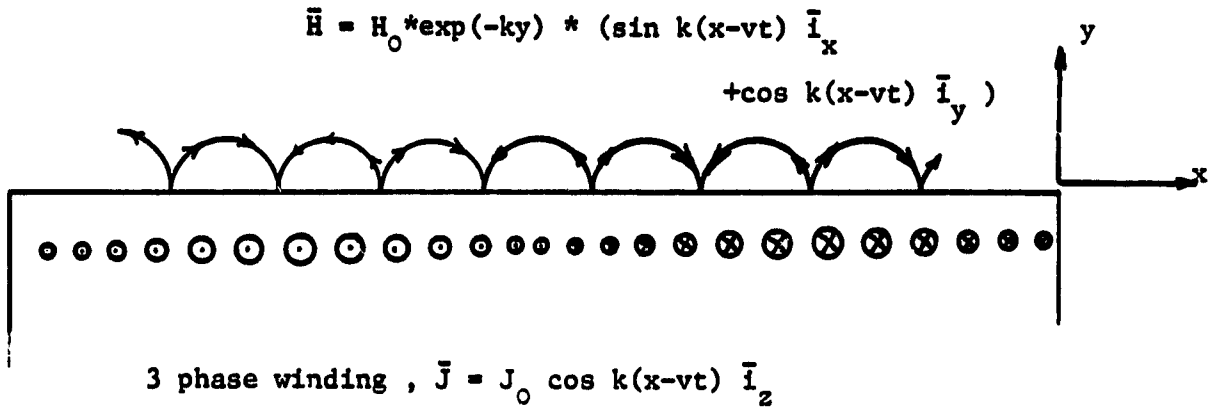
The force expression (2-2) is subject to the following two restrictions:

- 1) The particle is much smaller than the characteristic length over which the field changes, i.e., the assumption of constant \bar{H} external over the particle's dimension is valid.
- 2) Particle-Particle interactions are small.

For the largest particles the author will be using (100 μm in a field structure wavelength of 5 cm, assumption (1) is quite valid.

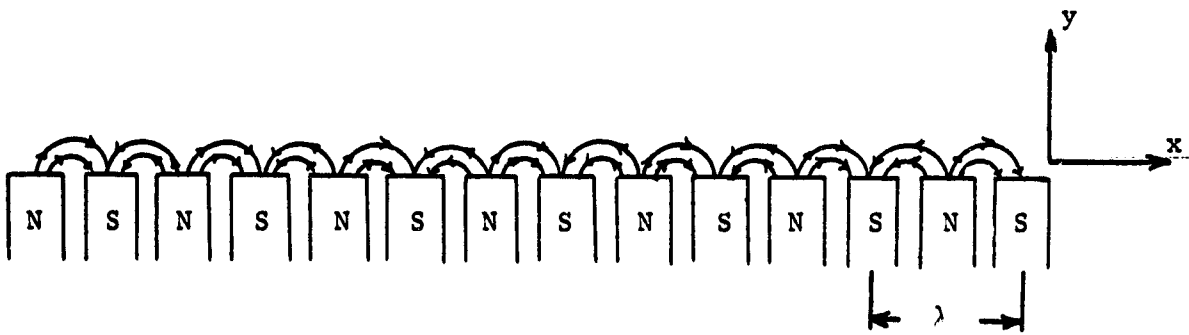
The second assumption is questionable when heavy precipitation occurs. The particles agglomerate into hair-like structures and enhancement of local field gradients undoubtedly occurs. This effect is only significant in the vicinity of precipitated agglomerates. (The author attempted to restrict the amount of precipitant to low levels.)

The two field structures used in this work are shown in Fig. 2-1. The sinusoidal wave structure used in the ducting experiments excites a trav-



(a) Traveling Wave Structure

$$\vec{H} = H_0 \sum_{\substack{m=1 \\ \text{odd}}}^{\infty} \frac{4}{m\pi} \left[\exp(-mky) * \sin(mkx) \vec{i}_x + \exp(-mky) * \cos(mkx) \vec{i}_y \right]$$



(b) Permanent Magnet Square Wave Structure

Figure 2-1 Field Structures Used

eling wave, the speed of which is determined by the frequency and winding pole pitch. The field above the motor is Laplacian, decaying exponentially in the y direction with the same wave number k as the drive current J.

The permanent magnetic square wave structure has an infinite number of odd harmonics, again Laplacian and falling off in magnitude in the y direction as the inverse of the harmonic. Thus, a square wave field structure with surface field H_0 would yield in the upper half plane

$$\bar{H} = H_0 \sum_{\substack{m=1 \\ \text{odd}}}^{\infty} \frac{4}{m\pi} e^{-mky} \begin{cases} \sin mkx \hat{i}_x \\ \cos mkx \hat{i}_y \end{cases} \quad (2-2)$$

The field above such a structure is in reality not a square wave. Figure (2-2) shows the typical surface normal magnetic force density 1/4" above the permanent magnet structure. This field can be decomposed into its Fourier components and represented as

$$\bar{H} = \sum_{m=1}^{\infty} H_m e^{-mky} \begin{cases} \sin mkx \hat{i}_x \\ \cos mkx \hat{i}_y \end{cases} \quad (2-3)$$

Using the first harmonic sinusoidal field of Fig. (2-1(a)) along with eqn. (2-1), one arrives at the particle force

$$\bar{F} = -\alpha' (2k) e^{-2ky} H_0^2 \hat{i}_y \quad (2-4)$$

or

$$\bar{F} = -\alpha k e^{-2ky} \hat{i}_y$$

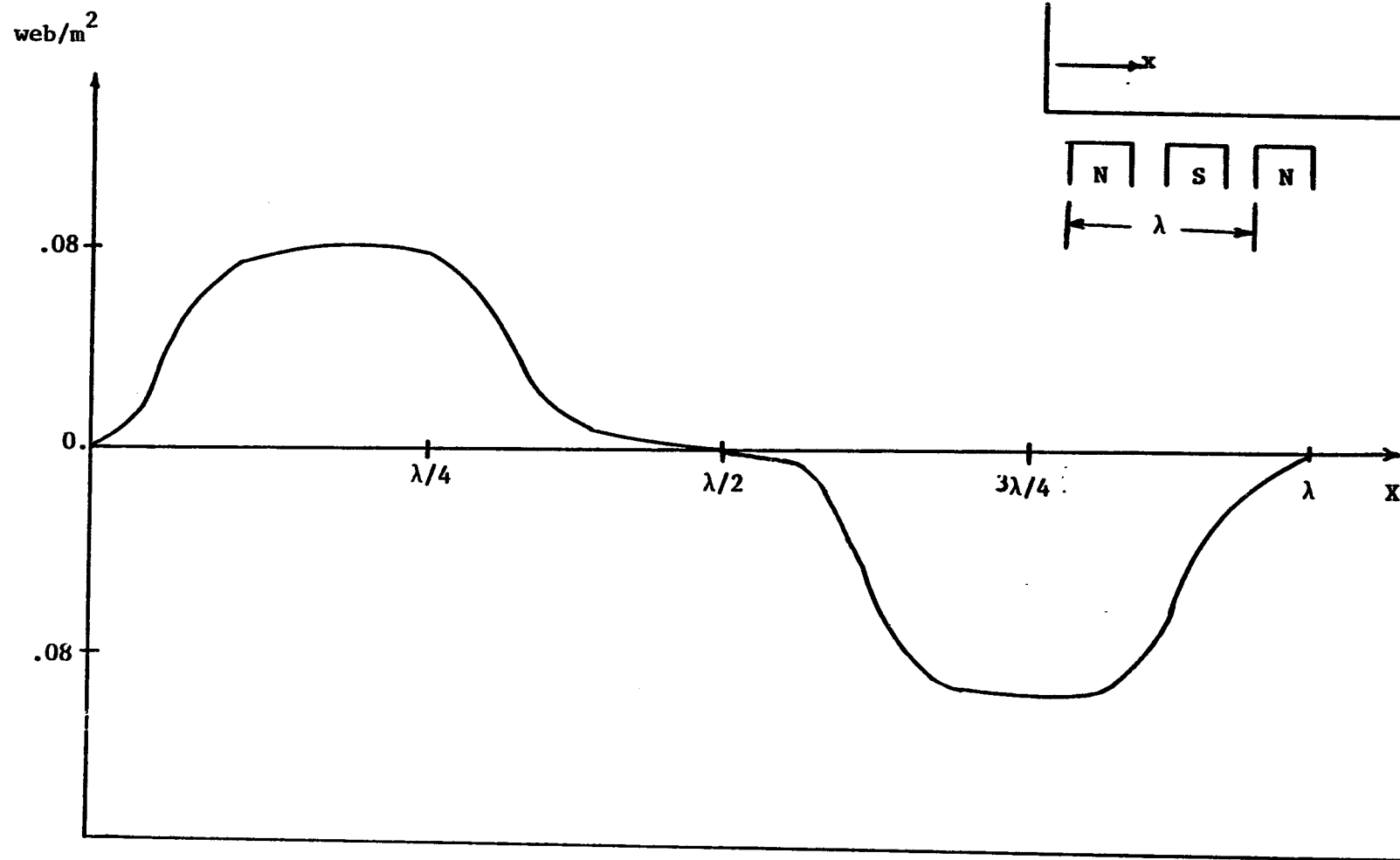


Figure (2-2) Normal Surface Force Density 1/4" Above Permanent Magnet Structure

where
$$\alpha = \left(\frac{4}{3} \pi a^3\right) \left(\frac{3}{2 + \frac{\mu}{\mu_0}}\right) \left(\frac{\mu}{\mu_0} - 1\right) \mu_0 H_0^2$$

Note, the net force is y directed only and independent of x.

For the more general Fourier expanded field of (2-3) $\vec{H} \cdot \vec{H}$ becomes

$$\sum_{m=1}^{\infty} \sum_{l=1}^{\infty} H_m H_l e^{-(m+l)ky} \cos(m-l)kx \quad (2-5)$$

The force is obtained by taking the gradient of (2-5) and multiplying by the constant α' of (2-3)

$$\vec{F} = -\alpha' \sum_{m=1}^{\infty} \sum_{l=1}^{\infty} H_m H_l \begin{cases} (m+l) k e^{-(m+l)ky} \cos(m-l) kx \hat{i}_y \\ (m-l) k e^{-(m+l)ky} \sin(m-l) kx \hat{i}_x \end{cases} \quad (2-6)$$

Equation (2-6) contains many components that will contribute little to a particle's motion, When $m = l$, all the x directed force components vanish. Furthermore, if $m \neq l$, both the x and y force components have a sinusoidal x dependence which averages out for interaction lengths greater than one wavelength. This averaging is more effective when l and m are quite different. Thus the significant force contributions occur when $l = m$ and is y directed.

$$\vec{F} = -\alpha' \sum_{m=1}^{\infty} H_m^2 (2mk) e^{-2mky} \hat{i}_y \quad (2-7)$$

The reader may wonder if there are other significant mechanisms for producing a magnetic force not accounted for by this model. Remembering that the force per unit volume is $\mu_0 \bar{M} \cdot \nabla \bar{H}$, it is evident that the existence of a permanent moment \bar{m} yields a force other than in the direction $\nabla(\bar{H} \cdot \bar{H})$. Non-colinear alignment of \bar{m} and \bar{H} results in a torque on the particle and a consequent particle spin. Hysteresis would have the effect of giving rise to a non-colinear magnetization in a changing external field. Increasing temperature can cause permeability to decrease (true of most ferromagnetic materials) or to increase (e.g. magnetite below the Curie temperature). None of these effects will be considered in this thesis. The author will be using ferromagnetic powder ($\rho \sim 7 \times 10^3 \text{ kg/m}^3$) with a permeability much greater than μ_0 .

B. General Precipitation Remarks

The author shall for the remainder of the chapter limit the discussion to particle flows where inertia is unimportant. The aim, specifically, in this section, is to gain an understanding of the important general properties common to electric and magnetic precipitators. The added complication of inertia effects will be considered in Chapter 4.

We shall consider the flow of particulate in a fluid of velocity \bar{u} acted on by a migration force \bar{F} . The particle flux is

$$\bar{T} = n(\bar{u} + \bar{F}/\beta) \tag{2-8}$$

where n = particle density
 β = Stokes drag coefficient $6\pi\eta r$
 and $q\bar{E}$ = electric precipitation
 $\bar{F} = \alpha' \nabla \bar{H} \cdot \bar{H}$ = magnetic precipitation

Since $\frac{\partial n}{\partial t} + \nabla \cdot \bar{\Gamma} = 0$, the Lagrangian density follows (assuming $\nabla \cdot \bar{u} = 0$)

$$\frac{dn}{dt} = - \nabla \cdot \left(\frac{\bar{\Gamma}}{\beta} \right) n$$

along

(2-9)

$$\frac{d\bar{r}}{dt} = \bar{U} + \bar{F}/\beta$$

When inertia is negligible, Eqn. (2-9) describes the state of the particulate. The problem with (2-9) is that the velocity \bar{U} in turbulent flows is a highly fluctuating quantity. A typical electric precipitation with negligible self field effect has a divergence free force field ($\nabla \cdot q\bar{E} = 0$). In such an electric precipitator, the particulate density is constant along any trajectory flow line. One might wonder if the density would ever decrease in a channel even when precipitation occurs. Equation (2-9) shows that whenever a packet of particulate enters the volume of interest, the density in the packet remains unchanged no matter how random or fluctuating its path. The particulate associated with a trajectory is removed from the flow when it meets a surface. Trajectories entering through solid surfaces (e.g. side walls in a channel) enter the volume of interest with zero density. It is the continued mixing of these zero density trajectories with initial particulate trajectories (which are themselves constantly being removed by precipitation) in turbulent flow that leads to a density decay down a channel with a constant cross-sectional value. This is in fact the Deutsch model we shall examine in the next section. The point is that all analyses can be said to be specializations of eqn. (2-9), the key issue being how to

handle the \bar{u} of eqn. (2-9,b). Before applying this general theory to electric and magnetic precipitation in a channel, the author wishes to point out a general property of all magnetic systems.

It follows from (2-9,(a)), that it is impossible to act on particulate with a force field whose divergence is positive definite, and have the density increase with time. This explains self charge spreading in an electric system where $\nabla \cdot \bar{F}$ is proportional to the charge squared. The author will now prove that the density always decays along trajectories for magnetic systems in curl-free regions (in quasistatics this means no current density \bar{J}).

The proof follows by demonstrating the divergence of the force field ($-\nabla(\bar{H} \cdot \bar{H})$) is positive definite. A simplification of the force term can be made

$$\nabla(\bar{H} \cdot \bar{H}) = 2\bar{H} \cdot \nabla \bar{H} + 2\bar{H} \times (\nabla \times \bar{H}) = 2\bar{H} \cdot \nabla \bar{H} \quad (2-10)$$

Using the Einstein summation convention, the term of interest can be written

$$\nabla \cdot \nabla(\bar{H} \cdot \bar{H}) = 2 \frac{\partial}{\partial x_j} (H_i \frac{\partial}{\partial x_i} H_j) = 2 \frac{\partial}{\partial x_j} \frac{\partial}{\partial x_i} (H_i H_j) \quad (2-11)$$

The last step follows after applying $\nabla \cdot \bar{H} = 0$. Applying the divergence free requirement to the last term in (2-44) again leads to

$$\nabla \cdot (\nabla \bar{H} \cdot \bar{H}) = 2 \frac{\partial H_i}{\partial x_j} \frac{\partial H_j}{\partial x_i} \quad (2-12)$$

Now since $\nabla \times \bar{H} = 0$, $\frac{\partial H_i}{\partial x_j} = \frac{\partial H_j}{\partial x_i}$ and the proof of a decaying particulate density is accomplished.

C. Electric Versus Magnetic Precipitation

Before examining in detail the full precipitation problem, it is helpful to consider the nature of the precipitation process, and to identify the inherent difference between electric and magnetic precipitators. Electric precipitators have been around for some time and analyzed extensively, but there lies in the physics of the magnetic precipitator a fundamental dissimilarity that warrants special attention. With this goal in mind, the author will compare the performance of a charged particle precipitator in the limit of complete mixing (the Deutsch model) and the limit of laminar flow with the magnetic precipitator in the same flow regimes.

Electric Precipitation: Figure (2-3) is the basis for modeling electric precipitation in a fully-mixed turbulent duct flow. Particles of charge q in a plug flow velocity U are acted on by a constant vertical field E_0 . It is assumed for the moment, that gravitational forces are negligible. The particles are charged before entering the precipitation region, perhaps by a corona source. The axial dependence of density is derived from mass conservation arguments. In this mixing model, also referred to as the Deutsch model after its originator, the density is uniform over any cross-section because of the turbulent mixing. Balancing the particle flux entering with the flux precipitated and the flux leaving gives

$$U(n(x + \Delta x) - n(x)) 2aw = - \frac{qE_0}{\beta} w \Delta x \quad (2-13)$$

or

$$\frac{dn}{dx} = - \frac{q E_0}{2aU\beta} \quad (2-14)$$

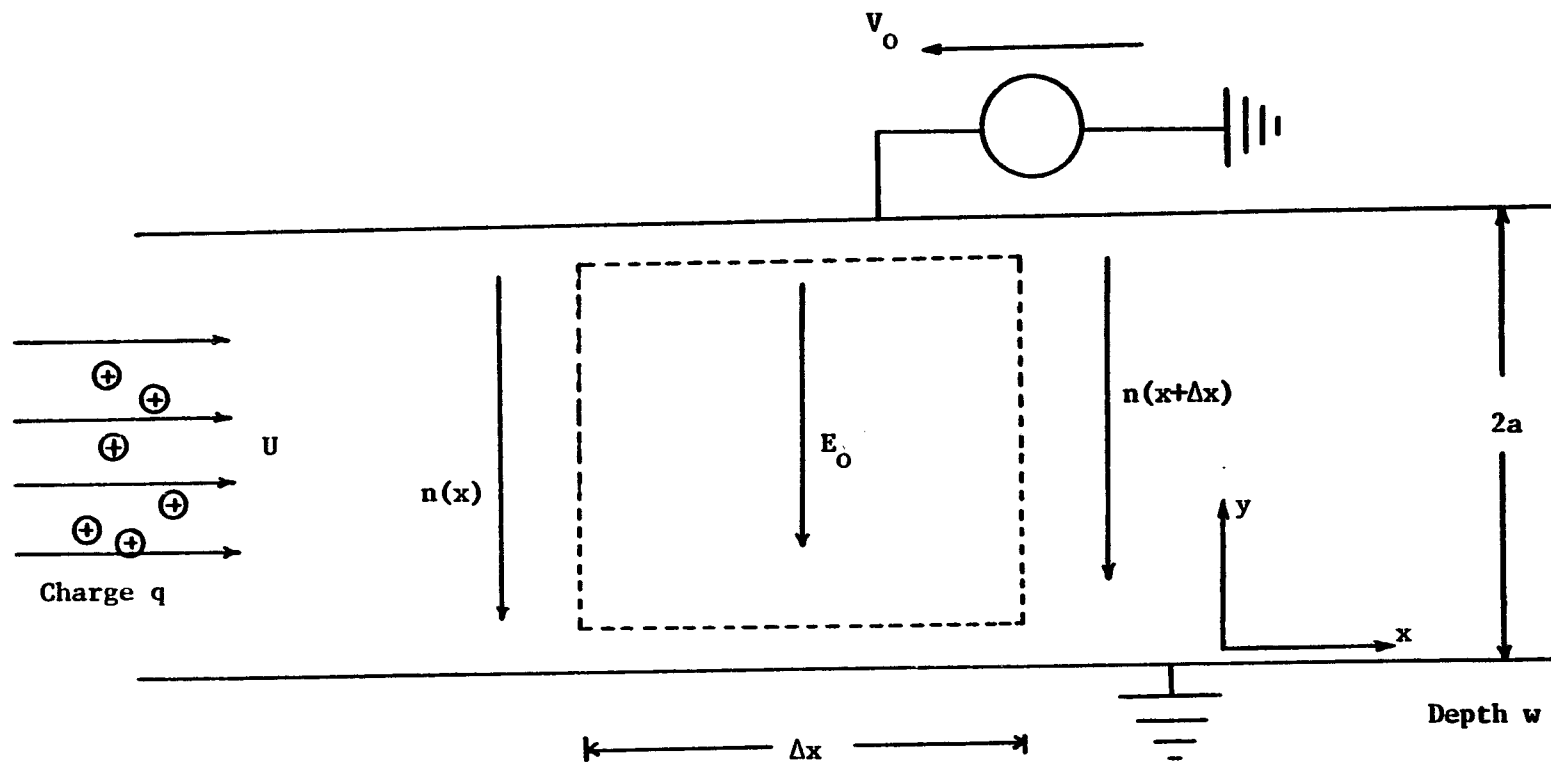


Figure 2-3 Fully Mixed Turbulent Flow Electrostatic Precipitator

The density then decays exponentially as

$$\frac{n}{n_0} = \exp - \frac{(x - x_0)}{l_{p_1}} \quad (2-15)$$

where

$$l_{p_1} = \frac{2a U}{2E_0/\beta}$$

The precipitation length p_1 represents that length when roughly 2/3 of the initial material has been precipitated.

The equivalent precipitator in the laminar flow model is shown in fig. (2-4). An analysis based on mass conservation again follows but the trajectory flow lines are of importance now. The flux at any position in the duct is given by

$$\bar{T} = nU \bar{i}_y - \frac{qE_0}{\beta} n \hat{y} \quad (2-16)$$

Since the divergence of flux must equal the negative time rate of change of the density, it follows that

$$\frac{\partial n}{\partial t} + (U \bar{i}_x - \frac{qE_0}{\beta} \bar{i}_y) \cdot \nabla n = 0 \quad (2-17)$$

Note that the divergence of the \bar{E} field should appear on the RHS of (2-17), ignoring this term is equivalent to assuming self charge effects are negligible and that migration is dominated by the imposed field \bar{E} . Any divergence-free force field will result in a constant density along the trajectory lines.

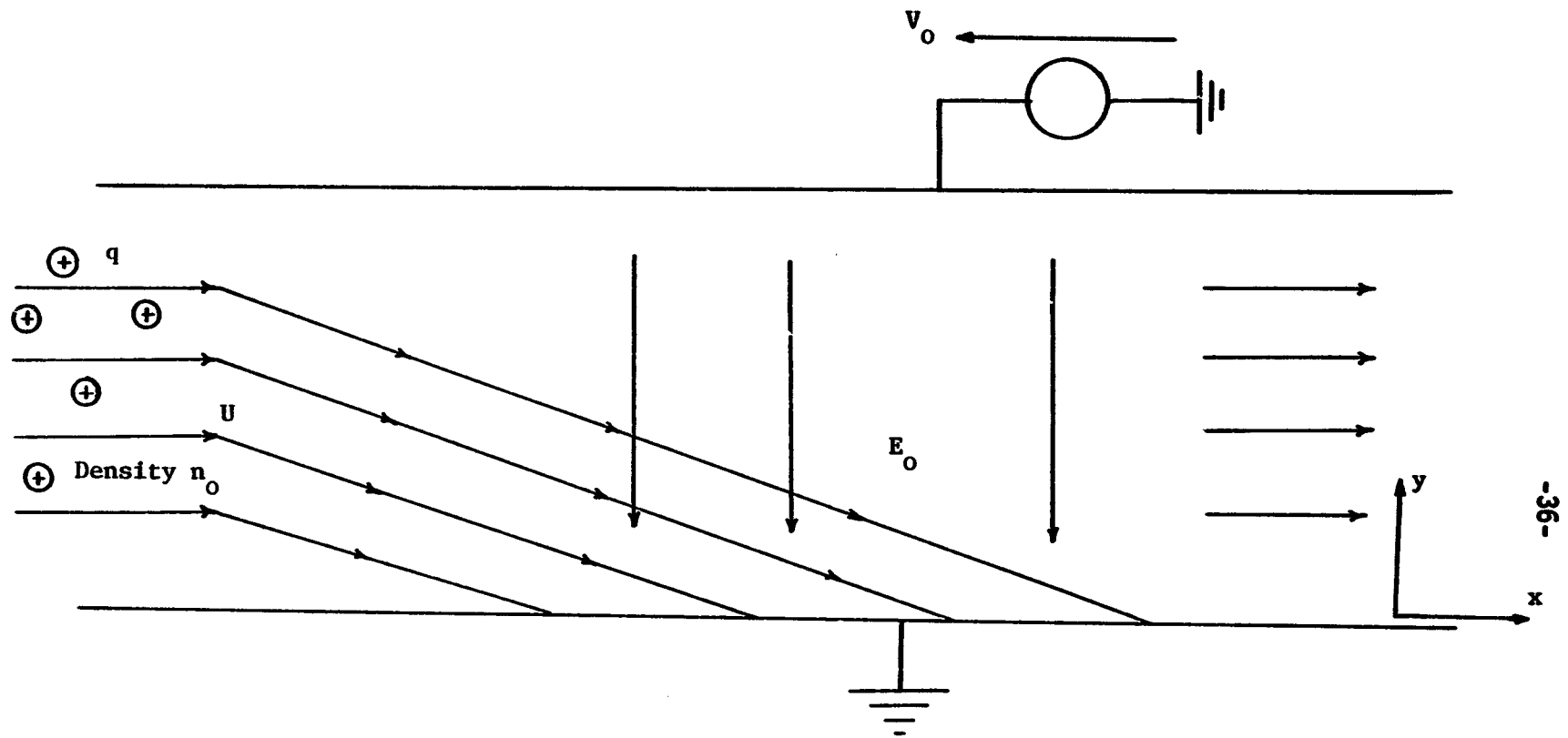


Figure 2-4 Laminar Flow Electrostatic Precipitator Trajectory Model

In the particle's reference frame, (2-17) can be written

$$\frac{dn}{dt} = 0 \quad \text{along}$$

$$\frac{d\bar{r}}{dt} = U \bar{i}_x - \frac{qE_0}{\beta} \bar{i}_y \quad (2-18)$$

Equation (2-18) reveals that all particles are removed in the time it takes for particles to fall the height of the duct ($t = 2a/2E_0/\beta$). The turbulent model never removes all the precipitant. The equivalent precipitation length in the laminar model is

$$\lambda_{p2} = \frac{2a(1 - \frac{1}{e}) U}{q E_0/\beta} \quad (2-19)$$

Not only does the Deutsch model predict that the precipitant is never completely removed, it predicts a longer precipitation length, their ratio being

$$\frac{\lambda_{p2}}{\lambda_{p1}} = 1 - \frac{1}{e} \quad (2-20)$$

The fact that these two lengths are comparable should be quite surprising. In the Deutsch model, particles are supplied to the wall via the turbulent mixing and then precipitated because of the electric field. In the laminar model, migration to the wall is dominated by the electric field force. The precipitation lengths will provide a basis of comparison in examining the magnetic precipitation equivalents.

Magnetic Precipitation: The fully mixed magnetic precipitation model is shown in Fig. (2-5). Magnetizable particles of permeability μ , radius a ,

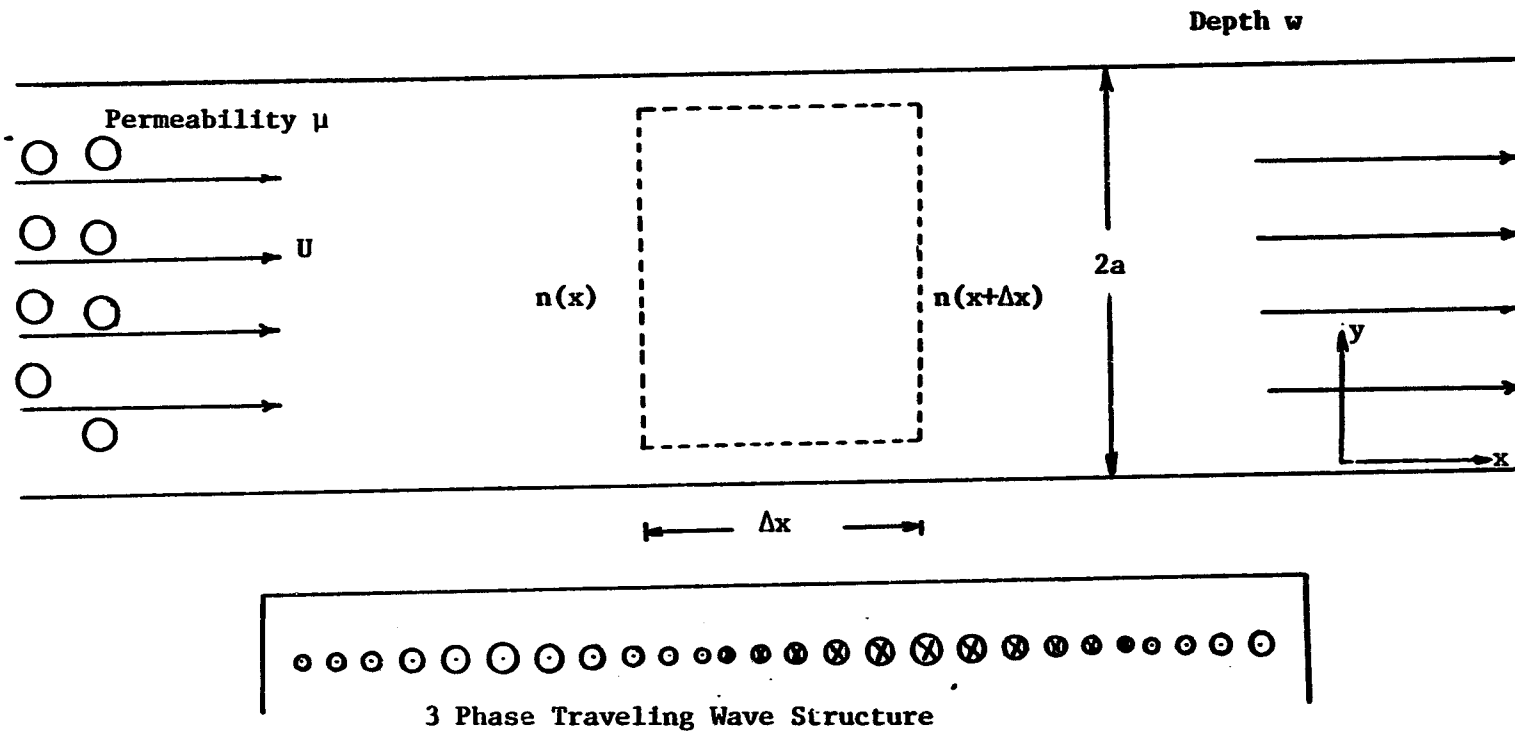


Figure 2-5 Fully Mixed Magnetic Precipitation

and density n enter the duct with plug velocity U . A flux conservation balance requires

$$U 2a (n(x+\Delta x) - n(x))w = \frac{F_y}{\beta} \Delta x w \quad (2-21)$$

where F_y is the magnetic force (ignoring gravity). If the magnetic field structure is a linear travelling wave, (2-5) gives the force as $-\alpha k e^{-2ky} \bar{i}_y$ and (2-21) becomes)

$$\frac{1}{n} \frac{dn}{dx} = - \frac{\alpha k e^{-2ky}}{U\beta(2a)} \quad (2-22)$$

Since the precipitation occurs at the wall where $y = 0$,

$$\frac{n}{n_0} = \exp - \frac{(x-x_0)}{l_{p3}}$$

where (2-23)

$$l_{p3} = \frac{2a U}{\alpha k / \beta}$$

Again particles are supplied to the wall by the turbulent eddy mixing and precipitated via the magnetic force at the wall. Equation (3-23) reveals that the most effective precipitation occurs when k is very large, i.e., when the traveling wave structure has a very small wavelength. The physics discussed earlier would dictate that a small wavelength field would have a high gradient and thus a large particle force.

In the laminar flow model (Fig. 2-6), particles of permeability μ and initial density n_0 enter the duct in plug flow with velocity \bar{U} . A traveling wave source again exerts a vertical force $\alpha k e^{-2ky} \bar{i}_y$. The particle flux is

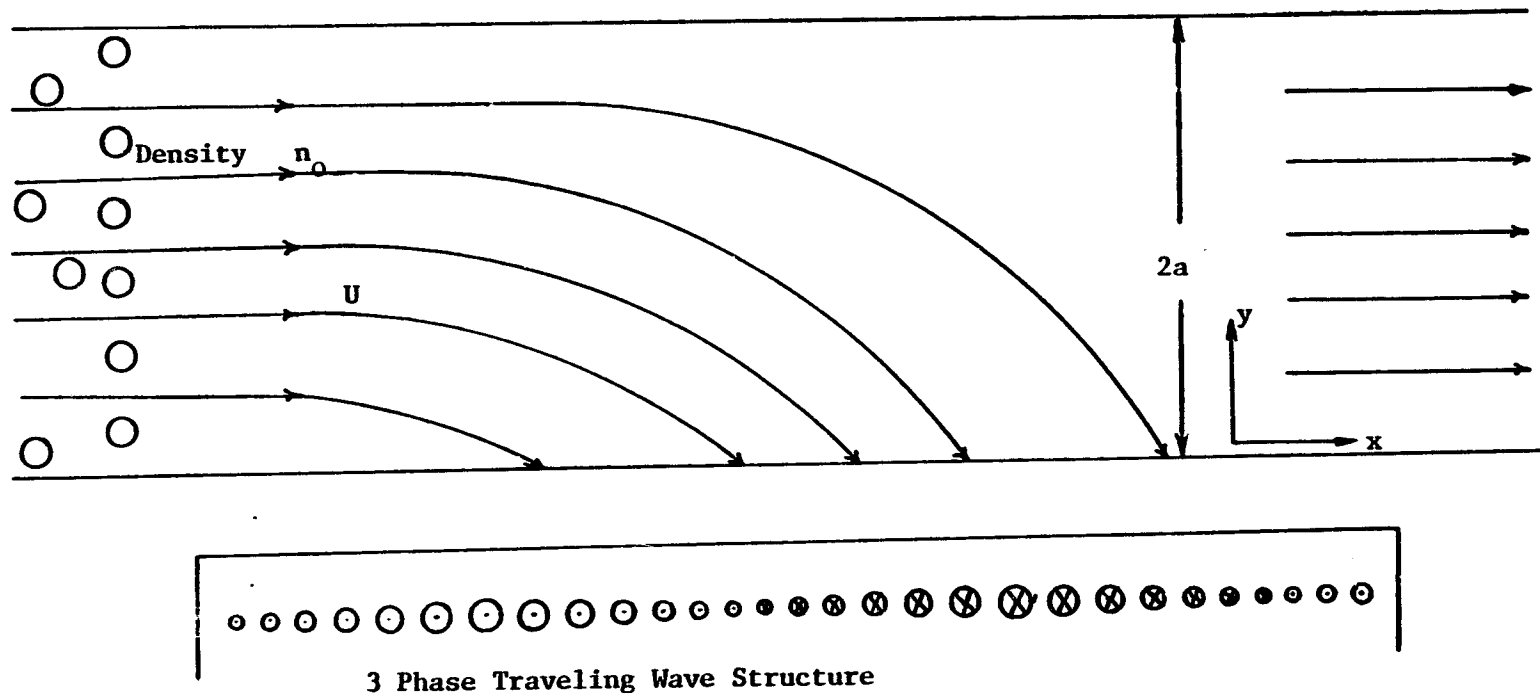


Figure 2-6 Laminar Flow - Magnetic Precipitation Flow Trajectories

$$\bar{T} = U n \bar{T}_x - \frac{\alpha k e^{-2ky}}{\beta} n \hat{i}_y \quad (2-24)$$

Equating the flux divergence with the negative time rate of change of density gives

$$\frac{\partial n}{\partial t} + (U \bar{T}_x - \frac{\alpha k e^{-2ky}}{\beta} \bar{T}_y) \cdot \nabla n = - \frac{2\alpha k^2 e^{-2ky}}{\beta} n \quad (2-25)$$

This is a case where the imposed force field has a limited divergence (see eqn. 2-9,(a)), unlike our electric precipitator. Thus eqn (2-22) can be written

$$\frac{dn}{dt} = - \frac{2\alpha k^2}{\beta} e^{-2ky}$$

along

$$\frac{d\bar{r}}{dt} = U \bar{T}_x - \frac{\alpha k}{\beta} e^{-2ky} \bar{T}_y \quad (2-26)$$

The decay is consistent with the spreading of the particle trajectory lines. By contrast in the electric case, the two-dimensional trajectories are parallel. Integration of (2-26(b)) gives the particle trajectory x and y dependence on time as

$$x = Ut \quad (2-27)$$

$$y = \frac{1}{2k} \ln(e^{2ky_0} - \frac{2\alpha k^2 t}{\beta}) \quad (2-28)$$

where the particle is assumed to begin its trajectory at $x = 0$ and $y = y_0$. The density is found by substituting for y in equation (2-26(a)) and integrating to give

$$\frac{n}{n_0} = 1 - \frac{2 \frac{\alpha k^2}{\beta} t}{e^{2ky_0}} \quad (2-29)$$

The examination of these results as a function of starting position y_0 is found by substituting (2-27) into (2-28) and setting $y = 0$ to give

$$x = \frac{U\beta}{2\alpha k^2} e^{2ky_0} - 1 \quad (2-30)$$

From this result or eqn (2-26,b) it is evident that there exists an optimum wave number for minimizing precipitation length. Setting $\frac{dx}{dk} = 0$ in (2-30) gives

$$e^{2ky_0} (ky_0 - 1) + 1 = 0 \quad (2-31)$$

The solution to this equation occurs when $ky_0 = 0.8$. Because y_0 can be no longer than $2a$, optimum precipitation occurs for the wavelength

$$\lambda = \frac{(2\pi)(2a)}{.8} = 1 \text{ m for a } 12.7 \text{ cm duct.} \quad (2-32)$$

One can now compare the precipitation lengths for the two limiting regimes using this optimum k as was done in the electric case study. The result is that the ratio of the laminar to Deutsch length is .55. This comparison would give the laminar case an unfair advantage. The author wishes

to stress the difference of the above case study results from the electric analog.

The electric case showed no difference (to an order of magnitude) of precipitation lengths for two entirely different flow regimes. The magnetic case gives entirely different results depending on the wavelength. The correct precipitator design for a highly mixed turbulent flow where particulate is supplied to the walls primarily by turbulent diffusion is to install a very short wavelength field structure at the precipitating surface. A good design in a laminar flow regime asks for a wavenumber roughly equal to the reciprocal half duct height. Too small a wavelength means little field penetration into the duct volume, while too large a wavelength results in little field gradient and thus little force. This regime has no help from fluid motion to get particles to the wall.

The foundation of two basic precipitation models is now laid. Further extensions to these models such as the inclusion of additional field harmonics to more accurately represent the \bar{H} -field could be made at this time, but the author wishes to incorporate these into the full precipitation models. A refinement of the magnetic precipitation models presented in this section is developed in Appendix B and the model predictions appear for comparison purposes with other results in Chapter 6.

III. TURBULENCE PHENOMENA

The essential problem in effectively predicting the profiles of magnetizable particles in turbulent air streams is to account for the effect of the turbulent diffusion. Three major camps have evolved in the study of particles in turbulent air stream: the flux conservation camp, the momentum or force balance analysis, and the stochastic or statistical attack. Much empirical work is intermixed with theory and as a result, many terms and seemingly, unrelated variables are used to represent effective turbulent diffusivities. The author wishes to introduce some congruity to these three avenues by an initial section defining the relevant parameters and discussing their interrelation.

A. Parameter Introduction and Interrelationships [1,2]

In laminar flow, it is known that the following relations hold for viscous stress τ and molecular diffusion D .

$$\frac{\tau_{xy}}{\rho} = \nu \frac{\partial v_x}{\partial y} \quad (3-1)$$

$$\frac{\partial n}{\partial t} = D \nabla^2 n \quad (3-2)$$

where ρ = density of the fluid

n = concentration of the particulate ($1/m^3$)

v_x = fluid velocity in the flow (horizontal) direction

y = direction perpendicular to the duct walls

ν = kinematic viscosity

By analogy, it is hypothesized that there exists a similar relationship in turbulent flows, i.e.,

$$\frac{\tau_{xy}}{\rho} = (\nu + \nu_t) \frac{\partial v_x}{\partial y} \approx \nu_t \frac{\partial v_x}{\partial y} \quad (3-3)$$

$$\frac{\partial n}{\partial t} = (D + D_t) \nabla^2 n \sim D_t \nabla^2 n \quad (3-4)$$

Here ν_t , the turbulent or eddy viscosity (often given the symbol ϵ) and D_t , the turbulent diffusivity (often given the symbol ϵ_s) are much larger than the kinematic viscosity and molecular diffusivity respectively.

The conventional starting point in most fluid mechanics derivations is to begin with the Navier-Stokes equations, split the velocity components into mean and fluctuating parts (e.g. $v_x = \bar{v}_x + v'_x$), and then average these equations in time [3]. The x component of the momentum equation becomes

$$\frac{\partial \bar{v}_x}{\partial t} + \bar{v}_x \frac{\partial \bar{v}_x}{\partial x} + \bar{v}_y \frac{\partial \bar{v}_x}{\partial y} + \frac{\partial}{\partial x} (\overline{v_x'^2}) + \frac{\partial}{\partial y} (\overline{v'_x v'_y}) = \frac{1}{\rho} \frac{\partial p}{\partial x} + \nu \nabla^2 \bar{v}_x \quad (3-5)$$

where $\nabla \cdot \bar{v}$ is assumed zero, second order terms have been dropped, no z dependence exists, and $\overline{v_x'^2}$ represents the average of the x directed perturbation velocity squared. In steady state this reduces to

$$0 = - \frac{\partial}{\partial y} (\overline{v'_x v'_y}) + \nu \nabla^2 \bar{v}_x \quad (3-6)$$

The first term on the right hand side of (3-6) is hypothesized to be

$$- \frac{\partial}{\partial y} \left(\nu_t \frac{\partial \bar{v}_x}{\partial y} \right)$$

which completes the connection with equation (3-3). Since the ratio of $\frac{D}{\nu}$ is a constant again, by analogy, it is believed that D_t/ν_t would be a constant. Thus the ultimate goal of determining D_t could be found if ν_t were

known. The major drive then is to determine v_t .

One of the earliest schemes for determining the so called Reynolds stress $(\overline{v'_x v'_y})$ was through the large scale eddy mixing length, given the symbol ℓ . The net flux of particles/area/time in the y direction assuming particles are transferred across a horizontal plane by the same perturbation velocity v'_y is

$$\Gamma_y = v'_y n(y + \Delta y) - v'_y n(y) = v'_y(n(y) + \Delta y \frac{\partial n}{\partial y}) - v'_y n(y)$$

or

$$\Gamma_y = v'_y \ell \frac{\partial n}{\partial y} \tag{3-7}$$

where the representative length in the y direction has been replaced by the Prandtl mixing length. The Prandtl mixing length is effectively the mean free path of a pulse of liquid and is thus a measure of the scale of the turbulent eddies. Comparing (3-7) with (3-3) and (3-4), one sees that $v'_y \ell = D_t$ if v_t equals D_t . Davies [2] points out that due to the elongation, both shear and angular, the processes of momentum and mass transfer will be effected. The mixing length ℓ should be replaced by slightly larger length which would depend on the physical properties of the system and the intensity of the turbulence. A further extension of the mixing length concept is to relate it to the shear stress as follows:

$$\frac{\tau}{\rho} = \ell^2 \left(\frac{\partial v_x}{\partial y} \right)^2 \tag{3-8}$$

giving

$$v_t = \ell^2 \left(\frac{\partial v_x}{\partial y} \right)^2 \tag{3-9}$$

Another parameter, the shear velocity U_* , has been used to evaluate v_t .

$$U_* = \sqrt{\frac{\tau_0}{\rho}} \quad (3-10)$$

Here, τ_0 is the shear stress at the wall. The shear velocity can be calculated by determining the pressure drop between two points in a duct; the details are outlined in a thesis by Videla [3]. From relations (3-7), (3-8), and (3-10), it follows that

$$U_* = \ell \left. \frac{\partial \bar{v}_x}{\partial y} \right|_{\text{wall}} = \left. v'_y \right|_{\text{wall}} = \frac{D_t}{\ell} \quad (3-11)$$

Prandtl first suggested that mixing length was proportional to distance away from the wall through the Von Karman constant ($k \sim 4$).

$$\ell = k_y \quad (3-12)$$

Michel et al. [5] and McDonald, et al. [6] have calculated relationships for mixing length as a function of distance from the wall, but their transition across the boundary layer is questionable (see Fig. 3-1). Videla voices a caution about developing the mixing length approach. Apparently a more realistic transition can be framed by focusing on the character of the eddy viscosity and its associated shear stress rather than the mixing length concept.

An approach the author feels may be more fruitful was first fostered by Taylor [7]. The argument runs as follows: the position $y(t)$ of a given fluid particle is

$$y(t) = \int_0^t v'_y(t') dt' \quad (3-13)$$

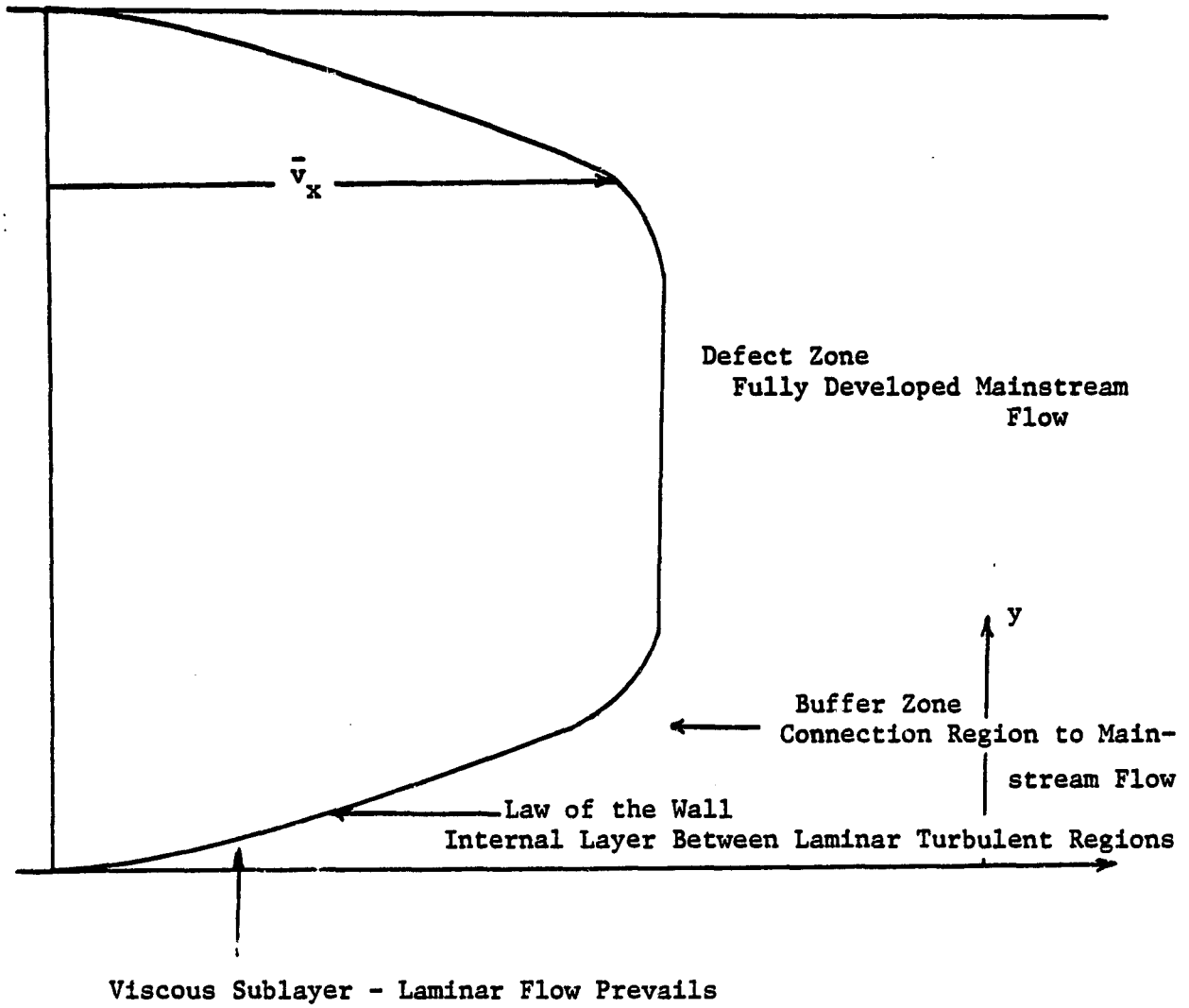


Figure 3-1 Different Regions of Turbulent Duct Flow

where $v'_y(t')$ is the Lagrangian perturbation particle velocity in the vertical direction. (We could just as well analyze the perturbation from the mean in the x direction.) Now

$$\overline{v'_y(t) v'_y(t)} = \frac{1}{2} \frac{\partial}{\partial t} \overline{y^2(t)} = \int_0^t \overline{v'_y(t') v'_y(t)} dt' \quad (3-14)$$

where the overbar signifies average (i.e., the integrand is first averaged over t). Finally, it follows that after a change of variables ($T = t - t'$) and for long times

$$\frac{1}{2} \frac{\partial}{\partial t} \overline{y^2(t)} = \overline{v_y'^2} \int_0^\infty \frac{\overline{v'_y(t) v'_y(t-\tau)}}{\overline{v_y'^2}} dt' = \overline{v_y'^2} T \quad (3-15)$$

where $\overline{v_y'^2}$ is the turbulent intensity in the y direction obtained by squaring the perturbation velocity in that direction and then averaging on time.

The symbol T is called the Lagrangian integral time scale and represents the time it would take for neighboring fluid eddies to become completely uncorrelated. It is often tied in with the Lagrangian integral scale length and related to the integral time scale through the average turbulent velocity [8].

$$L = T \overline{v_x} \quad (3-16)$$

This length or Lagrangian eddy scale as it is also called, represents the length a fluid element would travel before originally neighboring fluid elements would become uncorrelated. It represents the size of the energy carrying eddies, those which get their energy from the main stream flow. The smaller eddies dissipate their energy through viscosity. Another form

of this length scale is given as

$$L = \int_0^{\infty} R(y) dy \quad (3-17)$$

where $R(y)$ = velocity correlation = $\frac{\overline{v'_y(\xi) v'_y(y)}}{\overline{v'^2_y}}$ averaged on ξ

The alternate correlation in space

$$R_y(t) = \frac{\overline{v'_y(t') v'_y(t'-t)}}{\overline{v'^2_y}} \quad \text{averaged on } t' \quad (3-18)$$

Hinze [8] argues, must be equivalent to the space correlation when working with Eulerian velocities.

Before drawing the connection between (3-15) and D_t , it should be observed that in homogeneous turbulence (which is what the author will be assuming) the above analysis follows in all directions. Furthermore, the time and integral length scale will be the same. Finally, the above analysis was valid in a Lagrangian frame where tagged particles are followed. The measurements done in this paper will be Eulerian. Following a lead by Barfield, et al. [9], the author chooses to assume the Eulerian statistics are valid. The reader is referred to a thesis by Chadam for further discussion of this topic [10].

The differential mass in the control volume of Fig. 3-2 is

$$dm = \rho dx dy dz \quad (3-19)$$

Locally, the normal gradient of velocity is approximately a constant $\partial \bar{v}_x / \partial y$. The differential x-directed momentum is

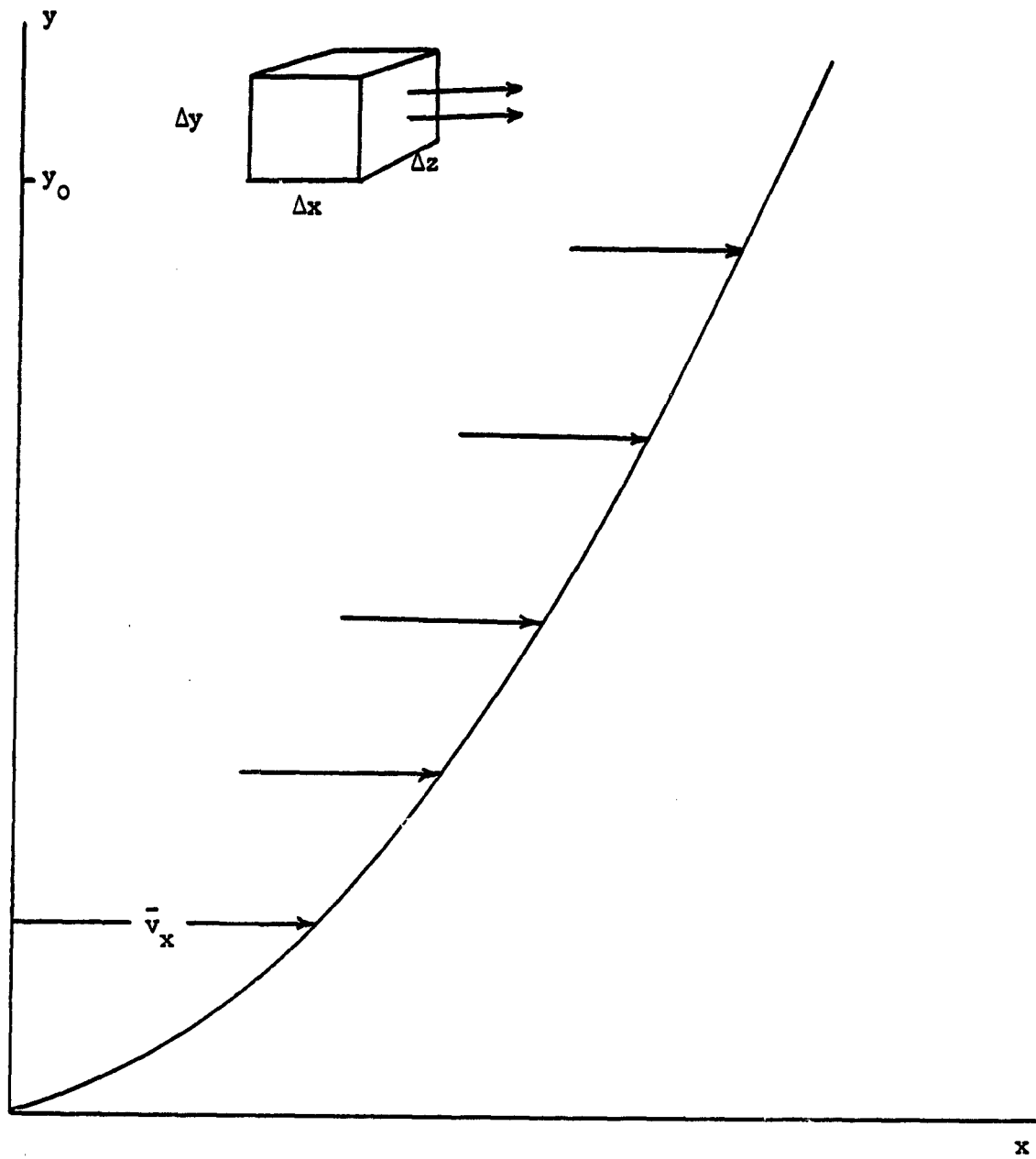


Figure 3-2 Momentum Transfer in Turbulent Flow

$$dP_x = \rho \left(\frac{\partial \bar{v}_x}{\partial y} \right) \Delta y (dx \, dy \, dz) \quad (3-20)$$

Integrating over y gives the net x directed momentum over this infinitesimal rectangular area

$$P_x = \frac{1}{2} \rho \frac{\partial \bar{v}_x}{\partial y} (y-y_0)^2 \Delta x \Delta z \quad (3-21)$$

Differentiating and averaging gives the net longitudinal stress as

$$\tau_{xy} = \frac{1}{2} \rho \frac{\partial \bar{v}_x}{\partial y} \frac{d}{dt} (\bar{y}^2) \quad (3-22)$$

Thus one observes from (3-15) that the turbulent intensity \bar{v}'^2 and the Lagrangian time scale are related to the turbulent kinematic viscosity.

$$\nu_t = \bar{v}'^2 \tau \quad (3-23)$$

One more point needs to be considered before the procedure is consistent. Yermolli and Taggart [11] have shown after a lengthy study that the diffusivity and eddy viscosity are not equal and indeed vary with particle size, density, and mixture concentration. A more accurate procedure would be to let

$$D_t = \beta \nu_t \quad (3-24)$$

(see Videla [3]). However, their results showed β varied between .9 and 2 for sundry sizes and mixtures. In addition, Chien and Einstein [12] showed that for various mixtures, β was almost nearly one. The author will in this work consider $\beta = 1.0$ henceforth. There is a fourth approach based on the time scale necessary to dissipate the energy of the eddies.

$(\sqrt{\frac{\partial^2 R(t)}{\partial t^2}})$ but the interested reader is referred to Hinze.

To summarize, the different methods of approximating turbulent diffusion are as follows:

(a) through mixing length

$$v_t = \ell^2 \frac{\partial \bar{v}_x}{\partial y} = v_y' \ell \quad (3-25)$$

(b) through shear velocity $U_* = \sqrt{\frac{\tau_0}{\rho}}$

$$v_t = U_* \ell \quad (3-26)$$

(c) through turbulent intensity and the Lagrangian (= Eulerian) time scale

$$v_t = \bar{v}'^2 T \quad (3-27)$$

All of the above assume that $D_t = \beta v_t \approx v_t$. It remains to demonstrate how these three attacks can be used to determine particle concentration.

B. Flux Conservation

The earliest work using this method for approaching turbulent diffusion was done by Schmidt (1925) and Prandtl (1926) [13]. A detailed analysis of the theory is outlined by Bauday [14]. We shall for the remainder of this chapter consider no other external forces aside from gravity. Beginning with the mass conservation equations, all quantities are broken up into steady state and fluctuating parts as was suggested earlier, yielding an equation of the form

$$\overline{n' v_y'} + n w_y = 0$$

where $y =$ vertical direction

v'_y = perturbation velocity in the y direction

w_y = fall velocity in the y direction

n = average concentration

(3-28)

n' = perturbation from average concentration

Here Schmidt hypothesized the $\overline{n'v'} = D_t \frac{\partial n}{\partial y}$ which yields the so-called Schmidt equation

$$D_t \frac{\partial n}{\partial y} + w_y n = 0 \quad (3-29)$$

The author wishes to outline a flux conservation argument because of its applicability to forthcoming work. If $\bar{\Gamma}$ represents the flux of particles, then the net particle flux $\bar{\Gamma}$ (particles/area/time) becomes

$$\begin{aligned} \bar{\Gamma} &= \text{convection} + \text{diffusion} + \text{migration (gravity)} \\ &= \bar{v}n + (D_t + D_{\text{molecular}}) \nabla n + \bar{w}n \end{aligned} \quad (3-30,a)$$

The divergence of flux must equal the negative time rate of change of concentration.

$$\frac{\partial n}{\partial t} = \frac{\partial(v_x n)}{\partial x} + \frac{\partial(v'_y n)}{\partial y} + \frac{\partial(v_z n)}{\partial z} + (D_t + D_m) \nabla^2 n + \frac{\partial(\omega_y n)}{\partial y} \quad (3-30,b)$$

A simpler expression of (3-30) results from noting that the net y directed flux must be zero. Averaging (3-30(b)) and neglecting $D_{\text{molecular}}$ as small, gives

$$D_t \frac{\partial n}{\partial y} + w_y n = 0 \quad (3-31)$$

The reader should note that three assumptions are inherent in (3-31)--steady state conditions exist, the particulate is dispersed evenly over the channel and is therefore considered a continuum, and no net buildup of particulate

occurs.

The work the author has examined is quite extensive and centers on manipulations of equation (3-31) [15,16,17,18]. Graf and Raudkivi and Yalin also give a broad scope of the general analysis, Csanady is quite clear, and Hinze is the most detailed and complete. Taggart and Yermolli as well as Videla are clear, supplying much of the background justification.

The key to the problem is in finding a diffusion coefficient to match a given turbulent flow. Assuming D_t is constant as Hurst (1929) [11] first did,

$$\frac{n}{n_0} = \exp \left[- [w_y(y-a)]/D_t \right] \quad (3-32)$$

where n_0 is the concentration in the center of the duct at position $y = a$.

A more realistic approximation to D_t may be gotten through (3-3). In a turbulent rectangular channel, the shear stress is [11]

$$\tau = \tau_0 \left(1 - \frac{y}{y_0} \right) \quad (3-33)$$

where τ_0 is the stress at the wall and y_0 is the distance to the center of the duct. Ippen [19] expressed the flow in a turbulent channel as

$$\frac{\bar{v}_x}{\bar{v}_{x_{\max}}} = \frac{\ln \left(1 + \frac{y}{\sqrt{k}U_*} \right)}{\ln \left(1 + \frac{y_0}{\sqrt{k}U_*} \right)} \quad (3-34)$$

Von Karman and Prandtl independently determine the turbulent velocity relation in 1934 [11] to be

$$\frac{\bar{v}_x - \bar{v}_{x_{\max}}}{U_*} = \frac{1}{k} \ln \left(\frac{y}{y_0} \right) \quad (3-35)$$

using (3-34), (3-33) and (3-3), one can integrate to get

$$\frac{n}{n_0} = \left[\frac{y_0 - y}{y_0 - (\nu/k U_*)} \right] \left[\frac{2(\nu/k U_*)}{y + \nu/k U_*} \right]^{-1} \frac{1}{\beta} \frac{w_y}{k U_*} \quad (3-36)$$

and if (3-35) is used,

$$\frac{n}{n_b} = \left[\frac{y_0 - y}{y_0 - b} \frac{b}{y} \right] \frac{w_y}{\beta U_* k} \quad (3-37)$$

where n_b is the concentration at some height b .

Indeed the various attempts to obtain an accurate approximation for D_t are quite involved. Videla chooses to evaluate different diffusion coefficients in the different flow zones shown in Fig. 3-1. The notion that ν_t depends on distance from the wall seems reasonable because of the smaller scale eddies near the wall and the altered flow in the boundary layer. The summary of his work is as follows:

Laminar sub-layer	$\nu_t = \nu$	
Buffer zone	$\nu_t = \nu \left\{ 1 + \frac{k_y U_*}{\nu} \tanh \left(a \frac{y U_*}{\nu} \right) \right\}$	
Wall zone	$\nu_t = \nu k y \frac{U_*}{\nu} \frac{(1-y)}{(1-y^m)}$	where y = non-dimensional vertical
		$m = \text{constant}$
Defect zone	$\nu_t = U_* y_0 k \frac{y(1-y)}{1-y^m}$	(3-38)

Finally, White attempts to make correlations between ν_t and the Prandtl mixing length [20].

Several observations have sparked research along alternate lines [17]. For example, experiments indicate that the Von Karman constant (3-35) of

flow with suspensions of neutrally buoyant particles decreases with increasing concentration while the turbulent intensity increases. This runs contrary to the assumption that flows of neutrally buoyant particles should remain unaffected since no energy is required to suspend them.

C. Momentum Equation Attack

The first major attempt to describe the motion of particles in a turbulent stream was by Tchen [21]. His starting point was the momentum equation for the particle

$$\underbrace{\frac{4}{3} \pi r_p^3 \rho_p \frac{dv_p}{dt}}_1 = \underbrace{6\pi\mu r_p (v_f - v_p)}_2 + \underbrace{\frac{4}{3} \pi r_p^3 \rho_f \frac{dv_f}{dt}}_3 + \underbrace{\frac{1}{2} \frac{4}{3} \pi r_p^3 \rho_f \left(\frac{dv_f}{dt} - \frac{dv_p}{dt} \right)}_4$$

$$+ \underbrace{6r_p^3 \sqrt{\pi\rho_f\mu} \int_{t_0}^t \frac{\left(\frac{dv_f}{dt'} - \frac{dv_p}{dt'} \right)}{\sqrt{t-t'}} dt'}_5 + \underbrace{F_e}_6 \quad (3-39)$$

The subscripts p and f refer to particle and fluid respectively. The terms are explained as follows:

- 1) force required to accelerate particle
- 2) Stokes viscous resistance force
- 3) pressure gradient force in the fluid surrounding the particle caused by acceleration of the fluid
- 4) force to accelerate the virtual added mass of the particle relative to the ambient fluid
- 5) force due to the fluctuating, non-steady state flow pattern
- 6) external force field such as gravity or electromagnetic forces

The analysis involves auto correlations of the fluid velocity, via a Fourier integral switch into the frequency domain. The result is an expectation value of the square of the particle's position [22,8,17]. The theory involves several assumptions, one of which requires that the neighboring fluid near the particle not change with time. This assumption reduces the Tchen analysis to a pedagogical exercise for turbulent flows.

Khosla and Lederman [23] attempt to build on Tchen's theory and alter the above limiting assumption. Instead of allowing time rates of change of the particle ($\frac{d}{dt}_p$) to equal those of the fluid ($\frac{d}{dt}_f$), they hypothesized

$$\frac{dv_p}{dt_p} = \frac{dv_p}{dt_f} + \gamma v_p \quad (3-40)$$

where γ is an empirically determined constant. The analysis again proceeds by going into the fourier frequency regime, and seeks to find the ratio of the diffusivities of particle and fluid. They conclude that the results are sensitive to temperature, density of fluid, and the presence of various particles. These factors limit the method to low frequency and low speed turbulent flow.

A momentum attack that has much credibility and links back to Taylor's early work [7] was first fostered by Chadam [10] and later elaborated by Barfield, et al. [9]. With only the external force of gravity, the equation of motion of the particle is

$$\frac{d\bar{v}_p}{dt} = \bar{a}(t) - \beta \bar{v}_p - \left(1 - \frac{\rho_f}{\rho_p}\right) \bar{g} \quad (3-41)$$

where

$$\beta = \frac{6\pi\eta r_p}{\rho_p}$$

$$\frac{\rho_f}{\rho_p} = \frac{\text{density fluid}}{\text{density particle}} \ll 1$$

and $a(t)$ = the accelerative forces imparted to the particle by the fluid turbulence. If the particle was being dragged by the turbulent fluid, in a Stokes type drag, one could represent this acceleration as $\beta v_f(t)$, which is what the author will assume.

Chadam integrates (3-41) directly but without including the effect of gravity. His analysis proceeds as follows:

$$v_p(t) = v_0 e^{-\beta t} + e^{-\beta t} \int_0^t e^{-\beta \xi} a(\xi) d\xi \quad (3-42)$$

$$x_p(t) = \frac{v_0}{\beta} (1 - e^{-\beta t}) - \frac{1}{\beta} e^{-\beta t} \int_0^t e^{\beta \xi} a(\xi) d\xi + \frac{1}{\beta} \int_0^t a(\xi) d\xi \quad (3-43)$$

Squaring and averaging gives

$$\overline{x(t)^2} = \frac{2\bar{A}}{\beta^2} t + \frac{v_0^2}{\beta^2} (1 - e^{-\beta t})^2 + \frac{\bar{A}}{2\beta^2} (-3 + 4e^{-\beta t} - e^{-2\beta t}) \quad (3-44)$$

where $\bar{A} =$

$$\int_t^{t+\Delta t} \int_t^{t+\Delta t} a(\xi) a(\theta) d\xi d\theta$$

and

$$\bar{A} = \beta^2 \int_0^{\infty} v_f(t) v_f(t-\tau) d\tau$$

where the note after (3-41) has been used.

With the analogy in (3-15) with Taylor's work, a connection to D_t follows

$$D_t = \frac{1}{2} \frac{d}{dt} \overline{x^2} \rightarrow t_{\text{large}}, \overline{x^2} = \frac{2\bar{A}t}{\beta^2} \rightarrow \begin{cases} D_t = \int v_f(t) v_f(t-\tau) d\tau \\ D_t = \overline{v'^2} t \end{cases} \quad (3-45)$$

$$t_{\text{small}}, \overline{x^2} = v_0^2 t^2 \rightarrow D_t = \overline{v'^2} t$$

Note, attention is fixed on the change in average squared position. The v_0 introduced in (3-42) is a turbulent perturbation velocity, the same as v' introduced earlier. The objective is to determine the fluctuation from the steady laminar type flow.

The author would suggest another approach--to integrate (3-41). First, rewrite the basic equation as ($\bar{g} = 0$)

$$\frac{dv'_{xp}}{dt} + \beta v'_{xp} = \beta v'_{xf} \quad (3-46)$$

The homogeneous solution of (3-46) gives $e^{-\beta(t-\tau)}$ as the impulse response $U_0(t-\tau)$ of the system. With $\beta v'_{xf}$ the drive, v'_{xp} becomes

$$v'_{xp}(t) = \int_{-\infty}^t e^{-\beta(t-\tau)} \beta v'_{xf}(\tau) d\tau \quad (3-47)$$

Thus

$$x_p(t) = \int_0^t \int_{-\infty}^t e^{-\beta(t-\tau)} \beta v'_{xf}(\tau) d\tau dt \quad (3-48)$$

interchanging the order of integration gives

$$x_p(t) = \int_{-\infty}^t \{1 - e^{-\beta(t-\tau)}\} v'_{x_p}(\tau) dt \quad (3-49)$$

Barfield [9] (after erroneously writing (3-49)) claims that it is reasonable to assume that the turbulent diffusion process is Gaussian and has a variance equal to

$$\sigma^2 = \bar{A} \int_0^t (1 - e^{-\beta(t-\tau)})^2 dt \quad (3-50)$$

and a probability distribution function

$$f(x_p) = \left(\frac{1}{\sqrt{4\pi\sigma^2}} \right) \exp\left(-\frac{1}{2} \frac{x_p^2}{\sigma^2} \right) \quad (3-51)$$

Evaluation of (3-40) gives the same result as in (3-44) which agrees with Chadam. Barfield then generalizes this attack by including the gravitational field. Integrating (3-41) as before gives (from 3-49 but in the y direction)

$$y_p(t) = \int_{-\infty}^t \{1 - e^{-\beta(t-\tau)}\} [v'_y(\tau) - \frac{g}{\beta}] dt \quad (3-52)$$

or

$$y_p + \frac{g}{\beta^2} (\beta t - 1) = \int_{-\infty}^t [1 - e^{-\beta(t-\tau)}] v'_y(\tau) dt \quad (3-53)$$

where the lower bound on the particle's position is changed to zero for physical reasons. Barfield again argues that a normal Gaussian distribution applies and the the probability distribution of the function

$$G = y(t) + \frac{g}{\beta^2} (\beta t - 1) \text{ is}$$

$$f(G) = \left(\frac{1}{\sqrt{4\pi\sigma^2}} \right) \exp\left(-\frac{1}{2} \frac{G^2}{\sigma^2} \right) \quad (3-54)$$

with a mean of

$$\bar{y} = -\frac{g}{\beta^2} (\beta t - 1) \quad (3-55)$$

and the same variance as in (3-51).

The Gaussian assumption is generally accepted especially where turbulent diffusion occurs in the atmosphere [18]. Indeed, fine particle plume concentration analyses are developed from this view point. If one begins with the diffusion equation, the analysis is as follows:

$$\frac{\partial n}{\partial t} + \bar{v}_p n = D_T \nabla^2 n \quad (3-56)$$

whose solution is

$$n = \frac{n_0}{2\sqrt{\pi D_t t}} e^{-x^2/4D_t t} \quad (3-57)$$

The spread variance is

$$\sigma_x^2 = \frac{1}{n_0} \int_{-\infty}^{\infty} x^2 n dx = 2 D_t \quad (3-58)$$

This variance is identical with Barfield and perhaps guided his reasoning along these lines. If one thinks of σ_x^2 as \bar{x}_p^2 and remembering (in line with Taylor's work) that $D_{t_x} = \frac{1}{2} \frac{d}{dt} x^2$ the 3-D plume spread from a point becomes [8,18] (in a uniform x directed flow)

$$n = \frac{n_0}{(2\pi)^{3/2} \sigma_x \sigma_y \sigma_z} \exp \left\{ -\frac{(x - \bar{v}_x t)^2}{2\sigma_x^2} - \frac{y^2}{2\sigma_y^2} - \frac{z^2}{2\sigma_z^2} \right\} \quad (3-59)$$

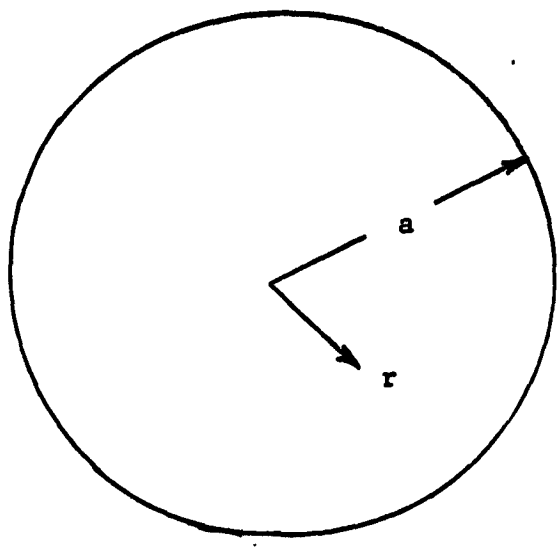
where C_0 is the number of kilograms released per unit time at the origin. In line with (3-45) it follows that $\sigma_x^2 = \overline{v_x^2} t^2$ for short times (distances) and is $2\overline{v_x^2} T t$ for long times. The steady state source distribution is ob-

tained by integrating (3-59) from zero to infinity with $\sigma_x^2 = 2v_x'^2 Tt$, $\sigma_y^2 = 2v_y'^2 Tt$, $\sigma_z^2 = 2v_z'^2 Tt$ at large distances. Thus

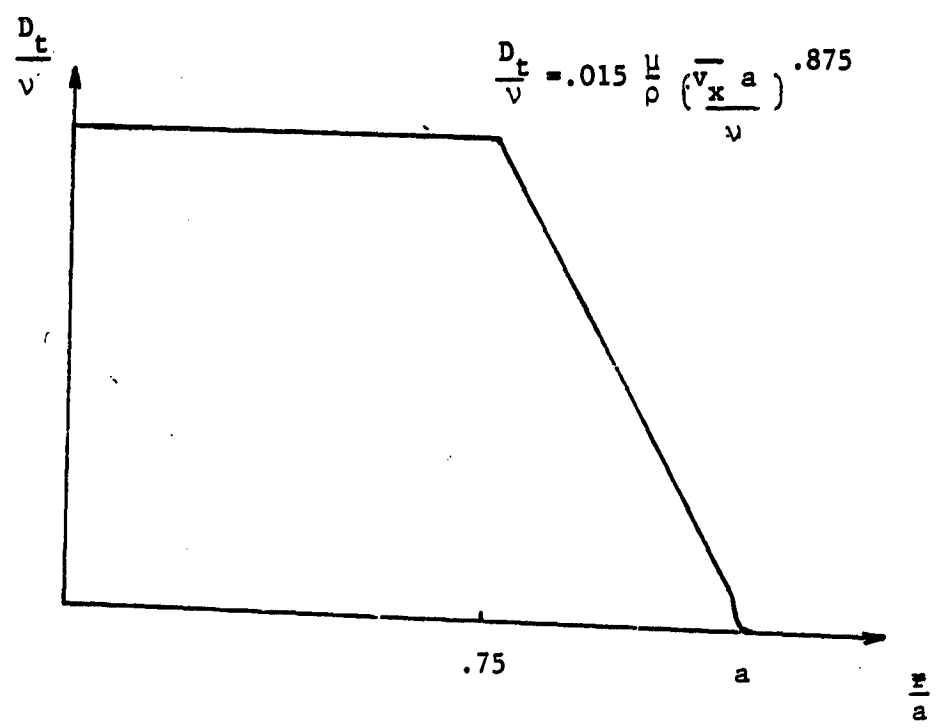
$$n = \frac{1}{4\pi(v_x'^2 v_y'^2 v_z'^2 T^3)^{1/2} \left[\frac{x^2}{v_x'^2 T} + \frac{y^2}{v_y'^2 T} + \frac{z^2}{v_z'^2 T} \right]^{1/2}} \exp - \frac{v_x}{2v_x'^2} \sqrt{v_x'^2 T} \left\{ \left(\frac{x^2}{v_x'^2 T} + \frac{y^2}{v_x'^2 T} + \frac{z^2}{v_x'^2 T} \right)^{1/2} - x \right\} \quad (3-60)$$

The author wishes only to point out the connection to the momentum Gaussian approach here. Chadam makes the connection between this probability distribution and the flux diffusivity model using statistical arguments (in the next section). However, one last point should be made concerning the connection between time and distance relationships of diffusivity as seen in sections B and C. Equation (3-44,b) points out that D_t represents the correlation of the fluid velocity with itself, that is the time it takes a fluid element to forget its neighbor. The diffusivity is constant for long times when fluid velocities are uncorrelated. Davies shows that in the center of pipes diffusivity is constant and changes over the wall region, as shown by Fig. (3-3). Near the wall, turbulent eddies are more correlated than at the center. (This is not exactly the same for rectangular ducts.) This process is considered ergodic in the sense that time averages are related to space averages. Herein lies the reliability of the formulas listed in section A showing space dependence.

Lastly, a method for obtaining diffusivity in the main core of the channel based on the pipe friction factor has been fostered by Dhanak [27] and used in predicting the performance of electrostatic precipitation [28].



(a) Pipe Cross Section



(b) Radial Dependence

Figure 3-3 Pipe Diffusivity

Dhanak begins by expressing the eddy viscosity ν_t in terms of the Fanning friction factor f of the channel, where

$$f = \frac{2g}{\rho_f} (\bar{v}_x)^2 \tau_0 \quad (3-61)$$

This factor is determined by either pressure differences down the pipe or the Blasius's equation. Although the formula derivation is uncertain, Dhanak concludes that

$$D_t = .0708 R_{e_a} \nu \sqrt{f} \quad (3-62)$$

He compares the above prediction with

$$D_t = \frac{\frac{\overline{v'_x v'_y}}{\partial \bar{v}_x}}{\partial y} \quad (3-63)$$

(Which agrees with (3-6)) and finds good agreement.

D. Statistical Approach

Chadam [10] closes the loop between the Gaussian normal approximation outline in section C and the diffusion equation. He defines a function $W(v; t, v'_0, t_0)$ to be the probability of a fluid element with velocity v_0 at time t_0 to have velocity v' at time t . A similar function $W(x, t, x_0, t_0)$ is defined for transition of particles from position x_0 to x . Csanady states that most turbulent flows behave according to a Markov process, one in which the velocity autocorrelation

$$R(t) = \frac{\overline{v'_x(\tau) v'_x(\tau-t)}}{v'^2_x} = e^{-t/T} \quad (3-64)$$

where the numerator overbar indicates an average over τ .

Chadam shows that in such a process, which can be assumed Gaussian,

$$W(v', t, v'_0, t_0) = \frac{1}{2\pi \frac{A}{\beta} (1 - e^{-2\beta t})^{1/2}} e^{-\left\{ \frac{(v' - v'_0 e^{-\beta t})^2}{\frac{2A}{\beta} (1 - e^{-2\beta t})} \right\}} \quad (3-65)$$

where A is defined in (3-44)

Furthermore,

$$W(x, t, x_0, t_0) = \frac{1}{(2\pi x^2)^{1/2}} \exp. - \frac{(x - x_0)^2}{2x^2} \quad (3-66)$$

which would agree with Barfield et al.'s equation (3-52). His next step however is to find the probability distribution $P(x, t)$ of finding a particle at position, and time t using

$$P(x, t) = \int_{-\infty}^{\infty} P(x', t') W(x, t, x', t') dx' \quad (3-67)$$

It is shown that the function

$$B(\Delta t) = \int_t^{t+\Delta t} a(\xi) d\xi \quad (3-68)$$

has a Gaussian expectation value

$$W(B(\Delta t)) = \frac{1}{(4\pi \bar{A} \Delta T)^{1/2}} \exp \left\{ -\frac{(B(\Delta t))^2}{4\bar{A} \Delta t} \right\} \quad (3-69)$$

The following mathematical Taylor expansion

$$\begin{aligned}
 P(x', t') + \frac{\partial P}{\partial t'}(x, t') &= P(x, t') - \int \Delta x (P'W + PW) d(\Delta x) \\
 &+ \int \frac{\Delta x^2}{2} (PW'' + 2W'P' + P''W) d\Delta x \\
 &+ O(\Delta x)^3
 \end{aligned} \tag{3-70}$$

(where the primes in the integrals indicate space derivatives)
 reduces with (3-67) to

$$\frac{\partial P}{\partial t'} = \frac{\bar{A}}{\beta^2} \frac{\partial^2 P}{\partial x^2} \tag{3-71}$$

Thus, again a turbulent diffusivity results equal to $\bar{v}'^2 \tau$.

The author wishes for completeness to examine two more approaches. Batchelor [24] defines a characteristic function $\phi(\xi)$ in a normally distributed Gaussian field

$$\phi(\xi) = \exp \left[j \frac{mg}{\beta} t - \frac{1}{2} \xi_i^2 \xi_j \overline{x_i x_j^2} \right] \tag{3-72}$$

(adopting Einstein summation convention)

Conditional probabilistic arguments are then used to link $\phi(\xi)$ to $P(r, t)$. This involves transforming between ξ space to x space. The details are given in Barfield [4]. The result after much calculation is

$$\frac{\partial}{\partial t} P[\bar{r}, t] = \frac{\partial}{\partial t} (\overline{x_i x_j}) \frac{\partial^2 P(\bar{r}, t)}{\partial x_i \partial x_j} + \frac{mg}{\beta} \cdot \nabla P(\bar{r}, t) \tag{3-73}$$

and

$$\frac{\partial}{\partial t} (\overline{x_i x_j}) - \frac{1}{2} v_i' v_j' \int_0^t R_{ij}(\tau) + R_{ji}(\tau) d\tau \quad (3-74)$$

where $R_{ij}(\tau) = \frac{v_i(t)v_j(t+\tau)}{\overline{v_i} \overline{v_j}}$ (averaged on t)

Now for large times the integral in (3-74) becomes the Lagrangian time scale T and (3-71) becomes

$$\frac{\partial P(\bar{r}, t)}{\partial t} = v_i' v_j' T \nabla^2 P(\bar{r}, t) + \frac{m\bar{g}}{\beta} \cdot \nabla P(\bar{r}, t) \quad (3-75)$$

Finally, Soo [25] begins by expanding the fluid velocity in an infinite spectrum of harmonics (isotropic turbulence)

$$v_x' = v_y' = v_z' = \sum_{m=1}^{\infty} A_m \sin 2\pi t \quad (3-76)$$

He then couples this into the force equation

$$\frac{d\bar{v}_p'}{dt} = \beta(\bar{v}_f - \bar{v}_p) + \bar{g} \quad (3-77)$$

Next, (3-76) is squared and averaged to give

$$\overline{v_{x_p}'^2} = \frac{1}{2} \sum_{m=1}^{\infty} \frac{A_m^2}{1 + (\frac{2\pi m}{\beta})^2}$$

$$\overline{v_{y_p}'^2} = \frac{1}{2} \sum_{m=1}^{\infty} \frac{A_m^2}{1 + (\frac{2\pi m}{\beta})^2} + \frac{g^2}{\beta^2} \quad (3-78)$$

After expressing the correlation function $R(\tau)$ in terms of these infinite components and the scale of turbulence $\int_0^x R(x) dx$, the Einstein equation for diffusivity [26] is used to relate the diffusivities of one phase of the flow to the other phase. The analysis is intended for intimately mixed or multiphase systems. His conclusion is that the correlation, scale, and intensity of one phase of the system can be calculated from statistical relations on the other phase.

The author will henceforth adopt the position that the turbulence effects can be incorporated into a diffusivity model where $\bar{T}_{\text{Diffusion}} = D_t \nabla n$ and D_t is represented by the turbulent intensity $\overline{v'^2}$ times the Lagrangian time scale $T = \int_0^\infty \frac{\overline{v'(\tau) v'(t-\tau)} dt}{\overline{v'^2}}$. The time scale is physically related to the approximate time for turbulent eddies to decay. It is related to the integral scale L (size of largest eddies) through the mean flow $\overline{v_x}$.

$$T = \frac{L}{\overline{v_x}} \quad (3-79)$$

D_t has been found to behave roughly as $b e^{-\psi y} + d$ in channels. Its measurement will be described in Chapter 5.

Chapter III - Bibliography

1. Tennekes, H., and Lumley, J.L., A First Course in Turbulence, MIT Press, Cambridge, 1972, pp. 1-24.
2. Davies, J.T., Turbulence Phenomena, Academic Press, New York and London, 1972.
3. Videla, J., "Interaction of Two Dimensional Turbulent Flow with Suspended Particles," Ph.D. Thesis, Civil Engineering, MIT, 1973.
4. Barfield, B., "Studies of Turbulence in Shallow Sediment Laden Flow with Superimposed Rainfall," Water Resources Inst., Texas A & M University, Tech. Rept. 11, College Station, Texas, 1968, pp. 106.
5. Michel, R., Quemard, C., and Durant, R., "Hypothesis on the Mixing Length and Application on the Calculation of the Turbulent Boundary Layer," Proceedings AFOSR--Stanford Conference on Boundary Layers, 1968.
6. McDonald, H. and Camarta, F.J., "An Extended Mixing Length Approach for Computing the Turbulent Boundary Layer Development," Proceedings AFOSR--Stanford Conference on Boundary Layer, 1968.
7. Taylor, G.I., "Diffusion by Continuous Movements," Proceedings London Math. Soc., 20, January 1920m pp. 196-212.
8. Hinze, J.O., Turbulence, McGraw Hill Book Co., 2nd ed., 1975.
9. Barfield, B., Smordon, E., Hiler, E., "Prediction of Sediment Profiles in Open Channel Flow by Turbulent Diffusion Theory," Water Resources, Research, Vol. 5, No. 1, February 1969, pp. 291-299.
10. Chadam, J.M., (1961) A Theory of Turbulent Diffusion, M.S. Thesis, Math. Department, MIT.
11. Taggert, W., and Yermolli, Carlow, "Effects of Sediment Size and Graduation on Concentration Profiles for Turbulent Flow," M.S. Thesis Civil Engineering, 1972, MIT.
12. Chien, N., and Einstein, H.A., Effects of Heavy Sediment Concentration Near the Bed on Velocity and Sediment Distribution, University of California, Institute of Engineering Research, Berkley, California, August, 1955.
13. Graf, Walter, Hydraulics of Sediment Transport, McGraw Hill, New York, 1971.
14. Bandry, Lionel, "Deposition of Cohesive Sediment in Turbulent Flow," 1969, Civil Enigneering, MIT.

15. Yalin, Mechanics of Turbulent Transport, 2nd Edition, Pergamon Press, 1977.
16. Zagustin, K., "Sediment Distribution in Turbulent Flow," *Journal of Hydraulic Research*, 6, No. 2, 1968, pp. 163-172.
17. Raudkivi, A.J., Loose Boundary Hydraulics, Pergamon Press, Oxford, 1967.
18. Csanady, "Turbulent Diffusion in the Environment", Reidd Publishing Co., Vol. 3, 1975.
19. Ippen, A.T., "A New Look at Sedimentation in Turbulent Streams," *Journal of Boston Society of Civil Engineers*, Vol. 58, No. 3, July 1971.
20. White, Viscous Fluid Flow, McGraw Hill, 1974.
21. Tchen, C.M., "Mean Value and Correlation Problems Connected with the Motion of Small Particles Suspended in a Turbulent Fluid," Ph.D. Thesis, Delft, 1947.
22. Soo, S.L., Fluid Dynamics of Polyphase Systems, Blaisdell Publishing Co., Waltham, 1967.
23. Khosla, P. and Lederman, A., "Motion of a Spherical Particle in a Turbulent Flow," Dept. of Aerospace Engineering and Applied Mechanics, PIBAL Dept., No. 73-22, Brooklyn Polytech, November 1973.
24. Batchelor, G.K., "Diffusion in a Field of Homogeneous Turbulence," *Aust. J. Sci. Res.*, Vol. 2, No. 4, 1949, pp. 437-450.
25. Soo, S., "Statistical Properties of Momentum Transfer in Two-Phase Flow" *Chemical Engineering Science*, Vol. 5, No. 2, April, 1956, pp. 57-67.
26. Latimer, G.A., "Mechanism of Fluid-Phase Mixing in Fixed and Fluidized Beds of Uniformly Sized Spherical Particles," Ph.D. Thesis, Chemical Engineering, Princeton University, 1951.
27. Dhanak, A., "Momentum and Mass Transfer by Eddy Diffusion in a Wetted Wall Channel," *A.I.Ch.E. Journal*, June 1968, pp. 190-196.
28. Williams, J., and Jackson, R., "The Motion of Solid Particle in an Electrostatic Precipitator," *Proceedings of the Symposium on the Interactions Between Fluids and Particles*, Published by I.Ch.E., London, June, 1962, pp. 282-288, Discussion 289-298.

IV. TURBULENT PRECIPITATION THEORY

A. Introduction

Two precipitation models have been pursued in Chapter 2:

- (1) a fully mixed turbulent model (Deutsch) where the particulate is supplied to the wall via eddy mixing and the cross sectional density is uniform (representing an effective D_t for transverse diffusion equal to infinity)
- (2) a trajectory model where the flow lines are determined from particle conservation and in this method of characteristics analysis the density is found to decrease along trajectory lines.

This chapter outlines a method of predicting magnetizable particulate precipitation from a turbulent airstream. Two analyses emerge based on the above models. The first, appropriate to light particles, applies where particle inertia is negligible. The theory is analogous to the Deutsch model so far as the physics of the problem (both accent the importance of turbulent diffusion), and the analysis parallels that in the trajectory model. The net particle flux has four components:

$$\Gamma = \text{convection} + \overset{\text{gravitational}}{\text{migration}} + \overset{\text{magnetic}}{\text{migration}} + \text{diffusion}$$

$$= \bar{U}n + \frac{m\bar{g}}{\beta} n + \alpha' \frac{\nabla(\bar{H} \cdot \bar{H})}{\beta} n + DVn$$

where $D = D_{\text{molecular}} + D_{\text{turbulent}} \approx D_{\text{turbulent}}$ (4-1)

The diffusion equation results after setting the divergence of (4-1) equal to zero.

The second heavy particle analysis considers particles in which inertial effects are important. In the consideration of very heavy particles, the theory to the laminar flow study of chapter 2. The particles with large

inertia ride through turbulent eddies, and diffusion can be neglected. This analytical theory is expressed by the particle momentum equation which produces information of particle trajectories:

$$\frac{m d\bar{v}_p}{dt} + 6\pi\eta r_p \bar{v}_p = 6\pi\eta r_p \bar{v}_f + m\bar{g} + \alpha' \nabla (\bar{H} \cdot \bar{H}) \quad (4-2)$$

The important point of this investigation is in connecting these two analyses to produce an explanation of particle precipitation. Summarized in Table (4-1) is the interconnection of particle size, fluid flow, and the two analyses. The heavy particle turbulent section is split to indicate the model dependency on the degree of turbulence (lower graph). In reality there exists a gray area in which both diffusion and inertia are important; for this, a hybrid model will be developed in Section D-2.

A synopsis of this chapter is shown in Table 4-2. The decision of which size-dependent analysis is valid must proceed from consideration of the relevant system characteristic times. Three models evolve in the light particle diffusion analysis. The three differ by diffusivity representation, boundary conditions, and computer simulation used. The heavy particle analysis is subdivided according to whether diffusive effects are considered.

B. Characteristic Times

The major question to be answered is, "For what size particles are the effects of diffusion and inertia important?" This is best answered by examining the characteristic times of the system. In balancing the inertial and viscous terms in equation (4-2), one arrives at the inertial-viscous time

$$\tau_{in-vis} = \frac{m}{6\pi\eta r} = \frac{2}{9} \rho \frac{r^2}{\eta} = \begin{cases} 1.659 \times 10^{-3} \text{ sec } 8\mu \text{ iron particle} \\ .3137 \text{ sec } 110\mu \text{ iron particle} \end{cases} \quad (4-3)$$

Flow Size Particle	Laminar Flow	Turbulent Flow
Heavy	Trajectory Model	Trajectory Model Hybrid Model (medium heavy)
Light	Trajectory Model	Diffusion Model

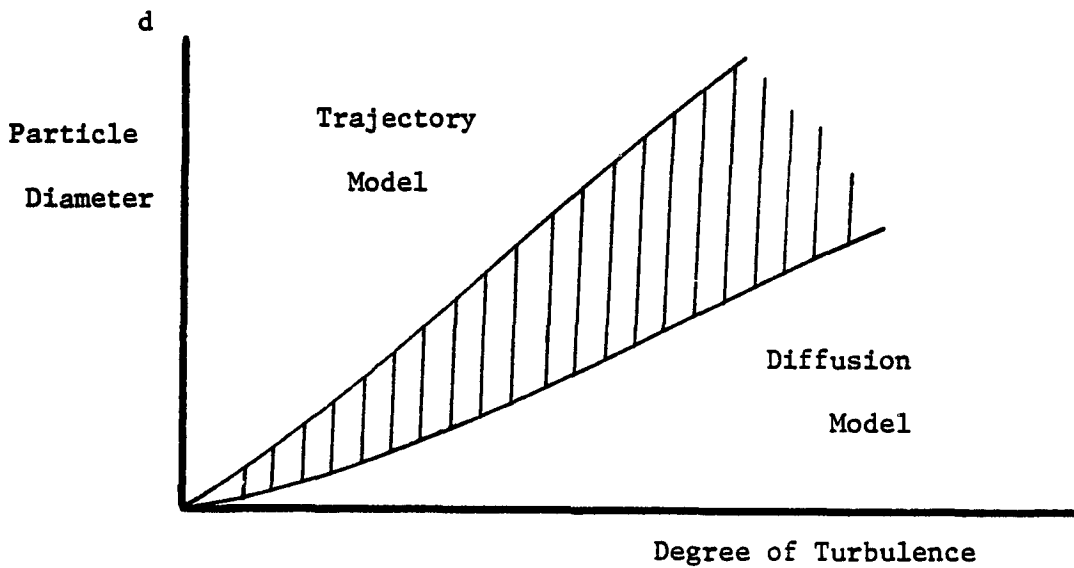
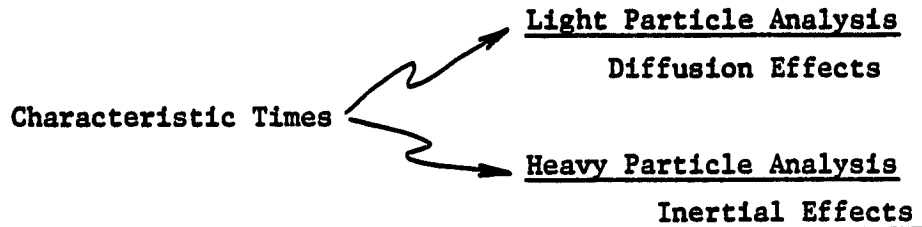


Table 4-1 Model Applicability given Particle Size and Fluid Flow



LIGHT PARTICLE ANALYSIS			
	Non-Causal Model	Causal Perfunctory Model	Causal Fundamental Model
D_t	Core; $D_t = D_t(x)$ no y dependence Boundary layers; $D_t = 0$	Core; $D_t = D_t(x,y)$ Lower Region; $D_t = 0$	Core; $D_t = D_t(x,y)$ Lower Region; $D_t = 0$
Transverse Boundary Conditions	$\frac{\partial n}{\partial y} = 0$ on top and bottom of core	$n = 0$ on top $\frac{\partial n}{\partial y} = 0$ on bottom of core	$n = 0$ on top no lower condition
Computer Simulation	balanced 2-sided y derivatives forward 1-sided x derivatives axial march along channel	1-sided backward migration y derivatives 1-sided backward x derivatives march in x with simultaneous solution of transverse points	
HEAVY PARTICLE ANALYSIS			
	Inertia Model	Hybrid Model	
	Momentum Equation Attack - particles ride through turbulent eddies-no diffusion (like laminar flow theory)	Hybrid Momentum Attack - diffusion term added to momentum equation by superposition	

TABLE 4-2

For processes involving times shorter than τ_{in-vis} experiments show that inertial forces must be considered; a system where the characteristic times were longer than τ_{in-vis} can be shown experimentally to be accurately represented by the viscous dominated flux expression (4-1).

The choice of proper characteristic system time deserves careful consideration. Because the particle's residence time is defined to be how long it takes a particle to traverse half the height of the duct, special attention to force terms of the RHS of equation (4-2) is in order. The basis of comparison is the time it takes a particle to fall the duct half-height in a viscous dominated environment. The gravitational-viscous time is

$$\tau_{grav-vis} = \frac{a}{mg/\beta} \Rightarrow \begin{cases} 3.905 \text{ sec } 8\mu \text{ particle} \\ .02066 \text{ sec } 110\mu \text{ particle} \end{cases} \quad (4-4)$$

The equivalent magnetic-viscous time calculation requires more information concerning the field strength and wavelength. For a single harmonic sinusoidal field, the magneto-viscous time becomes

$$\tau_p = \int_a^0 - \frac{1}{\frac{\alpha k e^{-2ky}}{\beta}} dy = \frac{\beta}{2\alpha k^2} (e^{2ka} - 1) \quad (4-5)$$

and with $\alpha = \frac{4\pi r^3}{3} \left(\frac{3}{2 + \frac{\mu}{\mu_0}} \right) \left(\frac{\mu}{\mu_0} - 1 \right) \mu_0 H_0^2$, a 1000 Gauss, 8 cm wavelength field gives

$$\tau_{mag-vis} = \begin{cases} 102.5 \text{ sec } 8\mu \\ .542 \text{ sec } 110\mu \end{cases} \quad (4-6)$$

Finally, the analogous diffusion time is

$$\tau_p = \frac{a}{D \frac{v_n}{n}} \sim \frac{a^2}{D} \quad (4-7)$$

The measurement of the turbulent coefficient D_t ($\sim D$) discussed in Chapter 2 is outlined in Chapter 5. A representative diffusivity for such a system is $.002 \frac{m^2}{sec}$. Thus, the diffusion time becomes

$$\tau_D = 2.016 \text{ sec, independent of particle size} \quad (4-8)$$

Examination of the times in equations (4-5) to (4-8) allow a more intelligent handling of equation (4-2). For the 8μ particle, the inertial-viscous time is much shorter than the characteristic migration or diffusion time, indicating that the viscous-dominant flux analysis posed in (4-1) is valid. In the heavy particle analysis, however, the characteristic inertial-viscous time is not short. Therefore, inertia has a significant influence. The fact that the diffusion time is much longer than either of the migration terms, however, illustrates the reduced effect turbulent diffusion has with larger particles. The momentum equation (4-2) without the diffusion term appears to be the correct approach here. Thus there exist two well defined avenues of analysis depending on the size of particle being used and the resulting relative time constants.

The larger particles used in the experiments were 55-65 microns in diameter in which the gravitational viscous time and magneto-viscous time are .082 seconds and 2.08 seconds respectively. Clearly these particles fit into an intermediate domain where diffusion is not negligible, especially over distances smaller than the duct half height (e.g. the injection tube diameter). This intermediate region will be considered in section D of this chapter.

C. Diffusion Model - 4μ Particles

The above analysis revealed that 4μ particles are viscous dominated, inertial effects are negligible, and thus a flux, particle conservation approach using equation (4-1) is in order. Assuming steady state operation, the divergence of Γ can be set equal to zero to give

$$-\nabla \cdot (D\nabla n) + \left[\left(\frac{\alpha' \nabla (H \cdot H)}{\beta} \right) n \right] - \frac{mg \partial n}{\beta \partial y} + U \frac{\partial n}{\partial x} = 0 \quad (4-9)$$

Using a single harmonic field with the magnetic force equal to $\alpha k e^{-2ky}$, (4-9) becomes

$$-\nabla \cdot (D\nabla n) + \left(-\frac{\alpha k e^{-2ky}}{\beta} - \frac{mg}{\beta} \right) \frac{\partial n}{\partial y} + U \frac{\partial n}{\partial x} + \frac{2\alpha k e^{-2ky}}{\beta} n = 0 \quad (4-10)$$

The next step in the analysis is to check whether any simplifications can be made. In this study and indeed for most boundary layer analyses, the convective horizontal flux dominates the corresponding diffusive flux. A characteristic density analysis elucidates this point.

Given a uniform injection of particulate during a time sufficient for 10 grams to be spread over 2 meters of duct, the average concentration is

$$\text{avg.} = \frac{10^{-2}}{(.127)^2 2} \sim 0.3 \frac{\text{kg}}{\text{m}^3} \quad (4-11)$$

and assuming a linear axial concentration profile, the density n is typified by

$$n \sim -0.6 (x-2) \frac{\text{kg}}{\text{m}^3} \quad (4-12)$$

In a $4.3 \frac{\text{m}}{\text{sec}}$ flow with a diffusivity of $.004 \frac{\text{m}^2}{\text{sec}}$, the convective and diffusive fluxes are respectively

$$\Gamma_{\text{convective}} = 1.3 \frac{\text{kg}}{(\text{m}^2 \cdot \text{sec.})} \quad (4-13)$$

$$\Gamma_{\text{diffusion}} \approx (.004)(.6) = .0024 \frac{\text{kg}}{(\text{m}^2\text{-sec})} \quad (4-14)$$

Thus the axial diffusion term is justifiably ignored. As shown in the last section, vertical diffusion must be considered to be at least comparable to gravitational and magnetic migration.

The equation to be solved then reduces to

$$\begin{aligned} -D \frac{\partial^2 n}{\partial y^2} - \frac{\partial D}{\partial y} \frac{\partial n}{\partial y} - \frac{mg}{\beta} \frac{\partial n}{\partial y} - \frac{\alpha k e^{-2ky}}{\beta} \frac{\partial n}{\partial y} + U_{\text{max}} \left(\frac{a-|y-a|}{a} \right)^{\frac{1}{9}} \frac{\partial n}{\partial x} \\ + \frac{2\alpha k^2 e^{-2ky}}{\beta} n = 0 \end{aligned} \quad (4-15)$$

where D is a function of y and x. Including the field harmonics, (4-15)

becomes

$$-D \frac{\partial^2 n}{\partial y^2} - \frac{mg}{\beta} \frac{\partial n}{\partial y} - V_m(y) \frac{\partial n}{\partial y} + U_{\text{max}} \left(\frac{a-|y-a|}{a} \right)^{\frac{1}{9}} \frac{\partial n}{\partial x} + V'_m(y)n = 0 \quad (4-16)$$

where

$V_m(y)$ = vertical magnetic migration velocity

$$= \frac{4}{3} \pi r^3 \left(\frac{\mu}{\mu_0} - 1 \right) \left(\frac{3}{2 + \frac{\mu}{\mu_0}} \right) \frac{k}{\mu_0} \sum_{m=1}^{\infty} m B_m^2 e^{-2kmy}$$

$$V'_m(y) = \frac{\partial V_m}{\partial y} = \frac{4}{3} \pi r^3 \left(\frac{\mu}{\mu_0} - 1 \right) \left(\frac{3}{2 + \frac{\mu}{\mu_0}} \right) \frac{2k^2}{\mu_0} \sum_{m=1}^{\infty} m^2 B_m^2 e^{-2kmy}$$

The imposition of the proper boundary conditions on equation (4-15) is necessary for numerical solution. The fact that (4-16) is first order in x and second order in y suggests two boundary conditions on y (one each at the top and bottom of the duct) and one on x (at the entrance to the duct). The boundary condition on x is simply the specification of the incoming

particle density (n_0). The principle of conservation of particle flux must be employed to arrive at the vertical boundary conditions.

Further analysis is best pursued in stages. This step progression is needed to highlight the internal issues involved in a self-consistent solution. First, a non-causal theory is developed assuming a uniform diffusivity across the duct with a step change to zero a distance Δ from the walls. The equations are then represented in difference form. Axial differentiation will be represented by forward one-sided derivatives yielding a very straight-forward solution. This is then followed by two more exact causal theories in which representations of diffusivity are used. Boundary conditions and representation of axial and vertical derivatives are examined carefully to be consistent with causality.

1. Non-Causal Diffusion Model

The measurements of turbulent diffusivity (Chapter 5) along with the observations of Davies discussed in chapter 3 indicate the diffusivity is approximately constant over the duct cross-section and decreases to zero near the walls. If turbulent contributions to the particle flux at the walls are negligible, a reasonable model is one with the problem divided into

(1) a boundary layer region close to the wall where diffusion is insignificant.

(2) a region over the duct interior where turbulent diffusivity is constant with y , but does has an axial dependence.

Thus, in both regions, the $\frac{\partial D}{\partial y}$ term in (4-16) drops out.

The above assumptions (summarized in Fig. (4-1)) along with flux conservation suffice to give the vertical conditions for the inner diffusion region. At the lower boundary ($y = \Delta$), flux continuity demands

$$\left[-D_t \frac{\partial n}{\partial y} - mgn + \alpha' \nabla (\mathbf{H} \cdot \mathbf{H}) n \right]_{y = \Delta_t} = \left[-mgn + \alpha' \nabla \mathbf{H} \cdot \mathbf{H} \right]_{y = \Delta_-} \quad (4-17)$$

or $\frac{\partial n}{\partial y} = 0$ at $y = \Delta_+$ (4-18)

At the upper boundary ($y = 2a - \Delta$), continuity again requires

$$\left[-mgn + \alpha' \nabla \mathbf{H} \cdot \mathbf{H} \right]_{y = (2a-\Delta)_+} = \left[-D_+ \frac{\partial n}{\partial y} - mgn + \alpha' \nabla \mathbf{H} \cdot \mathbf{H} \right]_{y = (2a-\Delta)_-} \quad (4-19)$$

Equation (4-19) implies

$$\frac{\partial n}{\partial y} = 0 \text{ at } y = (2a-\Delta)_- \quad (4-20)$$

In the layer regions it is appropriate to apply flux conservation, but with $D_t = 0$. This is identical with the particle trajectory theory discussed in Chapter 2.

Each of the above model divisions will now be examined in more detail. The greatest difficulty is with the lower boundary. There are two physical conditions that must be realized in the lower region--no particle reintrainment occurs, and diffusivity for iron particles in the laminar sublayer must be zero (i.e. molecular diffusivity and brownian motion do not enter for the size scale particles we are concerned with).

An understanding of approaches employed by hydraulic and chemical engineers to the precipitation problem is helpful. A method used often in hydraulic's literature (Barfield, et. al. - see Bibliography, Ch. 3) for modeling an absorbing wall is to force the density to zero at the wall. The pertinent diffusivity is considered to remain high near the wall in sedimentation research, for instance. This zero density requirement implies two

conditions which give credence to this assignment.

- (1) zero density at the wall insures a positive gradient away from the wall and thus only downward diffusive flux.
- (2) large migration (gravitational) flux to the wall with abnormal depletion of the core region is prohibited by the assignment $n = 0$ at the wall. The density is required to be small in the neighborhood of the wall, since any large gradient would constitute a correspondingly large diffusive flux (which could not exist in steady state).

A typical engineering problem is the dissolving of a salt at a wall into a flowing liquid. The wall molecular diffusivity is very important again. The wall for such a problem is often supplying flux into the duct or keeping the particle density in equilibrium, in which case the diffusive and migration fluxes balance (implying a negative density gradient at the wall). At the laminar sublayer where the diffusivity increases tremendously, the normal density must be nearly zero.

Appendix D shows the analytical solution of a three region diffusion problem (Fig. 4-1) with only gravitational migration, and no x dependence. The boundary conditions are $n = n_0$ at $y = 2a$ and $n = 0$ at $y = 0$. The diffusivities are allowed to be nonzero in the laminar sublayers. The result is that the normal density gradient at the boundary layer equals the ratio of the diffusivity in the sublayer to the diffusivity in the core. Also plotted are density profiles for various ratios of core to layer diffusivity as well as variation effects of diffusive to gravitational migration times. The density gradient in the sublayer is determined from trajectory theory and is fixed by the gravitational and magnetic migration terms (Appendix B). Negligible layer diffusivity therefore implies zero

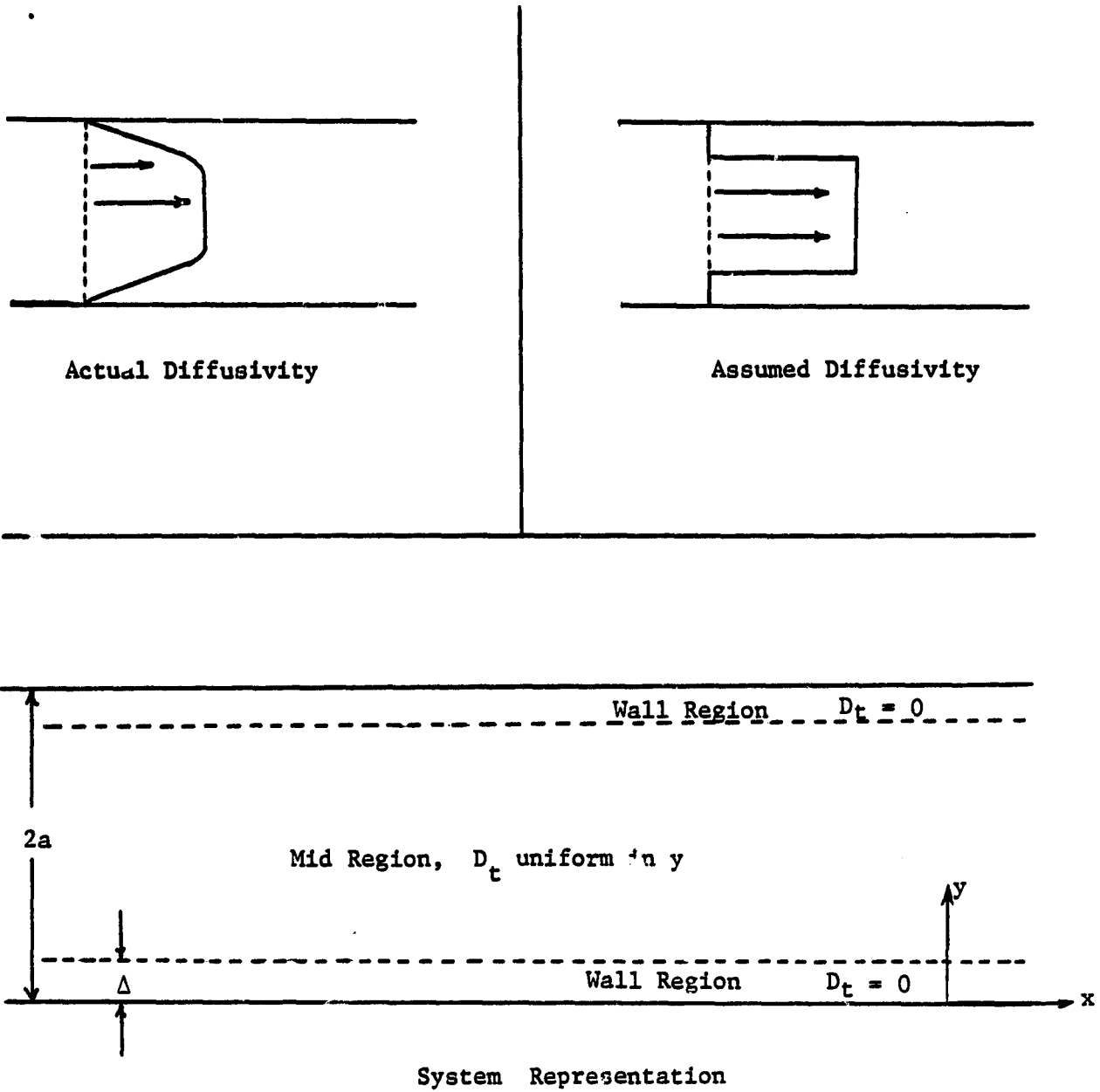


Figure 4-1 Small Particle Diffusivity Assumptions -
Non-Causal Model

core gradient.

The condition can be examined less rigidly through the exponential magnetic force decay in the duct. Changes occur less rapidly axially than transversely. Small axial flux changes imply a somewhat constant transverse flux. (This hypothesis will be used to explain density profiles in chapter 6). In the core, magnetic migration is small. One mechanism by which flux is conserved from the core to the layer region is by diffusive flux diminishing at the lower layer where magnetic migration increases. The diminishing flux appears as a decreasing gradient near the lower layer.

Figure (4-2) shows characteristic profiles of these two cases as well as a calculated density profile for magnetizable particulate deposition where the wall is absorbing (i.e., no reentrainment occurs) and molecular diffusivity in the laminar sublayer is zero. Zero sublayer diffusivity is a reasonable assumption for 2-8 micron iron particles.

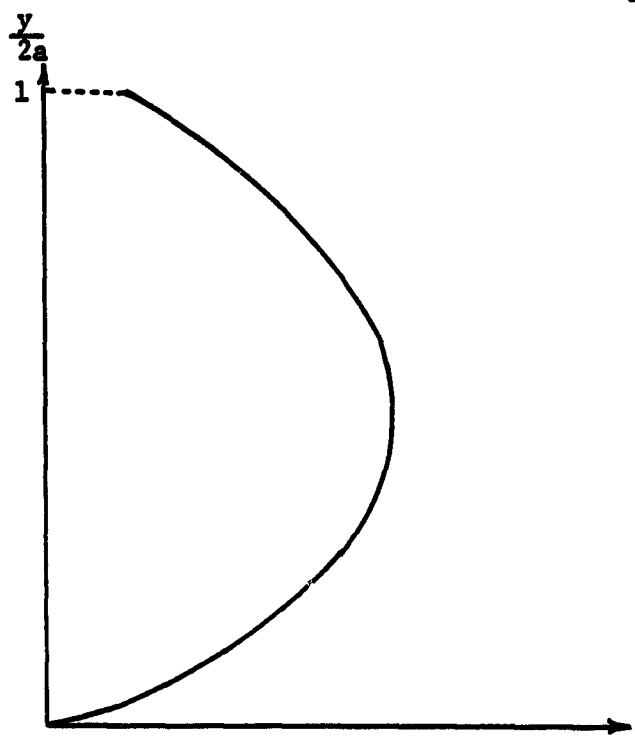
From this there appears to be a sound basis for approaching the problem as a multi-region one, the core being a constant diffusivity diffusion problem with boundary conditions $\frac{\partial n}{\partial y} = 0$ at $y = \Delta$ and $y = 2a - \Delta$. Differences with other engineering disciplines have been considered.

There now remains the task of matching the core region solution to the laminar sublayer regions. Because $D = 0$ in the sublayers, the method of characteristics approach discussed in chapter 2 can be applied. With a single harmonic field the pertinent equation is

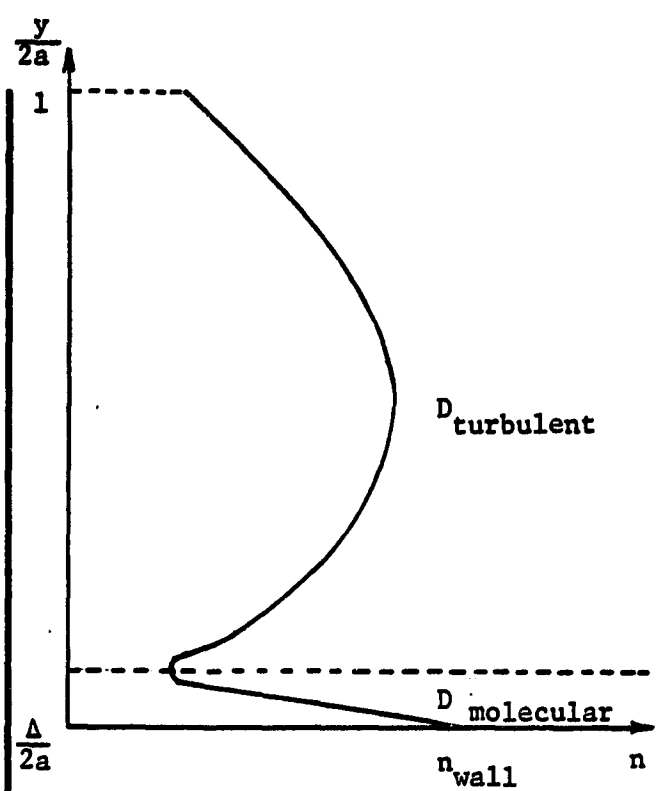
$$\frac{dn}{dt} = \frac{2\alpha k^2 e^{-2ky}}{\beta} n \quad \text{along} \quad \frac{dr}{dt} = U + \frac{mg}{\beta} - \frac{\alpha k e^{-2ky}}{\beta} l_y \quad (4-21)$$

and with the full harmonic field (4-21) becomes

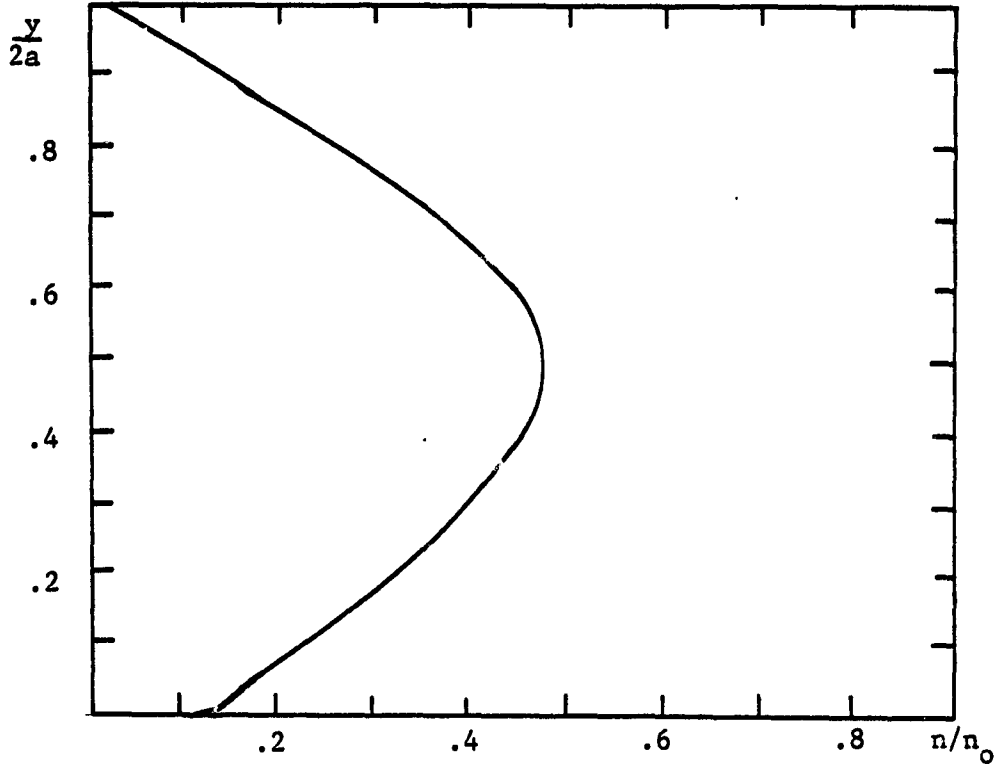
$$\frac{dn}{dt} = -V'_m(y)n \quad (4-22(a))$$



(a) Density Profile-Absorbing Wall



(b) Density Profile-Dissolving Salt



(a) Computed Density and Diffusivity, $\lambda=12\text{cm}$, $x=.956\text{m}$

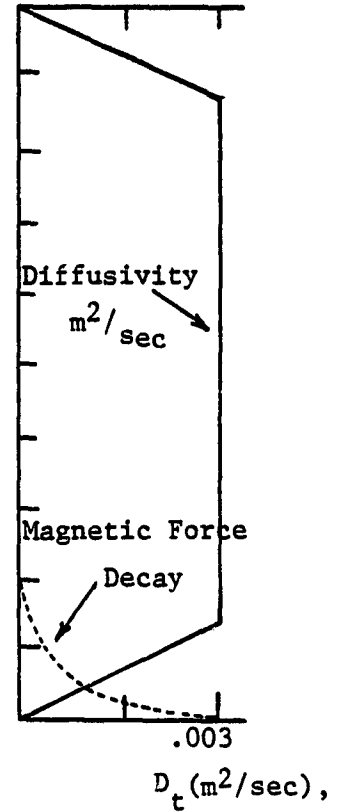


Figure (4-2) Density Profiles

along

$$\frac{dr}{dt} = U_{\max} \left(\frac{a-|y-a|}{a} \right) \bar{I}_x - \frac{mg}{\beta} \bar{I}_y - V_m(y) \bar{I}_y \quad (4-22(b))$$

Here the explicit form of \bar{U} has been inserted. Integration of (4-21,a) shows that along the particle trajectory lines (4-22,b), the density decays as

$$\frac{n}{n_1} = \frac{mg + V_m(y_0)}{mg - V_m(y)} \quad (4-23)$$

where n_1 and y_0 are the initial density and position of the particulate in the layer (i.e. at $y = \Delta$). The particulate distribution on the bottom of the duct is given by (4-23) with three specifications -- n_1 is set equal to the density of the diffusion analysis ((4-16) at $y = \Delta$), y is set equal to zero, and the appropriate axial position for each density is found by numerically integrating (4-22,b) across the boundary layer. The splicing of the different region solutions is thus accomplished.

The upper layer must be investigated from a different perspective, because all vertical migration is downward. Since the diffusivity goes to zero in the upper layer, no mechanism exists for particles to enter this region. In other words, the particle trajectory lines emanating from the upper boundary must have zero as their initial density. The upper layer correct boundary conditions are: - $n = 0$ and $\frac{\partial n}{\partial y} = 0$. Although numerical integration shows that the two conditions give nearly identical precipitation results, the densities do differ throughout the volume. The zero density condition is only a result of no upward migration forces. The zero gradient condition exists independent of migration force direction--this latter condition therefore seems to be more fundamental. Figure (4-3) summarizes the system representation and boundary conditions used.

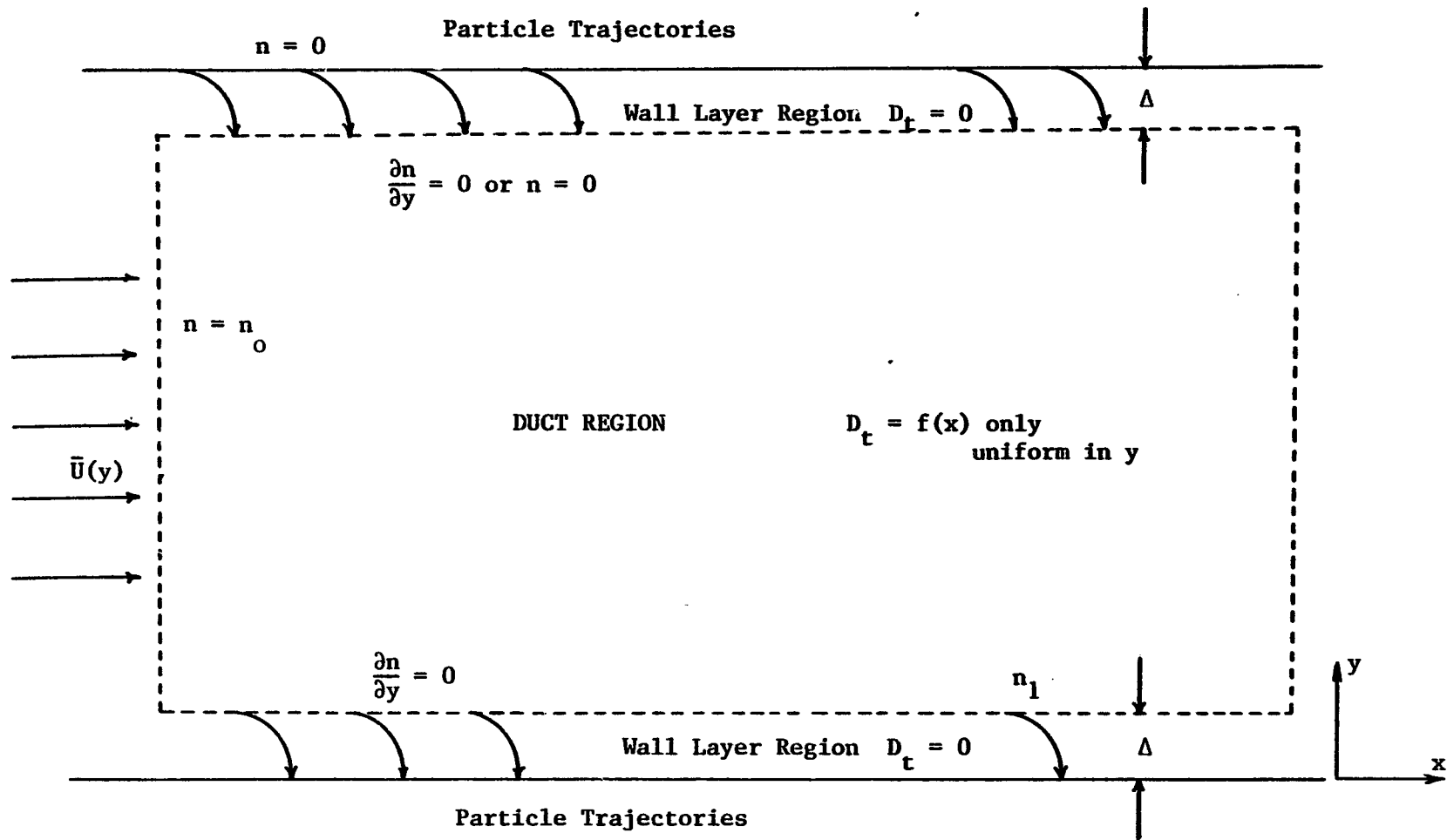


Figure 4-3 Non-Causal Model Small Particle System Representation and Boundary Conditions

Before examining the numerical method of solution, it is helpful to normalize the defining equation (4-16). Variable normalizations and relevant times are as follows:

$$\underline{y} = \frac{y}{2a}$$

$$\underline{x} = \frac{x}{L}$$

$$\underline{t} = \frac{t}{\tau_{\text{Diff}}}$$

$$\underline{n} = \frac{n}{n_0}$$

$$\tau_{\text{Diff.}} = \frac{(2a)^2}{D_t} \tag{4-24,a}$$

$$\tau_{\text{grav-vis}} = \frac{2a}{(mg_\beta)}$$

$$\tau_{\text{magnetic-vis}} = \frac{2a}{V_m}$$

$$\tau_{\text{Res}} = \frac{L}{U_{\text{max}} \left[\frac{a - ly - al}{a} \right]^{1/9}}$$

$$\tau_{\text{mag-k}} = \frac{1}{V_m}$$

The diffusion equation is now written

$$-\frac{\partial^2 \underline{n}}{\partial \underline{y}^2} - \frac{\tau_{\text{Diff}}}{\tau_{\text{grav-vis}}} \frac{\partial \underline{n}}{\partial \underline{y}} - \frac{\tau_{\text{Diff}}}{\tau_{\text{mag-vis}}} \frac{\partial \underline{n}}{\partial \underline{y}} + \frac{\tau_{\text{Diff}}}{\tau_{\text{Res}}} \frac{\partial \underline{n}}{\partial \underline{x}} - \frac{\tau_{\text{Diff}}}{\tau_{\text{mag-k}}} \underline{n} = 0 \tag{4-24,b}$$

The boundary conditions are that $\underline{n} = 1$ at $x = 0$; $\frac{\partial \underline{n}}{\partial \underline{y}} = 0$ at $\underline{y} = \frac{\Delta}{2a}$;

$$\text{and } \begin{cases} \frac{\partial \underline{n}}{\partial \underline{y}} = 0 \\ \text{or } \underline{n} = 0 \end{cases} \text{ at } \underline{y} = 1 - \frac{\Delta}{2a}$$

Method of Solution

The proper method of solution in the duct diffusion region with an initial boundary condition on x is to sequentially step in x space. A finite difference system was used to numerically solve equation (4-15).

Figure (4-4) shows the partitioning of the diffusion region into a number of points separated vertically by Δy and horizontally by Δx . In finite difference form, equation (4-24) at point i,j becomes,

$$-\left(\frac{n_{i+1,j} + n_{i-1,j} - 2n_{i,j}}{\Delta y^2}\right) - \tau_{\text{Diff}} \left(\frac{1}{\tau_{\text{grav-vis}}} + \frac{1}{\tau_{\text{mag-vis}}}\right) \left(\frac{n_{i+1,j} - n_{i-1,j}}{2\Delta y}\right) + \frac{\tau_{\text{Diff}}}{\tau_{\text{Res}}} \left(\frac{n_{i,j+1} - n_{i,j}}{\Delta x}\right) - \frac{\tau_{\text{Diff}}}{\tau_{\text{mag-k}}} n_{i,j} = 0 \quad (4-25)$$

Because all the first column elements are known ($n_{-,j-2} = 1$), expressing (4-25) for the (j-2) elements yields a solution of the (j-2) elements. The net system solution is obtained by stepping column-wise from left to right. At the lower boundary if one were to specify that the next row of elements (i+3) have the same value as the (i+1) row elements of the same column, then the condition $\frac{\partial n}{\partial y} = 0$ at $y = \frac{\Delta}{2a}$ would be insured. Matching the (i-2) row elements with the (i) row elements at the upper boundary insures the same condition on the normal density gradient at the top. If the alternate condition ($n=0$) is desired at $y = 1 - \frac{\Delta}{2a}$, then the last set of difference equations must stop within the diffusion region, i.e., at row (i). Appendix E lists the programs KDDI4 used with $n=0$ on the upper layer, and KDDI9 with $\frac{\partial n}{\partial y} = 0$ at the upper layer. The correlation of the experimental result with the above predictions is discussed in chapter 6.

A point about stability is necessary before concluding this approach. The worst possible solution perturbation is oscillatory in y having the form

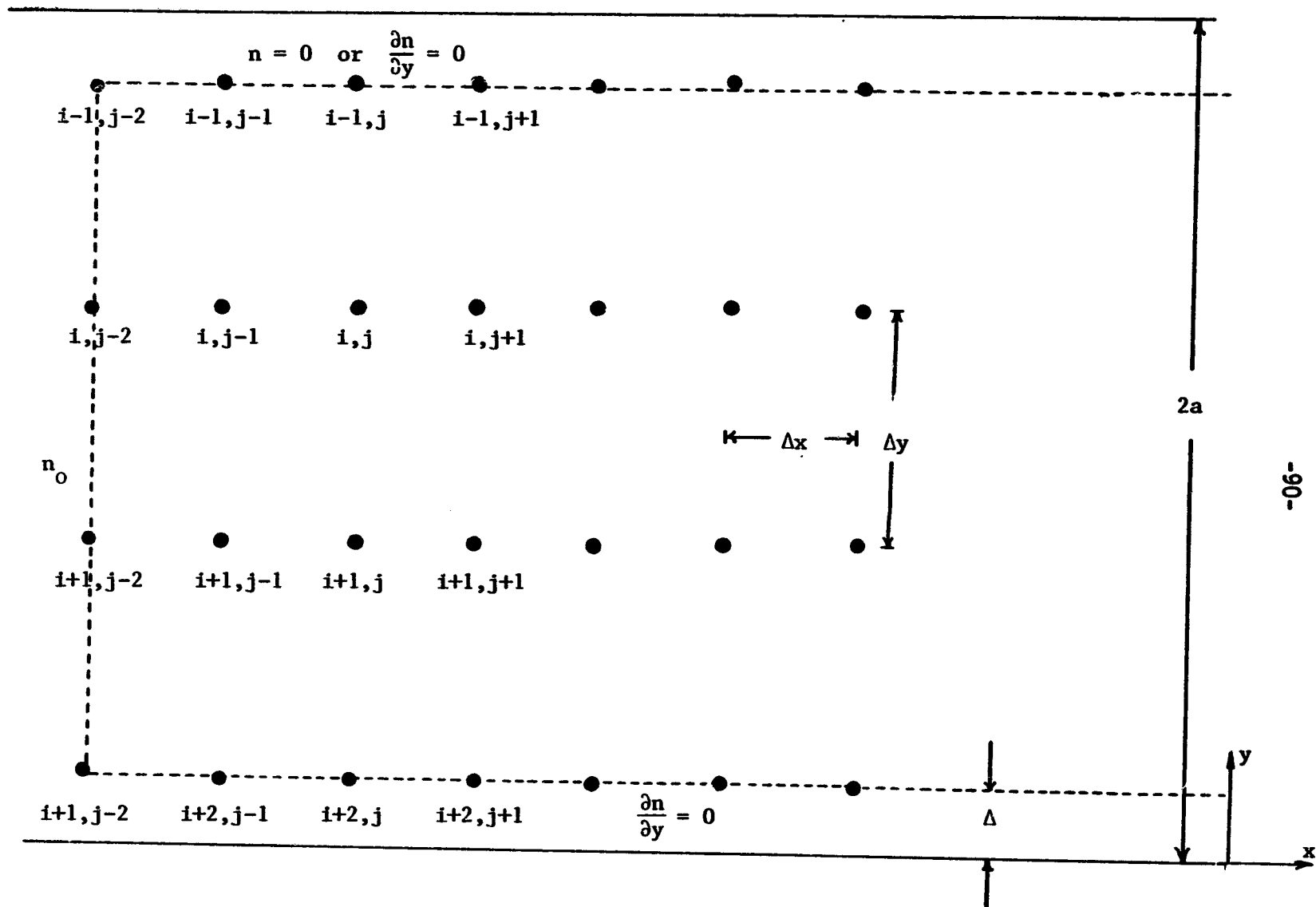


Figure 4-4 Numerical Solution of Diffusion Region

at a given grid point (see Fig. (4-5))

$$f_{i,j} = f_j (-1)^i \quad (4-26)$$

The criteria for stability is that such a perturbation not grow in x. With such an oscillatory pattern, equation (4-25) including diffusion and convection terms only, demands that

$$\frac{(f_{i+1,j} + f_{i-1,j} - 2f_{i,j})}{\Delta y^2} = \frac{\tau_{Diff}}{\tau_{Res}} \frac{(f_{i,j+1} - f_{i,j})}{\Delta x} \quad (4-27)$$

or with equation (4-26)

$$f_{i,j+1} = f_{i,j} \left\{ 1 - \frac{4\Delta t}{\Delta y^2} \frac{\tau_{Res}}{\tau_{Diff}} \right\} \quad (4-28)$$

If the perturbation f is not to grow the second term in brackets must not exceed 2.0 in magnitude. This condition translates to a restriction on Δx , i.e.

$$\Delta x < \frac{\Delta y^2 \tau_{Diff}}{(2)^* \tau_{Res}} \quad (4-29)$$

For the present analysis with a typical residence time of 0.23 secs, a diffusion time of 4.03 secs ($D_t = .004$), and $\Delta y = .1$, Δx must be less than .087. In this analysis, Δx was set to .0125.

It is interesting that the first solution of (4-25) involved finite difference equations as above, but with two boundary conditions on x. A boundary condition of $\underline{n} = 0$ was imposed approximately 24 duct widths downstream. The finite difference system was imposed as above, but the network of equations was solved simultaneously using a Gauss-Jordan elimination technique. Except in the neighborhood of the downstream point, the solution was of the same order as the above stepping procedure. The stepping procedure

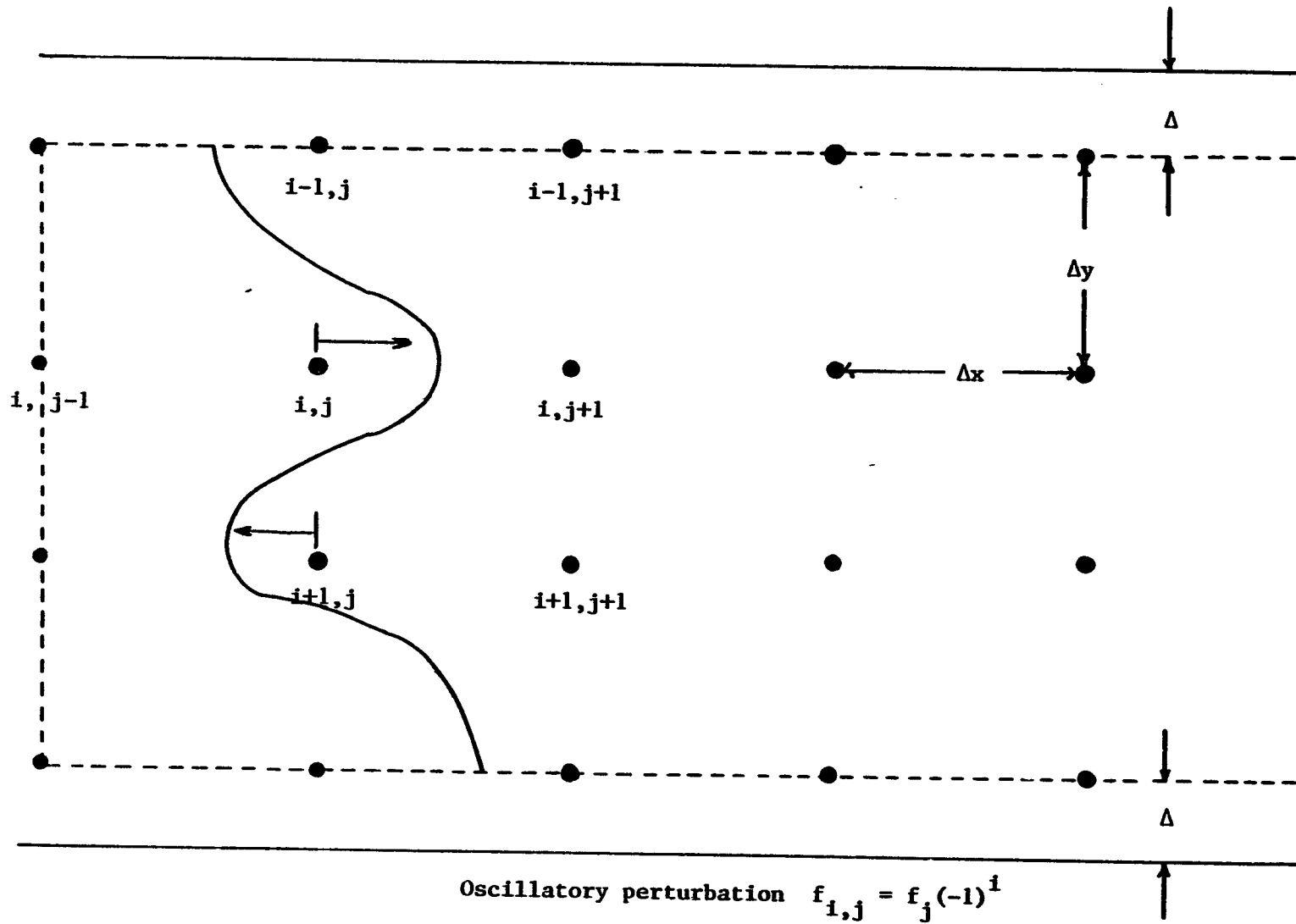


Figure 4-5 Stability of Diffusion Analysis

eliminated the need to solve simultaneous equations but the question of causality when using the one-sided forward derivative in x must be considered. The results of the non-causal deposition prediction are compared in Chapter 2-A.

2. Causal Perfunctory Model

Three modifications of the non-causal solution are in order. The question of causality points to the first refinement, calling for a more careful examination of the boundary condition imposition as well as representation of first order partial derivatives. With no diffusion, equation (4-24,b) becomes a first order partial differential equation which can be solved using characteristic trajectory theory. The correct analysis in this limit would impose one boundary condition wherever particle trajectories entered the region of interest. Spatial derivatives in x and y would be evaluated in a one-sided difference representation always using particle location information of earlier time. The exact solution should be consistent with the trajectory analysis and in fact, degenerate to it as diffusivity decreases. One approach to the problem then would be to extend a finite difference grid through the upper and lower laminar sub-layers, imposing the boundary condition $n=0$ at the upper surface. It would also be in order to use one-sided partial derivatives consistent with causality for non-diffusion terms. This solution would surely be more fundamental. Unfortunately, the refinement of the grid necessary to develop information through the boundary layer presented numerical difficulty to the small PDP 11-03 computer available in this study. It was decided to continue to split the problem into regions.

The nature and position of the split leads to the second solution refinement--the transverse dependence of the turbulent diffusivity. Equation (3-38)

reveals one representation of the diffusivity vertical dependence. The point was made in chapter 3 that according to Davies, the diffusivity is well represented by Figure (4-6). The turbulent diffusivity is linear over 1/4 of the duct half-height dropping very quickly to zero in the neighborhood of the laminar sublayer Δ . The thickness of the layer is computed from Schlichting (chapter 5-[1]) to be

$$\Delta \approx \frac{5\nu}{\sqrt{.03325 U_{avg}^{\frac{7}{4}} \nu^{\frac{1}{4}} a^{-\frac{1}{4}}}} = .031 \text{ cm} \quad (4-30)$$

Here U_{avg} , the average duct velocity, was assumed to be 4.57 m/sec. Schlichting also shows that the axial flow in the sublayer can be represented as

$$U = \frac{[.03325 U_{avg}^{\frac{7}{4}} \nu^{\frac{1}{4}} a^{-\frac{1}{4}}]}{\nu} \quad (4-31)$$

The equation to be solved in the core is identical to (4-24), but with the $\frac{\partial D}{\partial y}$ term of (4-16)

$$-\frac{\partial^2 \underline{n}}{\partial y^2} - \frac{\tau_{Diff}}{\tau_{grav-vis}} \frac{\partial \underline{n}}{\partial y} - \frac{\tau_{Diff}}{\tau_{mag-vis}} \frac{\partial \underline{n}}{\partial y} - \frac{1}{D} \frac{\partial D}{\partial y} \frac{\partial \underline{n}}{\partial y} + \frac{\tau_{Diff}}{\tau_{Res}} \frac{\partial \underline{n}}{\partial x} - \frac{\tau_{Diff}}{\tau_{mag-k}} \underline{n} = 0 \quad (4-32)$$

The normalization of (4-24b) was used in (4-32).

The model alterations incorporating these refinements appear in Figure (4-7). Boundary conditions are imposed on the top and left side of the duct where trajectories would enter. The grid is extended into the upper layer where the condition $\underline{n}=0$ is imposed.

The lower boundary condition at $y=\Delta$ is necessary if D_t is non zero at

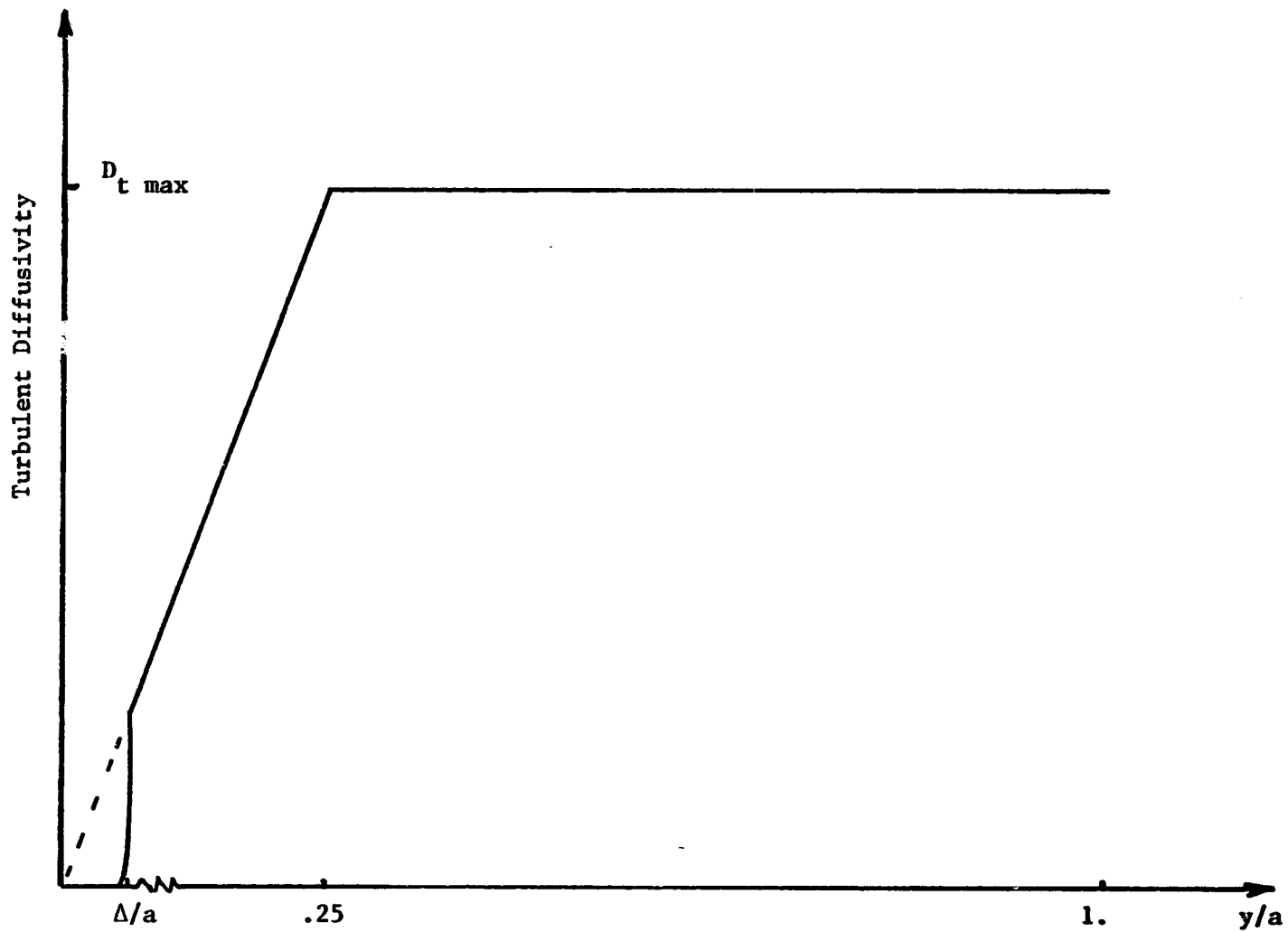


Figure 4-6 Turbulent Diffusivity Vertical Dependence

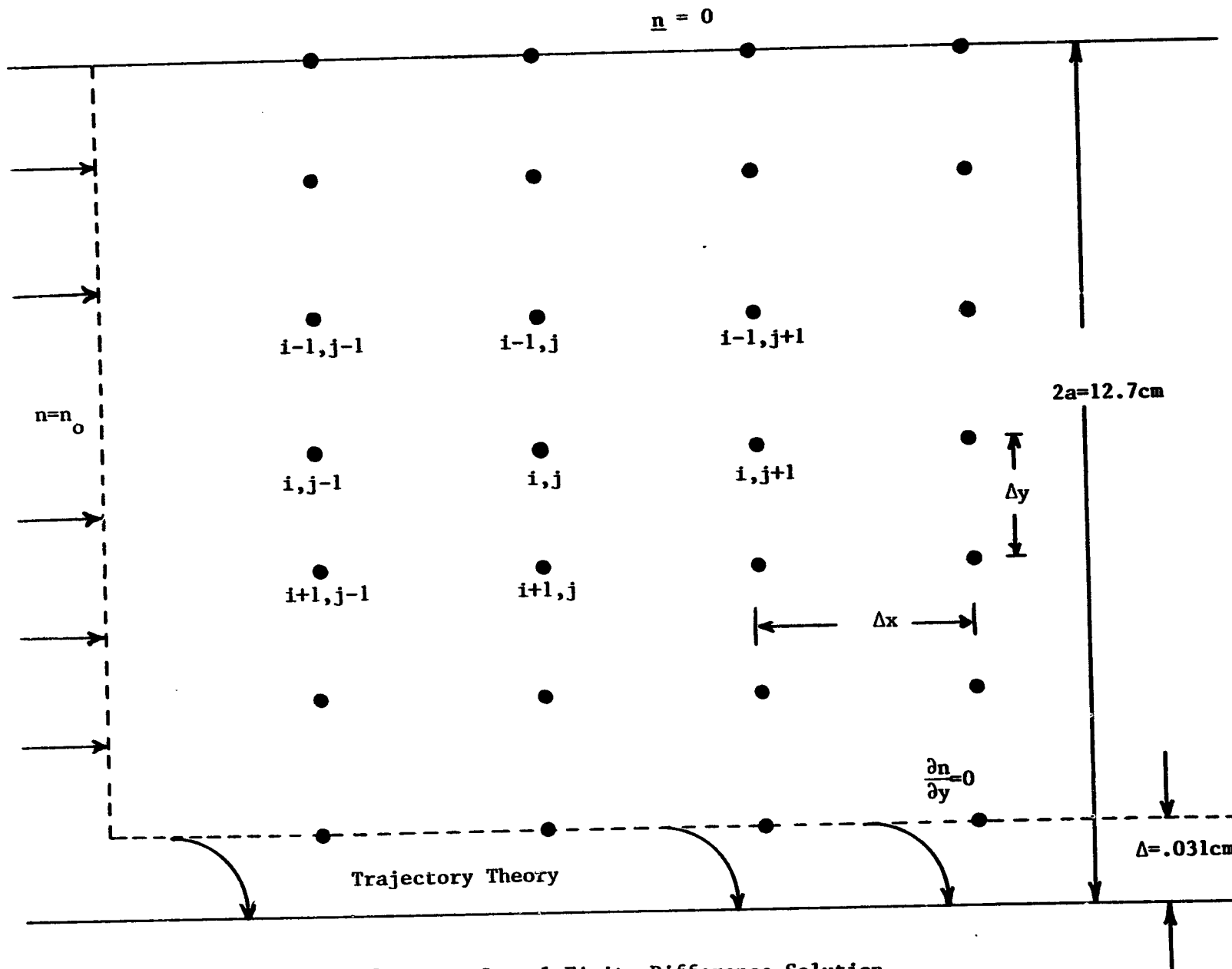


Figure 4-7 Perfunctory Causal Finite Difference Solution

that point (2nd order in y). As figure (4-6) points out, a discontinuity in D_t exists at $y=\Delta$. The imposition of $D_t=0$ at $y=\Delta$ implies significant alterations that will be discussed in the following section. The discussion in the causal model section of the boundary condition $\frac{\partial n}{\partial y} = 0$ at $y=\Delta$ applies in this model as long as D_t is non zero throughout the core.

The trajectory model was then meshed with the diffusion solution at $y=\Delta$ as explained in the approximate model solution.

The finite difference representation of (4-32) consistent with causality and degenerating to the trajectory analysis as D_t goes to zero becomes

$$\begin{aligned}
 & - \frac{(n_{i-1,j} + n_{i+1,j} - 2n_{i,j})}{\Delta y^2} \\
 & - \left(\frac{\tau_{\text{Diff}}}{\tau_{\text{grav-vis}}} + \frac{\tau_{\text{Diff}}}{\tau_{\text{mag-vis}}} \right) \left(\frac{n_{i-1,j} - n_{i,j}}{\Delta y} \right) \\
 & - \frac{1}{D} \frac{\partial}{\partial y} \left(\frac{n_{i-1,j} - n_{i+1,j}}{2\Delta y} \right) + \frac{\tau_{\text{Diff}}}{\tau_{\text{Res}}} \left(\frac{n_{i,j} - n_{i,j-1}}{\Delta x} \right) \\
 & - \frac{\tau_{\text{Diff}}}{\tau_{\text{mag-k}}} n_{i,j} = 0 \tag{4-33}
 \end{aligned}$$

Note the $\frac{\partial D}{\partial y}$ term uses a two-sided derivative of density, while the migration and convection terms use a one-sided derivative. The solution is quite general in that it is applicable to any type of migration. If migration were up in some region and down in others (e.g. due to positioning magnets at $y=2a$ as well as $y=0$) a point by point check of the direction of local migration would be necessary before one would know whether to choose $n_{i-1,j}$ or $n_{i+1,j}$ for evaluating $\frac{\partial n}{\partial y}$.

Causal representation of the x derivative convective term necessitates

C-2

the simultaneous solution of all densities in a single column before proceeding to the next column. The point to remember is that the axis in which diffusion is important will require simultaneous solution of all points along that axis. The other axes give the directions of sequential numerical stepping.

Appendix F lists the program KDPFZ used to predict the causal perfunctory light particle diffusion theory solution. The above discussion elucidates the requirements causality imposed on boundary conditions and numerical differentiation. A comparison of this models' precipitation prediction with experimental data is in chapter 6-2.

3. Causal Fundamental Diffusion Model

As shown in Fig. (4-6), there exists a discontinuity in diffusivity at $y=\Delta$. If D_t is set to zero at the lower layer, the core analysis requires no lower boundary condition. The diffusion equation representation for the final row of elements in Fig. (4-7) involves only elements above and to the left of their location (i.e., backward in time).

Except for the change in D_t and this boundary condition, the analysis is identical to the previous section. The program listing appears in Appendix G. The theory precipitation correlations with data follow in Chapter 6A. A comparison of these two causal solutions differing by the lower boundary condition is also discussed in Chapter 6-A. The zero boundary condition theory predicts a 5-10% lower particulate deposition than the zero gradient causal theory. The most surprising result was that the no lower boundary condition causal solution predicted a density profile identical in shape to the zero gradient theory, including a zero density gradient at $y=\Delta$! The conclusion is that this third no lower boundary condition causal solution is more fundamental.

D. Heavy Particle Analysis

(1) Inertial Model - ($r_p = 50\mu$)

As discussed in section (B), inertial effects must be considered for sufficiently large particles ($> 25\mu$). On the basis of the comparison used, even a 25μ particle had a migration time constant one order of magnitude smaller than the diffusion time constant. The question of inclusion of turbulent diffusion will be considered in the next section; for the following discussion, diffusion will be ignored. In this section, a particle trajectory analysis including particle inertia will be discussed.

In the Lagrangian coordinates, the momentum equation is

$$m \frac{d\bar{v}_p}{dt} + 6\pi\eta r_p \bar{v}_p = 6\pi\eta r_p \bar{U} + m\bar{g} + \bar{F}_{mag} \quad (4-34)$$

where

\bar{U} = the mean gas velocity

$$\bar{F}_{mag} = -\frac{4}{3} \pi r^3 \left(\frac{3}{2 + \frac{\mu}{\mu_0}} \right) \left(\frac{\mu}{\mu_0} - 1 \right) \frac{k}{\mu_0} \sum_{m=1}^{\infty} m B_m^2 e^{-2km\gamma} \bar{I}_y$$

A normalization is employed as before, but the base time is an inertial-gravitation time. (This normalization is altered in chapter 7 where gravity is ignored--the base time is a characteristic diffusion time).

$$\underline{y} = \frac{y}{2a}$$

$$\underline{x} = \frac{x}{L}$$

$$\underline{r}_0 = \frac{r_0}{2a}$$

$$\underline{t} = \sqrt{\frac{2a}{g}} \frac{t}{\tau}$$

$$\underline{v}_x = \sqrt{\frac{L^2 g}{2a}} v_x \quad (4-35)$$

$$\underline{v}_y = \sqrt{2ag} v_y$$

$$\tau_{\text{in-grav}} = \sqrt{\frac{2a}{g}}$$

$$\tau_{\text{in-mag}} = \sqrt{\frac{2a}{\frac{F_{\text{mag}}}{m}}}$$

$$\tau_{\text{in-vis}} = \frac{m}{6\pi\eta r_p} = \frac{2}{9} \frac{r_p^2}{\eta}$$

$$\tau_{\text{RES}} = \frac{L}{U} = \frac{L}{U_{\text{max}} \left[\frac{a-|y-a|}{a} \right]} \frac{1}{9}$$

Writing equation (4-34) for the x and y directions in terms of normalized variables gives

$$\frac{d^2 \underline{x}}{dt^2} = \frac{\tau_{\text{in grav}}}{\tau_{\text{in vis}}} \frac{dx}{dt} + \frac{\tau_{\text{in grav}}^2}{(\tau_{\text{in-vis}})(\tau_{\text{RES}})} \quad (4-36(a))$$

$$\frac{d^2 \underline{y}}{dt^2} = - \left(\frac{\tau_{\text{in grav}}}{\tau_{\text{in-vis}}} \right) \frac{dy}{dt} - 1 - \frac{\tau_{\text{in grav}}}{\tau_{\text{in-mag}}} \quad (4-36(b))$$

In general, one can express (4-36) in four first order differential equations.

$$\frac{d\underline{v}_x}{dt} = f(v_x, y, t) \quad (a)$$

$$\frac{dx}{dt} = \underline{v}_x \quad (b)$$

$$\frac{d\underline{v}_y}{dt} = g(v_y, y, t) \quad (c)$$

$$\frac{dy}{dt} = \underline{v}_y \quad (d)$$

Equations (4-37) can be numerically integrated if the y integrations (c,d) are performed first.

A fourth order Runge-Kutta numerical integration system was adopted marching equations (4-37) in time.^[1] The procedure made four approximations on the change in \underline{v}_y over the time interval Δt , taking a weighted average of these to get \underline{v}_y . The change in \underline{y} over this interval of time is found by a forward Euler approximation.

Given \underline{v}_{y_0} and y_0 at time \underline{t}

$$\Delta \underline{v}_{y_a} = \Delta \underline{t} g(\underline{v}_{y_0}; y_0; \underline{t}_0)$$

$$y_a = y_0 + \left(\frac{\Delta t}{2}\right) \left(\frac{1}{2}\right) (2\underline{v}_{y_0} + \Delta \underline{v}_{y_a})$$

$$\Delta \underline{v}_{y_b} = \Delta \underline{t} g\left(\underline{v}_{y_0} + \frac{\Delta \underline{v}_{y_a}}{2}; y_a; \underline{t}_0 + \frac{\Delta t}{2}\right) \quad 4-37)$$

$$y_b = y_0 + \frac{\Delta t}{4} (2\underline{v}_{y_0} + \Delta \underline{v}_{y_b})$$

$$\Delta \underline{v}_{y_c} = \Delta \underline{t} g\left(\underline{v}_{y_0} + \frac{\Delta \underline{v}_{y_b}}{2}; y_b; \underline{t}_0 + \frac{\Delta t}{2}\right)$$

$$y_c = y_0 + \frac{\Delta t}{2} (2\underline{v}_{y_0} + \Delta \underline{v}_{y_c})$$

$$\Delta \underline{v}_{y_d} = \Delta \underline{t} g(\underline{v}_{y_0} + \Delta \underline{v}_{y_c}; y_c; \underline{t}_0 + \Delta t)$$

$$\underline{v}_{y_1} = \underline{v}_{y_0} + \frac{1}{6} (\Delta \underline{v}_{y_a} + 2\Delta \underline{v}_{y_b} + 2\Delta \underline{v}_{y_c} + \Delta \underline{v}_{y_d})$$

$$y_1 = y_0 + (\Delta \underline{t}) \left(\frac{1}{2}\right) (\underline{v}_{y_0} + \underline{v}_{y_1})$$

The same procedure is then employed to obtain \underline{v}_{x_1} and x_1 over this time interval with y at midpoint approximated as $\frac{(y_0 + y_1)}{2}$. The integration

program KDDN4 is listed in Appendix H. The final result is the particle trajectory flight profiles for different exit positions from the injection tube. (figure 4-8).

The use of the flux conservation principle is necessary to obtain density information from these results. In steady state, the spreading of the trajectory lines is related to the density. Specifically, if the profile trajectories have an initial separation Δy and impact the lower duct wall with a separation (Th_0) , then

$$n_0 \Delta y_0 v_{x_0} = n \left| \frac{dy}{dt} \right|_{y=0} (Th_0) \Delta z \quad (4-38)$$

or after normalizing

$$\frac{n}{n_0} = \frac{\Delta y_0 v_{x_0}}{(Th_0) \left| \frac{dy}{dt} \right|_{y=0}} \quad (4-39)$$

Inherent in equation (4-39) is the assumption that the density is uniform over the injection tube cross section.

Inherent in eqn. (4-39) is the assumption that the problem is two-dimensional with no spreading in the transverse z direction. This assumption is consistent with using a multi-tube particle injector positioned at several z locations across the duct. A transverse slit may be ideal from this viewpoint but would surely perturb the air flow and generate a disruptive wake. (Figure 4-9(a)). The z dependence is not critical since all precipitation measurements were averaged over the duct width. The effects of turbulent diffusion considered in the next section tend to somewhat uniformly spread the precipitate after about two duct widths downstream, even for moderately

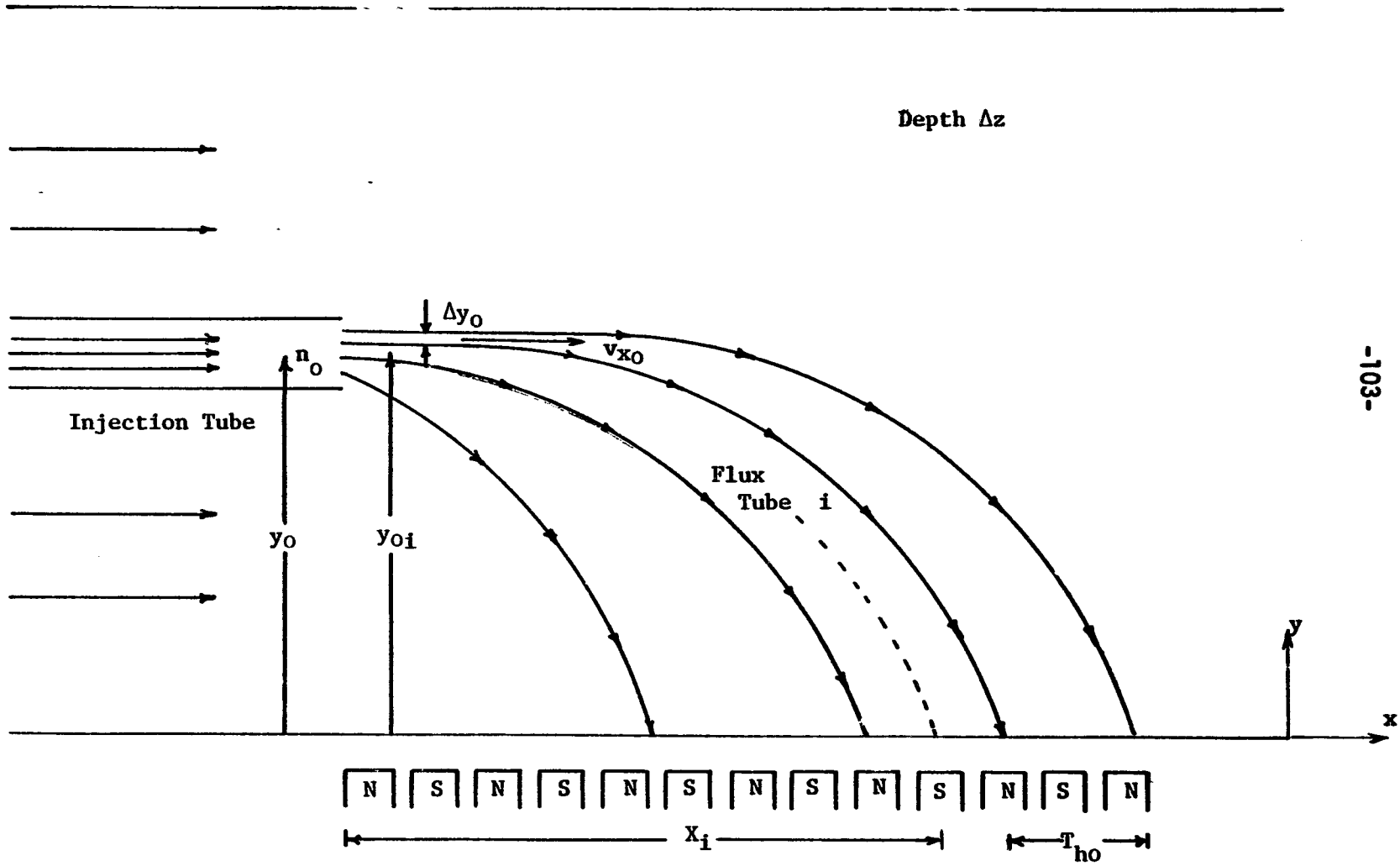


Figure 4-8 Particle Inertial Trajectories

large particles (100 μ). It was decided therefore to use a simple tube injector.

Figure (4-9(b)) depicts a reasonable flux profile upon exit from the injection tube. Quantitatively, the net flux should display the characteristic turbulent velocity tube profile dependence, i.e.,

$$\bar{\Gamma}_{x=0} = n_{\max} v_{x_{inj}} \left(\frac{r_0 - |y - y_0|}{r_0} \right)^{\frac{1}{9}} \bar{I}_x \quad (4-40)$$

where

$v_{x_{inj}}$ = the average injection velocity

r_0 = the tube radius

y = the position in the tube measured from the bottom of the duct

y_0 = the distance to tube centerline from the bottom of the duct

n_{\max} = the maximum density at the center of the tube

The net weight of particulate injected during a time t_0 in steady state is

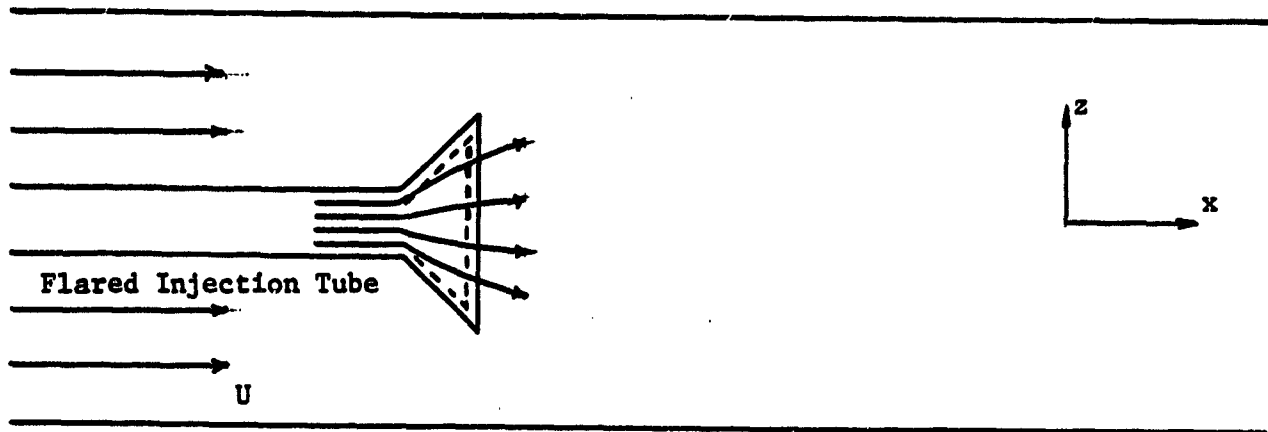
$$wt_{(injected)} = \int_0^{t_0} \int_{y_0 - r_0}^{y_0 + r_0} \rho (\bar{\Gamma} \cdot \bar{I}_x) w \, dy \, dt \quad (4-41)$$

and using equation (4-35)

$$wt_{(injected)} = (\rho) (2r_0) (9) (v_{x_{inj}}) n_{\max} t_0 \quad (4-42)$$

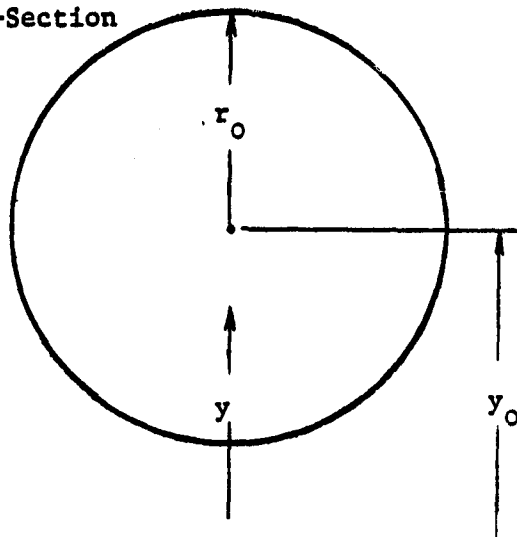
The flux and weight of precipitate collected on the bottom over an interval Δx are respectively:

$$\bar{\Gamma} = \left(\begin{array}{c} \text{axial} \\ \text{component} \end{array} \right) \bar{I}_x + \left(n \left(\frac{dy}{dt} \right)_{y=0} \right) \bar{I}_y \quad (4-43)$$



(a) Two-Dimensional Injection Tube

Tube
Cross-Section



$$\bar{\Gamma} = \Gamma_0 \left(\frac{r_0 - |y - y_0|}{r_0} \right)^{1/9} \bar{i}_x$$

(b) Flux Profile Exiting Injection Tube

Figure 4-9 Particle Injection System

$$C_{\text{collected}}^{\text{wt.}} = \int_0^{t_0} \int_{x_0 - \frac{\Delta x}{2}}^{x_0 + \frac{\Delta x}{2}} \rho (\bar{r}_{y=0} \cdot \bar{i}_y) w \, dx \, dt \quad (4-44)$$

Combining equation (4-44) with (4-42) it follows that the weight collected per unit interval Δx becomes

$$C_{\text{collected}}^{\text{wt}} = \frac{C_{\text{injected}}^{\text{wt}} \left(\frac{dy}{dt} \right)_{y=0} \Delta x \frac{n}{n_0}}{(.9) (2r_0) v_{x_{inj}}} \quad (4-45(a))$$

or normalized

$$C_{\text{collected}}^{\text{wt}} = \frac{C_{\text{injected}}^{\text{wt}} \left(\frac{dy}{dt} \right)_{y=0} \Delta x \frac{n}{n_0}}{(.9) (2r_0) v_{x_{inj}}} \quad (4-45(b))$$

Combining the above with equation (4-39) gives

$$C_{\text{collected}}^{\text{wt}} = \frac{C_{\text{injected}}^{\text{wt}} \frac{\Delta y}{\Delta t} \frac{\Delta x}{\Delta t}}{(.9) (2r_0) (Th_0)} \quad (4-46)$$

Thus a knowledge of the particle trajectories is enough to link the inertial theory on an absolute scale to experimental precipitation results. The experimental correlation is shown in chapter 6-c. This theory, ignoring turbulent diffusive effects altogether, predicts far too large a particulate deposition.

(2) Hybrid Inertial-Diffusion Model. ($10\mu < r_p < 50\mu$)

The results from the time constant analysis indicate migration times are an order of magnitude shorter than the duct diffusion time for 55μ particles. This was based however on diffusion over the duct half height. Upon exit from the injection tube, the vertical density gradient is quite large near the tube outer radius. Furthermore, chapter 5 reveals that the upstream diffusivity

is nearly an order of magnitude larger than the downstream value ($.002 \frac{m^2}{sec}$). An inclusion of diffusion effects appears necessary especially in the neighborhood of the injection nozzle. The problem then centers on incorporating both inertia and diffusion.

The aim is to accurately predict the density profile and precipitation of particles in the diameter range 55-75 microns. The above discussion would indicate a perturbation on the inertia theory analysis is more appropriate than a modification of the diffusion small particle theory for this particle range. Towards this end, it appears that the addition of a term to the momentum equation is acceptable because the solution degenerates to the diffusion model when inertia effects vanish. A possible solution meeting this requirement (basically superposition of models) is

$$m \frac{d\bar{v}}{dt} + 6\pi n r_p \bar{v}_p = 6\pi n r_p U + m\bar{g} + F_{mag} - 6\pi n r_p D_t \frac{\nabla n}{n} \quad (4-47)$$

With $m = 0$, multiplying by density n and dividing by $(6\pi n r_p)$ gives the flux expression (4-1). The diffusion model then follows by taking the divergence. Equation (4-47) is in Lagrangian coordinates, and thus the instantaneous particle density and gradient must be known along its trajectory. The evaluation can be made only by incorporating conservation of particle flux. This is to be expected since the nature of the diffusion term depends not on a single particle's parameters, but on the proximity of its neighbors.

One can now proceed along the lines of the previous section. The normalizations mimic those of (4-35) except for the x variables which are normalized to the duct height $2a$ for ease in evaluating density gradients.

$$\underline{x} = \frac{x}{2a}$$

$$v_x = \sqrt{2a} g v_x$$

$$\tau_{RES} = \frac{2a}{u} = \frac{2a}{U_{max} \frac{(a-|y-a|)}{a}} \frac{1}{g} \quad (4-48)$$

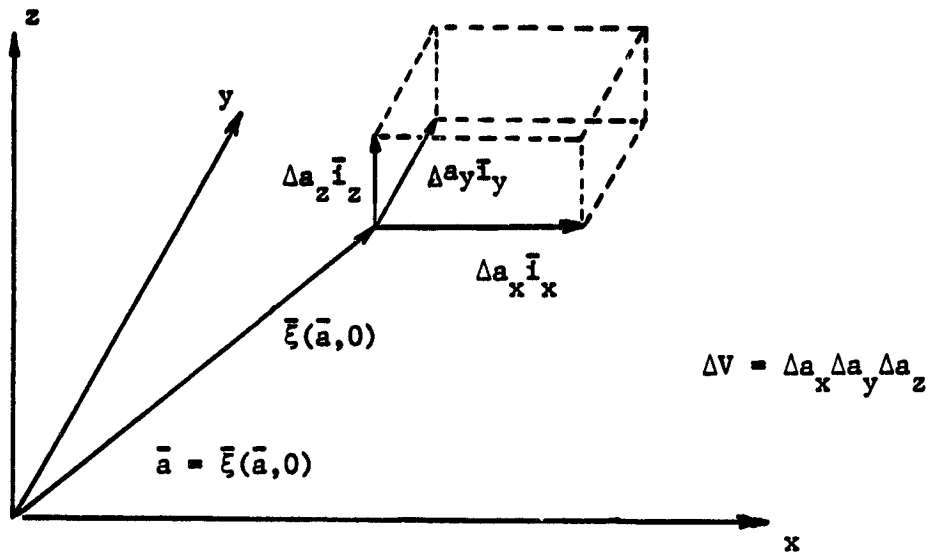
$$\tau_{Dif} = \frac{(2a)^2}{D_t}$$

As with the diffusion theory of section B, longitudinal diffusion will be assumed negligible when compared to convection. With these changes, the two normalized equations to be solved become

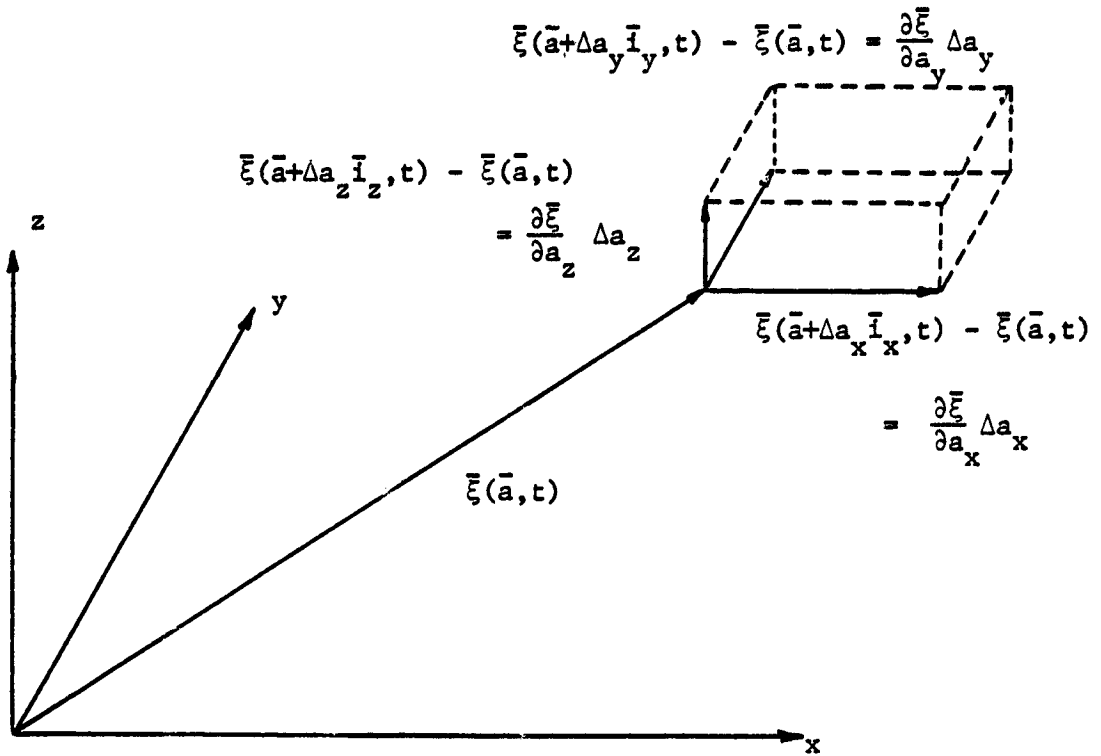
$$\frac{d^2x}{dt^2} = - \frac{\tau_{in-grav}}{\tau_{in-vis}} \frac{dx}{dt} + \frac{\tau_{in^2-grav}}{\tau_{in vis} \tau_{RES}}$$

$$\frac{d^2y}{dt^2} = - \frac{\tau_{in-grav}}{\tau_{in-vis}} \frac{dy}{dt} - 1 - \frac{(\tau_{in-grav})^2}{\tau_{in-mag}} - \frac{(\tau_{in-grav})^2}{\tau_{in vis} \tau_{Dif}} \frac{\partial n}{\partial y} \quad (4-49)$$

The method of integration is identical with the inertia model. Prior to the y integration however, the evaluation of the local density and density gradient is formulated for each flux tube (from the previous time step results), and this is used as the input for the next time step. The analysis requires that, the density be evaluated at every point. As the integration is carried out in Lagrangian coordinates, it is desired to compute the density in the same representation.^[2] All particle positions are specified by their initial position and time only. Figure (4-10,a) shows an incremental volume in space when t=0, the corner position designated $\bar{\xi} (\bar{a},0) = a$. By the time t, the volume element has changed location and shape as shown in Figure (4-10,b). The rate of change of the position vector $\bar{\xi}$ with respect to the initial volume element edge directions is found by observing the change of these edge vectors between the time 0 and t.



(a)



(b)

Figure(4-10) Lagrangian Representation of Incremental Volume

Element (a) $t = 0$, initial configuration (b) configuration at time t

Conservation of mass requires that

$$\rho(\bar{a},0) \Delta v (\bar{a},0) = \rho(\bar{a},t) \Delta v (\bar{a},t) \quad (4-50)$$

The initial volume of the differential elements is $(\Delta a_x \Delta a_y \Delta a_z)$. The final volume of the element at time t is just the parallelopiped volume of Fig.

(4-10,b), i.e.

$$\Delta v (\bar{a},t) = \frac{\partial \bar{\xi}}{\partial a_x} \Delta a_x \cdot \left(\frac{\partial \bar{\xi}}{\partial a_y} \Delta a_y \times \frac{\partial \bar{\xi}}{\partial a_z} \Delta a_z \right) \quad (4-51)$$

This volume is first found by taking the cross product and then carrying out the dot product of the volume element edge extentions. This operation on the derivatives of the position vector alone is known as the Jacobian J . Combining (4-50) and (4-51) gives

$$\rho(\bar{a},t) = \rho \frac{(\bar{a},0)}{J} \quad (4-52)$$

where $J \equiv$

$$\begin{vmatrix} \frac{\partial \xi_x}{\partial a_x} & \frac{\partial \xi_y}{\partial a_x} & \frac{\partial \xi_z}{\partial a_x} \\ \frac{\partial \xi_x}{\partial a_y} & \frac{\partial \xi_y}{\partial a_y} & \frac{\partial \xi_z}{\partial a_y} \\ \frac{\partial \xi_x}{\partial a_z} & \frac{\partial \xi_y}{\partial a_z} & \frac{\partial \xi_z}{\partial a_z} \end{vmatrix}$$

Each element of the Jacobian determinant, e.g. $\frac{\partial \xi_k}{\partial a_j}$, represents the change of position vector $\bar{\xi}$ in the k th direction of a particle beginning initially at $\bar{a} + \Delta a_j \bar{j}$ rather than at \bar{a} . In a two dimensional evaluation where

$$\frac{\partial \xi_i}{\partial a_z} = \begin{cases} 0 & i \neq z \\ 1 & i = z \end{cases} \quad (4-53)$$

$$\text{then } J = \begin{vmatrix} \frac{\partial \xi_x}{\partial a_x} & \frac{\partial \xi_y}{\partial a_x} \\ \frac{\partial \xi_x}{\partial a_y} & \frac{\partial \xi_y}{\partial a_y} \end{vmatrix} \quad (4-54)$$

The evaluation of the Jacobian and thus the density at position $\bar{\xi}_1$ ' time t, of figure (4-11) is obtained from knowledge of the trajectories of three other points beginning at position 2,3, and 4 at time t = 0. These elements are related to the position vectors as follows:

$$\begin{aligned} \frac{\partial \xi_x}{\partial a_x} &= \frac{(\bar{\xi}_{1'} - \bar{\xi}_{2'}) \cdot \bar{i}_x}{\Delta x_0} \\ \frac{\partial \xi_y}{\partial a_y} &= \frac{(\bar{\xi}_{3'} - \bar{\xi}_{4'}) \cdot \bar{i}_y}{2\Delta y_0} \\ \frac{\partial \xi_y}{\partial a_x} &= \frac{(\bar{\xi}_{1'} - \bar{\xi}_{2'}) \cdot \bar{i}_y}{\Delta x_0} \\ \frac{\partial \xi_x}{\partial a_y} &= \frac{(\bar{\xi}_{3'} - \bar{\xi}_{4'}) \cdot \bar{i}_x}{2\Delta y_0} \end{aligned} \quad (4-55)$$

where $\Delta x_0 = (v_{x_0}) \Delta t$, Δt being the incremental numerical time step.

Note that derivatives involving initial changes in vertical position Δy_0 were obtained from the displacement of position vectors to either side of the point in question to yield an effective two-sided derivative. This procedure was adopted throughout except at the upper and lower trajectories where a single vertical derivative was used.

The final step is to compute the vertical density gradient from this information. The attack employed here is to calculate the true gradient from a knowledge of the gradient component in two arbitrary directions. Consider

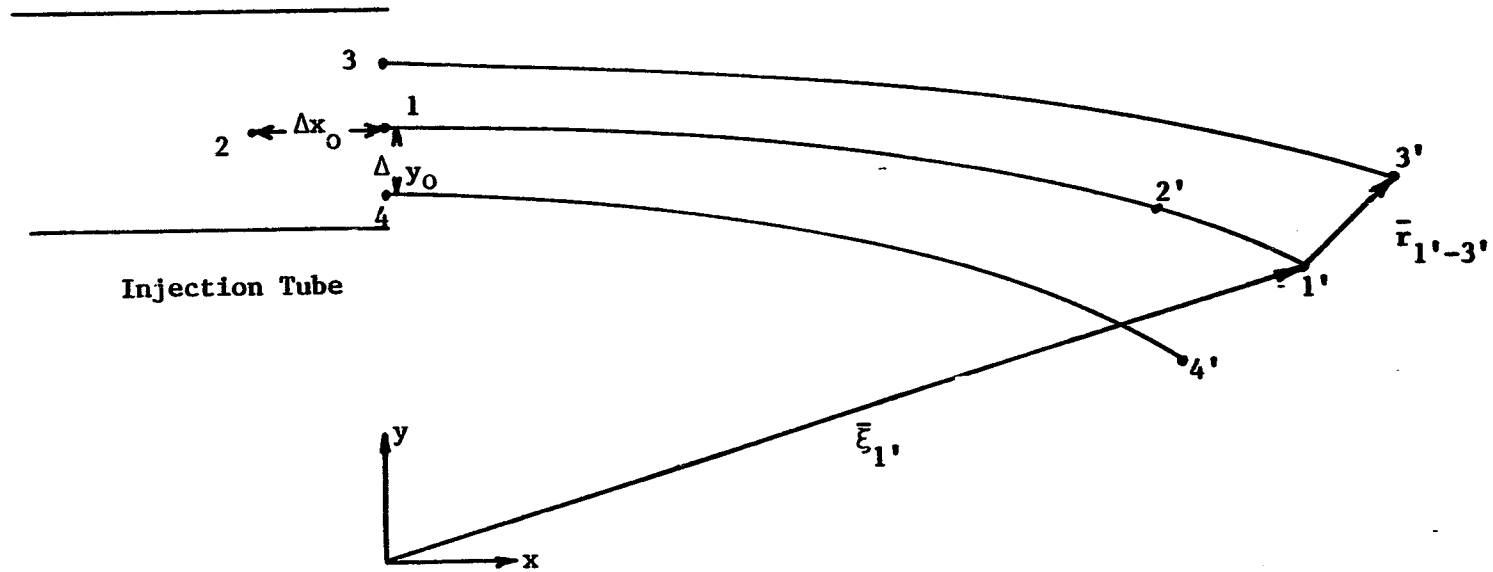


Figure 4-11 Particle Trajectories from Injection Tube

again figure (4-11) with the vector $\bar{r}_{1',-3'}$, representing the vector from point 1' to point 3' and $\bar{i}_{r_{1',-3'}}$, representing a unit vector in that direction.

Components of the density gradient are found as follows:

$$\nabla n \cdot \bar{i}_{r_{1',-3'}} = \frac{n_{3'} - n_{1'}}{|r_{3',-1'}|} \quad (4-56)$$

$$\nabla n \cdot \bar{i}_{r_{1',-2'}} = \frac{n_{2'} - n_{1'}}{|r_{1',-2'}|} \quad (4-57)$$

Splitting the gradient into x and y components and performing the dot product yields

$$\frac{\partial n}{\partial x} \frac{(x_{3'} - x_{1'})}{|r_{1',-2'}|} + \frac{\partial n}{\partial y} \frac{(y_{3'} - y_{1'})}{|r_{1',-3'}|} = \frac{(n_{3'} - n_{1'})}{|r_{3',-1'}|} \quad (4-58)$$

$$\frac{\partial n}{\partial x} \frac{(x_{2'} - x_{1'})}{|r_{1',-2'}|} + \frac{\partial n}{\partial y} \frac{(y_{2'} - y_{1'})}{|r_{1',-2'}|} = \frac{(n_{2'} - n_{1'})}{|r_{1',-2'}|} \quad (4-59)$$

Equations (4-58) and (4-59) can be solved to give the vertical gradient

$$\frac{\partial n}{\partial y} = \frac{(n_{3'} - n_{1'})(x_{2'} - x_{1'}) - (n_{2'} - n_{1'})(x_{3'} - x_{1'})}{(y_{3'} - y_{1'})(x_{2'} - x_{1'}) - (y_{2'} - y_{1'})(x_{3'} - x_{1'})} \quad (4-60)$$

This analysis is basically good except for the one-sided nature of the vertical point difference ($\bar{r}_{3',-1'}$). This one-sided difference was found to precipitate oscillations in the computer program. For trajectories other than the upper and lower ones, it was better to replace equation (4-56) with one involving points 3' and 4' to approximately represent the gradient at 1', i.e.,

$$\nabla n \cdot \bar{i}_{r_{4',-3'}} = \frac{n_{3'} - n_{4'}}{|r_{4',-3'}|} \quad (4-61)$$

The vertical gradient throughout most of the trajectory region becomes

$$\frac{\partial n}{\partial y} = \frac{(n_3, -n_4)(x_2, -x_1) - (n_2, -n_1)(x_3, -x_4)}{(y_3, -y_4)(x_2, -x_1) - (y_2, -y_1)(x_3, -x_4)} \quad (4-62)$$

It was desired to keep the incoming flux profile unchanged from the inertial assumption. To also avoid huge gradients at the tube periphery, the injection velocity was assumed constant across the injection tube exit area and the density given the characteristic turbulent profile, i.e.

$$\frac{n}{x=0} = \left(\frac{r_0 - |y-y_0|}{r_0} \right)^{\frac{1}{9}} \quad (4-63)$$

The linking of these results with the deposition on the lower wall proceeds exactly as in the previous section (equation (4-46)). The program KDIN7 used is listed in Appendix I.

One final comment concerning particulate spreading by turbulent diffusion is in order. Turbulent eddies can never cause movement of particulate faster than the turbulent perturbation velocity. It was necessary to put an upper limit on $\frac{D_t \Delta n}{n}$ at v' which from chapter 3 becomes

$$\frac{D_t \nabla n}{n} \leq \sqrt{\frac{D_t}{T}} \quad (4-64)$$

Furthermore, it was assumed sufficient in the perturbation type analysis to keep D_t uniform across the duct core region and setting it to zero one-half centimeter from the wall (D_t goes from 0 to maximum value in roughly 1 centimeter). The theory's insensitivity to the choice of cutoff layer thickness shown in chapter 6, justifies this action.

A comparison of this hybrid theory's precipitation prediction with experiment follows in chapter 6-B. The work in chapter 7 concerning particle

flight in a jet boundary layer builds on the hybrid diffusion theory.

Chapter IV - Bibliography

1. Carnahan, B., Luther, H., and Wilkes, J., Applied Numerical Methods, John Wiley & Sons, Inc., New York, 1969, pp. 361-366.
2. Mason, W., Physical Acoustics, Academic Press, New York, 1964, pp. 7-11.

V. DOCUMENTATION OF FIELDS AND FLOWS

A. Introduction

The thrust of this thesis is directed towards predicting the precipitation of magnetizable particulate in turbulent air flows. Towards this end, it is necessary to quantify turbulent eddy effects and magnetic field effects and magnetic field effects. The purpose of this chapter is three-fold:

- i) to describe the method used for inducing turbulence in the duct
- ii) to document the measurement of the channel turbulent diffusion coefficient
- iii) to give an account of the permanent magnet array field measurement

The goal of the first objective was to induce turbulence in the duct that would not decay as quickly as that incited by a screen. It was hoped that the design of a velocity profile grid might give rise to a channel intensity resembling fully developed turbulent flow. The result was in fact a turbulent intensity decaying an order of magnitude over the channel length (which is considerably better than the turbulence excited by a screen). The axial non-uniformity in turbulence was acceptable but necessitated measurement of turbulent diffusivity at several axial locations.

The result of the second objective was an experimental measure of the turbulent diffusivity's axial and transverse character in the duct. The outcome of this testing was the establishment of the credibility of linking these measurements to existent fluid turbulence diffusivity literature. Specifically, the data supported the decision to use the transverse diffusivity dependence documented by Davies (chapt. 3 [2]) with the peak magnitude obtained experimentally along the duct. This course of action was motivated by the desire to avoid using transverse experimental results be-

cause of the asymmetry they exhibited. The asymmetry was caused by the hot wire anemometer probe schroud; the schroud inhibited fluid flow differently when extended clear across the duct than when extended just past the insertion hole.

The third objective was to determine the nature of the magnetic field on the duct lower surface excited by the permanent magnet structure. The goal specifically was to ascertain the relative size of the different harmonics. As an aside, it was found that positioning the magnets 1/4" from the duct lower surface yielded a nearly sinusoidal field on the duct surface.

B. Inducement of Turbulence and the Velocity Profile Grid

This section describes the construction of a velocity profile grid intended to excite a fully developed turbulent flow. The grid design (an improvement over a plane screen) succeeded in inducing turbulence decaying an order of magnitude down the duct.

The desirability of a fully developed turbulent flow poses a problem in this experiment. Although the Reynolds number for this flow is well within the turbulent region (~36,000), the length of duct necessary for development of this flow is prohibitive. Schlichting [1] states that the point of transition at which an instability initiates a growing disturbance in the flow has been found empirically to occur when

$$R_e = \frac{U_o X}{\nu} \approx 3.5 \times 10^5 \quad (5-1)$$

For a 4.3 m/sec flow, this gives a transition length of 2.5 meters. Furthermore, the boundary layer thickness δ is given by

$$\delta(x) = (0.37) x \left(\frac{U_0 x}{\nu}\right)^{-1/5} \quad (5-2)$$

Thus the distance x for this boundary layer to grow half the duct width ($a = 6.35$ cm) is

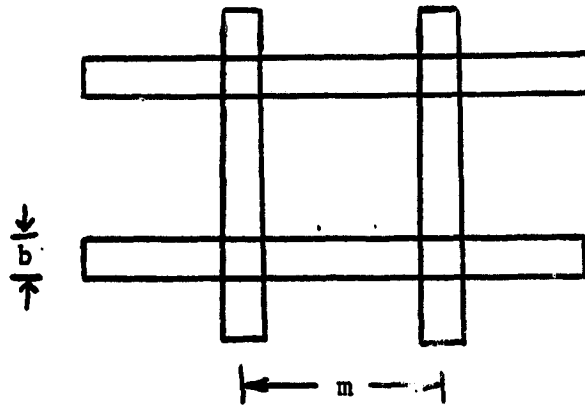
$$x = \left(\frac{\delta}{.37}\right)^{5/4} \left(\frac{U_\infty}{\nu}\right)^{1/4} = 2.6 \text{ meters} \quad (5-3)$$

It would take over 4.5 meters to insure fully developed turbulent flow.

One method of exciting turbulence in the duct is to use a screen or wire mesh. According to Baines and Peterson [2] the mesh size of the screen and the wire diameter (bar thickness) completely determine the character of the turbulence excited. Their results reveal that 5 - 10 mesh lengths (see Fig. 5-1) downstream from the screen are required to insure good flow establishment, i.e., homogeneity. It is the screen bar thickness b (wire diameter) however, which determines the turbulent intensity decay. The figure shows roughly this intensity versus distance downstream dependence in terms of number of bar thicknesses. It is desirable to work in the region where $v'/u = .01$, 100 bar thicknesses downstream. This option would however yield a very low intensity, and a roughly exponential decaying turbulent level would still exist in the experimental section. For this reason the option of using a nonuniform velocity profile grid rather than a screen was adopted.

There are at least two requirements that such a profile grid must meet to establish a fully developed turbulent flow--

- 1) The size of eddies excited by the grid spires must be the same as the large scale eddies (L) that would exist in the full developed turbulent duct flow.



Screen Mesh

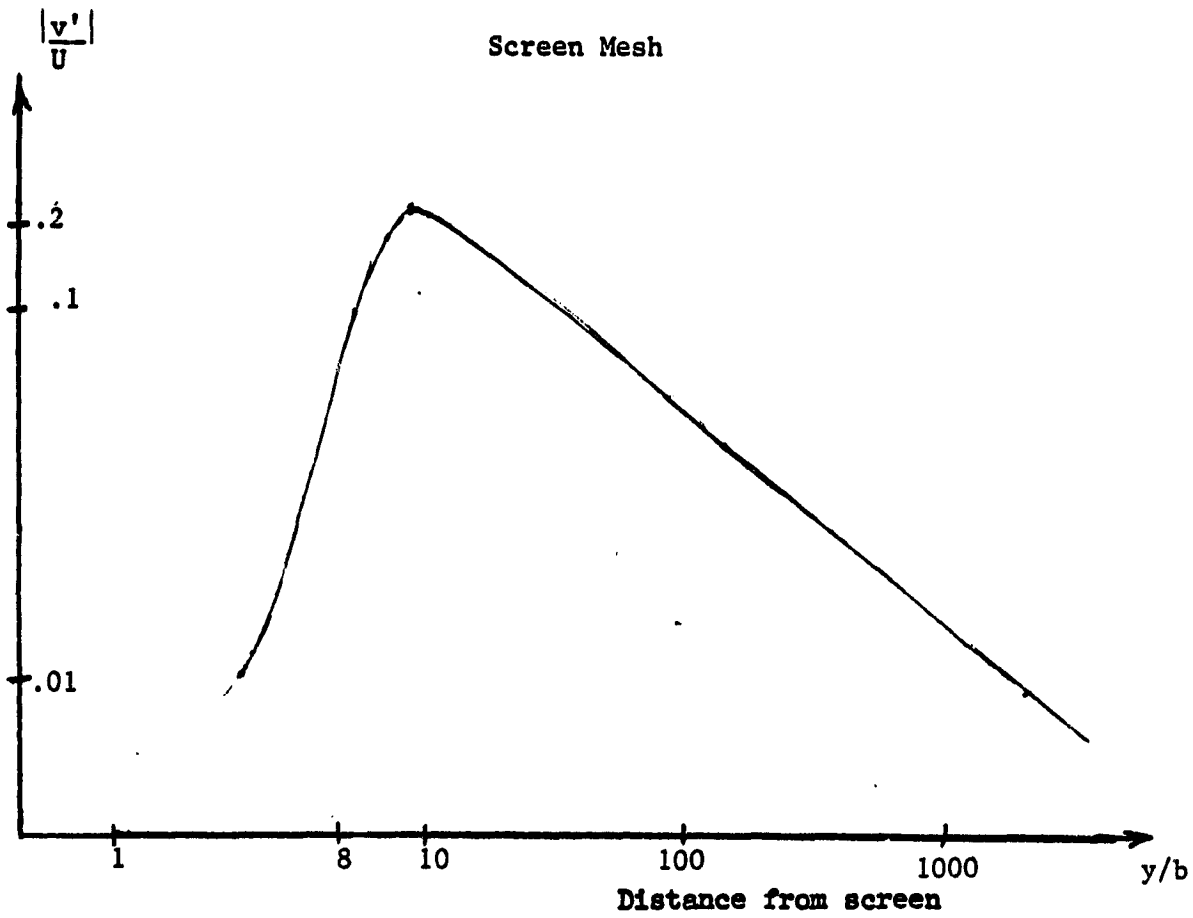


Figure 5-1 Turbulent Intensity Variation

- 2) The impedance presented by the grid to the upstream flow must be such that the average axial flow velocity U over the duct cross-section matches that of the fully developed turbulent flow.

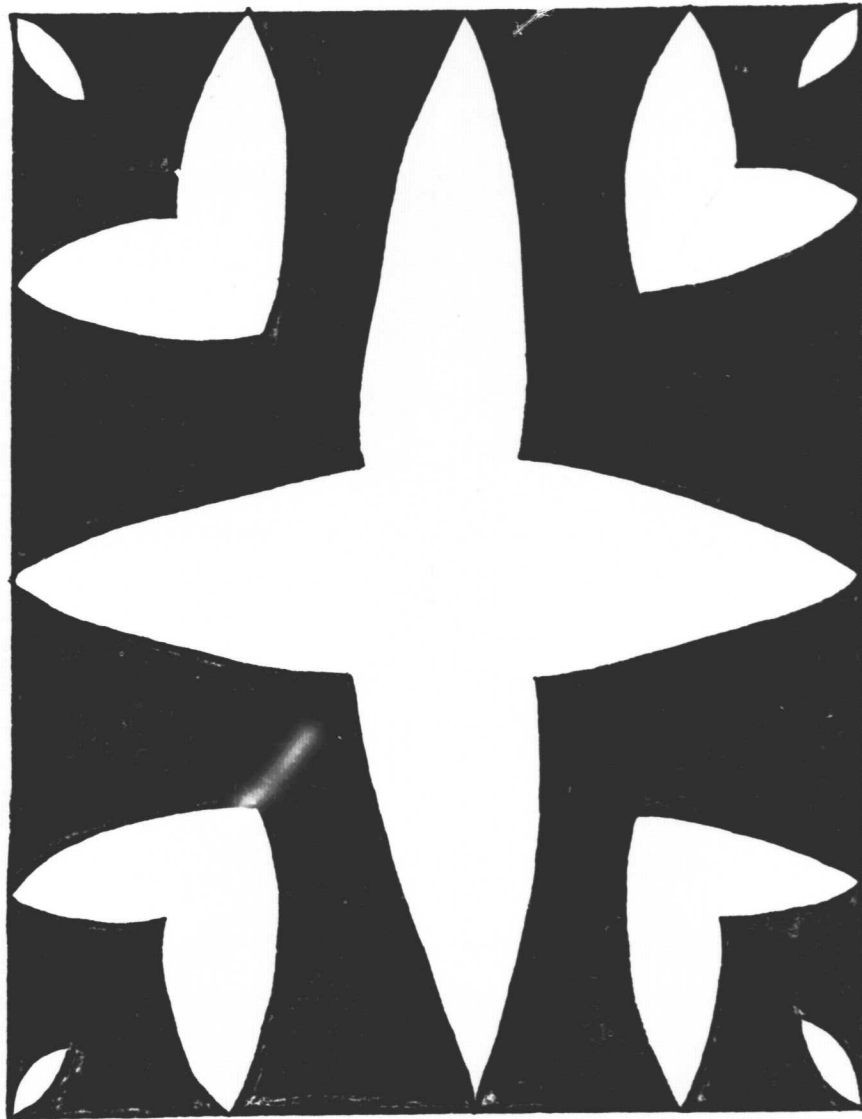
It is noted that this discussion does not consider the effect of duct walls on the turbulence growth.

Most work on profile grids has been done with circular ducts. A typical profile grid for a round pipe is shown in Fig. (5-2(b)). The grid consists of a number of radial spires, the size of which at any radius is chosen to match (i.e., insure the same velocity of) the fully developed flow. The number of spires is determined in meeting requirement (1) above. The average thickness of a spire (e.g. at half the radius) represents the average eddy scale excited; this must be the same order as the turbulent length scale for the circular duct flow desired.

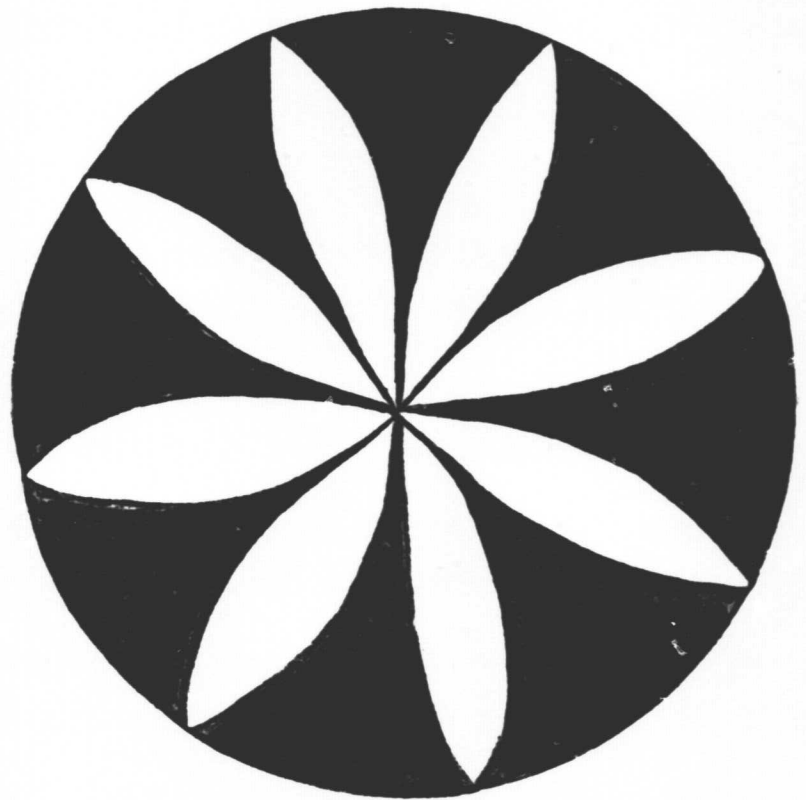
The corresponding grid for the rectangular duct is shown in Fig. (5-2(a)). Each side of the duct has the same number of spires extending toward the center, but each is terminated on the duct diagonals. The same procedure is used in determining the width and number of each spire.

It was concluded after private consultation [9] that the characteristic duct integral scale is roughly a quarter of the duct width. The eddy size excited by a spire will be roughly the same as the spire width. This would indicate four spires to a side as being the proper choice, which is what the author used.

The spire width calculation required more work. Frank Durgin [3] has studied the excitation of full scale turbulence in pipe flow, and has found that the spire width d and the spire spacing λ should be related as follows (see fig. 5-3):



(a)



(b)

Figure 5-2 Velocity Profile Grid (a) duct grid, (b) pipe grid - black indicates blocked portions

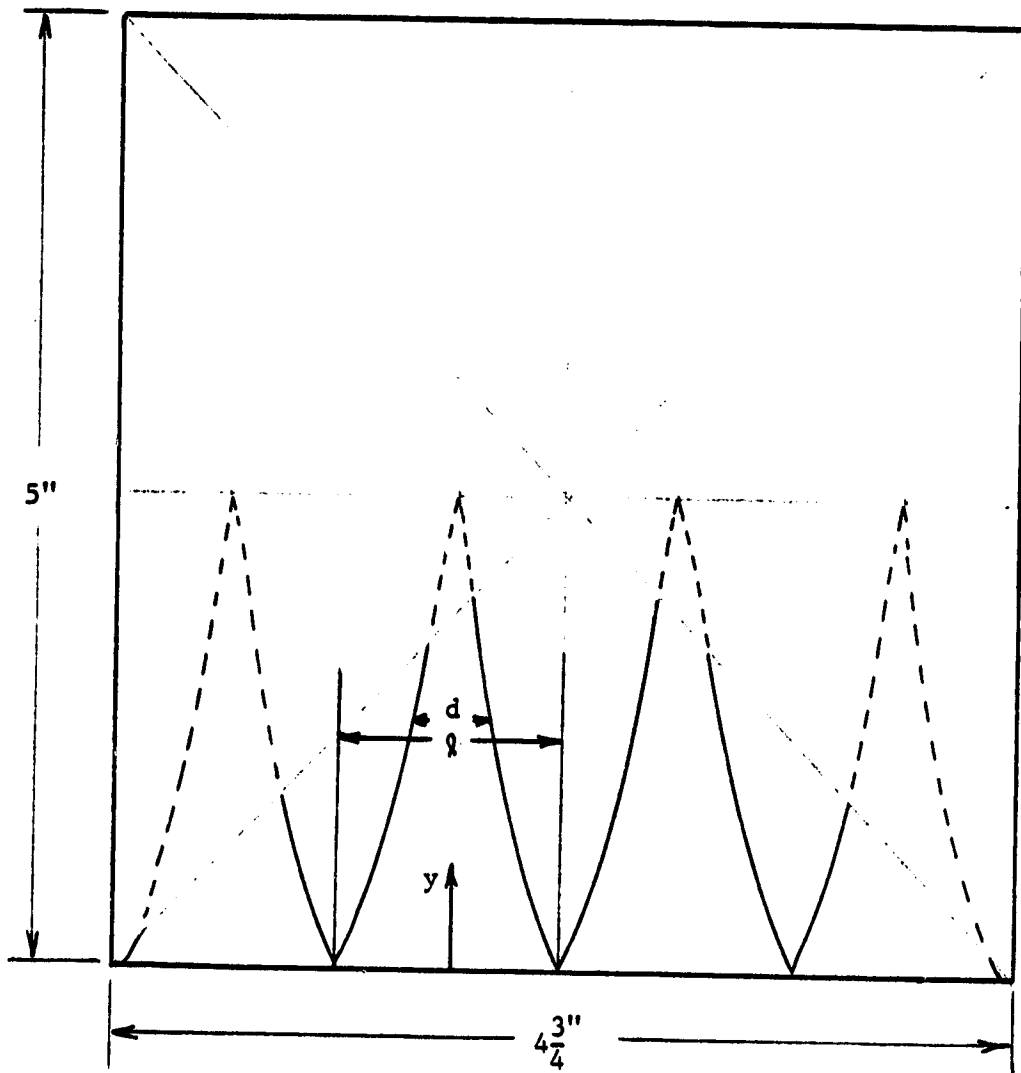


Figure 5-3 Profile Grid Construction (Dots indicate portions of spires cut off).

$$\left(\frac{U_0}{U}\right)^2 = 1 + k_1 \frac{(d/l)^2}{1-(d/l)^2} \quad (5-4)$$

where U = the average X directed velocity
 U_0 = the maximum midstream x directed velocity
 k_1 = constant

In circular pipe flow k_1 is about 4, but private discussion [9] has led the author to believe $k_1 = 10$ is more accurate for rectangular ducts.

To complete the calculation, a formula for flow velocity with position is needed. The author has measured the duct flow velocity with position. The results for maximum flow speeds of 850 ft./min. (4.3 m/sec) and 450 ft./min. (2/2 m/sec) are shown in Fig. 5-4. The asymmetry about the center line is attributed to two aspects of the anemometer probe:

- 1) At lower y positions, the probe extends across the entire duct impeding flow above the probe tip. At the upper positions leakage is occurring through the probe insertion hole.
- 2) The anemometer probe tip is completely surrounded by a metal shroud inhibiting sensitive measurements especially near the wall. This is undoubtedly the source of asymmetry exhibited in Figures (5-4) and (5-10).

The author has fitted several curves of the form

$$\frac{U}{U_0} = \left(\frac{y}{a}\right)^{1/n} \quad (5-5)$$

where ($n = a$ constant) to the above data. The best fit appears to occur when $n = 9$; these are plotted next to the experimental measurements in

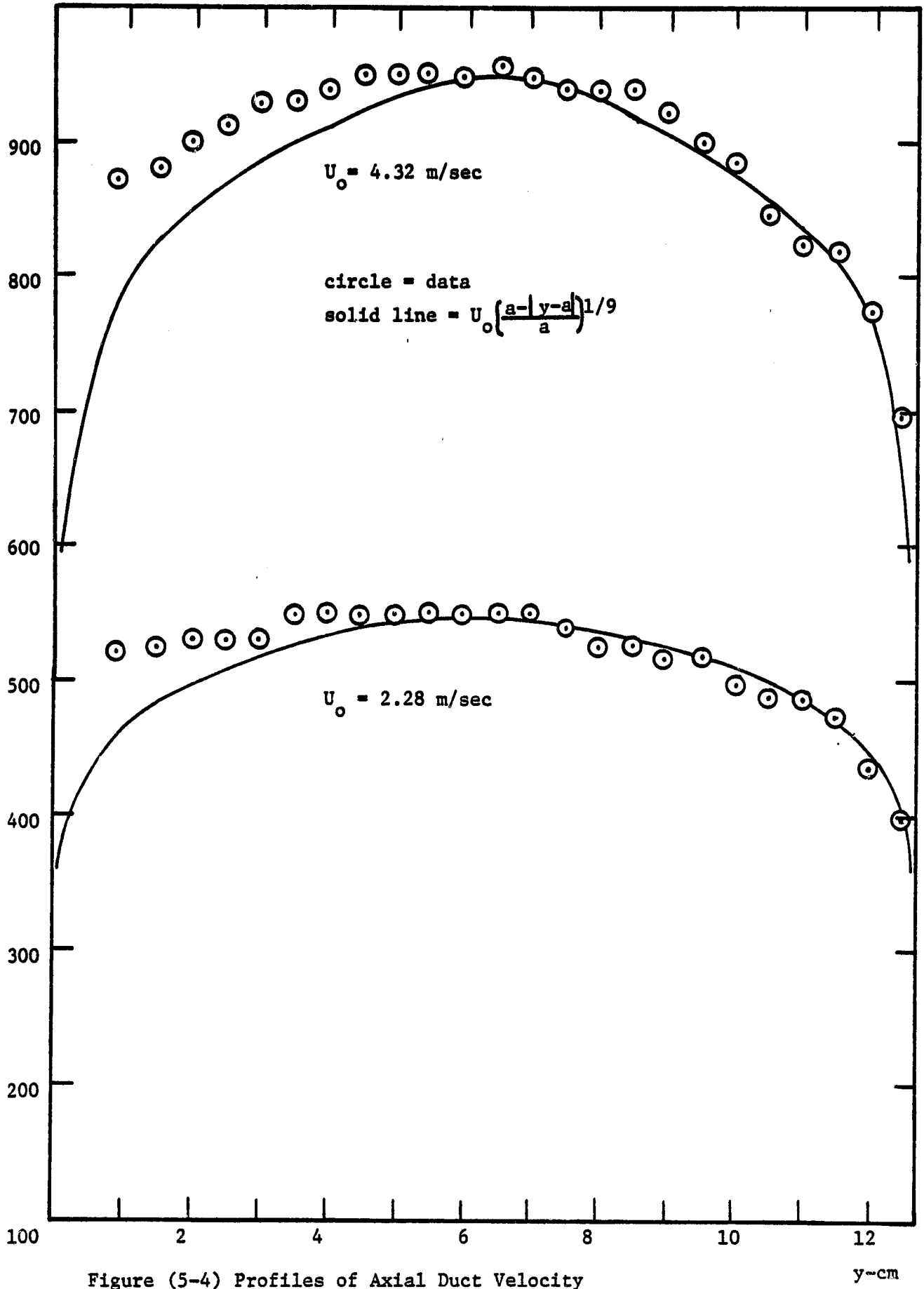


Figure (5-4) Profiles of Axial Duct Velocity

y-cm

fig. (5-4).

Using the above results, equation (5-4) transforms to

$$\frac{d}{\ell} = \frac{\sqrt{\frac{(\frac{a}{y})^{2/9} - 1}{10}}}{1 + \sqrt{\frac{(\frac{a}{y})^{2/9} - 1}{10}}} \quad (5-6)$$

Now since ℓ is equal to a quarter of the duct width, d is calculated for every position up to the center of the duct. ℓ and a are different for the vertical sides with rectangular ducts, but (5-6) applies. Thus the author constructed eight identical vertical spires and eight horizontal spires, positioning these as in Fig. 5-3 and cutting them along the duct diagonals.

As will be shown in the next section, the turbulence decay is consistent with screen literature predictions if the characteristic screen bar size is chosen equal to the thick base (1.25") of the spire. Choosing any other thickness of the spire as a representative bar size leads to the conclusion that the spires induce a turbulence that does not decay as rapidly as would screen turbulence (incidentally, 4 screen bars 1.25" thick would block the duct completely). The important point is that turbulence is induced and has an axial variation.

C. Turbulent Diffusion Coefficient Determination

Historically, work in the area of turbulent electrostatic precipitation [7] has been geared along one of two limits. One involves the assumption of an infinite diffusivity known as the Deutsch model, which implies the fluid turbulent eddies dominate all other forces in supplying particulate to duct walls where it can be precipitated. The second limit ignores diffusion and infers that particles have a large enough inertia that they are unaffected

by turbulent eddies. The work by Williams and Jackson [8] assumes a constant diffusivity (based on Dhanak's formula --chapter 3) falling instantly to zero a small distance δ from the walls. The intent of this section is to build upon the work of Davies (chap. 3, [2]), i.e., to use the transverse diffusivity dependence he documents with the midstream measured duct diffusivity.

The turbulent diffusion coefficient was found in Chapter 3 to be

$$D_t = \overline{v'^2} \tau \quad (5-7)$$

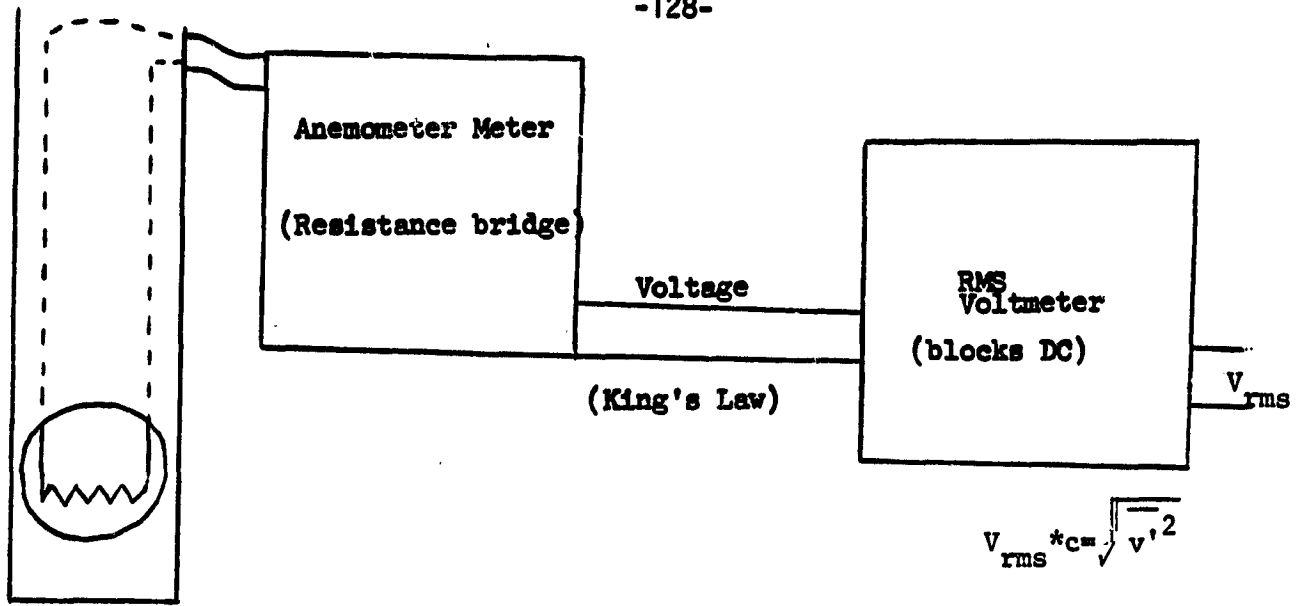
where $\overline{v'^2}$ is the time average squared perturbation velocity

$$\text{and } \tau = \int_0^{\infty} \frac{\overline{v'(\tau-t) v'(t)} d\tau}{\overline{v'^2}}$$

The long overbar in the Lagrangian time scale τ is understood to be an average in time t .

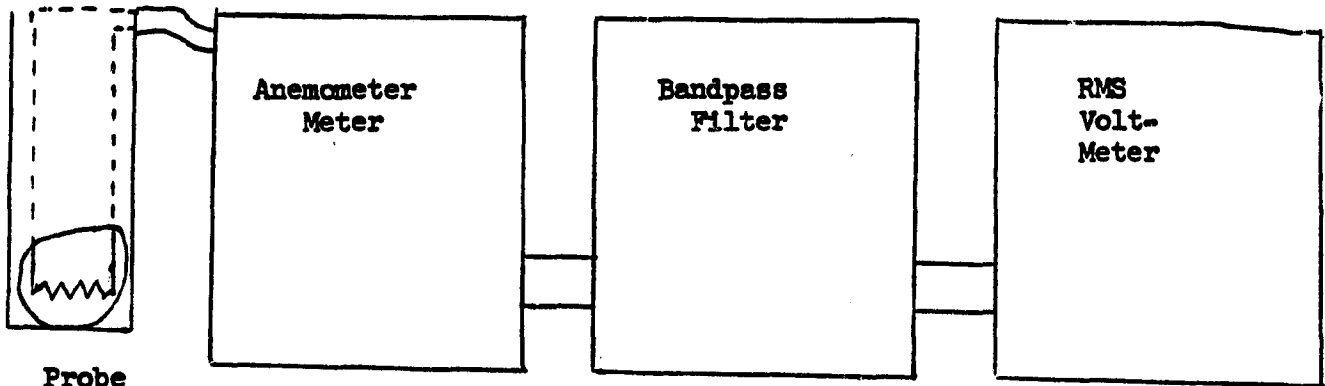
The turbulent intensity $\overline{v'^2}$ was measured with an RMS meter and an anemometer probe. The velocity probe signal feeds a resistance bridge in the anemometer which then in turn supplies a voltage to an RMS voltmeter that blocks any dc signal (see Fig. 5-5, a). The RMS voltage is then multiplied by a constant to give the turbulent intensity.

The output from the anemometer wire represents the resistance change resulting from the cooling of the hot wire probe. This velocity voltage relationship is sometimes referred to as the King relationship and is shown in Fig. 5-6. The anemometer signal can be fed into an equalizer to linearize the voltage dependence. If the interdependence is linear, then any perturbation velocity superimposed on the main flow, when filtered through an RMS



Anemometer Probe

(a) Turbulent Intensity Measurement



(b) Length Scale Measurement

Fig. 5-5 Diffusion Coefficient Measurement Scheme

voltmeter and multiplied by the slope (change in velocity with respect to voltage), will yield the turbulent intensity.

Because an equalizer was not available, a more approximate method had to be adopted. Figure (5-6) shows the anemometer voltage-velocity relationship. As long as the velocity perturbations about the steady mean are small, the RMS voltage is related to the average perturbation velocity through the local slope. By taking the slope from fig. (5-6) for the average flow at every position y in the duct (fig. (5-4)), one gets the proper multiplying factor, c , along the duct. The turbulent intensity measured in this manner is shown in Fig. 5-7 for mean flow velocities 4.32 m/sec and 2.28 m/sec.

The measurement of the turbulent time scale is more involved and requires a measurement of the energy spectrum, i.e., the turbulent energy in isolated frequency bands. Von Karman [4] and Berman [5], as well as Hinze's book ((pp. 165-174) referenced in Chapter 3) use stochastic theory to provide a connection between the integral of the velocity auto-correlation in eqn. (5-7) and the turbulent energy spectrum. Berman, as well as Durgin and Fannucci [6], specifically correlate the integral length scale with the frequency at which the turbulent intensity begins to fall, i.e.,

$$L = \frac{U_0}{2\pi f_b} \left(\frac{1}{\sqrt{1.8}} \right) \quad (5-8)$$

where U_0 = the maximum axial velocity
 f_b = the turbulent intensity break point frequency

Figure (5-8) shows the turbulent intensity in 20 Hz band widths with a main flow of 4.32 m/sec and 2.28 m/sec. The measurements were made in the center of the duct in both the x and y directions. The equipment set-up

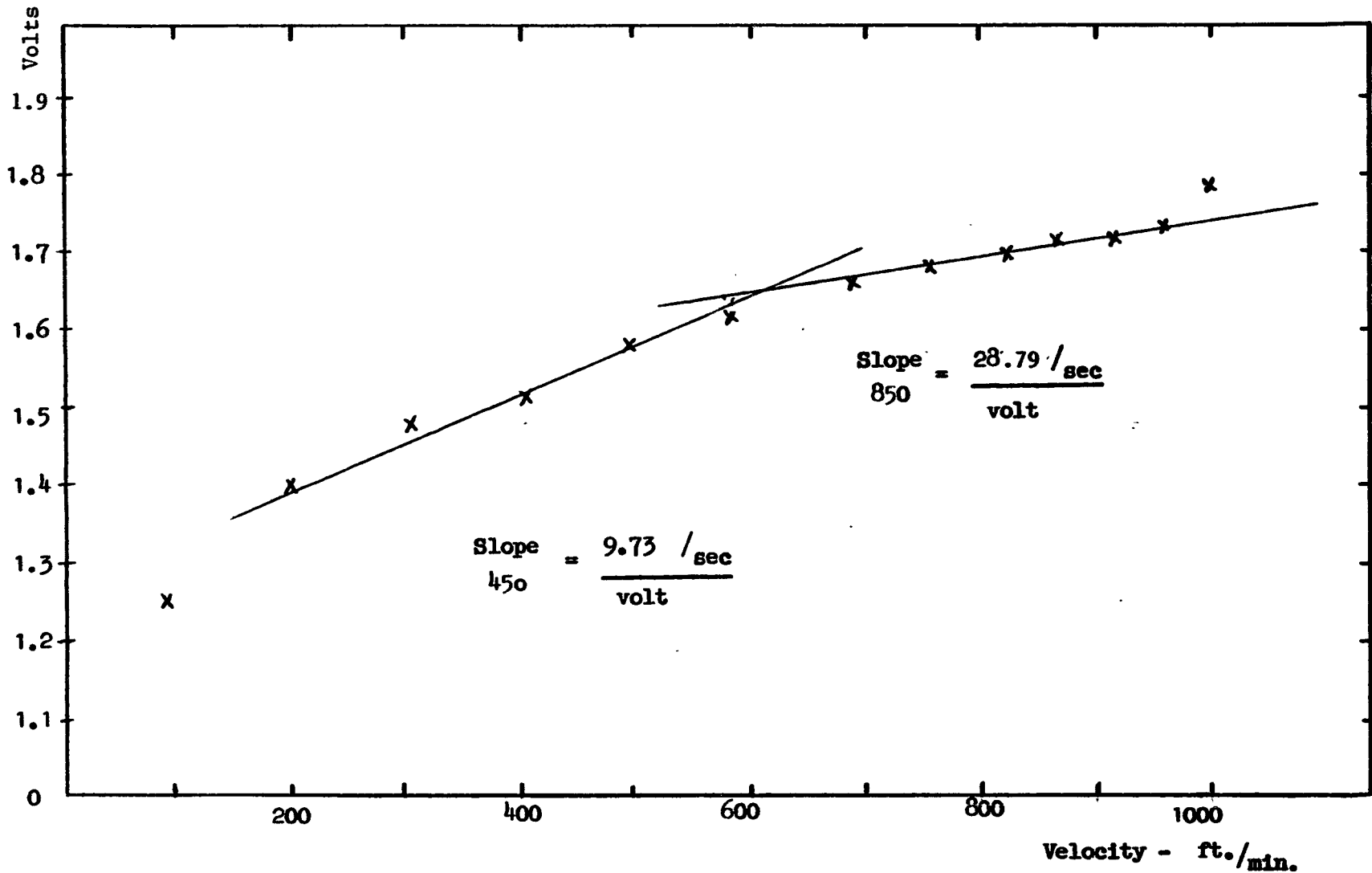


Figure 5-6 Anemometer Voltage - Velocity Curve

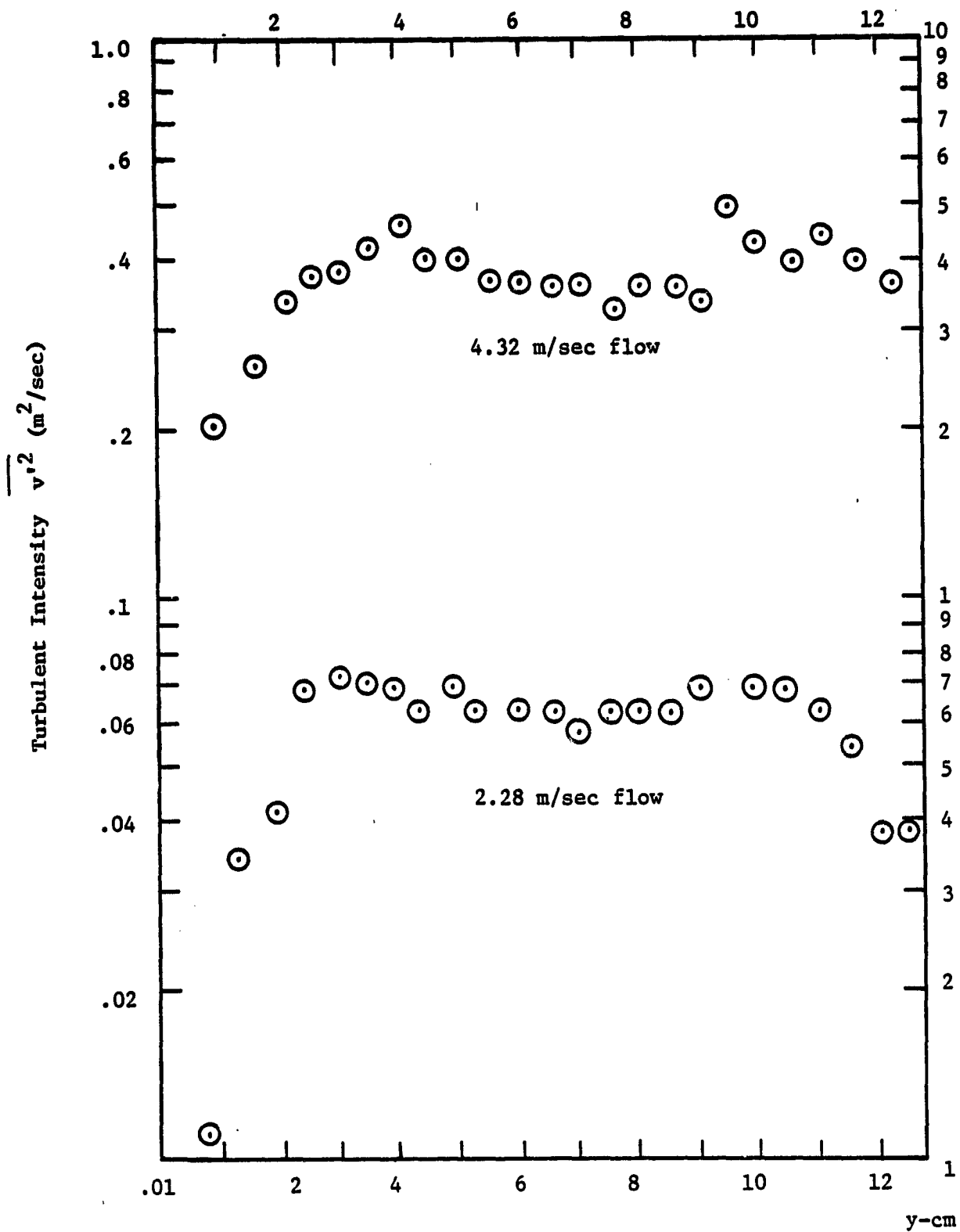


Figure (5-7) Turbulent Intensity Versus Position in Duct

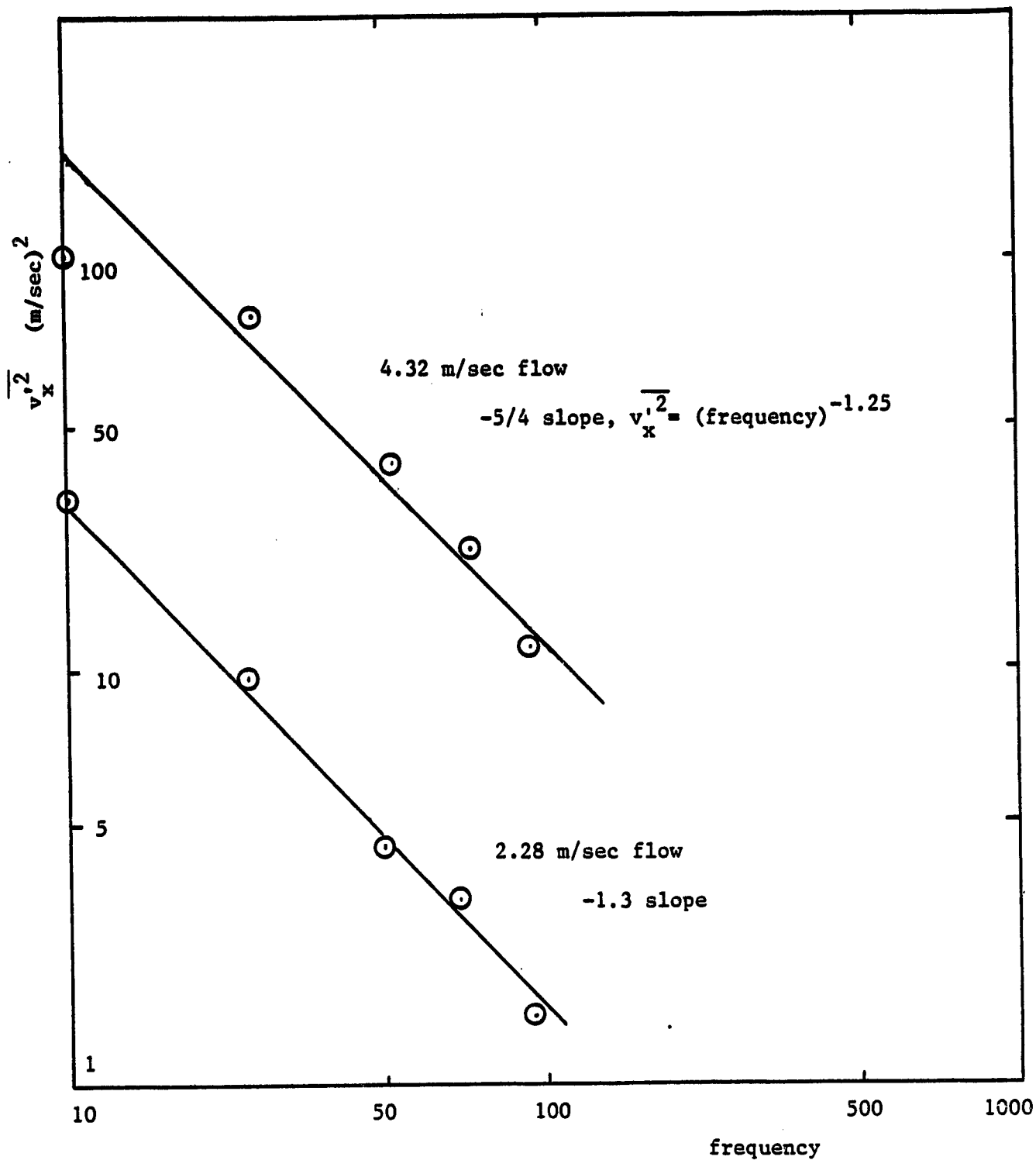


Figure 5-8 Turbulent Intensity for 20 hz Frequency Bands

is shown in fig. (5-5(b)). The process is identical to that above except for the addition of the bandpass filter. As fig. (5-8) shows, the 20 Hz bandpass test beginning at 10 Hz, revealed only the characteristic decrease in turbulent intensity with a 5/4 fall off. It was necessary to decrease the frequency bands to 4 Hz, centering the first at 4 Hz to observe a constant intensity and a break frequency. Figure (5-9) shows these results, again for measurements in the center of the duct for a 4.32 m/sec flow. The axial flow intensities for each flow exhibit a 19 Hz break frequency at 4.32 m/sec flow and a 15 Hz break frequency at 2.28 m/sec. flow.

Using equation (5-8) and the work from Chapter 3 in connecting the turbulent length and time scales ($T = L/U_0$), the desired turbulent parameters follow:

$$\begin{array}{l} 4.32 \text{ m/sec flow} \\ \\ 2.28 \text{ m/sec flow} \end{array} \left\{ \begin{array}{l} L = 2.7 \text{ cm} \\ T = .00624 \text{ secs.} \\ \\ L = 1.81 \text{ cm} \\ T = .00791 \text{ secs.} \end{array} \right. \quad (5-9)$$

Multiplying these time scales by the respective turbulent intensities of fig. (5-7) gives the turbulent diffusion coefficients shown in Figs. (5-10) and (5-11). Along with these experimental values are shown the diffusivities as predicted by Davies and Dhanak (see chapter 3). Davies's prediction based on the duct width Reynolds number gives

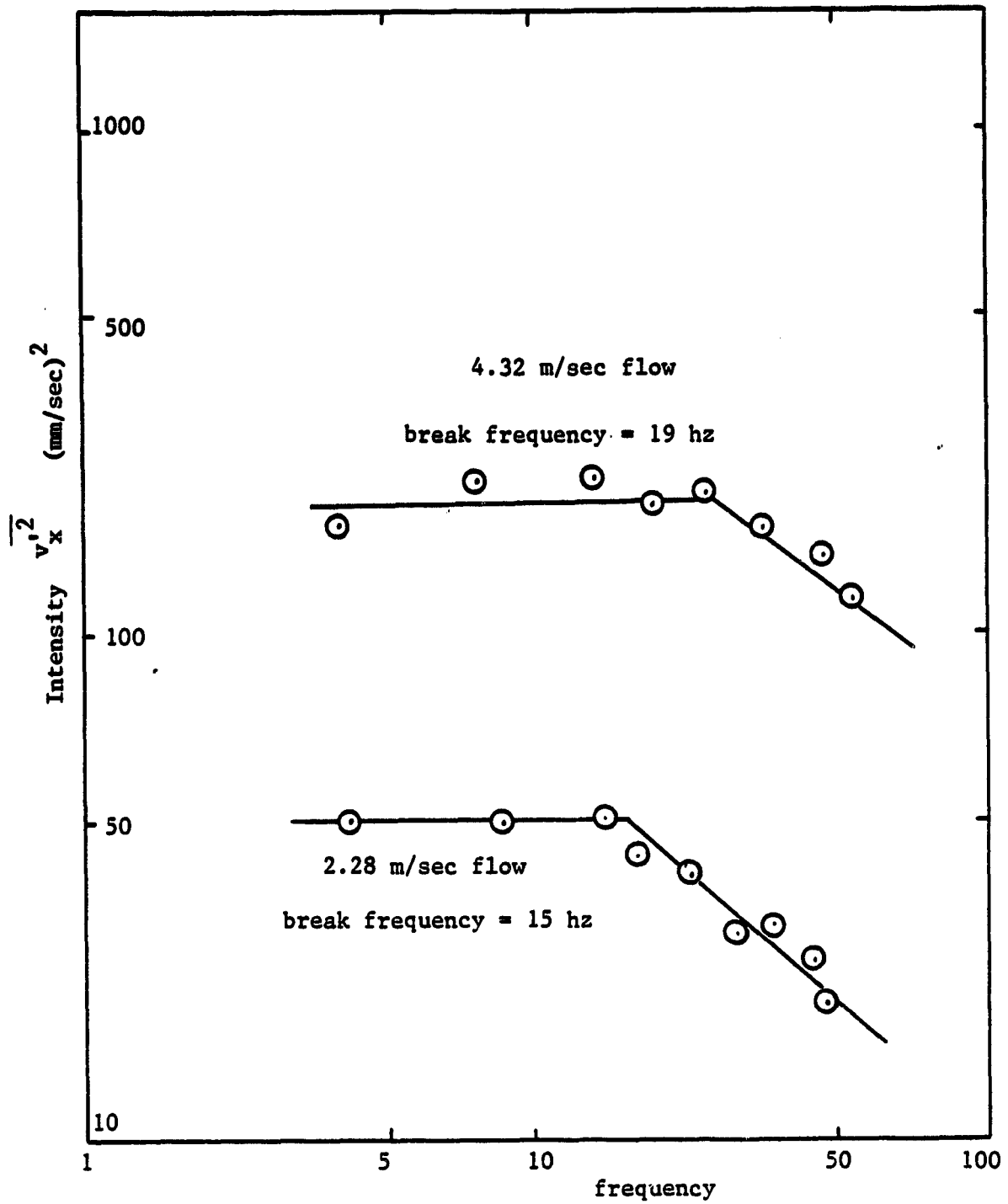


Figure 5-9 Turbulent Intensity for 4 Hz Frequency Bands

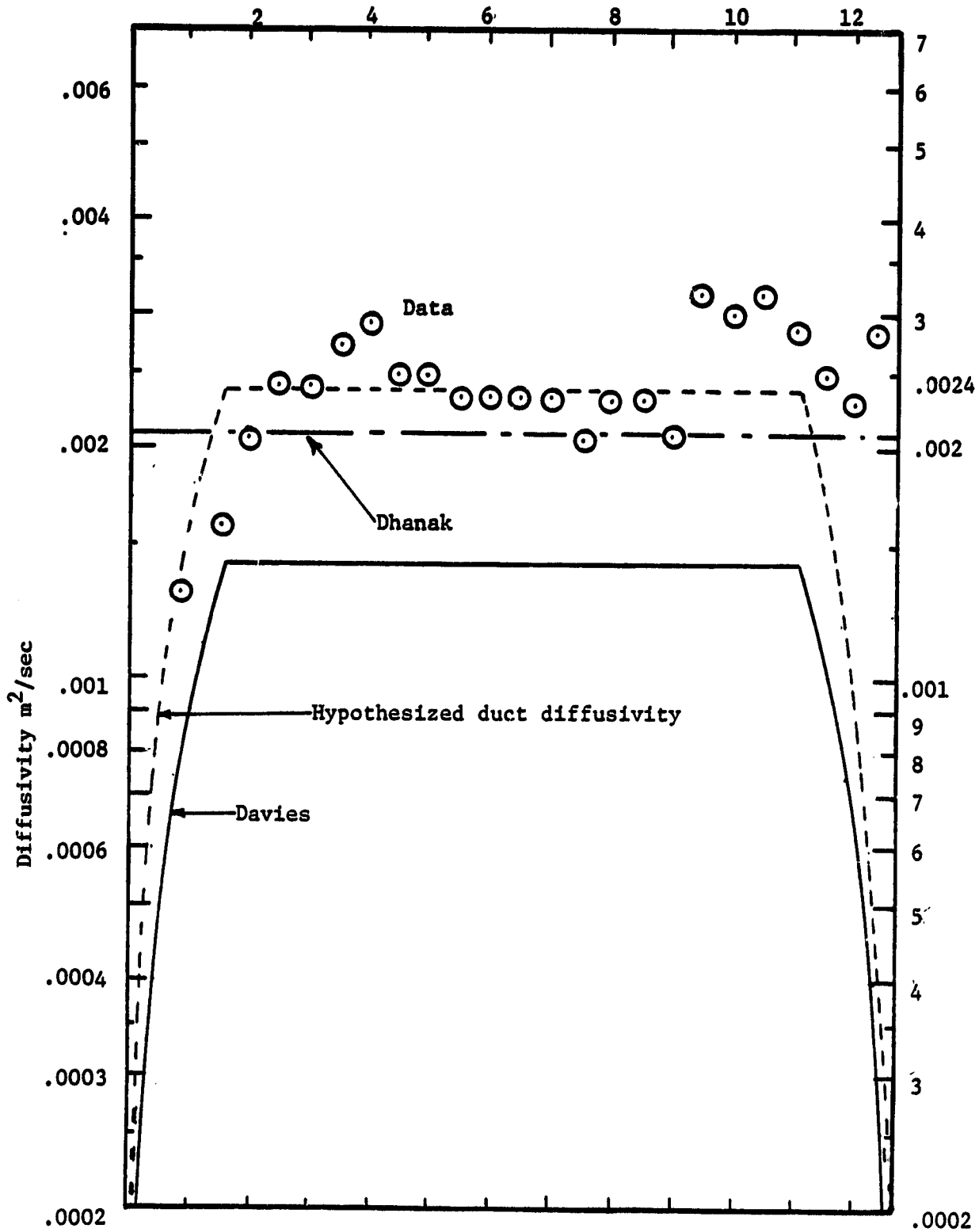


Figure (5-10) Diffusivity versus Position for a Main Stream Flow of 4.32 m/sec

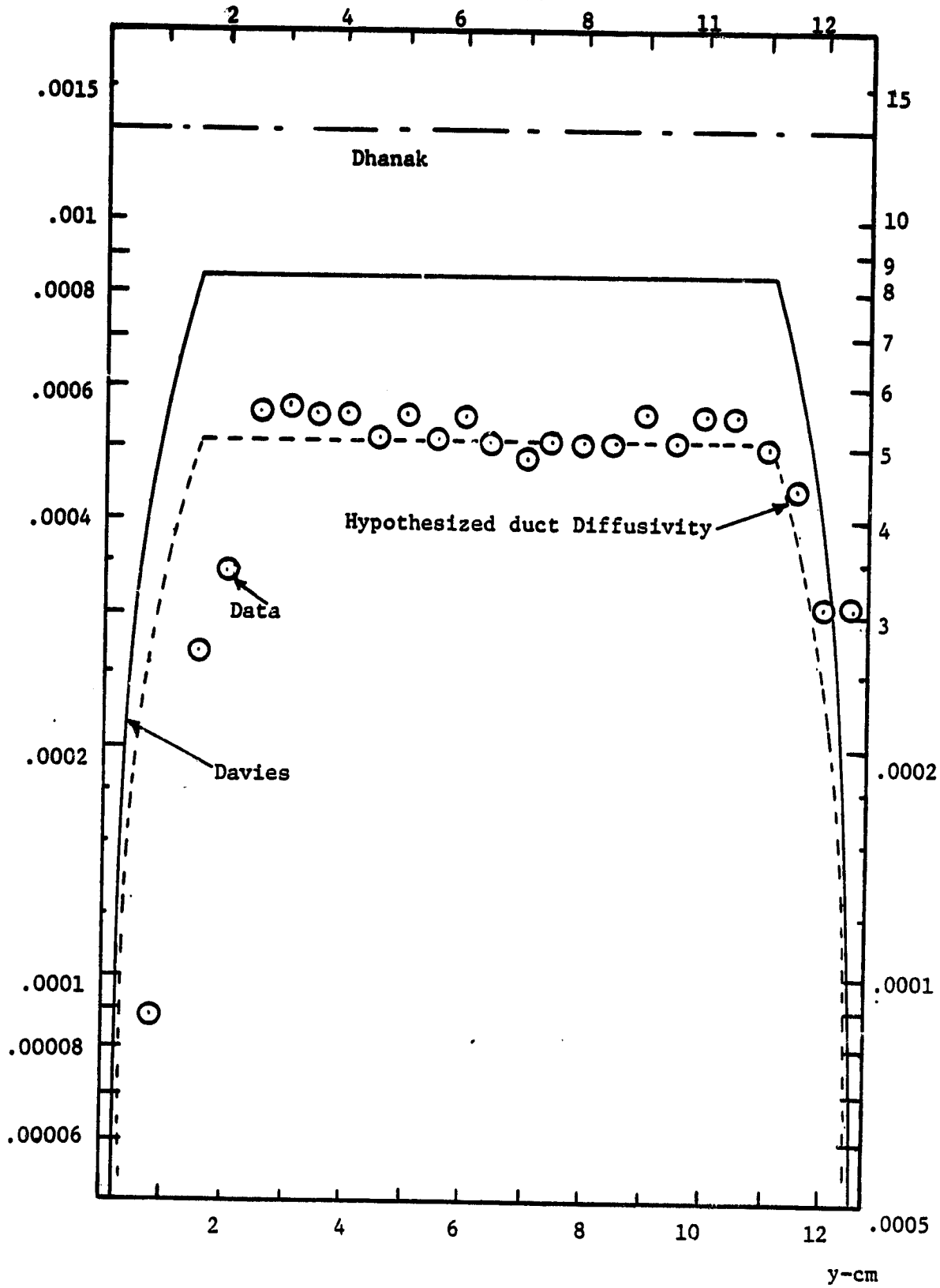


Figure (5-11) Diffusivity versus Position for a Main Stream Flow of 2.28 m/sec

$$D_{\dagger} = .01\nu(R_{e_{2a}})^{.875} \quad \left\{ \begin{array}{l} 4.32 \text{ m/sec } D_{\dagger} = .00147 \\ 2.28 \text{ m/sec } D_{\dagger} = .00084 \end{array} \right. \quad (5-10)$$

As shown in figs. (5-10,5-11), Davies assumes a rise in diffusivity to the above values in 1/8 of the channel width. Dhanak bases his diffusivity prediction on the duct half width Reynolds number as well as the duct friction factor.

$$D_{\dagger} = .0708 R_{e_a} \nu\sqrt{f} \quad \left\{ \begin{array}{l} 4.32 \text{ m/sec } D_{\dagger} = .00205 \\ 2.28 \text{ m/sec } D_{\dagger} = .0013 \end{array} \right.$$

Here it is assumed from Dhanak's empirical results that the friction flow factor for a dry air is .011 and .016 for the 4.32 m/sec and 2/28 m/sec flows respectively. This value which represents axial dependence only is intended to be valid in midstream. The rough agreement of the three is actually quite good when one remembers that these expressions are obtained empirically for specific flows.

One further point should be made concerning the generality of this approach. The diffusivity obtained was based on turbulent intensities measured in the flow direction. To apply this diffusivity to diffusion in the y direction, one must assume isotropic turbulence, which shall be assumed henceforth. It was hoped that the turbulent intensities might be measured in the transverse directions, but the probe multiplicative constant is difficult to determine near zero mean flow and the linearity

assumptions are questionable.

The diffusivity representation adopted in this work uses the transverse dependence of Davies with the measured experimental midstream diffusivity to determine longitudinal magnitudes. The hybrid diffusivities are shown dotted in figures (5-10) and (5-11). These measurements were taken just before the right-most flange of fig. 1-2. One rough order estimate of the diffusivity's axial dependence is obtained from screen turbulence literature, e.g., Baines and Peterson [2]. Given a screen bar size equal to the base spire width (1.25"), their results predict a grid turbulence level $(\frac{v'}{U})^2 = .16$ and a turbulength scale $L = .0095$ m, 6 inches from the screen. With a 7.62 m/sec flow the diffusivity is

$$D_t = \frac{L}{U} \left(\frac{v'}{U}\right)^2 U^2 = .0116 \text{ m}^2/\text{sec} \quad (5-12)$$

This would indicate an order of magnitude decay down the duct is likely.

Fig. (5-12) shows the measured diffusivity versus axial position. The region immediately following the grid where the velocity "necks" down exhibits a calm before a turbulent transition. This data was matched in a least squares polynomial fit using the MIT Math library subroutine LSFIT. The axial dependence past the 1' mark was found to be accurately represented as

$$\begin{aligned} D_t = & .0546 - .151 x + .202 x^2 \\ & - .0843 x^3 - .079 x^4 + .0289 x^5 + .0656 x^6 \\ & - .0336 x^7 \end{aligned} \quad (5-12)$$

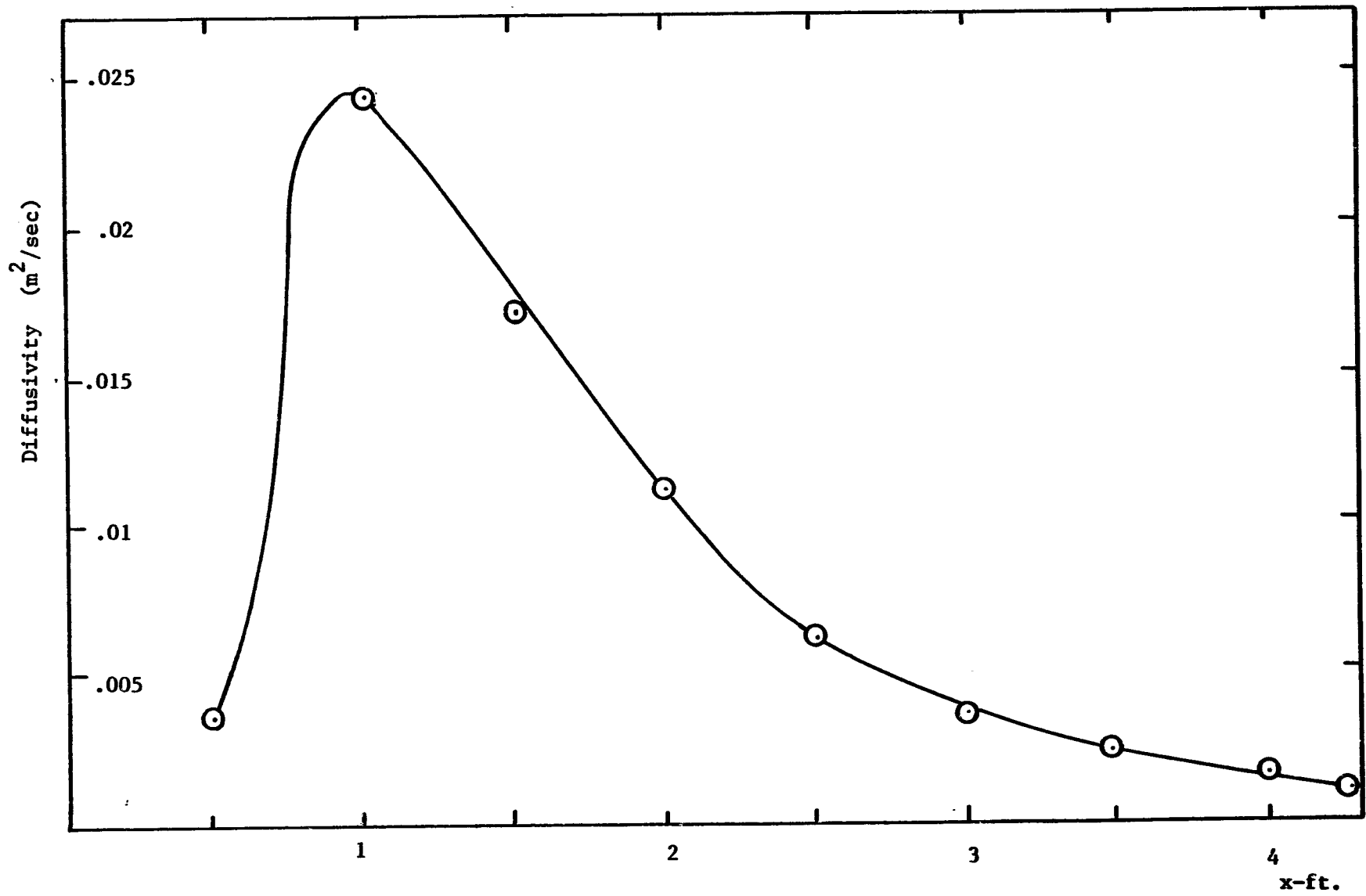


Figure 5-12 Turbulent Diffusivity versus Axial Position

This completes the measurement of diffusivity as a function of both x and y.

D. Magnetic Field Distribution

As mentioned in chapter 2, the permanent magnet field structure is not sinusoidal, but contains many harmonics. Given that the field pattern repeats over a length L and begins at zero, a reasonable representation would be

$$B_{\text{net}}(x) = \sum_{m=1}^m b_m \sin \frac{2\pi m x}{L} \quad (5-13)$$

Multiplying equation (5-13) by $\sin \frac{2\pi \ell x}{L}$ and summing over 2M-1 discrete X steps gives

$$\sum_{x=\Delta x_1}^{(2M-1)\Delta x_1} B(x) \sin \frac{2\pi \ell x}{L} = \sum_{x=\Delta x_1}^{(2M-1)\Delta x_1} \sum_{m=1}^m b_m \sin \frac{2\pi m x}{L} \sin \frac{2\pi \ell x}{L} \quad (5-14)$$

where $\Delta x_1 = L/2M$

Using the discrete orthogonality property for sinusoids wherein

$$\sum_{x=\Delta x_1}^{(2M-1)\Delta x_1} \sin \left(\frac{2\pi m x}{L} \right) \sin \left(\frac{2\pi \ell x}{L} \right) = \begin{cases} 0 & m \neq \ell \\ 1/2 (2M-1) & m = \ell \end{cases} \quad (5-15)$$

it follows that

$$b_m = \frac{2}{2M-1} \sum_{x=\Delta x_1}^{(2M-1)\Delta x_1} B_{\text{net}}(x) \sin \left(\frac{2\pi m x}{L} \right) \quad (5-16)$$

The normal flux density was measured 1/4" above the permanent magnet wave structure for each of three wavelengths—5.08 cm, 8 cm, and 12 cm using a Hall effect probe. For each case, a discrete Fourier analysis according

to the above discussion was performed using the computer program FOURIE listed in Appendix I. The measured field for the above three wavelengths along with the first 9 calculated harmonic components is shown in figs. (5-13) to (5-15).

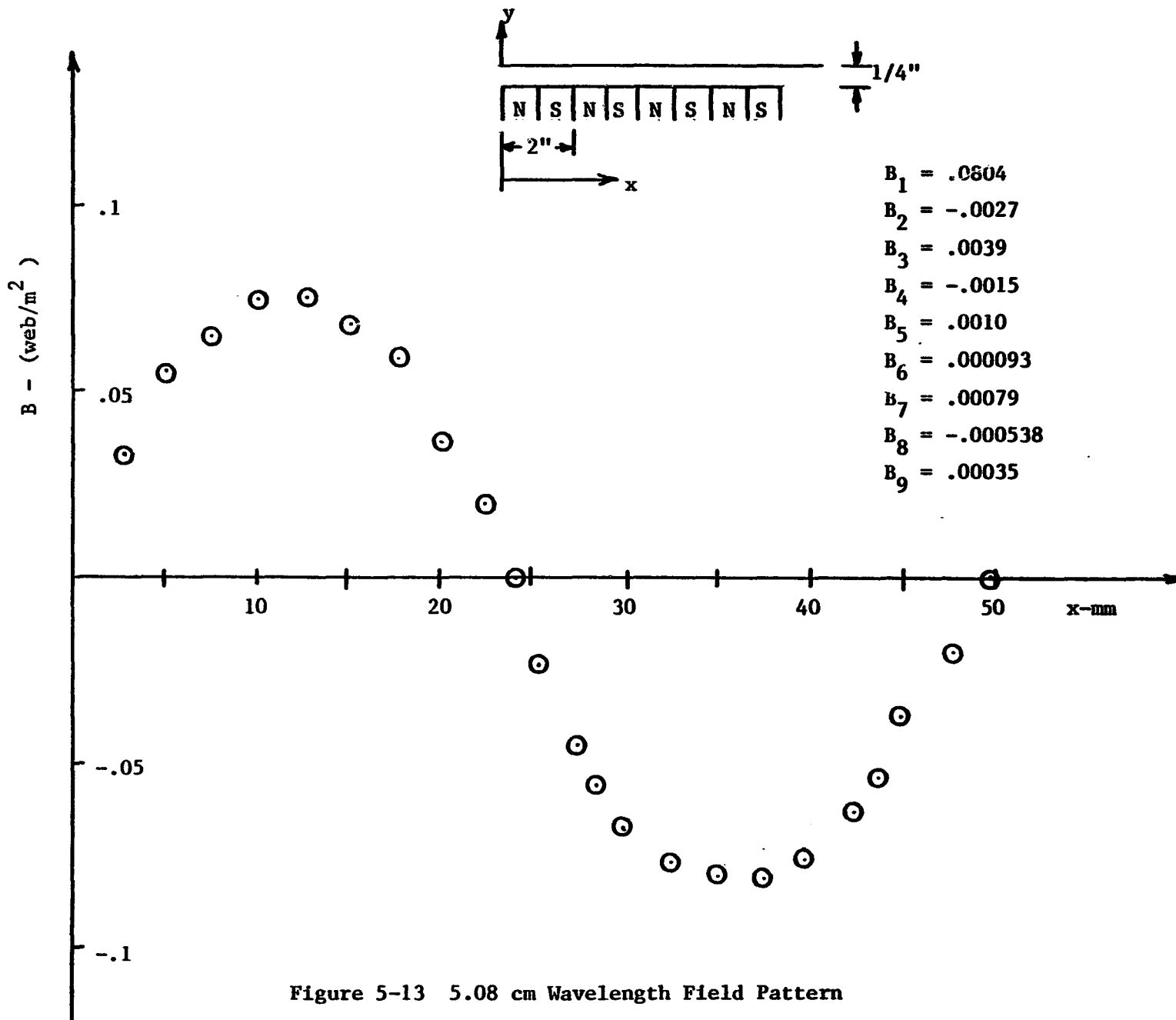


Figure 5-13 5.08 cm Wavelength Field Pattern

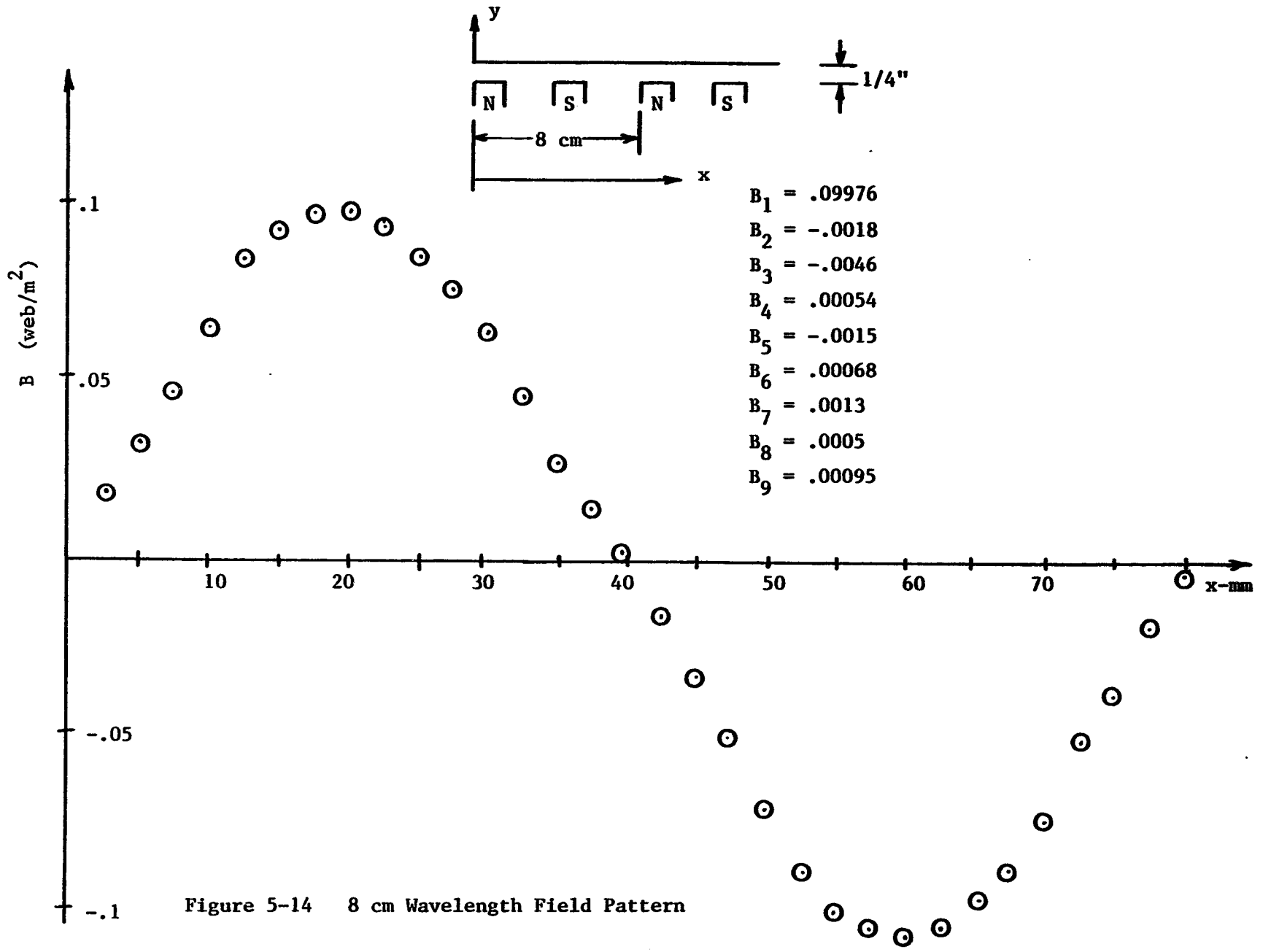
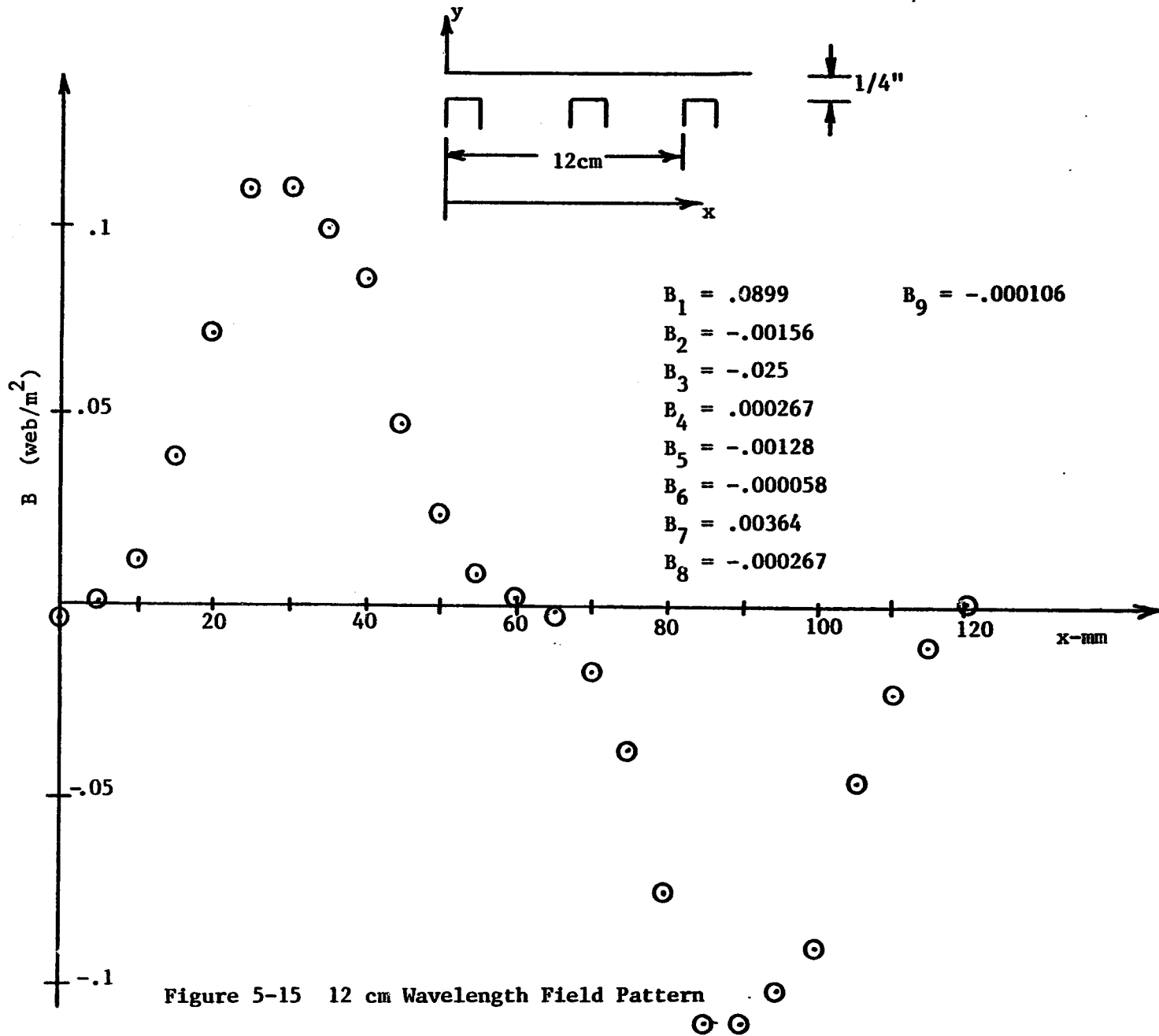


Figure 5-14 8 cm Wavelength Field Pattern



BIBLIOGRAPHY

1. Schlichting, Herman, "Boundary Layer Theory," McGraw Hill, 4th edition, 1960.
2. Baines, W. and Peterson, E., "An Investigation of Flow Through Screens," Trans ASME, July, 1951, pp. 467-477.
3. Durgin, F., An Improved Method for the Design of Wind Tunnel Velocity Profile Grids, Lincoln Labs Technical Support Note Report. 1970-38, December, 1970, 27pp.
4. Von Karman, T., "Progress in the Statistical Theory of Turbulence," Physics, Proc. NAS, Vol. 34, 1948, p. 530.
5. Borman, P.W., "Some Measurements of the Distortion of Turbulence Approaching a Two-Dimensional Bluff Body," J. Fluid Mechanics, Vol. 53, part 3, 1972, pp. 451-467.
6. Fannucci, J. and Durgin, F., "Some Characteristics of Stagnating Turbulent Flows Near Two and Three Dimensional Bodies," Wright Bros. Wind Tunnel Report, Tr 1104, MIT, Dec. 1977.
7. Robinson, M., "Turbulent Gas Flow and Electrostatic Precipitation," Journal of Air Pollution Control Assoc., Vol. 18, No. 4, April 1968, pp. 235-239.
8. Williams, J. and Jackson, R., "The Motion of Solid Particles in an Electrostatic Precipitator," Proc. Symp. Interaction Fluid Particles, Inst. Chem. Engrs., (1962), pp. 282-288, discussion 291-3, 297-8.
9. Durgin, Frank, Aeroelastic Laboratory, MIT, Cambridge, MA.

VI. Experimental Results and Correlations with Theoretical Models

A. Small Particle Dynamics

Figure (6-1) shows the experimental arrangement for the small particle tests. The injection nozzle is positioned approximately 3 feet before the magnetic structure to insure a uniform initial particulate density over the duct cross-section. Several tests appeared to indicate an injection distance 6" into the settling chamber gave reasonable uniformity. Where possible, precipitation was avoided in the local region just after the profile grid where flow necking and spurious wakes could cause unwanted side effects. The tests were performed for three field wavelengths - 5.08 cm., 8 cm., and 12 cm. For each experiment, the total weight of particulate injected was recorded, and the amount of material precipitated across the duct width per half wavelength axial distance was measured.

1. Correlation of Measured Parameters from Numerical Models

It is necessary to correlate the number of grams per half wavelength with the density dependence theory calculation. The correlation is based on the assumption that particulate at density n_0 is injected during a time interval t_0 seconds at the beginning of the precipitation structure. The total weight in grams of particulate injected is

$$\text{(Net Wt.)} = \int_0^{t_0} \int_0^{2a} \rho U n_0 w \, dy \, dt \quad (6-1)$$

grams

where

ρ = mass density of particles grams/ m^3

w = duct width-meters

U = axial flow velocity = $U_{\max} \left(\frac{a-|y-a|}{a} \right)^{\frac{1}{9}}$

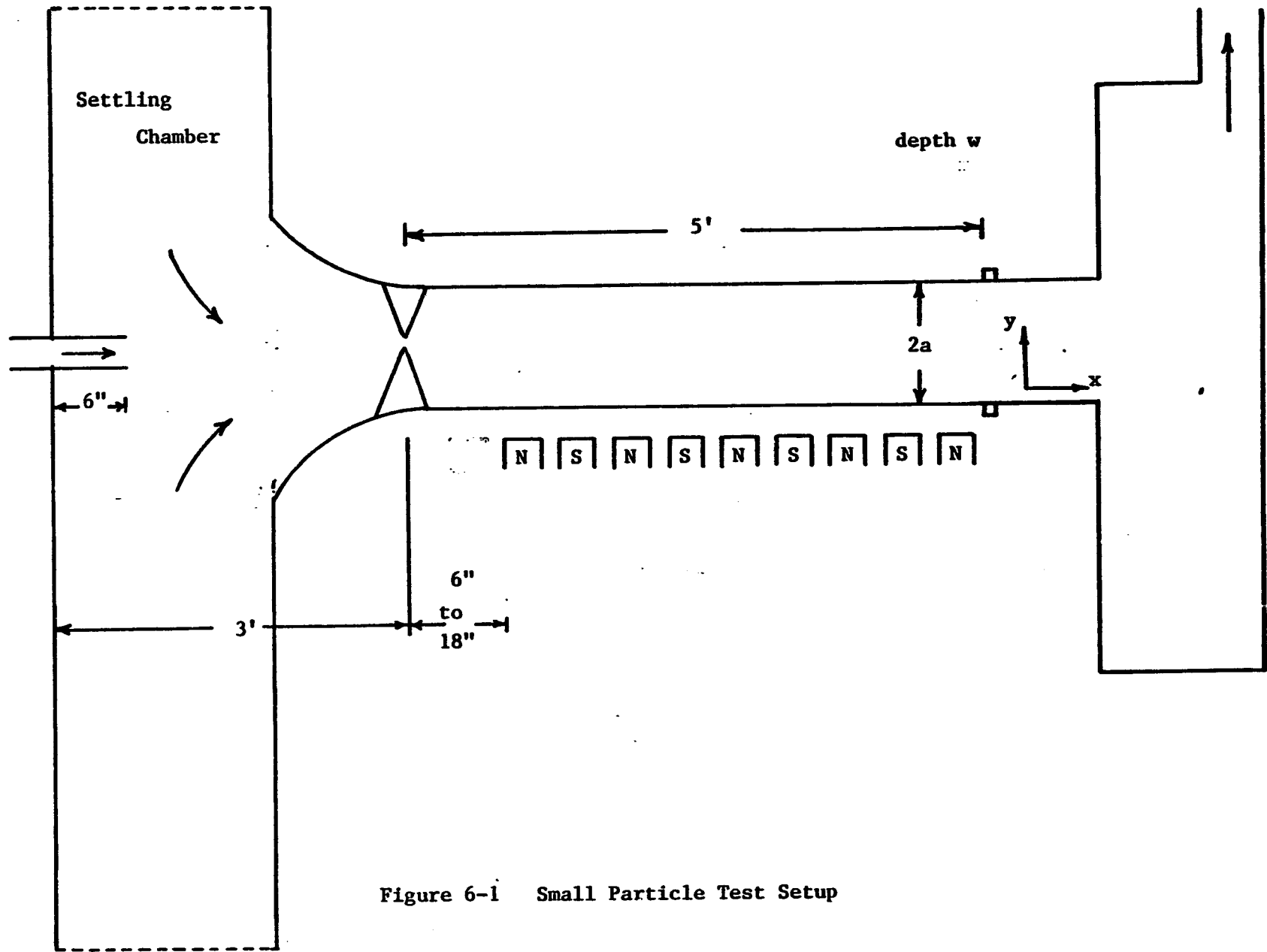


Figure 6-1 Small Particle Test Setup

Evaluation of (6-1) yields

$$\text{(Net wt.)} = \rho(2a)(.9 U_{\max}) w n_o t_o \quad (6-2)$$

grams

In terms of the vertical particle flux at $y = 0$, ($\bar{\Gamma}_y = 0$), the precipitated particulate per half wavelength strip in a steady state operation lasting t_o seconds is

$$\text{(measured)} = \int_0^{t_o} \int_{x-\lambda/4}^{x+\lambda/4} \rho(\bar{\Gamma}_y = 0 \cdot \bar{y}) w dx dt \quad (6-3)$$

output

where x is measured from the beginning of the magnetic precipitation structure.

The particle flux at $y = 0$ is in Stokes flow without diffusion so that

$$\begin{aligned} \bar{\Gamma}_y = 0 &= \left\{ \frac{mg}{\beta} + \frac{4}{(3\pi r)^3} \frac{\left(\frac{3}{2+\mu}\right)}{\mu_o} \left(\frac{\mu}{\mu_o - 1}\right) \frac{k}{\mu_o} \sum_{m=1}^{\infty} m\beta^2 m \right\} n \bar{y} \\ &= -\left(\frac{mg}{\beta} + \frac{F_{\text{mag}}}{\beta}\right) n \bar{y} \end{aligned} \quad (6-4)$$

Assuming there exists an average flux over any one axial half - wave strip whose magnitude is $\Gamma_o(x)$, the measured output (6-3) can be written

$$\text{(measured)} = \rho \Gamma_o w \left(\frac{\lambda}{2}\right) t_o$$

output

where Γ_o is evaluated at $(x + \frac{\lambda}{4})$ (6-5)

Using (6-3) this becomes

$$\text{(measured)} = \frac{\left(\frac{\text{grams of}}{\text{particulate}}\right) \left(\frac{\lambda}{2}\right) \left(\frac{mg}{\beta} + \frac{F_{\text{mag}}}{\beta}\right)}{(2a)(.9 U_{\max})} \left(\frac{n}{n_o}\right) \text{ avg. at } (x) \quad (6-6)$$

output

2. Correlation of Measured Parameters from Deutsch Model

The data will be compared to the refined Deutsch precipitation model developed in Appendix B. The Deutsch model analysis correlation proceeds in a similar fashion to section 1. The density developed is,

$$\frac{n}{n_0} = \exp \left(\frac{x - x_0}{2a U_{avg} \left(\frac{mg + \alpha k}{\beta} \right)} \right) \quad (6-7)$$

and is valid for plug flow U and a single harmonic B field. Including the full harmonic field and the actual flow velocity, (6-7) becomes

$$\frac{n}{n_0} = \exp \left(\frac{x - x_0}{2a U_{avg} \left(\frac{mg + F_{mag}}{\beta} \right)} \right) \quad (6-8)$$

where F_{mag} is defined in (6-4)

$$\text{and } U_{avg} = \frac{2}{2a} \int_0^a U_{max} \left(\frac{y}{a} \right)^{\frac{1}{9}} dy = .9 U_{max}$$

Integrating equation (6-3) with $\Gamma_y = 0$ given by (6-4) and substituting the total mass injected using equation (6-2) gives

$$\left(\frac{\text{measured output}}{\text{grams of particulate injected}} \right) \left\{ \exp \left[- \left(\frac{mg + F_{mag}}{2a U_{avg} \beta} \right) \left(x - \frac{\lambda}{4} \right) \right] - \exp \left[- \left(\frac{mg + F_{mag}}{2a U_{avg} \beta} \right) \left(x + \frac{\lambda}{4} \right) \right] \right\} \quad (6-9)$$

3. Observations of Theoretical Deposition Predictions

The theories of section 4-B are compared by examining the percentage of injected particulate collected per half wavelength on the lower duct surface.

Figure (6-2) shows the deposition predictions (with $4\frac{1}{2}$ μ particles, 9 cm field wavelength) for the four light particle theories--Deutsch, non causal, causal perfunctory, and causal fundamental as presented in chapter 4. The numerical theories are computed with the spacer grid representation discussed in section 4-C using 25 transverse points and 80 axial steps. Studies revealed the accuracy of numerical solution with such a grid assignment is questionable for two reasons, figure (6-2) is useful for comparing theories only in a cursory manner.

The first problem to be considered is that of numerical convergence. The causal theory downstream (7.5 cm) deposition prediction decreases 50% as the grid size is increased from 15 to 40 transverse points (axial = 80). Considerations of grid stability indicate the axial spacing Δx should be less than or equal to $(D_t U)$. This criteria sets the number of axial grid points into the thousands. The numerical density solution was calculated in the limit of constant diffusive and convective terms only, and compared to the analytical solution. When using 95 transverse points and 1000 axial steps the numerical solution demonstrated reasonable convergence and differed from the analytical solution only in the third significant figure (<1% difference).

The second problem of numerical accuracy is more subtle. The diffusivity and magnetic force in the lower portion of duct near the laminar sublayer change very rapidly. These facts added to the uncertainty as to the nature of the sublayer physics make it clear that the lower portion of the grid solution at the wall is the area of greatest uncertainty. The solution outlined in section (4-C) couples the migration fluxes to the

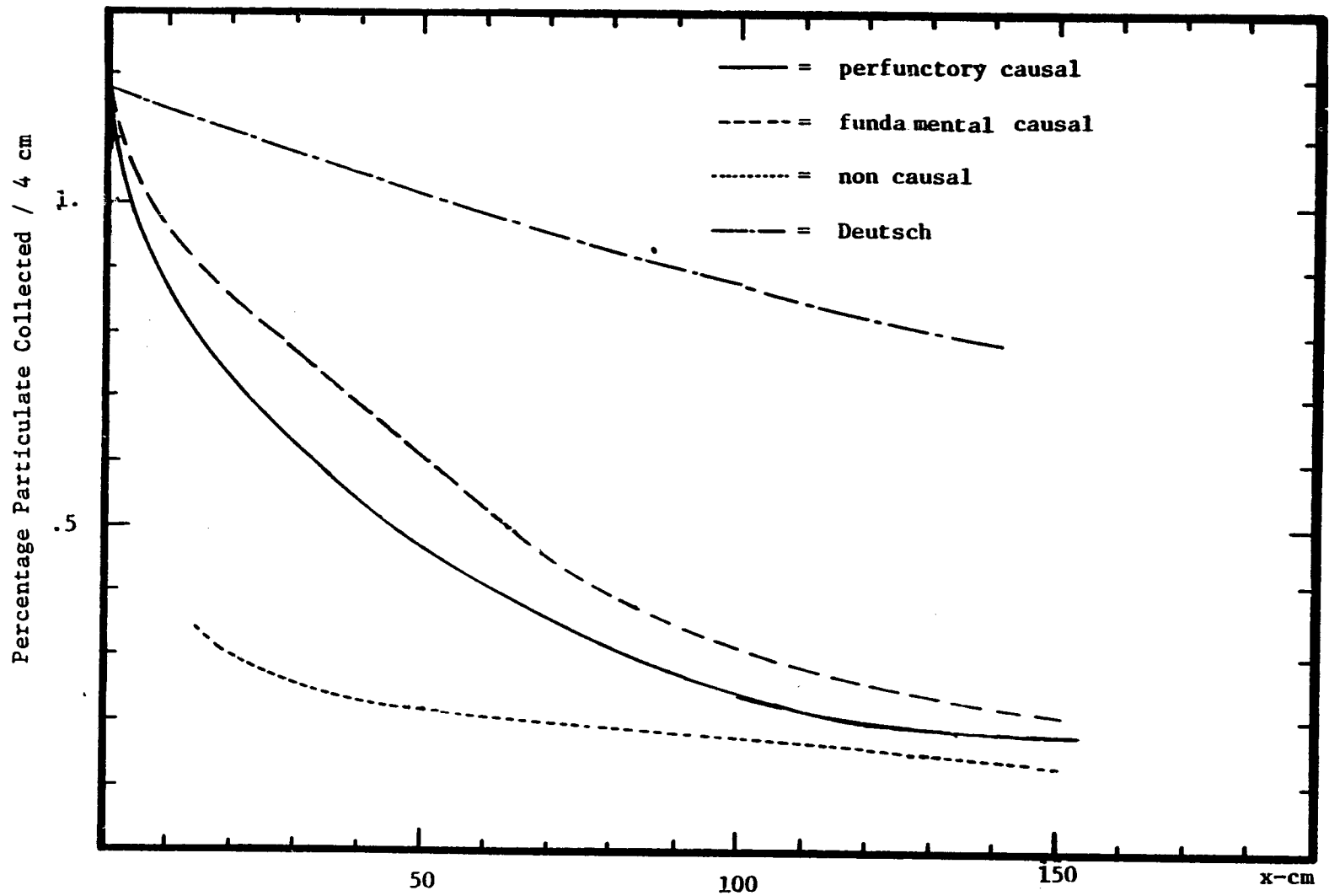


Figure (6-2) Comparison of Theories, $\lambda = 8 \text{ cm}$, $4 \frac{1}{2} \mu$ particles

density at the lower grid point (for each axial location) to arrive at deposition on the wall, although the net profile is relatively unaltered. Considerable changes in predicted densities occur for the lower transverse grid point locations when the number of transverse points is increased further.

An alternative to predicting deposition rates which effectively integrates through the region of numerical difficulty, involves applying the principles of mass conservation to the numerically calculated density profiles (for which the analytical model gives credibility). Specifically the transverse flux deposition on a strip Δx equals the difference of upstream and downstream axial fluxes. The procedure of using the density profiles of section (4-C) in this manner to arrive at deposition predictions is described in Appendix K, and the corresponding refined causal fundamental FORTRAN program KDFFL is listed in Appendix L.

Figure (6-3) shows the causal and refined causal deposition predictions (grid 95 x 1000) along with the Deutsch theory prediction for 8μ particles and an 8 cm field wavelength. The increased grid accuracy reveals the error of the unrefined model. Increasing the grid accuracy from (95 x 1000) to (500 x 2000) gave only a 5% decrease in deposition prediction (the 95 x 1000 grid assignment will be used for the remainder of this chapter). The refined perfunctory prediction exceeded only slightly the fundamental causal productions (<1% difference).

The Deutsch model, with an infinite diffusivity always predicts greater precipitation (except at the initial axial locations) than the finite diffusivity models and exhibits a less rapid initial decay. This observa-

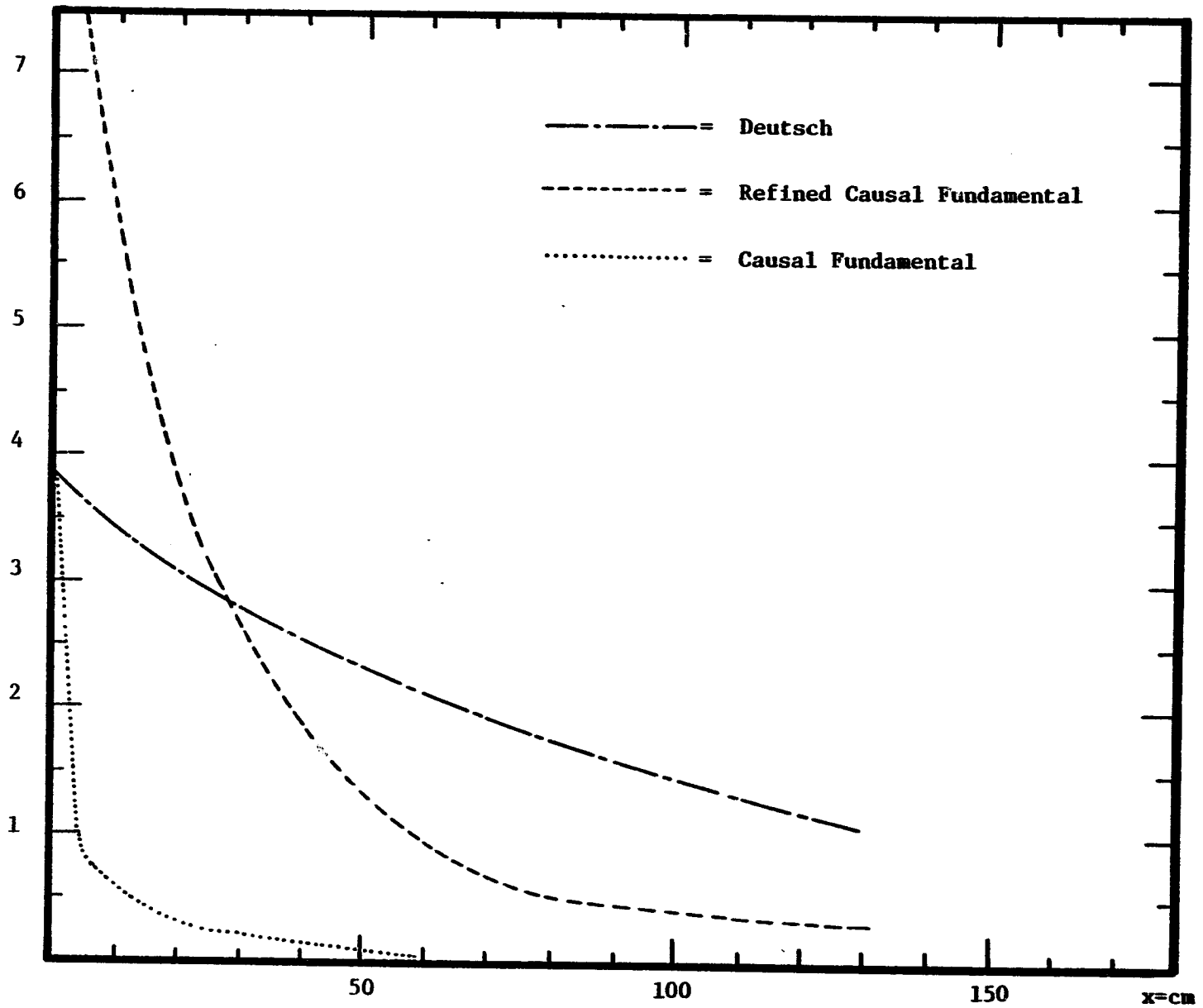


Figure (6-3) Theory Deposition Prediction, $\lambda = 8 \text{ cm}$, 8μ Particles

tion is linked to a property common to all the theories concerning the shape of the deposition prediction. Mass conservation dictates that the predictions must have the same integral (i.e., net area). Thus, steep initial deposition predictions must be balanced by slow downstream decays. Theoretical predictions are limited in how they can differ; the principle difference occurs in the nature of the initial deposition decay.

As pointed out in fig. (4-6), the diffusivity undergoes a rapid change in slope at the laminar sublayer. An attempt to simulate this change in the causal fundamental model (in which D_t goes to zero just above the sublayer) was made by increasing the magnitude of the slope by a factor of 10 for the last transverse core grid point only. This assignment is in fact an artifice, but may represent the diffusivity dependence more realistically. The numerical deposition prediction was not sensitive to this alteration; leaving the diffusivity slope unaltered results in a 0.5% lower deposition prediction (at $x = 7.5$ cm). The factor of 10 increase in diffusivity slope will be inserted into the last grid point assignment for the remainder of this section.

The refined causal fundamental model displayed a much smaller sensitivity to particle size than did the Deutsch theory ($4\frac{1}{2}$ μ tests were 13 to 20% lower at upstream locations, negligible downstream). It is expected that small downstream precipitation predictions should exist. Magnetic migration is extremely dependent on particle radius ($\sim r^2$); at upstream locations, magnetic forces remove particulate in the vicinity of the wall at different rates dependent on their size. After particulate is removed from this magnetic interaction region, further removal is more dependent

on turbulent diffusive effects which are independent of size. The only parameters important in the Deutsch model spring from migration forces which depend on the particle diameter squared.

Discussion of the representation of the field harmonics and their effect on theory predictions is in order. Numerical predictions differed little (approximately 1% for $\lambda = 12$ cm) when only one, rather than nine harmonics (chapter 5) were used to represent the field. The nine harmonic tests cannot be treated by superpositions, i.e., more harmonics yield a higher flux toward the wall, and thus greater precipitation. The actual field being more uniform in sections has a smaller field gradient, and thus a smaller force. The fundamental harmonic field computer test predicts greater precipitation. A nine harmonic field representation is used throughout this chapter.

Figure (6-4) shows the effect of removing the magnetic field altogether. The deposition decays slowly downstream. Such a drop in precipitation is not surprising since the magnetic force is 81 times larger at the wall ($\lambda = 8$ cm) than the gravitational force. Only a dusting of the duct lower wall was observed experimentally when all magnets were removed. Reentrainment made a true measurement of gravitationally deposited particulate difficult.

Figure (6-5) shows the theory sensitivity to the magnitude of D_t ; turbulence at larger diffusivities keeps particulate dispersed evenly over the upper portion of the duct and sweeps more particulate to the wall where it can be precipitated. The numerical solution should converge to the Deutsch prediction as diffusivity increases. The Deutsch precipitation

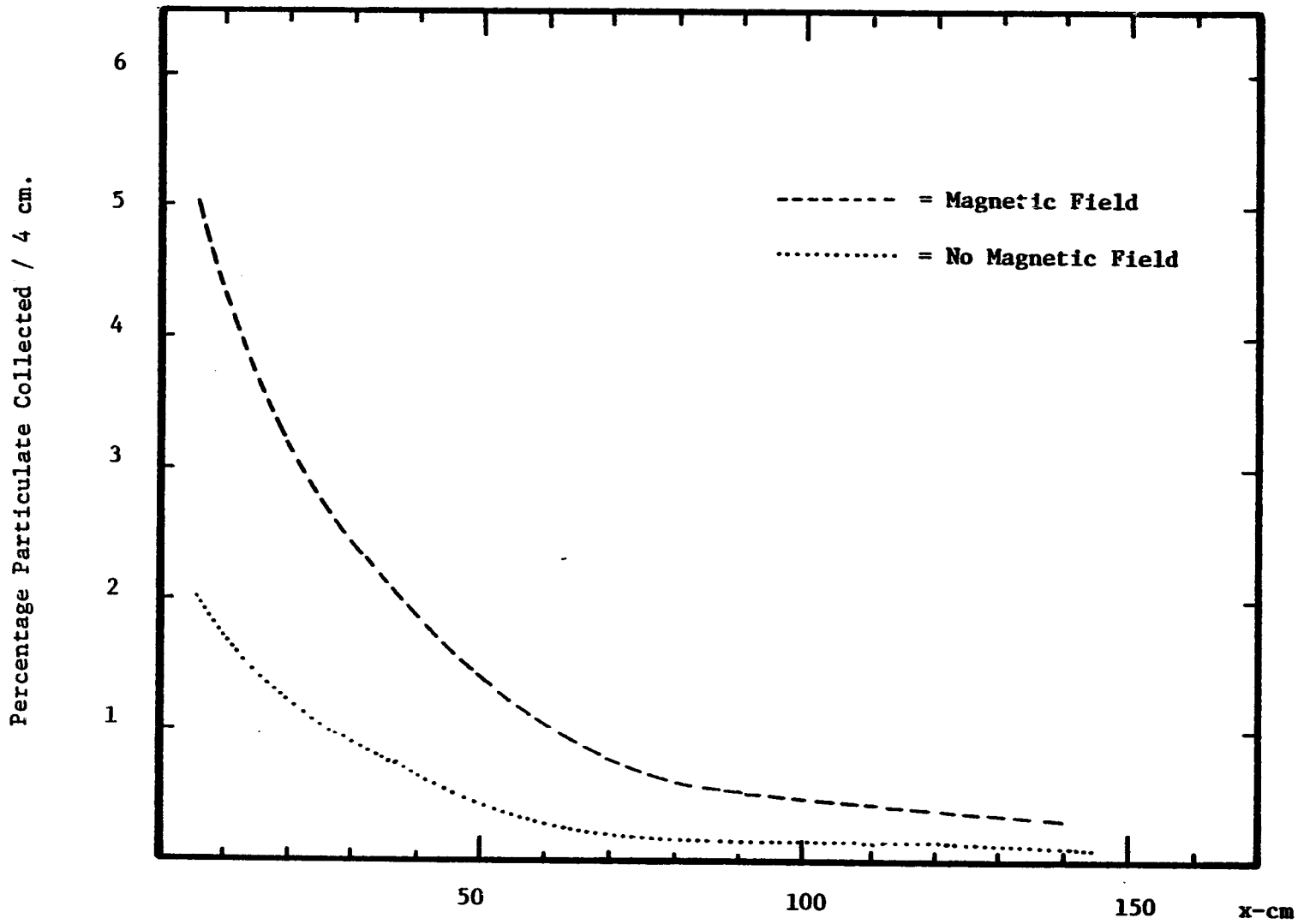


Figure (6-4) Refined Causal Fundamental Precipitation Results; Magnetic Versus Gravitational Migration, $\lambda = 8 \text{ cm}$, $4 \frac{1}{2} \mu$ Particles

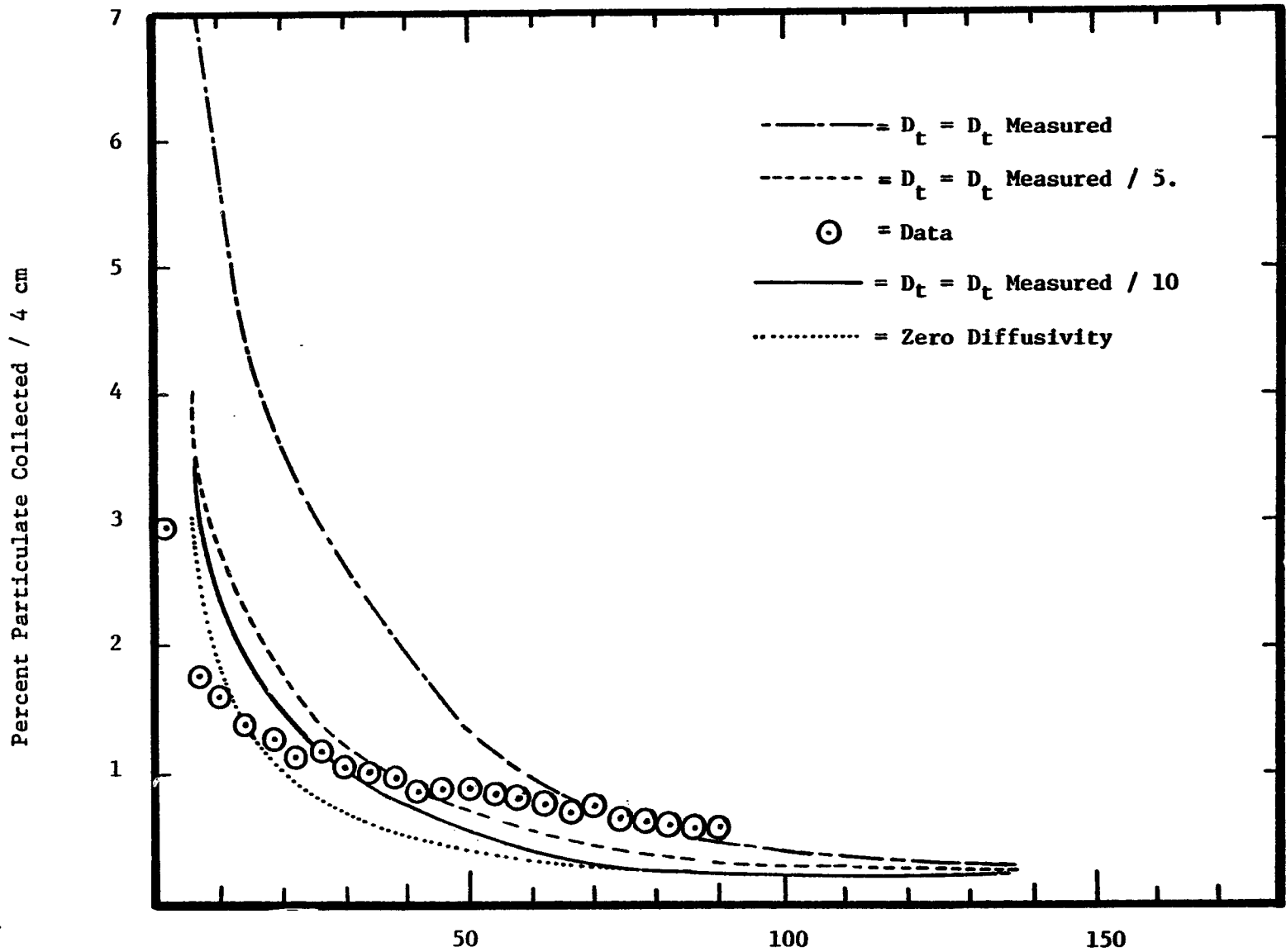


Figure (6-5) Refined Fundamental Causal Theory Sensitivity to Diffusivity, $\lambda = 8\text{cm}$
 8μ Particles.

prediction exceeds the causal model prediction further downstream, because particulate is not swept up to the top of the duct by eddies. In the limit of zero diffusivity, particles decay along trajectories; in section (2-C) it was shown that particles in trajectory precipitation are removed more quickly than the Deutsch model predicts. The point to emphasize is that precipitation at upstream positions is quite sensitive to the value of diffusivity.

4. Numerical Density Profiles

Figures (6-6) to (6-8) show the density profile transverse dependence at four axial locations for 5.08, 8, and 12 cm field wavelengths respectively with 8μ particles as predicted by the fundamental causal model (95 x 1000 pts). The density rises from zero at the top of the duct, peaks below the center, and decreases toward the lower wall. The greater the penetration of magnetic forces into the volume (i.e. at larger wavelengths), the greater is the decrease in density profile magnitude downstream due to particulate removal. This is confirmed in figs. (6-6) to (6-8).

The lowest density plotted is actually that calculated at the laminar sublayer ($y/2a = .002$). The final wall density ranges from .92 to .95 of the density at the sublayer (at $y = .002*2a$ cm) as predicated by the trajectory model of Appendix B.

The density gradient is greater in the sublayer than in the core (see fig. (4-2)). The perfunctory model imposes a zero gradient at $y = \Delta$, and as explained in chapter 4, it does so by assuming the density just below the core region to be the same as that above. This numerical assignment is certainly ad hoc, since the density does not increase in the sublayer.

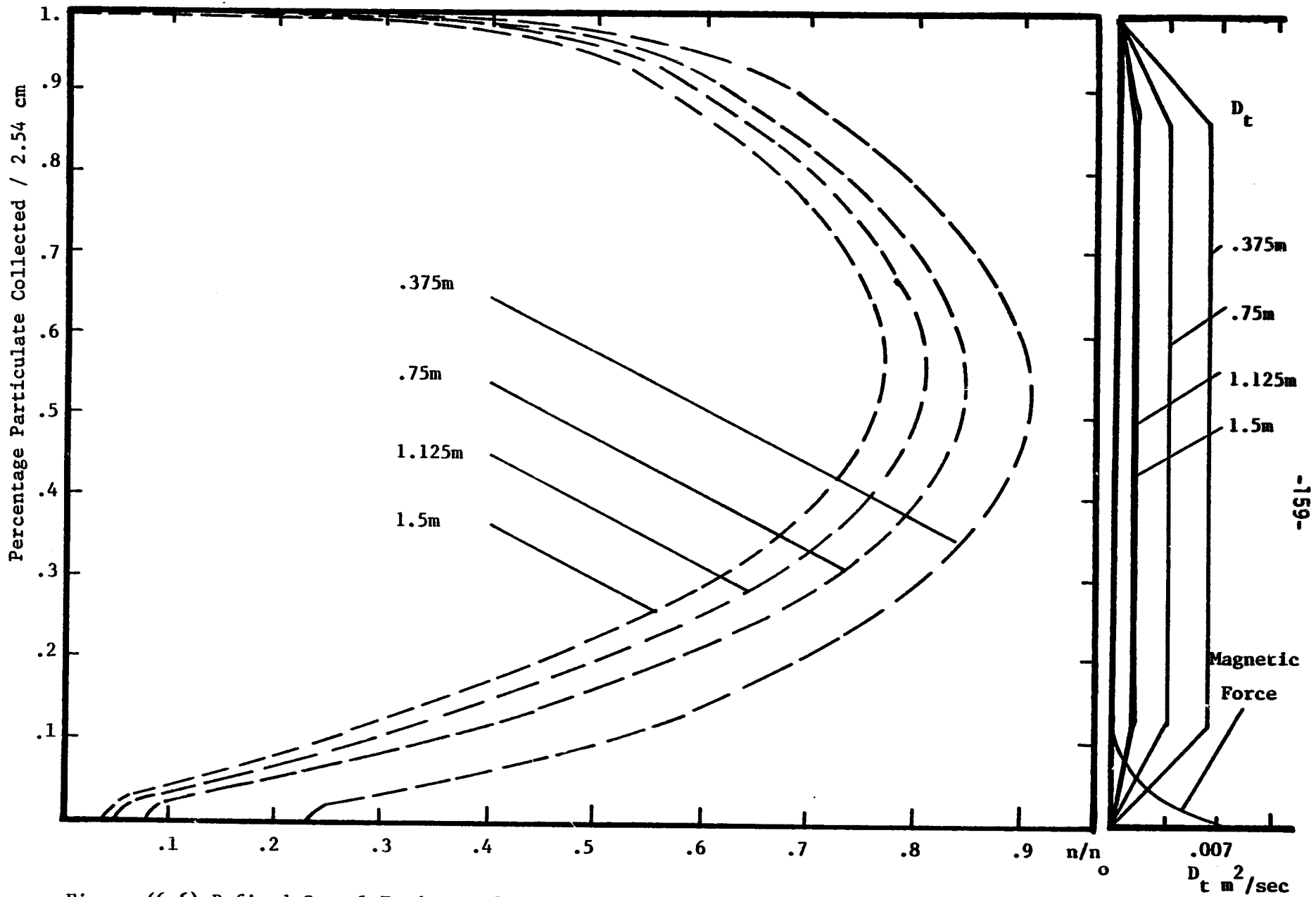


Figure (6-6) Refined Causal Fundamental Density Profiles with Diffusivity and Magnetic Force Decay

$\lambda=5.08\text{cm}; 8\mu$ particles

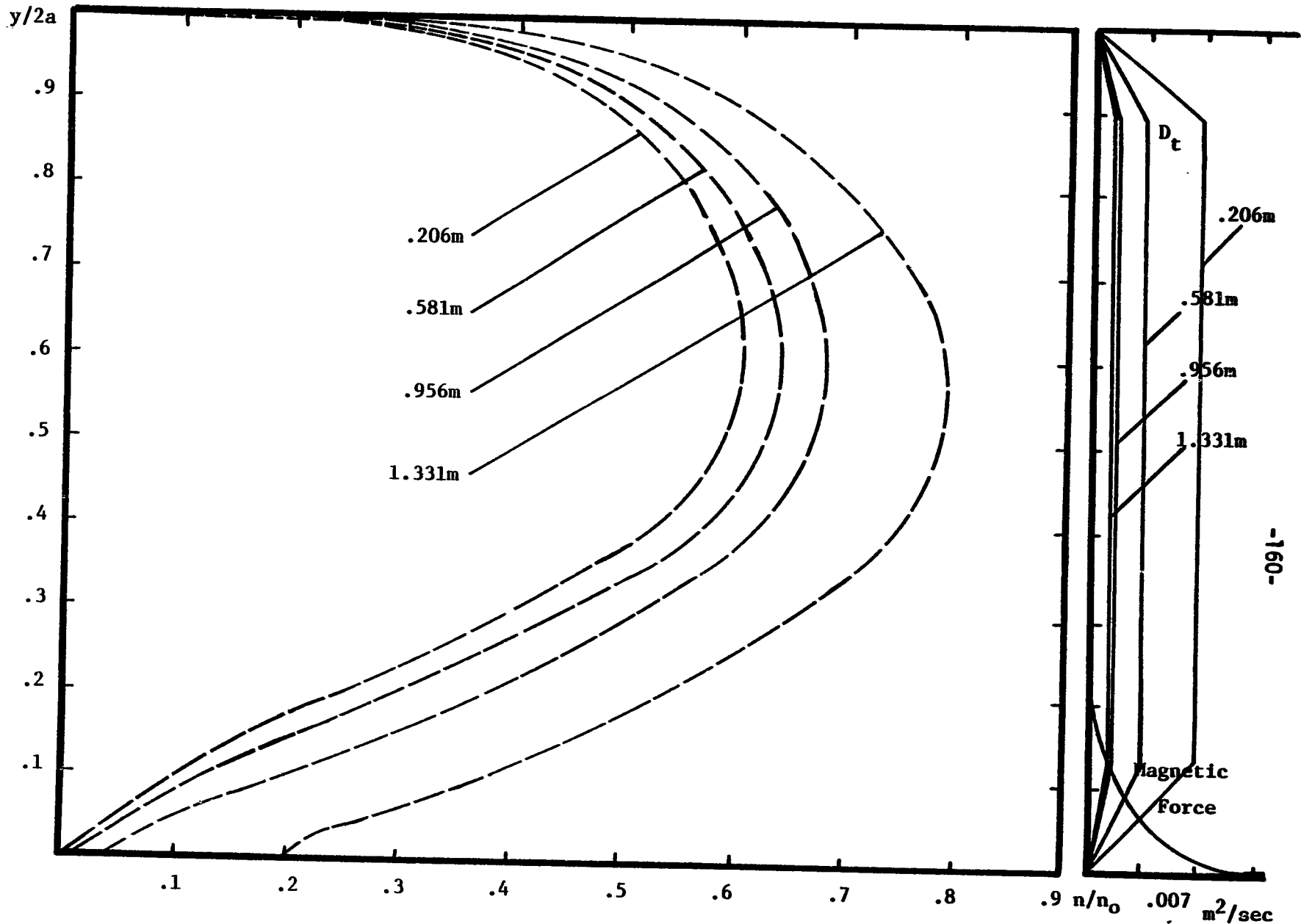


Figure (6-7) Refined Fundamental Causal Theory Profiles with Corresponding Diffusivity and Magnetic Force Decay, $\lambda = 8 \text{ cm } \mu$ Particles

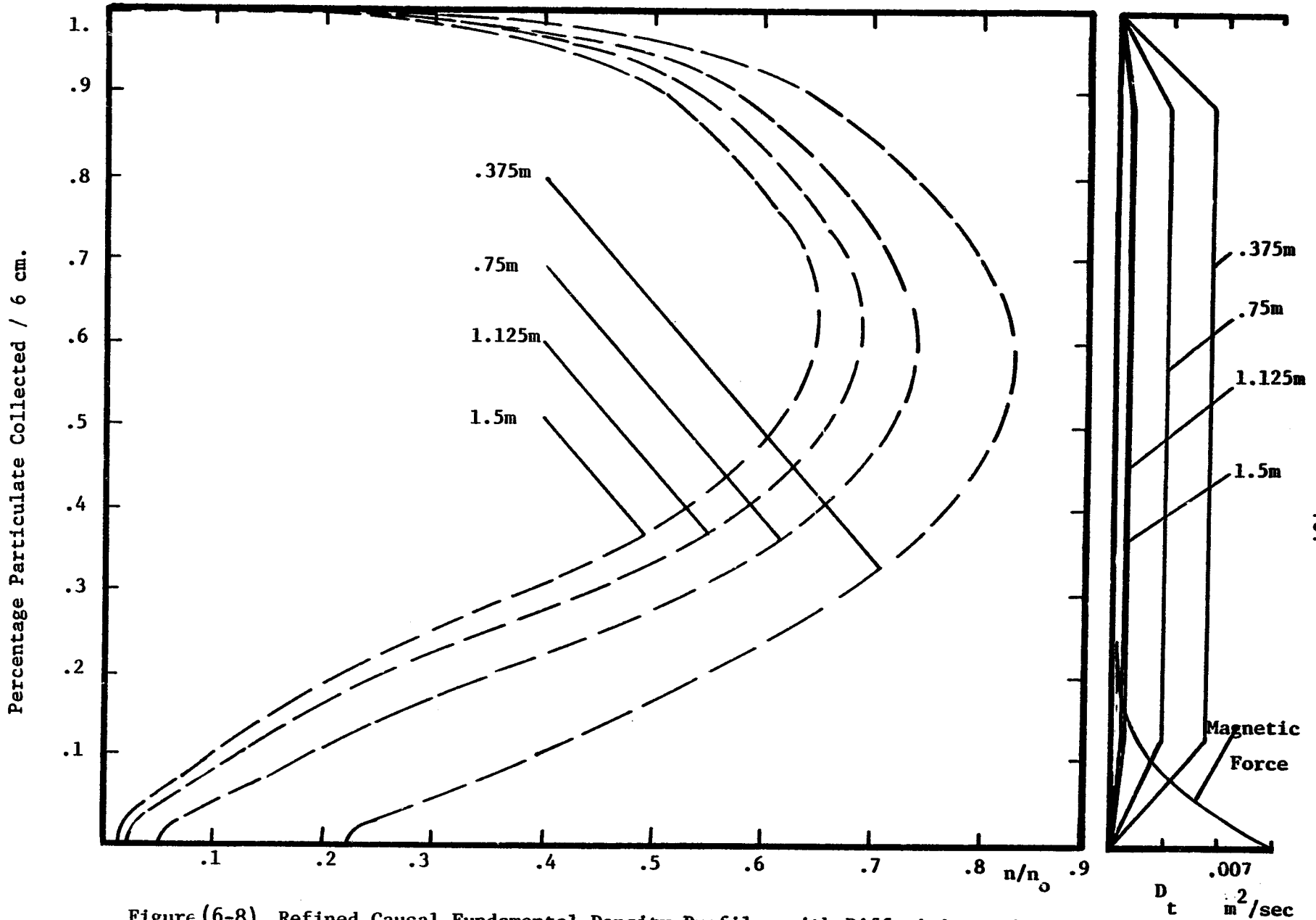


Figure (6-8) Refined Causal Fundamental Density Profiles with Diffusivity and Magnetic Force Decay

$\lambda = 12 \text{ cm}; 8 \mu \text{ particles}$

The splicing on of the trajectory model solution distorts what the core diffusion analysis assumed should exist below $y = \Delta$. The diffusivity of fig. (4-6) undergoes a power law decay to zero at the boundary layer, not a discontinuous decay. This implies from Appendix D that the sublayer density gradient be much larger than the core gradient. The fundamental model predicts this condition without imposing a difficult to justify boundary condition, and inherently represents a more realistic diffusivity by keeping D_t finite in the core region.

The fundamental model deserves the title "fundamental" for another reason. As the degree of turbulence diminishes, it is meaningful to think in terms of trajectories. In this limit the fundamental model imposes boundary conditions only where particle trajectories enter the region of interest.

Included with the plots of (6-6) to (6-8) are the diminishing diffusivities at the given axial locations as well as the exponential magnetic force decay. The results indicate magnetic migration is relevant over only 1/4 of the duct. The density profile resulting when magnetic forces are eliminated entirely is shown in fig. (6-9). The results confirm the proposition that the densities are not altered significantly over the upper three fourths of the duct. The smaller migration over the lower 1/4 of the duct yields a smaller deposition despite the large wall density. The densities in the uniform migration (no D_t) sublayer do not decay. Finally, it is interesting to consider the density profiles in the limit of no turbulence, i.e. $D_t = 0$. The density (fig. (6-10)) can only decay

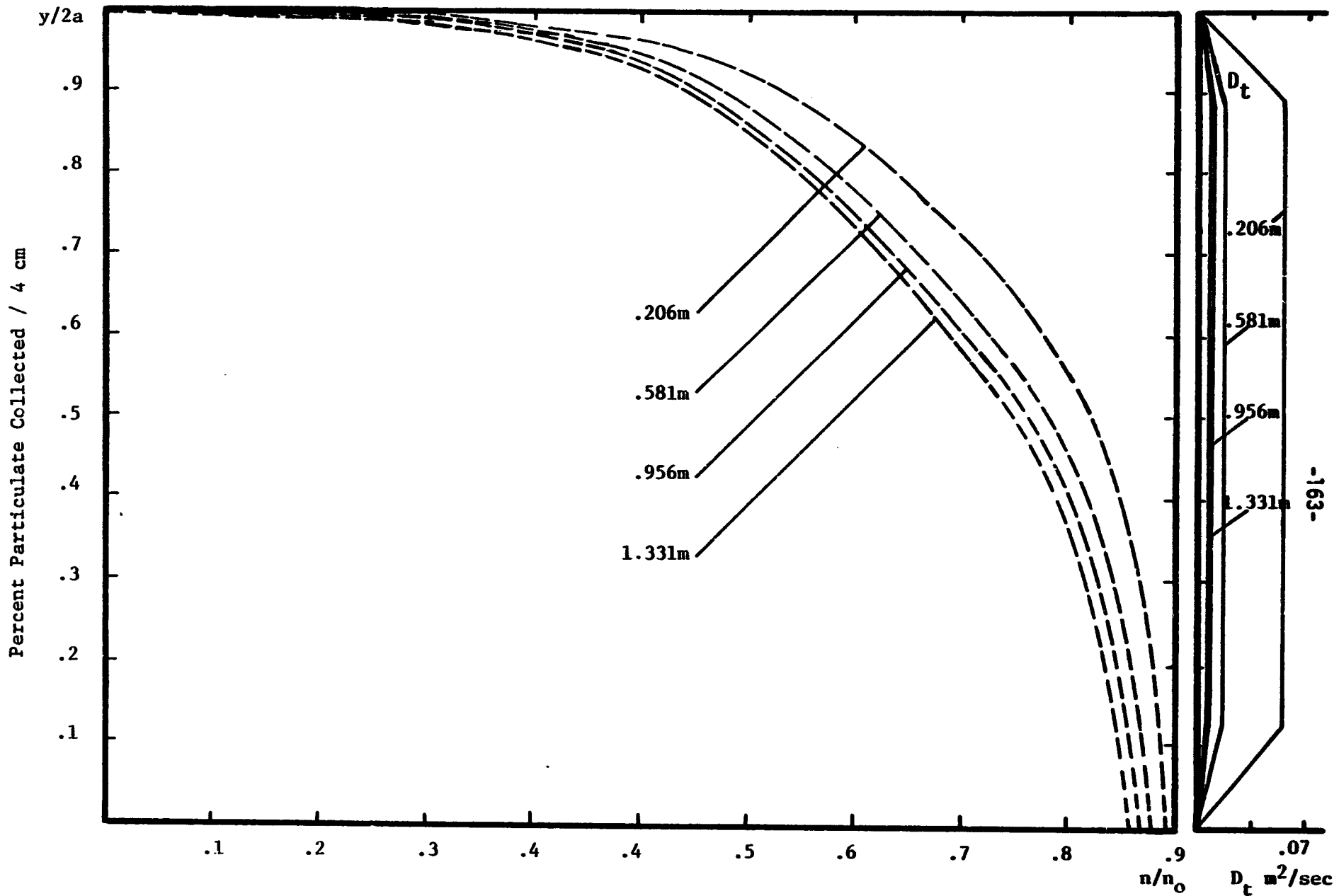


Figure (6-9) Refined Causal Model Profile and Diffusivity, 8 μ Particles, No Magnetic Migration

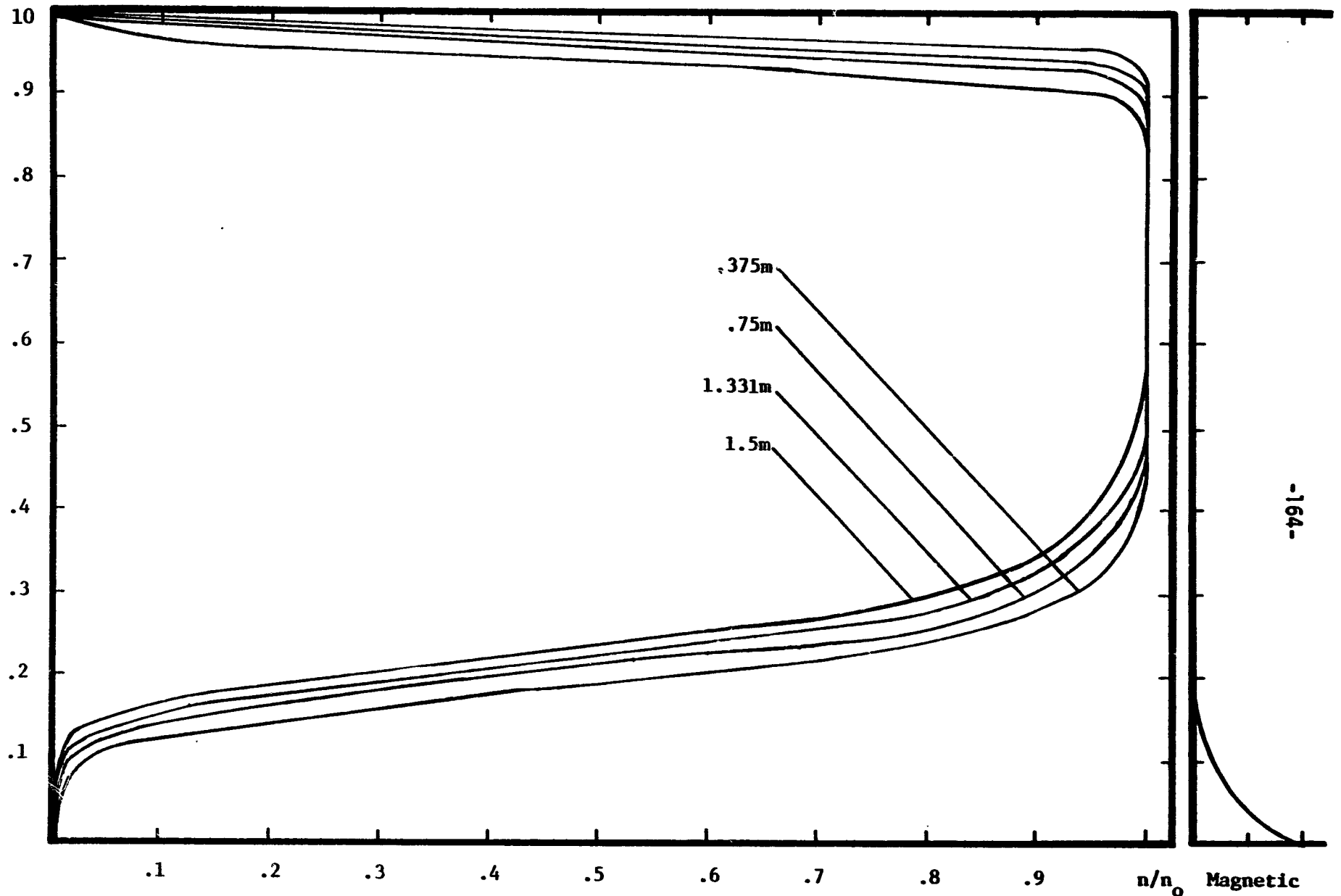


Figure (6-10) Transverse Density Profiles with Corresponding Magnetic Force Decay, No Diffusivity

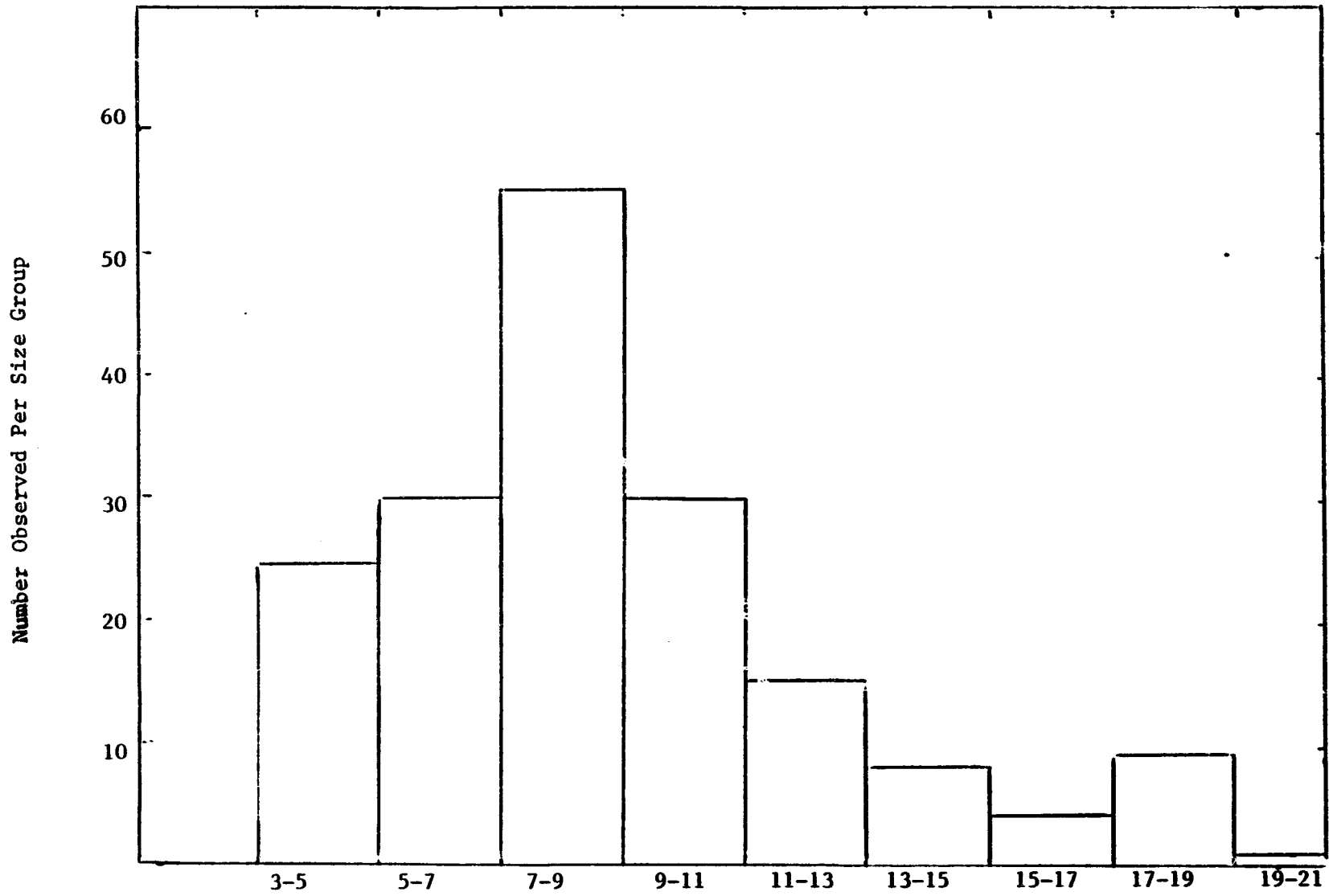
$$\lambda = 8 \text{ cm}; 8 \mu$$

over the lower portion of the duct where magnetic forces are significant. (No density decay occurs over the region of divergence-free force where gravity dominates.) The core region of the duct should have uniform density dropping discontinuously to zero near the upper region. The discontinuous density jump to zero represents the point above which all trajectories can be traced back to an entry point on the upper wall where the density is zero. All trajectories below the transition point have their origin at the entry plane $x=0$.

An examination of the experimental results and their correlation with theory will follow a discussion of the particle size distribution. The non-causal model will not be considered in this comparison; its predictions are for readily seen reasons, too low. The perfunctory model's predictions differed only slightly from the fundamental model. For this reason and the above discussion concerning difficulties in justifying the zero gradient boundary condition, the perfunctory model will not be compared with data either.

5. Particle Size

The iron powder used in the diffusion tests ranged in diameter from 1 to 26 micrometers. It was necessary to know to what extent the particles acted as agglomerates in flight. A microscope analysis (histogram) of the particle agglomerate size spread is shown in fig. (6-11). (The tests was prepared by blowing powder through the injection tube and allowing it to settle on an oil coated microscope slide.) The scope base particle size was about 4 micrometers. With the intent of determining more of the



Figure(6-11) Particle Sizing Spread for Light Particle Tests - Microscope Results

particle's size behavior in flight, an Anderson Impactor Test (which balances a particle's inertia forces with drag forces) was conducted. The results (fig. (6-12)) indicated that then equivalent aerodynamic diameter representing particles dispersed essentially as in the magnetic collection experiments ranged primarily from $4\frac{1}{2}$ to 8 microns in diameter. The microscope test procedure would favor collection of heavier particles; this may be the reason for the disparity.

6. Theoretical Predictions Compared to Experimental Deposition Data

The Deutsch and fundamental causal theory predictions are compared to experimental collection results at field wavelengths 5.08, 8 and 12 cm tests in figs. (6-13) to (6-15) respectively for particles as described in the previous sections. Included with Fig. (6-15) is the fundamental causal's prediction of deposition of 2μ particles. The data supports the causal model's steeper decay over the Deutsch model's gradual decline.

The Deutsch model prediction increasingly departs from the data with decreasing wavelengths. The $4\frac{1}{2}$ micron theory results shown in fig. (6-7) reveal that the Deutsch model still predicts a high particulate deposition at a 5.08 cm field wavelength, and a slow axial deposition decay. It was noted in chapter 2 that the Deutsch model is based on two major assumptions--

(1) Fluid turbulence is infinitely capable of supplying particles to the wall.

(2) The migration forces (primarily magnetic) hold the particle to the wall; their interaction in the duct is small.

Assumption (1) is always optimistic. At short wavelengths where assumption (2) is accurate, the Deutsch prediction should be high because of assumption (1). At the larger wavelengths (with the magnets spaced further apart),

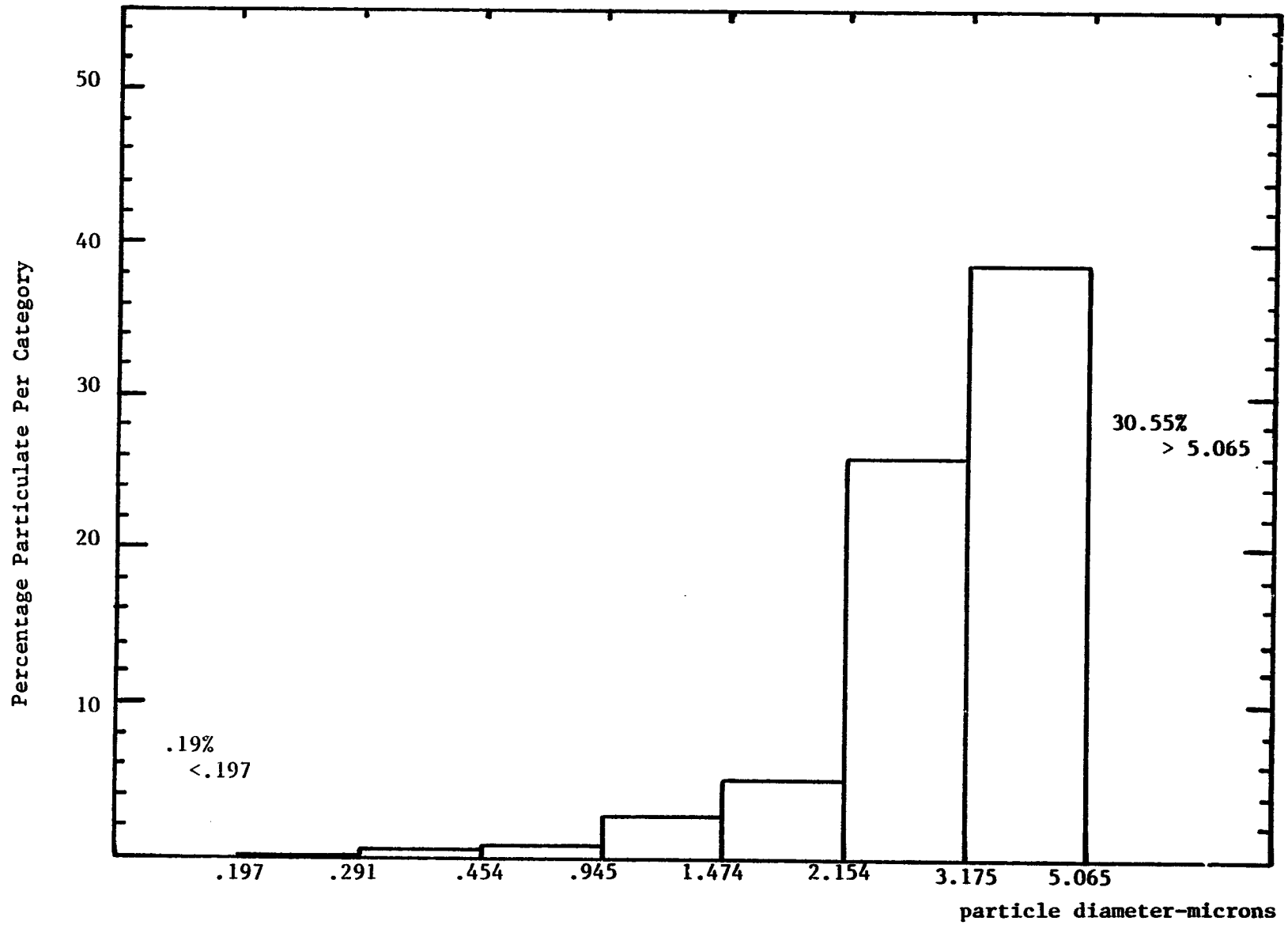


Figure (6-12) Anderson Impactor Particle Size Results

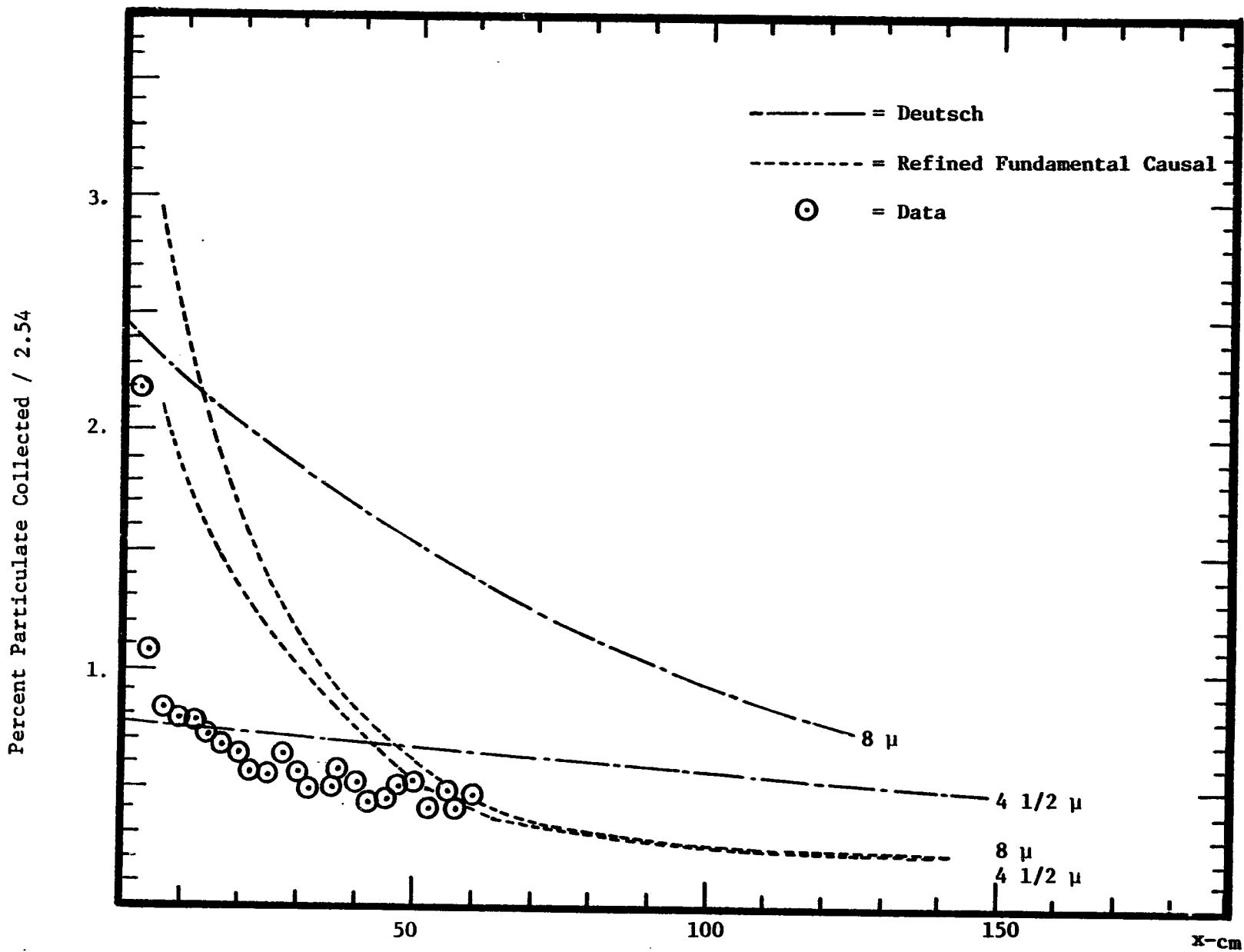


Figure (6-13) Refined Fundamental Causal Model Predictions with Deutsch and Experimental Data, $\lambda = 5.08$ cm.

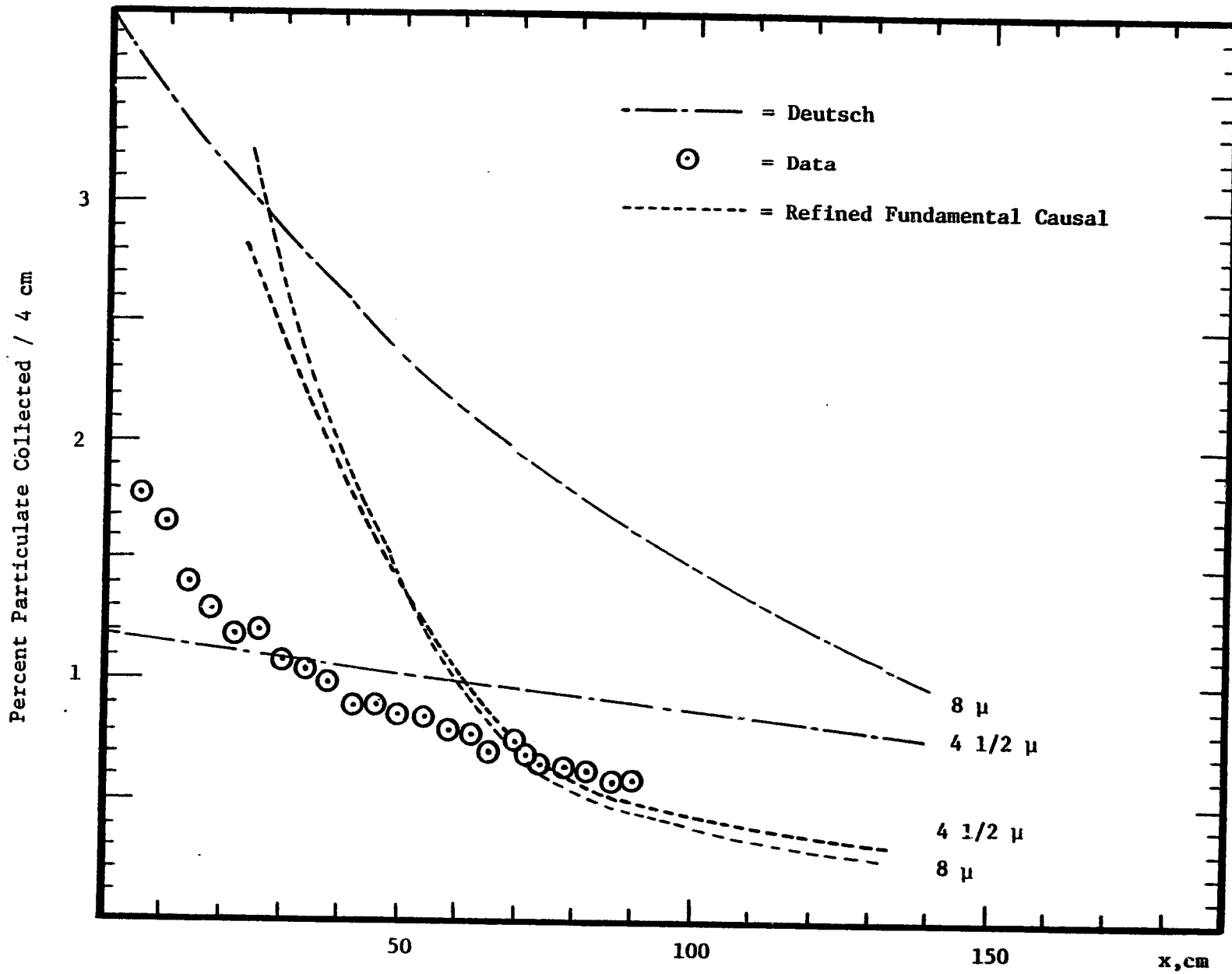


Figure (6-14) Fundamental Causal Refined Model Predictions with Deutsch and Experimental Data, $\lambda = 8$ cm.

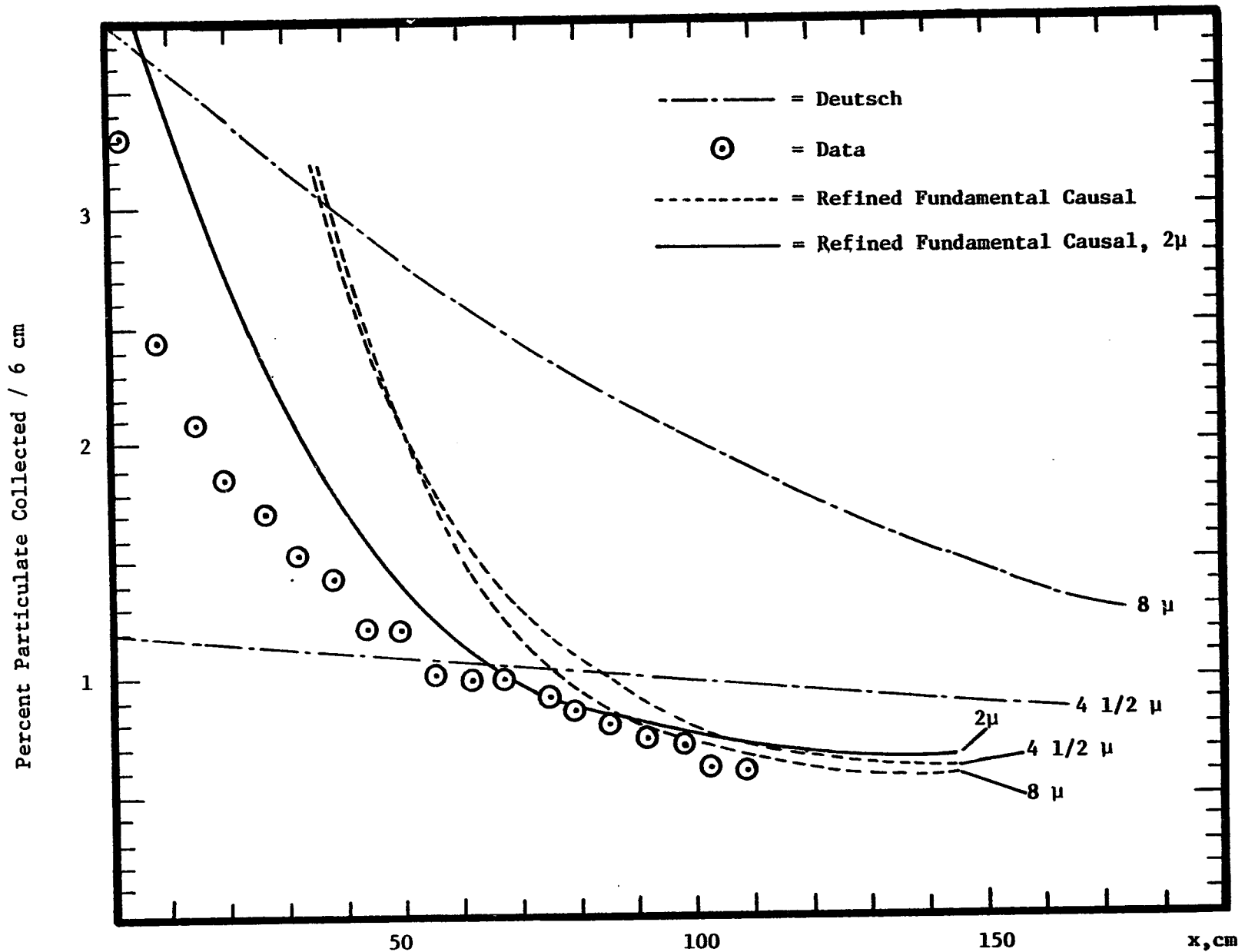


Figure (6-15) Refined Fundamental Causal Model with Deutsch Predictions and Experimental Collection, $\lambda = 12$ cm.

forces are larger at further distances from the wall, and thus augment the precipitation process (the optimum wave number is approximately the reciprocal duct height). The error of both assumptions then emerges in a trade off at larger wavelengths where the Deutsch model departs less from data.

7. Discussion of Results

Large initial deposition is expected since magnetic forces remove particles immediately at upstream locations in the magnetic field dominant region. Larger upstream theory depositions are in part caused by the step input in initial density (high density edge gradients; sine wave input yielded lower immediate initial deposition). Dividing the most uncertain parameter D_t by 10 (which makes upstream $D_t = 2 \cdot (\text{literature value}) - \text{developed flow}$) improves agreement with data. Altering the second uncertain parameter r_p (fig. 6-15) shows significant alteration in initial deposition also. In the light of these comparisons, model credibility along with a useful degree of accuracy in predicting precipitation and density profiles exist.

Three dimensional effects are the most significant effects deleted from the theory. The true velocity representation as well as magnetic field initial and edge gradient effects should enhance precipitation. Fruitful future research may be directed toward understanding the effect of precipitated dendrite augmented tip effects. Certainly one starting point for determining the magnitude of this effect is by determining whether the rate of deposition is altered by the loading of already existant precipitant. This effect of augmented gradient effects is a concerted interest to researchers in mineral beneficiation and particulate removal.

Of the effects discussed above, those related to wavelength are the enhanced gradient effects. Specifically the augmented field gradients due to magnet edge effects should become more prominent at large wavelengths. Furthermore, non-realistic representation of the transverse dependence of axial velocity may be wavelength dependent as well. Too large a velocity was adopted throughout the core analysis except at the center of the duct. Slower moving particulate would in reality have more interaction time with the field forces. This effect would be more significant when the force penetrates into the volume (i.e. at larger wavelengths).

It is hypothesized that those three-dimensional effects are not as important as accurate representation of the axial and transverse diffusivity dependence. Despite the lack of these refinements, the refined causal fundamental model has a useful degree of accuracy in predicting sedimentation in particle flows where inertia is unimportant.

B. Large Particle (50-100 μ) Analysis - Inertial Hybrid Model

Figure (6-16) shows the physical arrangement for the large particle tests. Unlike figure (6-1), the injection tube extends well into the duct, usually 14" past the profile grid. The number of grams injected as well as the amount precipitated per half wavelength is recorded for each test. Except for an isolated case, the injection velocity was adjusted to match the main duct flow in order to avoid secondary fluid mechanical effects due to non-isokinetic jet mixing. The jet was found to cause the diffusivity to increase only slightly in the duct. The new diffusivity profile was fitted with a least squares polynomial fit and used in the hybrid theoretical model discussed in Chapter 4, section D. The first nine harmonics of the magnetic field structure used in each test were used for the magnetic force calculation. The position of the injection tube varied roughly from one-third to two-thirds of the total duct height.

(1) Diffusion-free Model Results

The first test (figure 6-17) reveals the inaccuracy of the trajectory precipitation model (Appendix B) and the inertial model (chapter 4, section D) for 60 micron particles. Plotted are the particle paths from the top and the bottom of the injection tube for the two trajectory models along with the percentage particulate collected per half wavelength (6 cm). Particulate was injected isokinetically at 1500 ft/min. The inertia-free model predicts precipitation far too early primarily because of the immediate vertical viscous-limited velocity upon injection. The particle's inertia keeps the particle in flight longer and predicts precipitation in nearly the same region as the observed experimental collection peak. However, the inclusion of diffusion is clearly necessary if the trajectory spread is to have any correlation with the experimental observations.

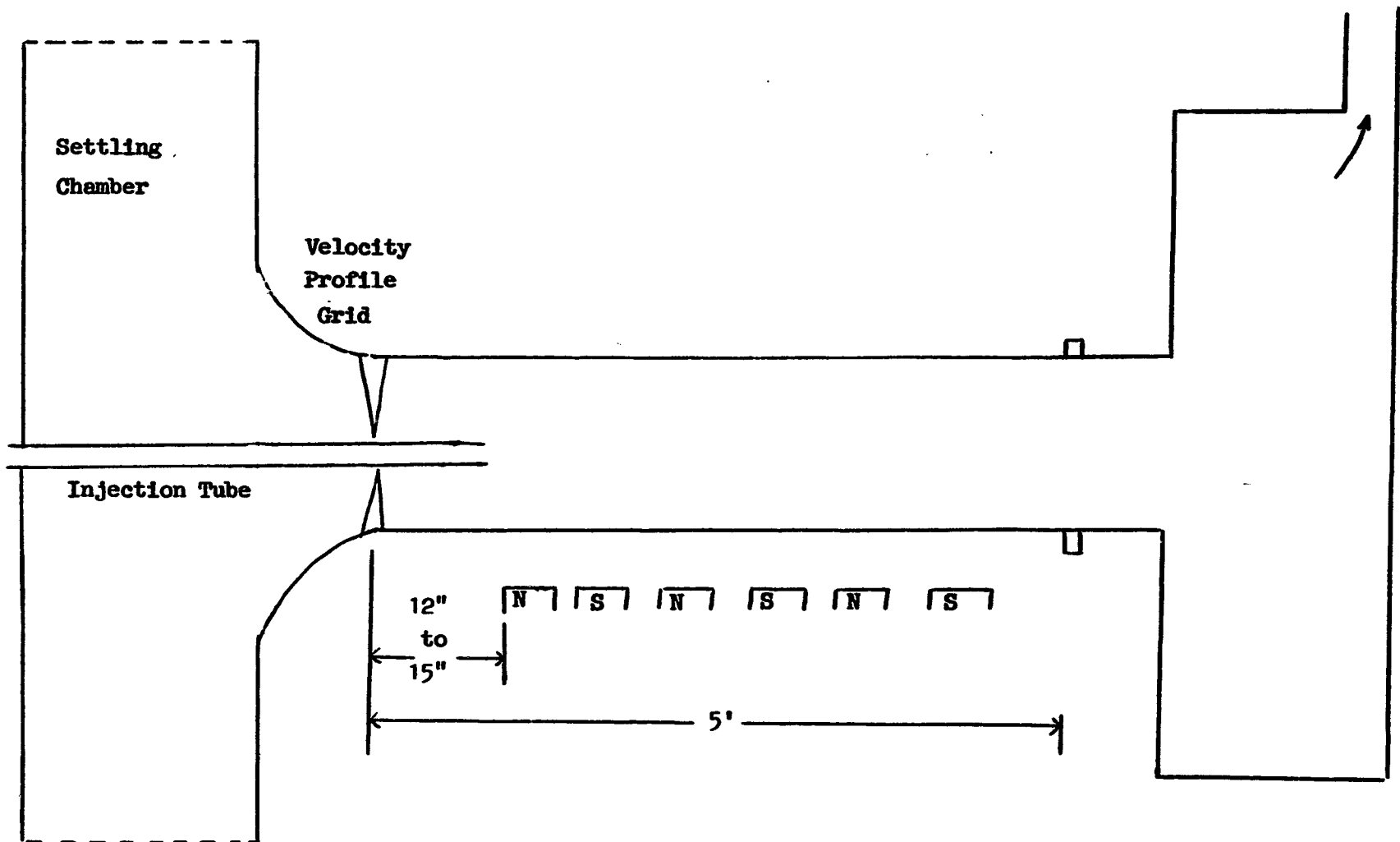


Figure (6-16) Large Particle (50-70 μ) Experimental Setup

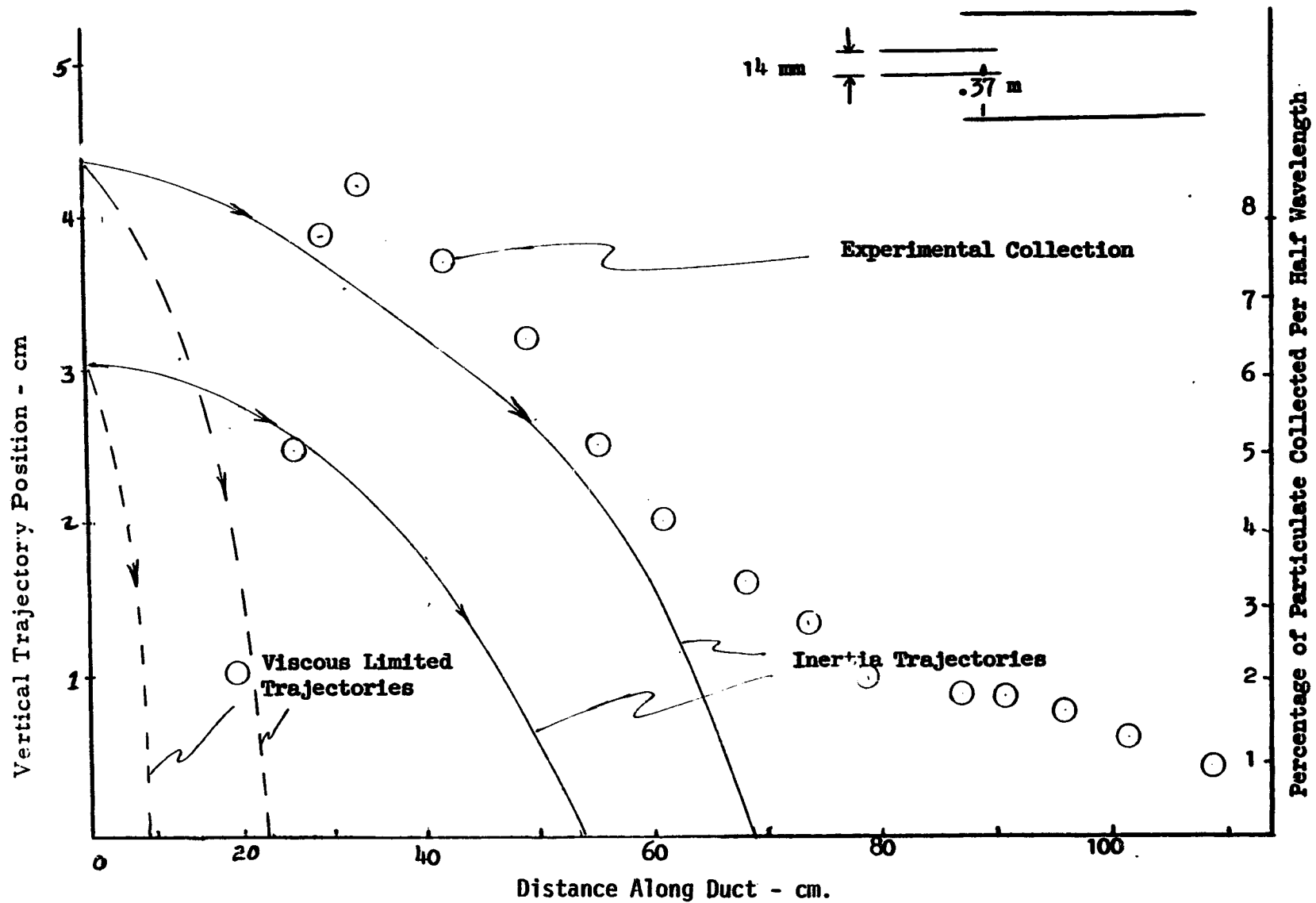


Figure (6-17) 60 Micron, 12 cm Wavelength, 1500 ft./min. Injection Trajectory Models with Experimental Collection; the left axis pertains to trajectories, while the right pertains to data deposition

Figure (6-18) shows the same test with 100-180 micron particles. The experimental collection spread is not as large but again exceeds the inertial model prediction. The peak collection again occurs near the inertia model's impact prediction. The viscous drag dominated model also predicts precipitation much too early. The percentage collection consistent with the above trajectory models was not shown because of its large value, being at least an order of magnitude larger than the observed collection for the 60 μ case.

(2) Hybrid Inertial-Diffusion Results

Figure (6-19) compares the experimental precipitation with the hybrid inertia-diffusion model prediction. As with the diffusion tests, the percentage particulate (of the total injected) collected per half wavelength is the precipitation ordinate. For this 12 cm wavelength, 70 micron particle test, the hybrid theory is seen to predict a comparable peak collection shifted downstream somewhat from the observed peak collection. The particulate spread is much larger now but still smaller than the experimental prediction. For illustration, the inertial theory prediction is shown at the top of the graph quite compressed in spread with a predicted precipitation an order of magnitude larger than the test results.

The results of 5.08, 8, and 12 cm wavelength tests for 60-70 micron particles are shown in figures (6-20) to (6-22). In all three cases the inertial diffusion hybrid model predicts larger precipitation with a peak somewhat downstream of the observed peak. Experimentally only 1/3 to 1/2 of the material injected was collected over the approximate four foot working section. The theory appears to always predict a short total collection distance, but this could only be thoroughly investigated with a longer duct working section.

(3) Particle Size Considerations

Particle size sensitivity is pertinent in all models. The iron particles

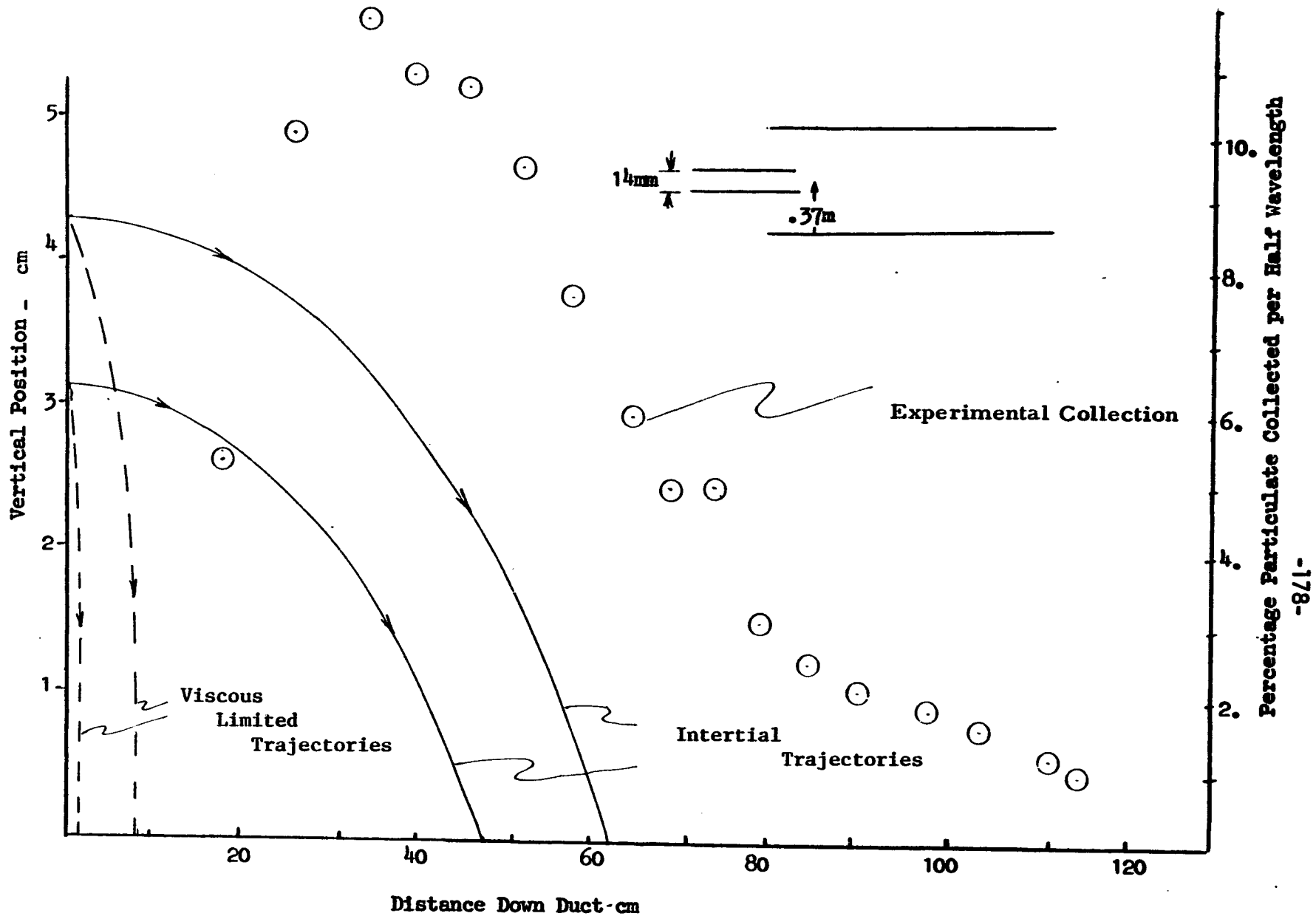


Figure (6-18) 100-180 Micron, 12 cm Wavelength, 1300 ft/min. Injection Trajectory Models with Experimental Collection; the left axis pertains to trajectories while the right pertains to data deposition

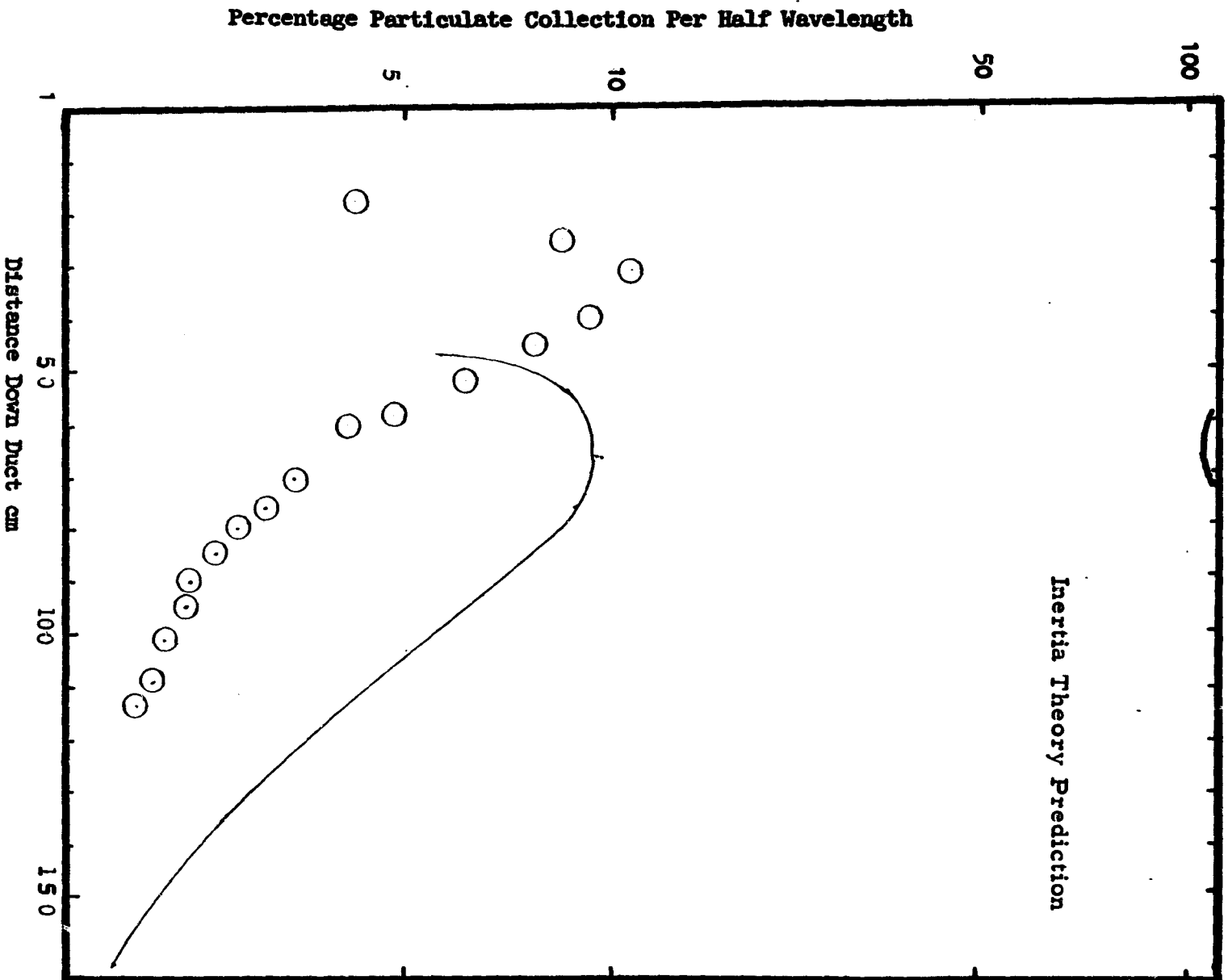
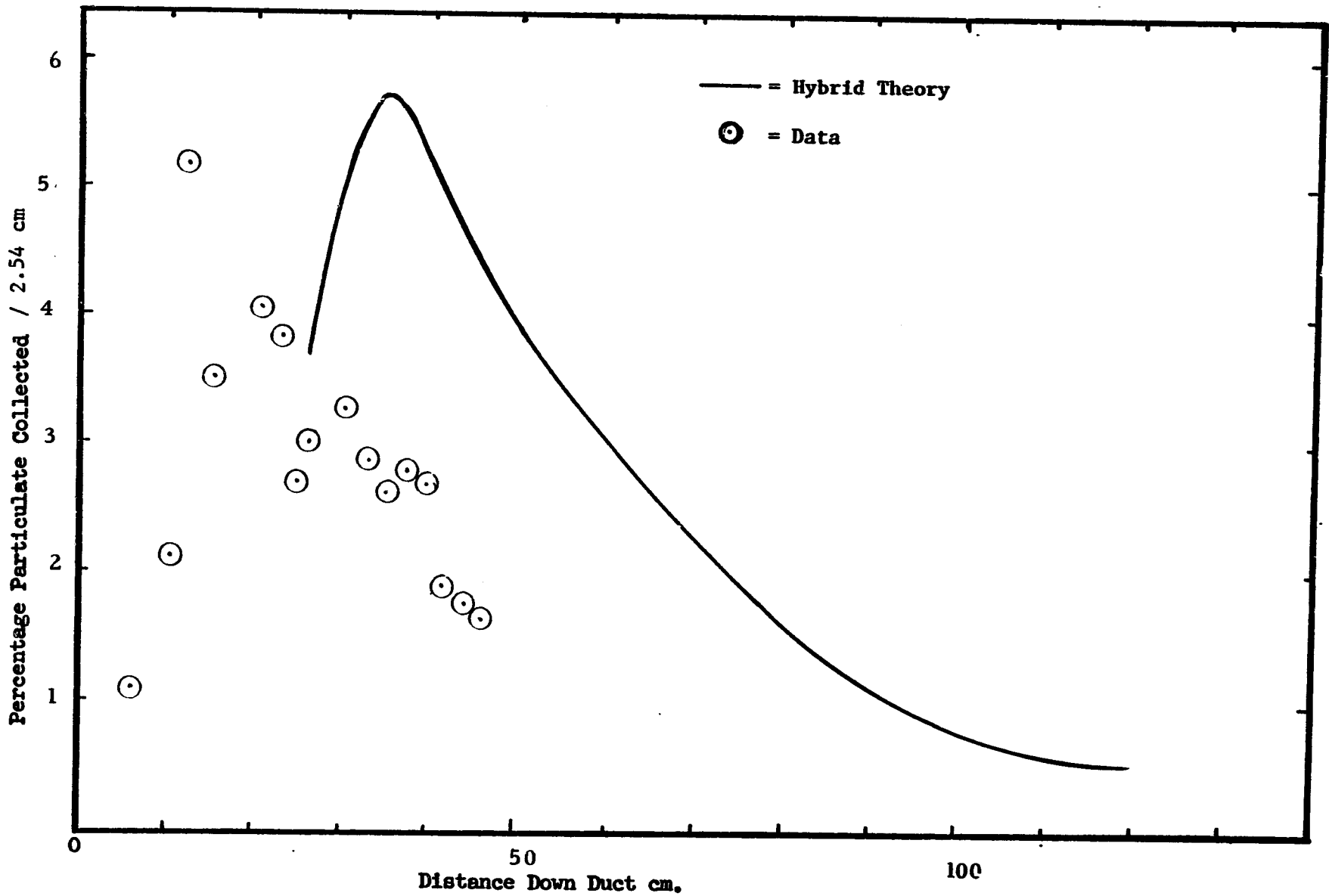


Figure (6- 19) 70 Micron, 12 cm Wavelength, 1380ft./min. Injection- Hybrid Model with Experimental Collection 76% Particulate collected in experiment



-180-

Figure (6-20) 5.08 cm Wavelength, 1000 ft./min. Injection, 70 Micron- Hybrid Model vs. Experimental Data
 51% Particulate collected in experiment

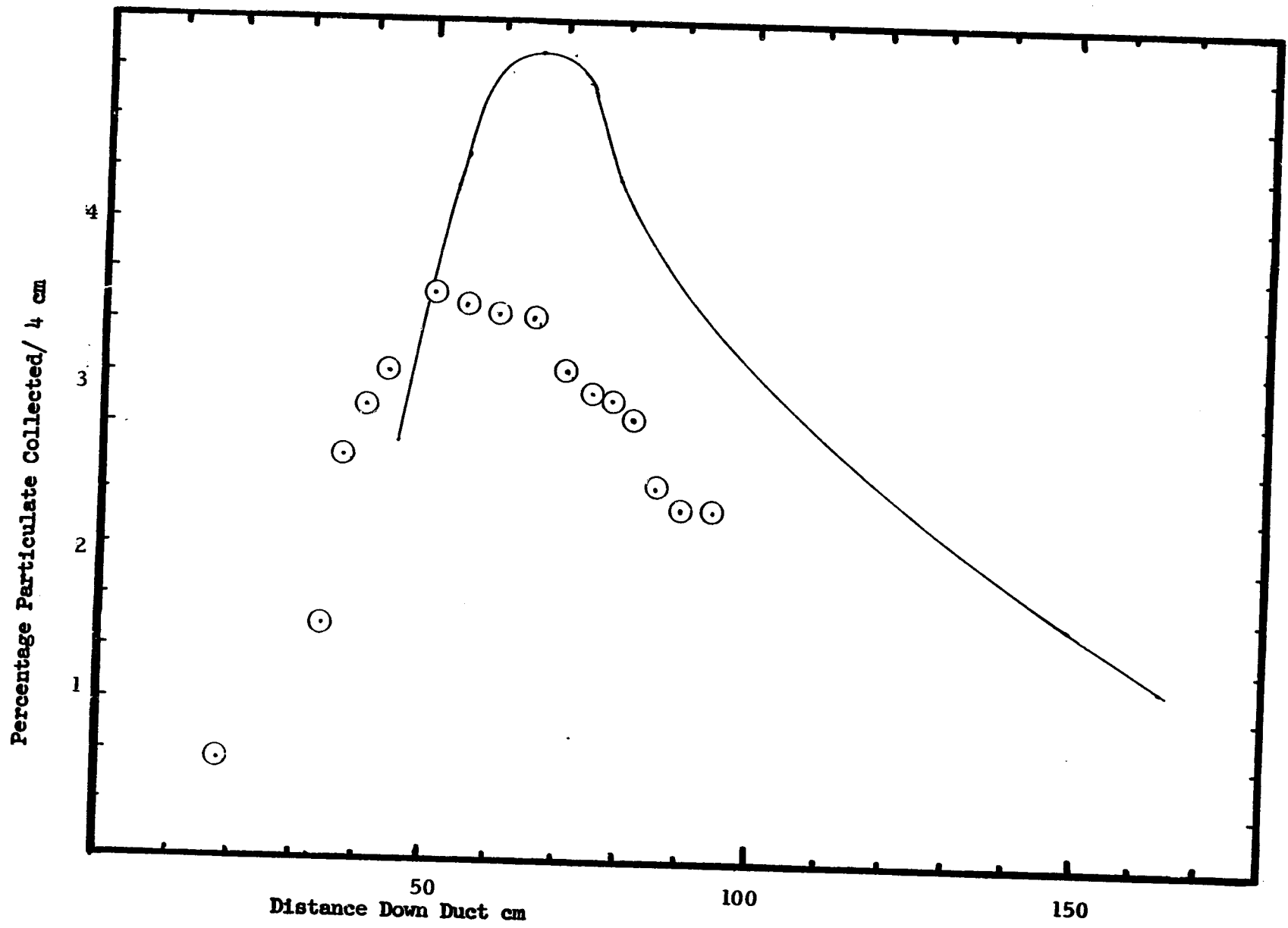


Figure (6-21) 8 cm Wavelength, 1400 ft./min. Injection, 60 Micron- Hybrid Model vs. Experimental Data
 46% Particulate collected in experiment

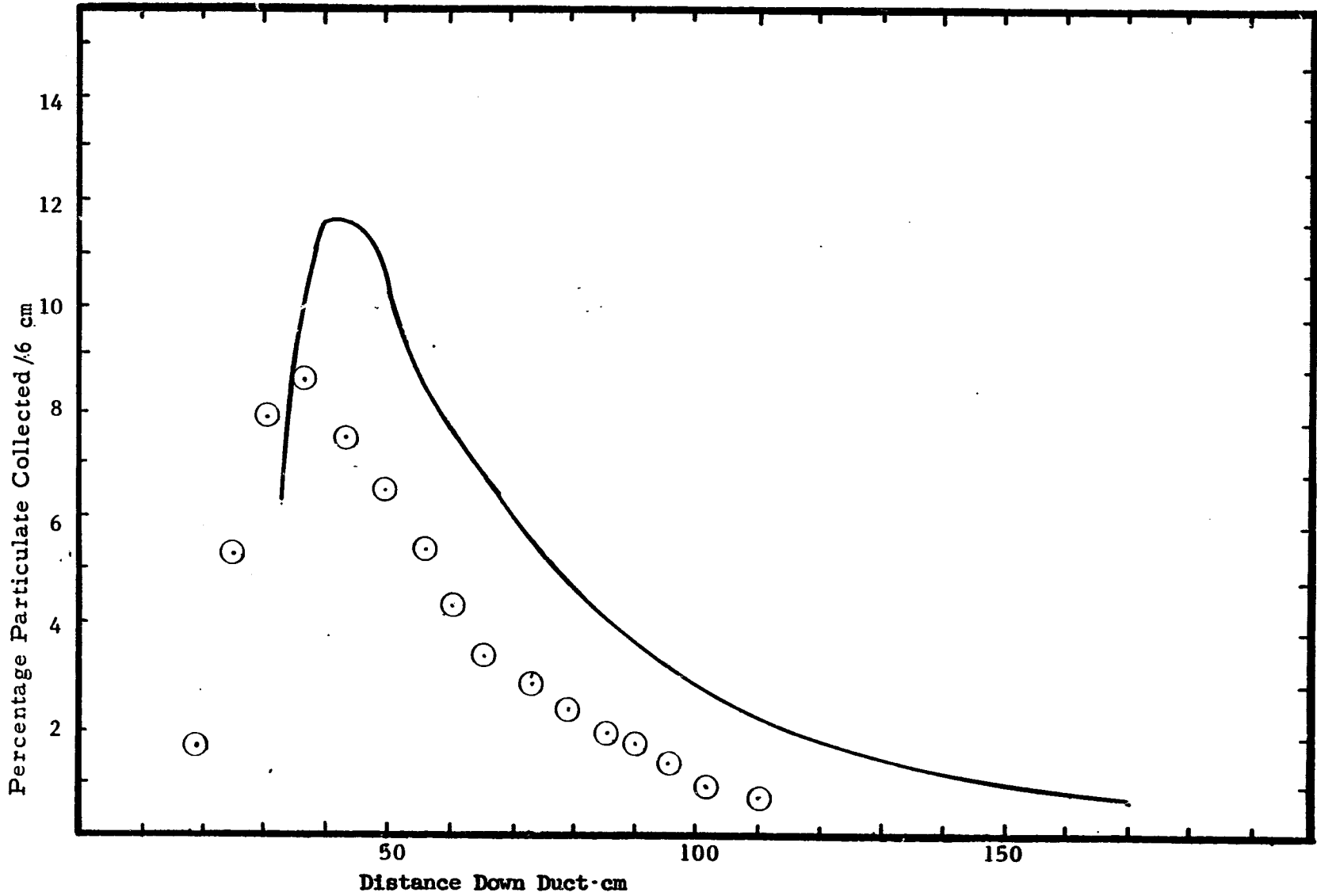


Figure (6-22) 12 cm Wavelength, 1500 ft./min. Injection, 60 Micron Hybrid Model vs. Experimental Data

64% Particulate collected in experiment

used in these tests were sized by sifting through several progressively smaller screen meshes. The smaller size particles used above were caught between 38 and 45 micron mesh screens, the hypotenuse of this size square opening being 54 and 64 microns respectively. The largest spherical particle must indeed be between 38 and 45 micron; most particles were however anything but spherical. Thus, ellipsoidal and elongated particles much heavier than a 45 micron sphere could surely exist in a batch. Observation of the particle group under the microscope revealed 60 micron to be the representative diameter of the 38-45 micron batch.

The particle size sensitivity of the hybrid model's particulate deposition prediction for the 8 cm wavelength case is shown in figure (6-23). As with the diffusion case, the size dependent parameters are proportional to the particle radius squared, a 20 micron spread appears to be quite significant indeed. The interesting result here is that the smaller particles with less inertia have a smaller deposition per half wavelength (over most of the precipitation region) and a peak deposition upstream of the larger ones. Figure (6-24) shows the hybrid model's deposition prediction for 40 micron spheres in this 38-45 micron sifted batch for a 12 cm wavelength field. Figures (6-25) and (6-26) show the equivalent comparisons for a 5.08 cm test 45-54 micron batch and an 8 cm, 38-45 micron batch. The upper trajectories in the 8 cm test are subject to question because they involved collisions with the upper wall.

The improved agreement leads one to believe that larger oblong particles behave in flight more like smaller spherical particles. This idea would certainly have credibility in terms of viscous drag forces. The streamlining of the heavier oblong particles and resulting lower drag would play against the larger gravitational and magnetic forces. The microscope, two-dimensional

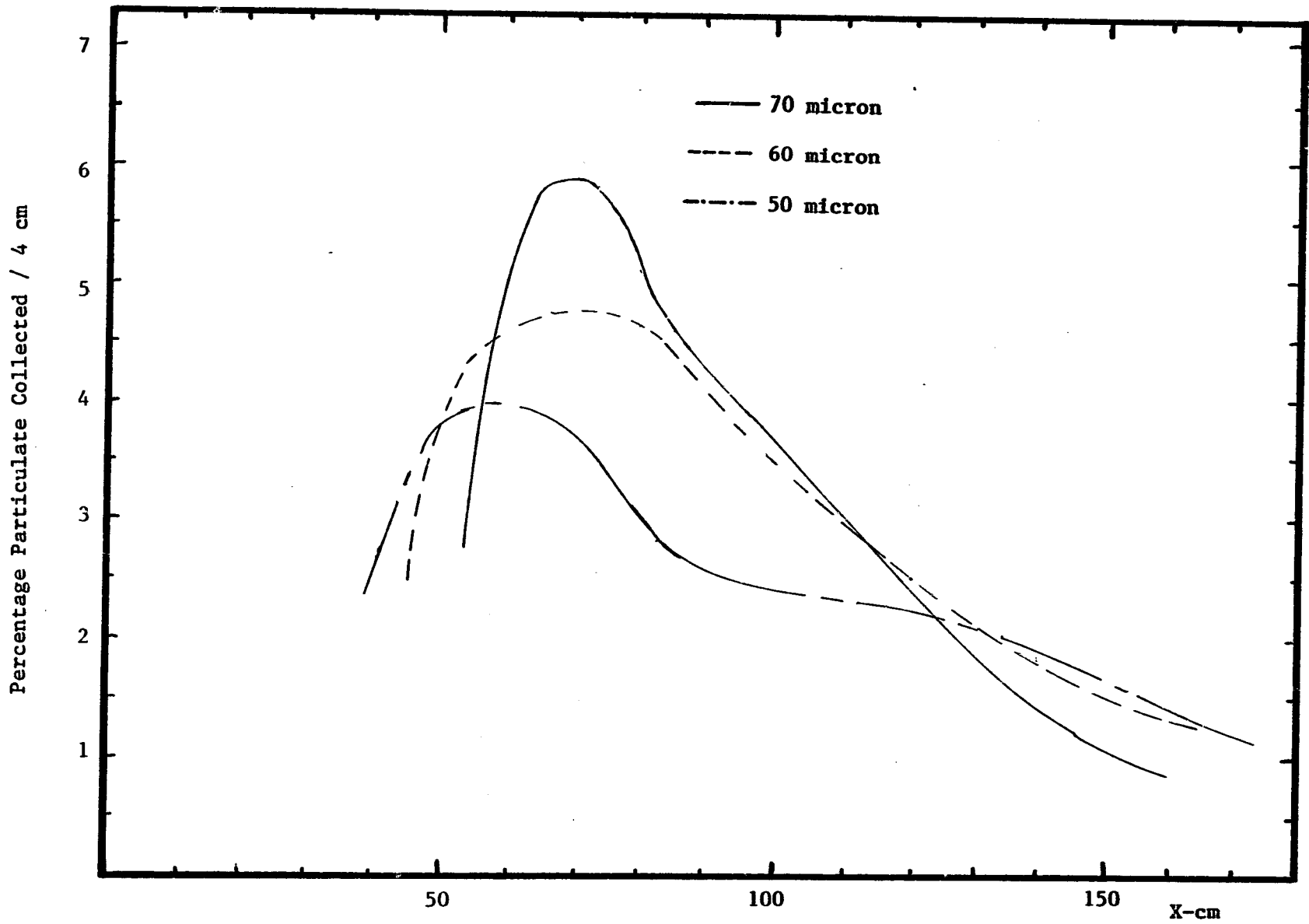


Figure (6-23) Hybrid Theory Particle Size Sensitivity, $\lambda=8$ cm, 8 mm tube, 1400 ft/min injection

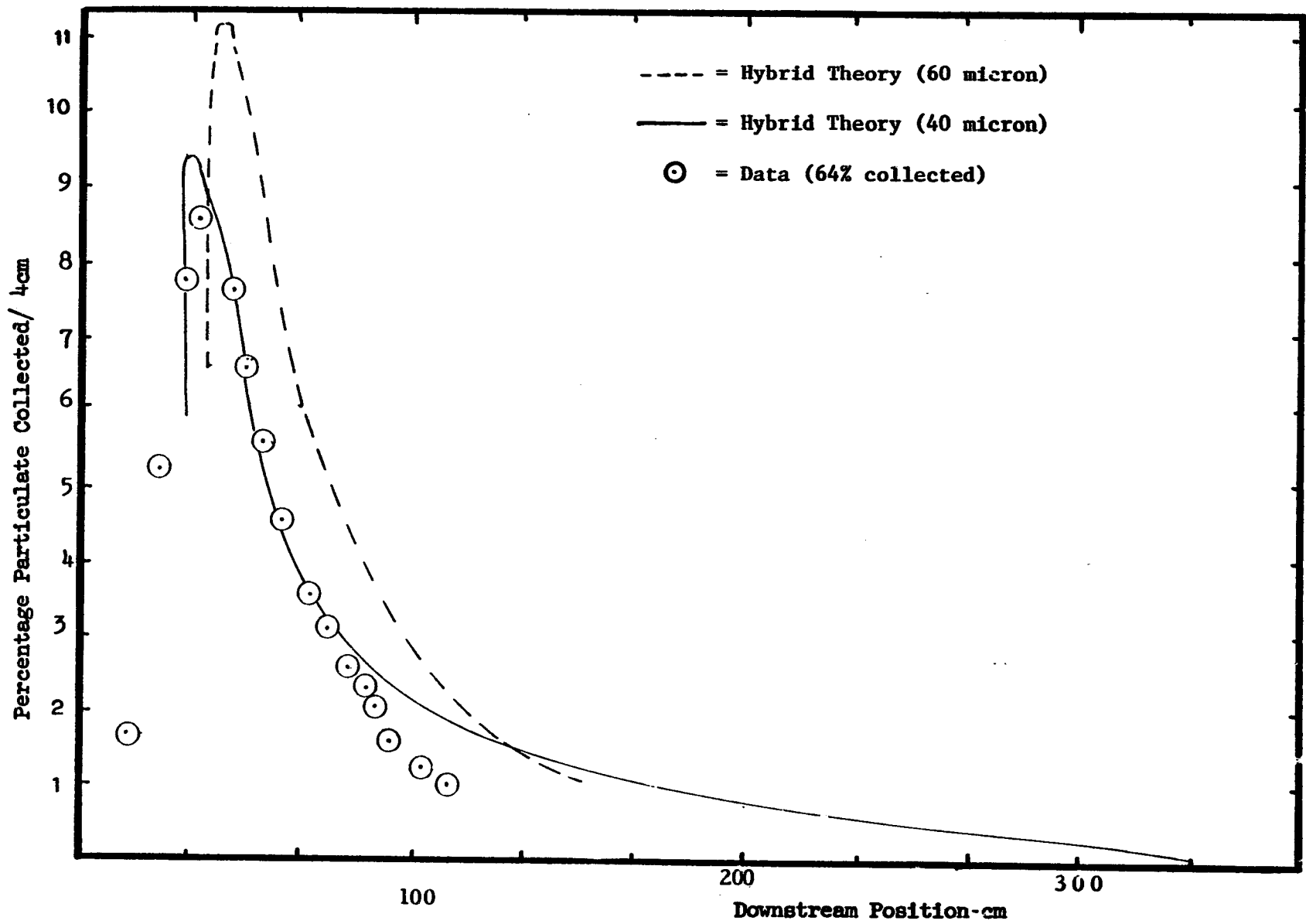


Figure (6-24) 38-45 Micron Batch, 12 cm Wavelength, 1500 ft./min injected, Hybrid Model Representative 40 Micron Spherical Prediction

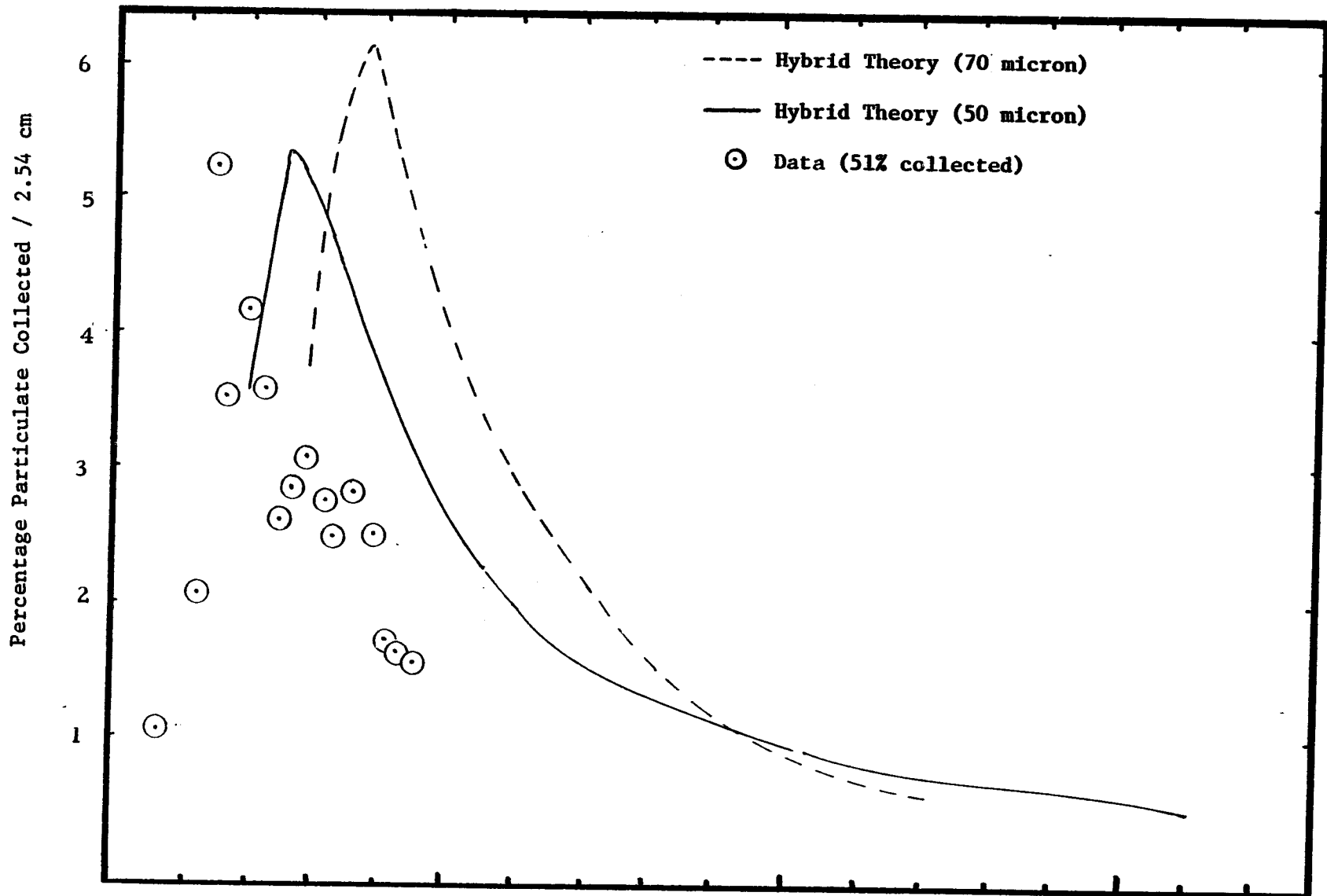


Figure (6-25), 45-53 Micron Batch, Comparison of 50 and 70 micron Computer Precipitation Predictions
 5.08 cm wavelength, $y_0 = .37$ m, 1000 ft./min. injection

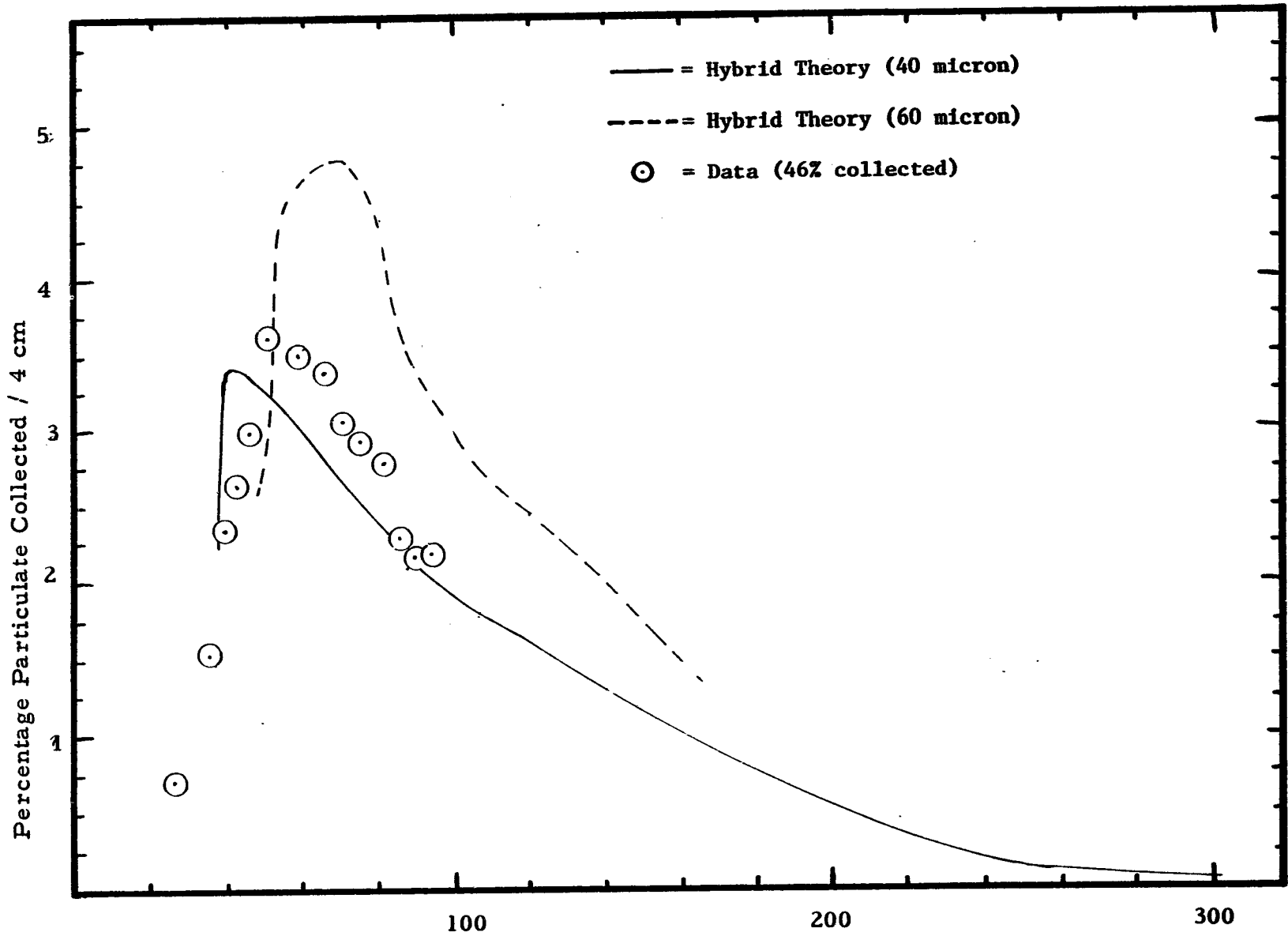


Figure (6- 26) 38-45 micron Batch, Comparison of 60 and 40 micron Theory Predictions, $\lambda=8\text{cm}$

slide picture is unfortunately lacking in its ability to reveal the total particle shape.

(4) Boundary Layer Thickness Sensitivity

For completeness, the question of model boundary layer thickness sensitivity must be addressed. The deposition predictions of the hybrid model at an 8 cm field wavelength with the boundary layer thickness varying from 1/4 to 3/4 cm are shown in figure (6-27). Unlike the diffusion case study, the results are relatively insensitive to thickness choice, varying only slightly at downstream duct positions. This is understandable because of the much greater role the migration forces should play with larger particles, especially the magnetic force (which grows exponentially towards the wall).

(5) Non-Isokinetic Injection

In all the precipitation tests, an effort was made to inject particles as close to the ambient duct flow velocity as possible. Figure (6-28) shows the collection results and theory predictions for a non-isokinetic test where the jet injection (2300 ft./min.) was more than twice the duct velocity (925 ft./min.). The working duct section was not long enough to observe the complete deposition pattern; less than half of the injected particulate was collected. The theory deposition prediction was based on a 70 micron particle representing a 45-53 micron grid batch (which, based on the above comments, is subject to question). Nevertheless, the results indicate a substantial difference between theory and experiment.

As figure (6-29) points out, there exists a region at the top and the bottom of the jet in which momentum is being exchanged between the two fluid streams. The thickness of the layer grows approximately as

$$\delta \sim \sqrt{vt}$$

(6-10)

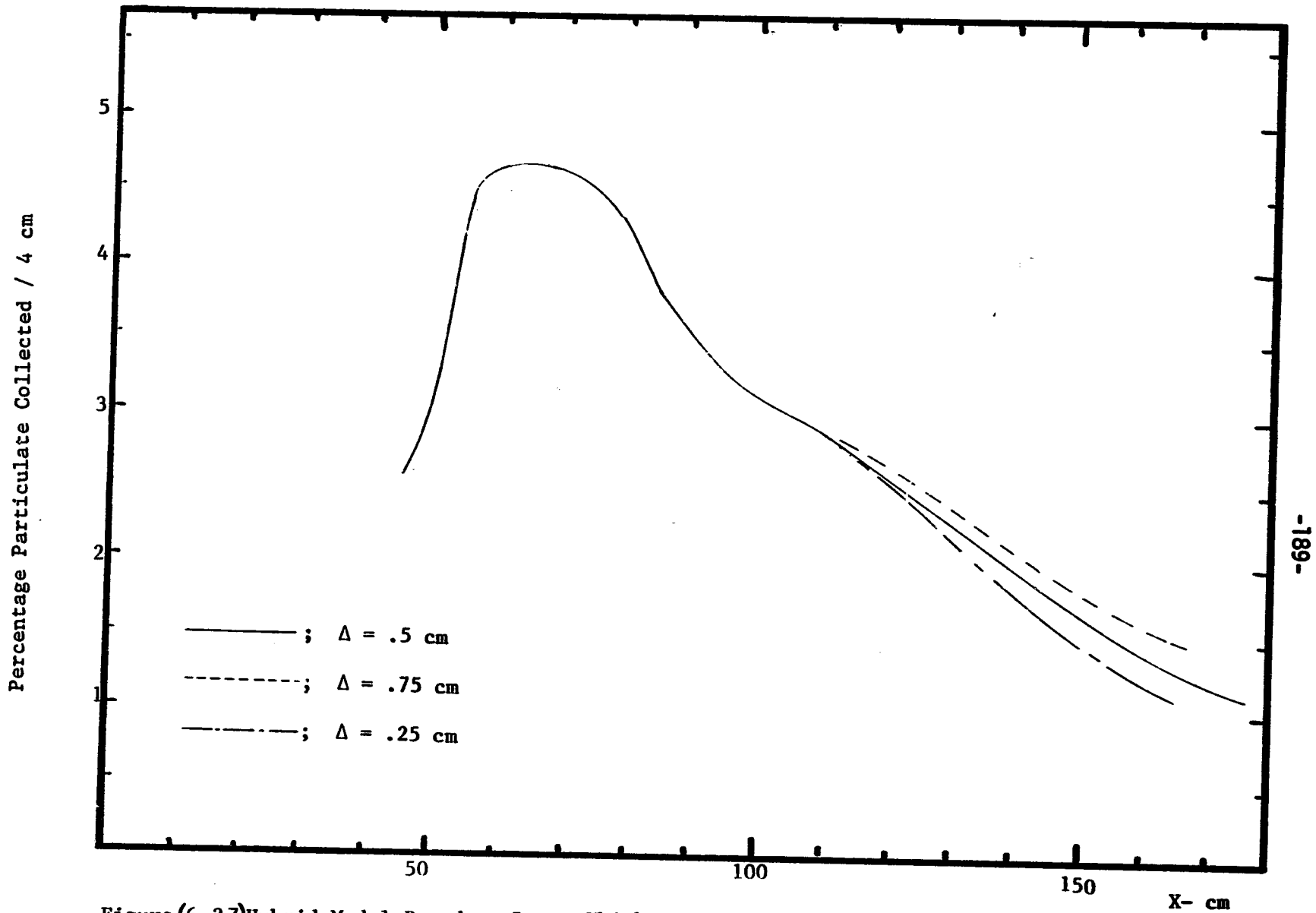


Figure (6-27) Hybrid Model Boundary Layer Thickness Sensitivity
 8 cm wavelength, 60 micron particle, 1400 ft./min. injection

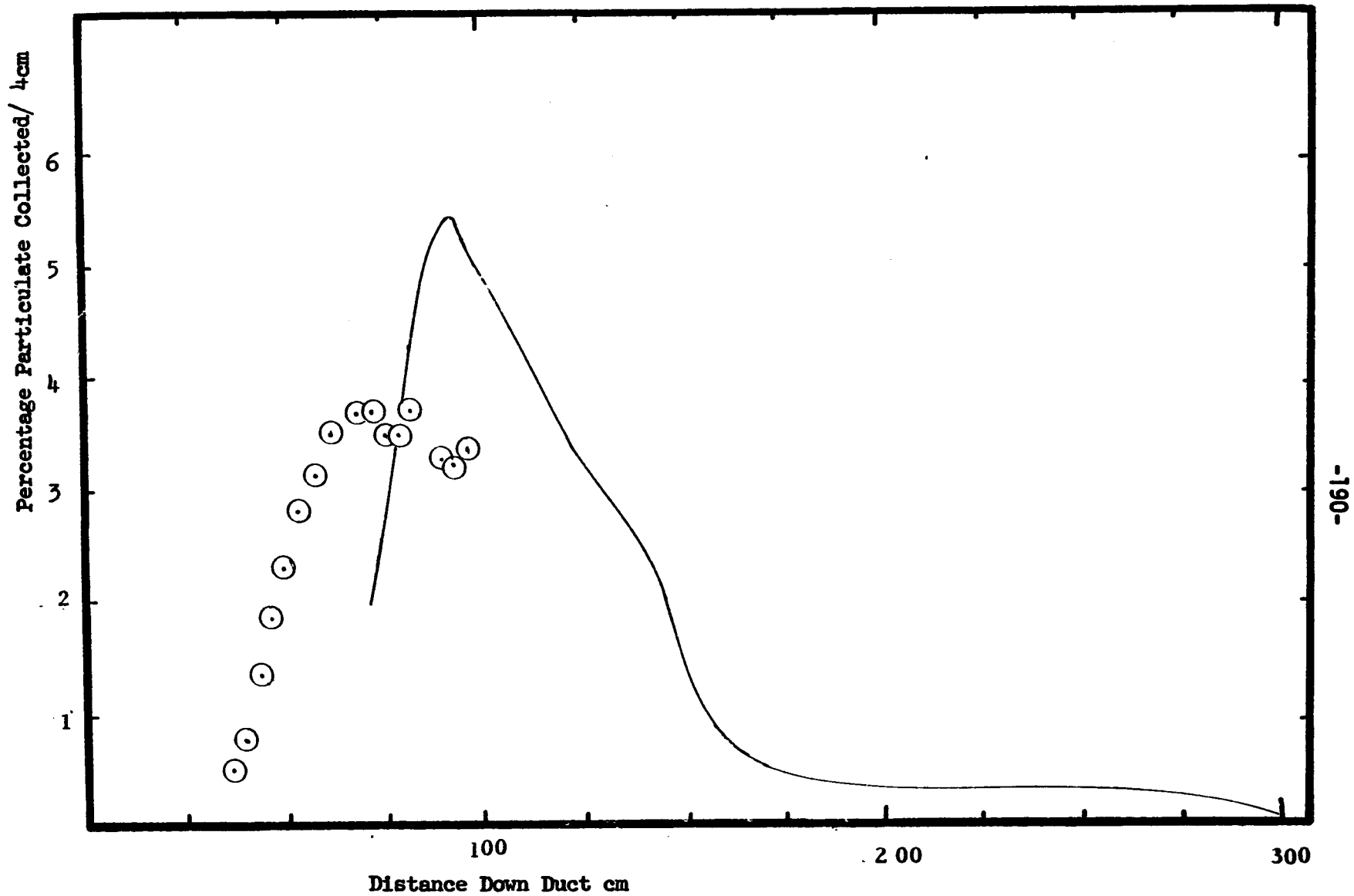


Figure (6-28) Non-isokinetic Particle Injection, 8 cm Wavelength, 2300 ft/min. injection, 45-53 micron batch
 Hybrid Theory and data; 39% collected, 70 micron

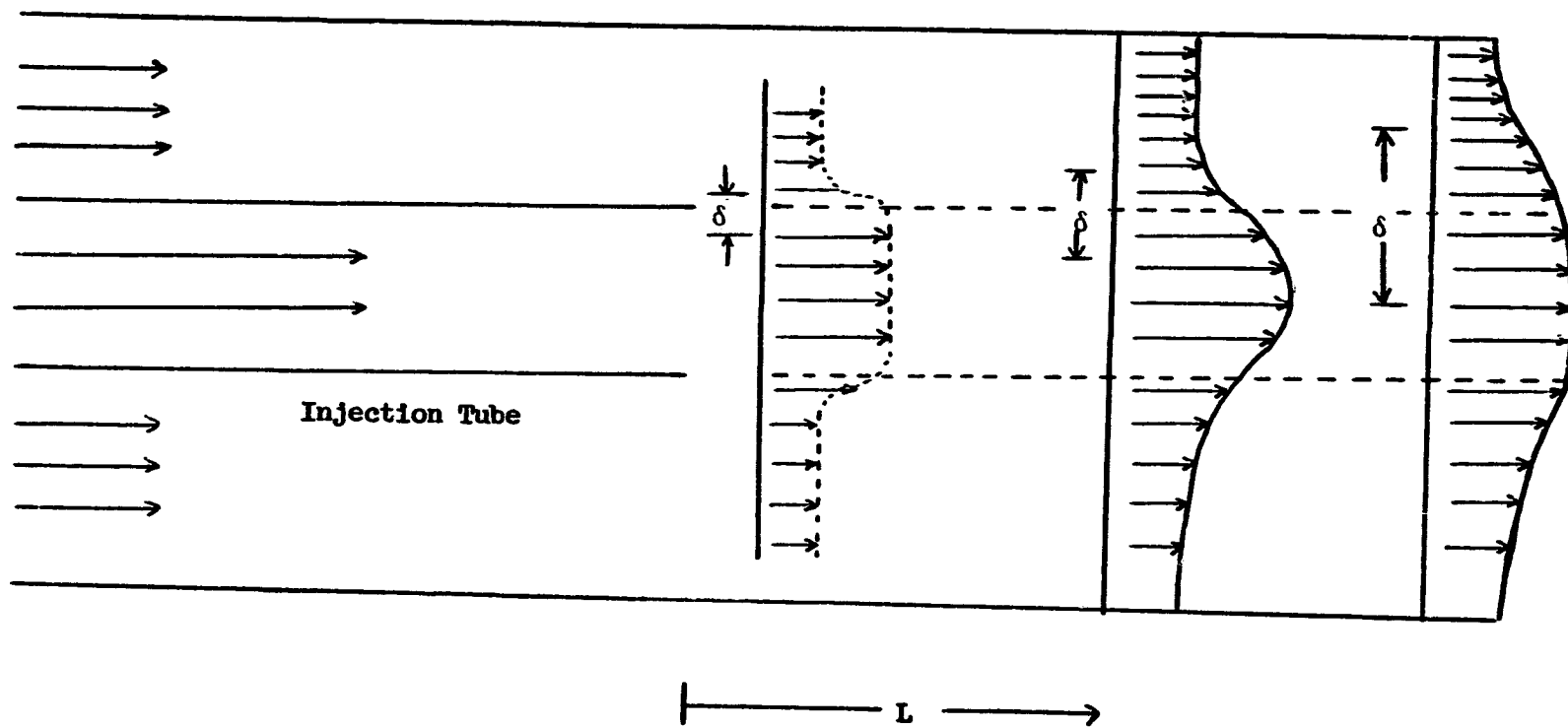


Figure (6-29) Growth of Turbulent Interchange Region for Non-Isokinetic Jet Injection

The fluid within this region δ is highly turbulent. Measurement of the fluid turbulence from such an injection showed little significant increase in diffusivity, but that may be attributed to the insensitivity of the anemometer probe and equipment.

(6) Field Harmonics

Finally, the inclusion of additional field harmonics has negligible effect on the precipitation level. Light particles are supplied by a relatively, strong diffusion force to the wall. The heavier particles depend on the magnetic force and gravity to get to the lower wall. As the fluid field decays exponentially into the volume (the harmonics to a greater extent $-e^{-kmy}$) their omission or addition changes little.

(7) Conclusion

The effect of adding diffusion to the momentum equation is to spread the particles out. The technique of marching in time in a Lagrangian frame, calculating density locally at every point in space is applicable to any geometry provided knowledge of the turbulent diffusivity is available. The diffusive term becomes more important when steep density gradients exist (e.g. at injection tubes). The next chapter will use the hybrid diffusion to analyze particle flight over a flat plate.

VII. Particle Flight Over Jet Fuselage

A. Introduction

The possibility of ducting particles with a permanent magnet structure will be considered in this section. The objective is to retain a substantial part of the particulate within the boundary layer as it evolves. A first attempt at this is to apply the hybrid inertial precipitation work of Chapter 4 to the problem.

The hybrid diffusion heavy particle computer model substantiated in chapter 6 will be the tool for analysis of this theoretical study. The flow and boundary layer development over a flat plate will be used to represent to first order the aerodynamics over an aircraft fuselage. All airstream compressibility effects will be ignored.

B. Fluid Mechanics and Diffusivity

Any analysis requires first, knowledge of the boundary layer thickness and diffusivity. The experimental evidence (Schlichting-see reference Ch. 5) indicates that if the boundary layer becomes turbulent at axial position $x=x_0$, its thickness will increase as

$$\delta = .37(x-x_0) \left(\frac{U_0(x-x_0)}{\nu} \right)^{-\frac{1}{5}} \quad (7-1)$$

where ν = local atmosphere kinematic viscosity and

U_0 = ambient air stream speed relative to the jet

The transition to turbulence occurs when

$$3 \times 10^5 < \frac{U_0 x}{\nu} < 3 \times 10^6 \quad (7-2)$$

For a passenger jet cruising at 40,000 feet, air speed 500 MPH, the onset of turbulence occurs about 24 inches after the leading edge and the boundary layer thickness is .68 meters, 10 meters downstream.

The turbulent diffusivity depends not only on the axial displacement along the fuselage, but also on the normal position in the boundary layer. Hinze (see chapter 2 reference, p. 645) shows Klebanoff's data for the eddy viscosity's distribution across the boundary layer. Equating the eddy viscosity with the turbulent diffusivity (as discussed in chapter 2) yields the diffusivity profile shown in figure (7-1). A least squares polynomial fit was made to represent D_t . The results are

$$D_t = .037U_o\delta \left\{ -.00103 + .291 \left(\frac{y}{\delta}\right) + .007 \left(\frac{y}{\delta}\right)^2 - 1.36 \left(\frac{y}{\delta}\right)^3 + .418 \left(\frac{y}{\delta}\right)^4 + 2.123 \left(\frac{y}{\delta}\right)^5 - .277 \left(\frac{y}{\delta}\right)^6 - 1.556 \left(\frac{y}{\delta}\right)^8 + 1.20 \left(\frac{y}{\delta}\right)^9 \right\} \quad (7-3)$$

Typically, injection would occur a few millimeters vertically into the boundary layer. As shown in figure (7-1), the diffusivity near the surface becomes negligibly small at downstream positions where δ is large. The diffusivity can be approximately represented as

$$D_t = (.037U_o\delta)(.07) \sin\left(\frac{\pi y}{\delta}\right) \quad (7-4)$$

Using the expression for δ from (7-1), the axial position for maximum D_t is found by setting the derivative of (7-4) equal to zero. The result is

$$\tan \frac{\pi y}{\delta} = \frac{\pi y}{\delta} \quad (7-5)$$

The graphical solution of (7-5), shown in figure (7-2), reveals that the only meaningful solution occurs where $\frac{\pi y}{\delta}$ goes to zero. The actual vertical dependence (7-3) of D_t goes to zero faster than $\sin\left(\frac{\pi y}{\delta}\right)$, indicating that for a given vertical location, diffusion will have a more pronounced effect at upstream (smaller boundary layer thickness) locations.

C-3

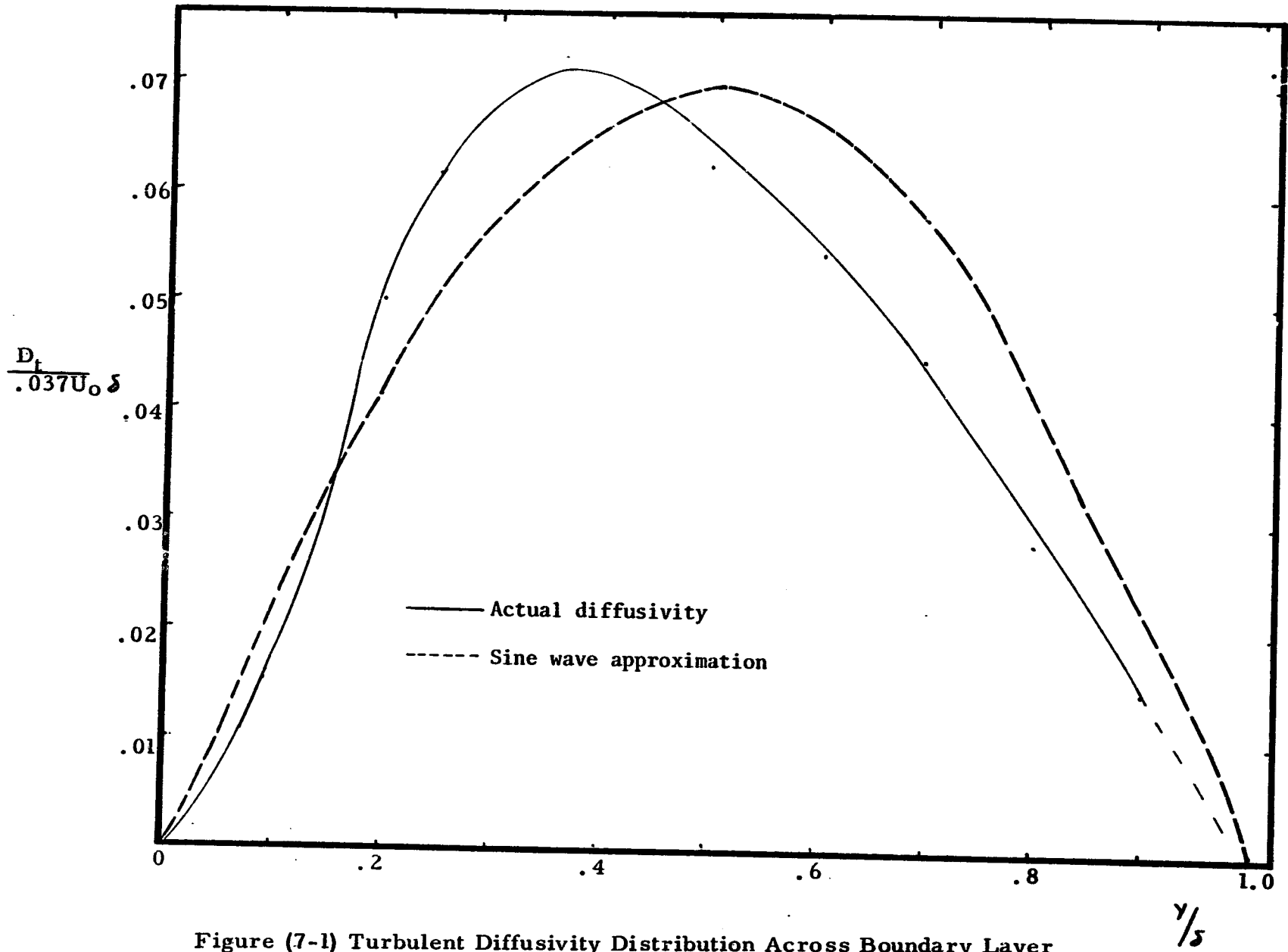


Figure (7-1) Turbulent Diffusivity Distribution Across Boundary Layer

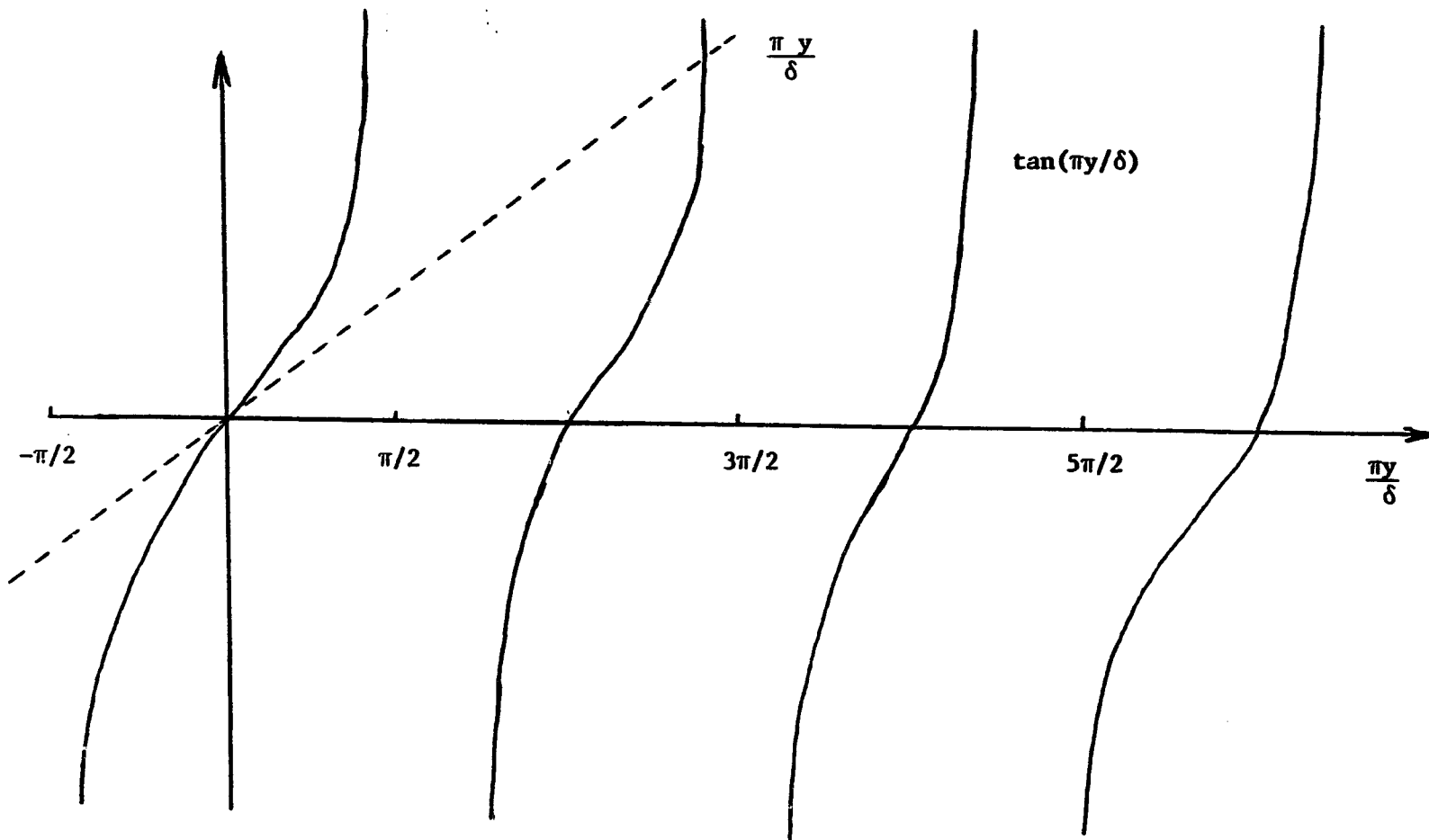


Figure 7-2 Determination of Maximum D_t

C. Typical Injected Density Profiles

Figure (7-3) shows computer calculations of particle trajectories for particulate injected isokinetically through an 8mm diameter tube into an aerodynamic boundary layer 6mm away from the plane skin. Injection for this calculation was set at just over 1 m downstream of the leading edge where the boundary layer thickness had grown to 7.3 cm. The calculation was identical to the hybrid inertial diffusion model developed in chapter 4 except that gravity was ignored here. The calculation was performed assuming use of 40 micron spheres, an eight cm wavelength field structure, and an ambient air speed of 500 MPH. The strength of the magnetic field was chosen to be comparable with commercially obtainable permanent magnets--the field strength on the aircraft skin 1/4" from the magnet being about $.095 \text{ web/m}^2$. Iron powder was chosen as the injected particulate, but any large μ material of density $\sim 7 \times 10^3 \text{ kg/m}^3$ would give equivalent results. A listing of the program KD747G used is listed in Appendix J.

The effect of the small layer thickness and thus large initial diffusivity, is seen to force the upper trajectories away from the plane structure. The lower trajectories are, however, precipitated rather quickly. It is not until the lower trajectories begin to precipitate and thus lower the densities among the upper trajectories, that they begin to drop as well. This upward diffusion makes it quite difficult to collect the last 5% of particulate. In the above calculation, the upper trajectory was only beginning to curtail its upward ascent 47 meters downstream, 7.5 cm above the skin. Because of the diminished effects of diffusion downstream at the same injection height, precipitation of all the particulate is easily accomplished (e.g. with $x_{\text{injection}} = 10\text{m}$, all particulate is collected in 3 meters). In any event, with an initial density injection profile characterized by a $(y/a)^{1/7}$ dependence, ducting is

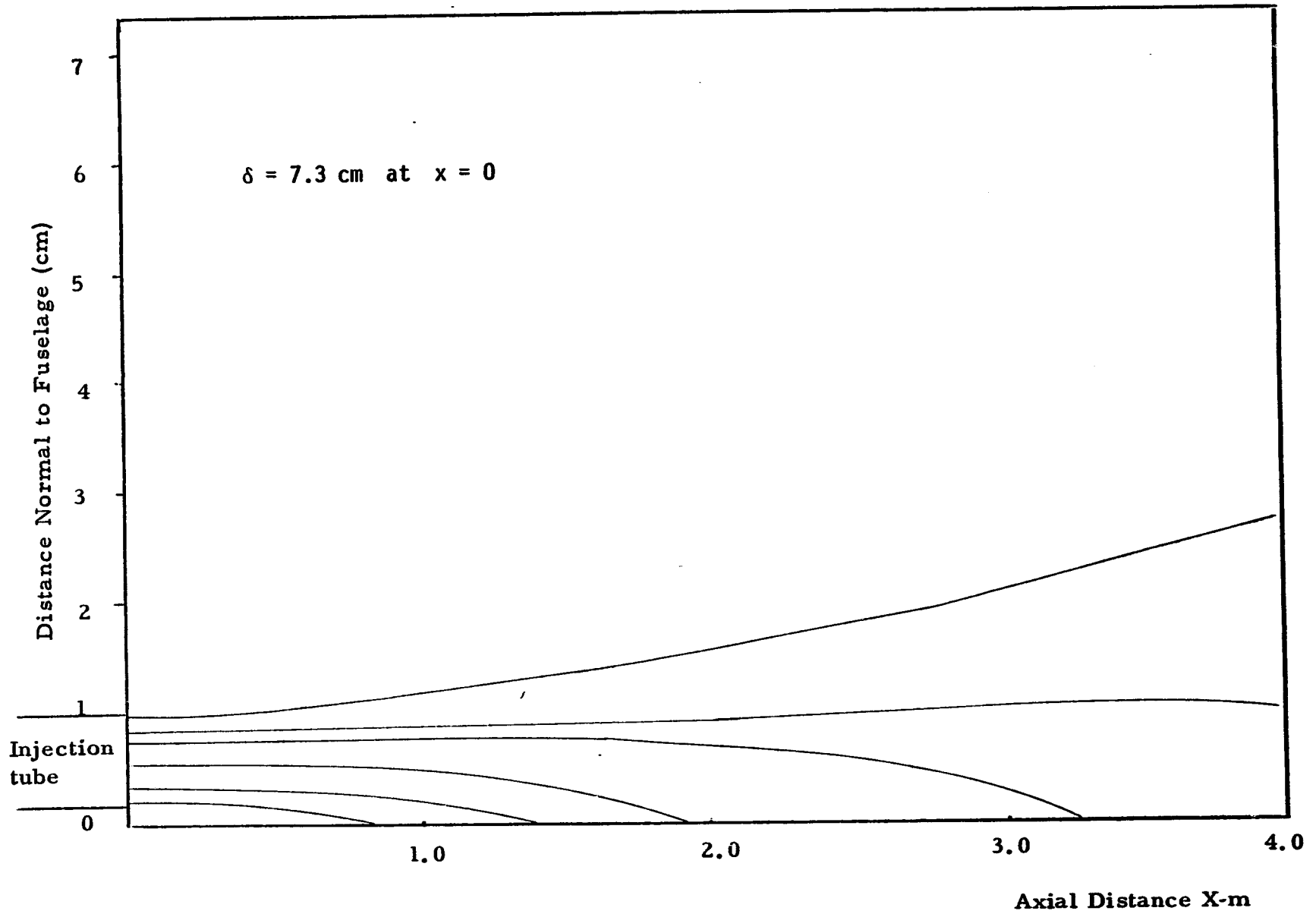


Figure (7-3) Particle Trajectories Over Jet Fuselage

not possible; either the particulate will be precipitated or lost.

D. Possibility of Quasi-Stationary Profiles

The question that must be considered is whether or not there exists an injection density profile that would yield a steady or quasi-steady positioning of particulate in the boundary layer. This would require a balance between the upward diffusive flux and the downward magnetic migration. From the results of chapter (4-D), this would require

$$-\frac{6\pi\eta r D_t}{n} + \frac{\partial n}{\partial y} - \frac{4}{3} \pi r^3 \left(\frac{3}{2 + \frac{\mu}{\mu_0}} \right) \left(\frac{\mu}{\mu_0} - 1 \right) \frac{k}{\mu_0} \sum_{m=1}^{\infty} m B_m^2 e^{-2kmy} = 0 \quad (7-6)$$

or with a fundamental harmonic field only

$$-\frac{6\pi\eta r D_t}{n} \left(\frac{\partial n}{\partial y} \right) - \alpha k e^{-2ky} = 0 \quad (7-7)$$

Equation (7-7) could be integrated if the density at some location y were known. Although the assignment of $n=0$ at $y=\delta$ is reasonable, D_t also goes to zero there and the evaluation of the first term above becomes a problem. Again approximating D_t as $(.037 U_0 \delta) (.07) \sin\left(\frac{\pi y}{\delta}\right)$. The analysis proceeds by assuming

$$\frac{n}{y \rightarrow \delta} = (\delta - y)^\rho \quad (7-8)$$

Equation (7-7) gives

$$\alpha k e^{-2ky} = (6\pi\eta r) (.037 U_0 \delta) (.07) \left[\frac{\pi}{\delta} (\delta - y) \right] \left[\frac{\rho (\delta - y)^{\rho-1}}{(\delta - y)^\rho} \right] \quad (7-9)$$

or

$$\rho = \frac{\alpha k e^{-2k\delta}}{(6\pi\eta r) (.037 U_0) (.07) \pi} \quad (7-10)$$

The constant in front of the exponential is equal to about 82 for parameters characteristic of the above text. The exponential power $2k\delta$, however, is 41, indicating that ρ is a very small number. The density is nearly uniform, but drops sharply at $y \sim \delta$ in the neighborhood of the boundary layer exterior. Designating the density at $y = \delta_-$ as n_0 , equation (7-7) can now be integrated to give

$$\int_n^{n_0} \frac{1}{n} dn = - \int_y^{\delta_-} \frac{\alpha k e^{-2ky}}{\delta(6\pi r)(.037U_0).07 \sin \frac{\pi y}{\delta}} dy \quad (7-11)$$

Reversing the order of integration, (7-11) becomes

$$\ln \left(\frac{n}{n_0} \right) = - \int_1^{\frac{y}{\delta}} \frac{\alpha k e^{-2k\delta \left(\frac{y}{\delta}\right)} d\left(\frac{y}{\delta}\right)}{(6\pi r)(.037U_0).07 \sin \frac{\pi y}{\delta}} \quad (7-12)$$

Equation (7-12) was integrated numerically beginning 10 ft. downstream from the transition to turbulent instability where $\delta = .26m$ for an 8 cm wavelength field. The calculation was quasistationary in that it assumed a constant boundary layer thickness. The resulting density profile is shown in figure (7-4) along with the necessary sharp cutoff dependence near $y = \delta$.

The large density at $y=0$ indicates a problem occurring in this region. There is no way to terminate the density in this region except as a step at $y=0_+$ from $n=0$ to a very large n almost instantaneously at $y=0+\epsilon$. At this point, the search for a possible steady profile becomes merely a mathematical exercise, since the profile in this region implies a very rapid precipitation ratio.

It is interesting to compare the spreading of two density profiles under the same conditions. The trajectory profiles with isokinetic injection of particulate 3 meters after the transition to turbulence, under the same condi-

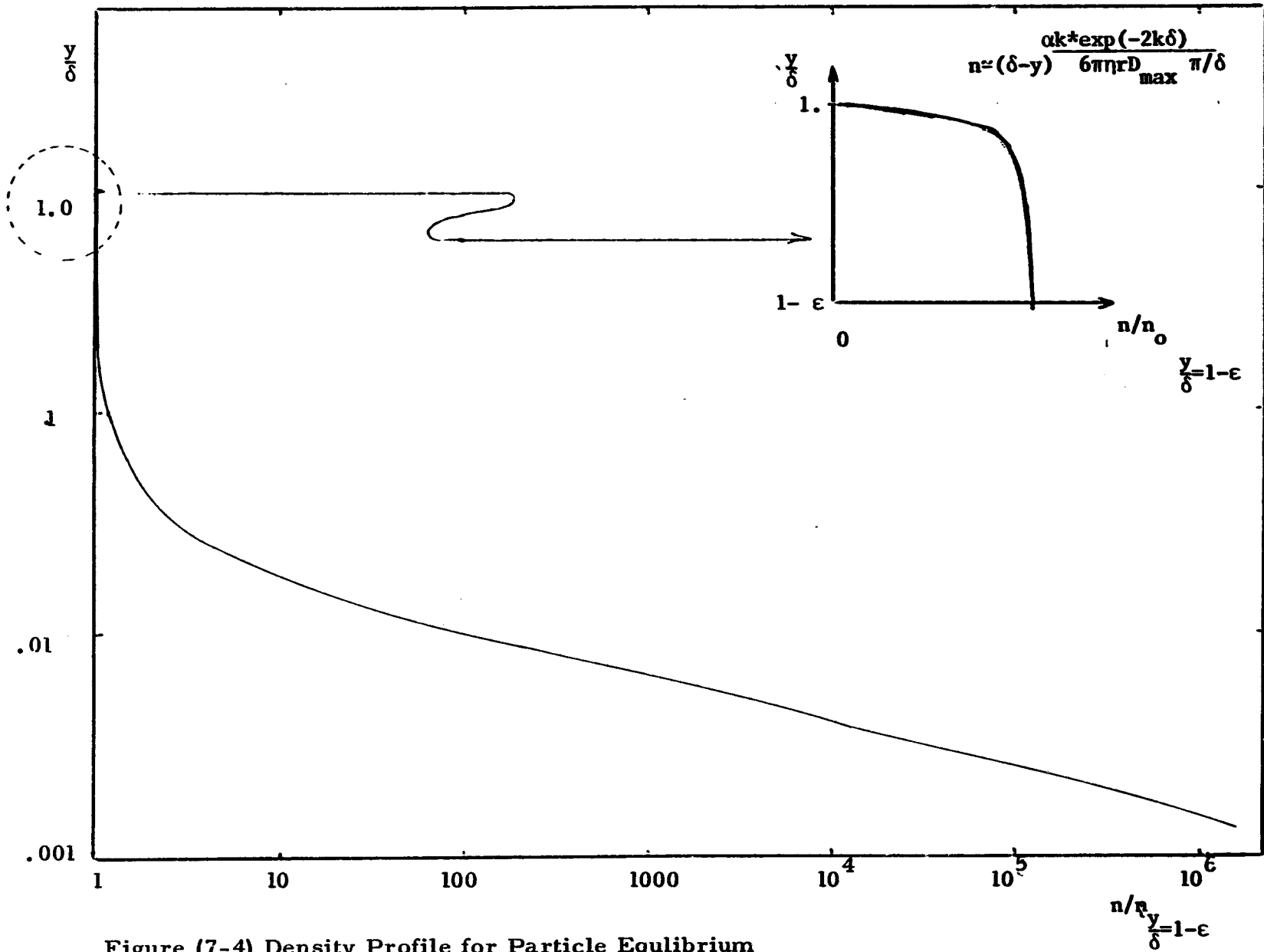
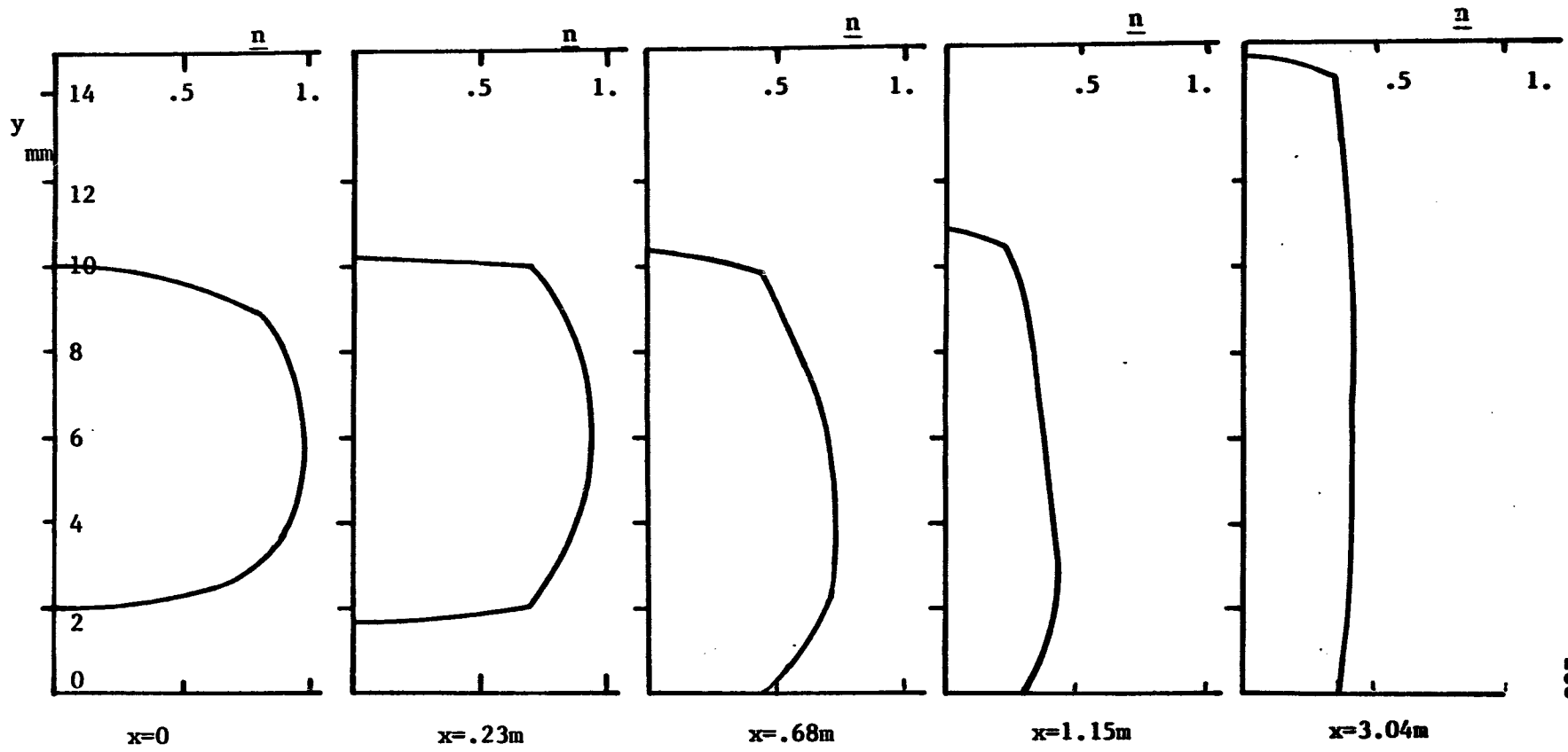


Figure (7-4) Density Profile for Particle Equilibrium

tions as the trajectories in figure (7-3), are shown in figures (7-5) and (7-6). The characteristic turbulent profile $(y/a)^{1/7}$ dependence is assumed in fig. (7-5), while an initial density profile similar to that in figure (7-3) is assumed in fig. (7-6). The calculated densities are plotted for various locations downstream. The results indicate the skewed profile case does indeed keep the mid to upper trajectories more horizontal for a longer axial distance. The precipitation of the lower trajectories occurs within the same distance as the normal density profile case however. Downward diffusion dominates at these lower trajectories since no particulate exists between the plane skin and the lower part of the injection tube initially. The density plots reflect just how quickly the effect of downward diffusion and migration of the lower trajectories propagates upward. The author's conclusion from the above analysis is that ducting of magnetizable particles in a turbulent boundary layer with a permanent magnet structure is unfeasible. Ninety percent of the particulate injected 6 mm above a flat surface in a 500 MPH airstream can be contained and collected within 4 m. The last 10% if collected, will be spread over the following 4 m stretch.



-203-

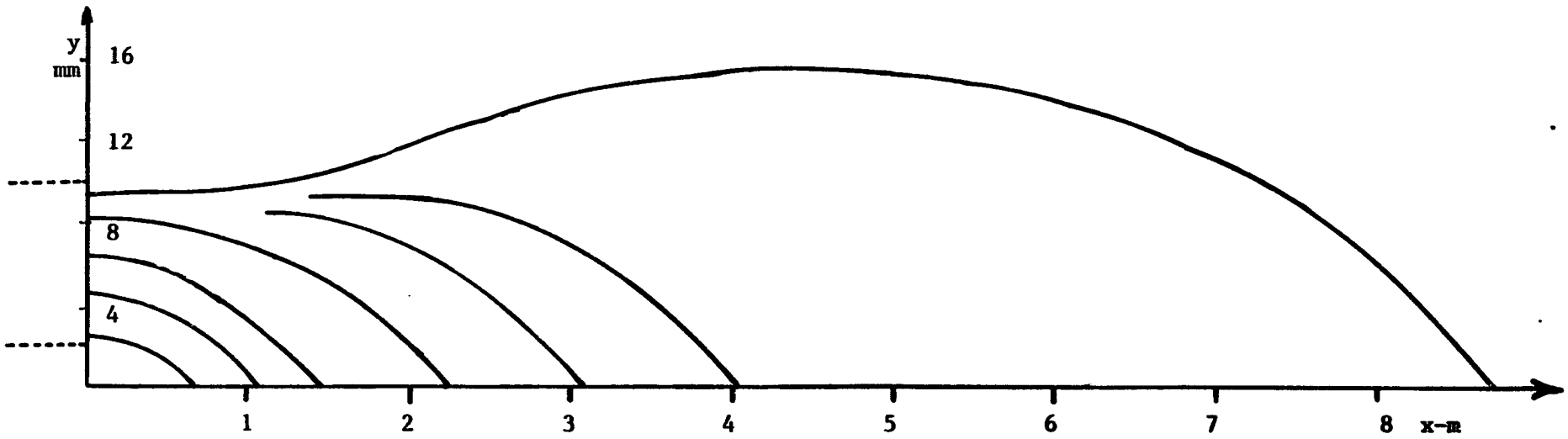


Figure 7-5 Trajectories and Densities in Boundary Layer-Typical Tube Profile Initially

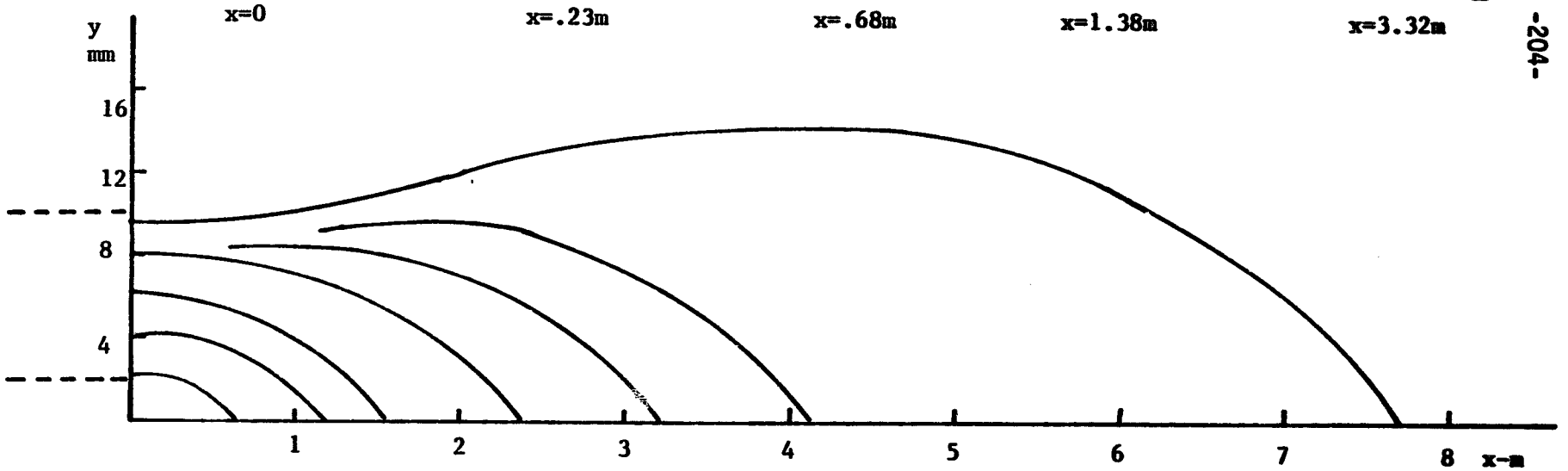
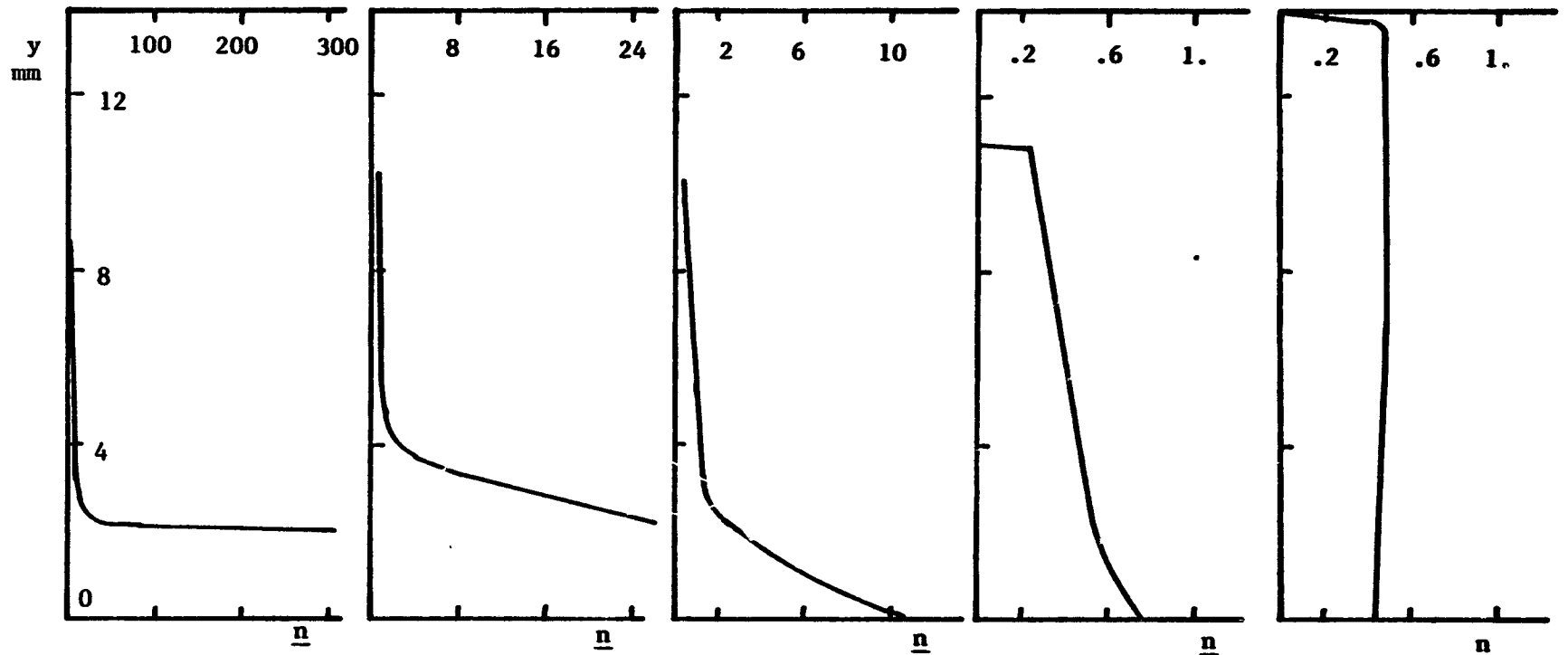


Figure 7-6 Trajectories and Densities in Boundary Layer; Skewed Profile at Time $t=0$.

VIII. Concluding Remarks

A. Particle Entrainment over Jet Fuselage

The process of entraining magnetizable particulate in a boundary layer may now be examined in the light of the chapter 7 results. If particulate is moving in near synchronism with the jet air speed, and collection of particulate and reintrainment at the front of the craft is in effect, it is reasonable to assume particulate undergoes one full cycle when the jet has traveled twice its length with respect to the air at "infinity". The density tests of chapter 7 indicate that at best 4% of the injected particulate will be lost per cycle.

(This assumes that particles collected prematurely are shuffled along the wall while still interacting with the boundary layer in some positive drag reducing manner.) Thus with these figures, a 100 ft. craft undergoing a 10 mile flight

(and hence $\frac{(10)5280}{2 \times 100}$ round trips) $100[1 - (1 - .04)^{\frac{(10)(5280)}{200}}] = 99.9979$ per cent of the original particulate would be lost.

Assuming the craft has a surface area of 4700 sq. ft. and specifying that 1 gram of powder be exposed to 2 sq. ft. of the craft skin at any instant, it would be necessary to begin the flight with 1.13×10^6 kg of powder stored on board! Clearly this is an unacceptable demand and an alternative in which constant interaction with particulate over the skin must be sought.

B. Travelling Wave Interaction with Particulate

A travelling wave structure mentioned in the introduction has been examined qualitatively as a means of shuffling particulate along the skin in an aerodynamic boundary layer. The experiment shown in fig. (1-2) involved injecting particulate just under the duct upper edge; particles were captured by the field, held against gravity, and shuttled downstream opposite to the

direction of the travelling magnetic field.

Figure (8-1) shows an inverted picture of the field region just above the wave structure with a right traveling wave, an observer at point P encounters a counter clockwise rotating field. Non-spherical agglomerates experience a counter-clockwise torque in such a field resulting in a reverse walking motion on a surface adjacent to the structure.

Figure (8-2) depicts a typical instantaneous picture of agglomerates on the duct upper wall. Particles generally form agglomerates in the magnetic field. Most of the agglomerates will cling to the end of the field structure. Agglomerates over the body of the structure actually bounce along the surface toward the downstream field edge. Particles and agglomerates gravitate to some degree toward the side edges as they propagate down the duct because of the edge effect gradient.

The flight of a single agglomerate is shown in fig. (8-3). The agglomerate literally walks end upon end; at low frequencies (1 Hz) this effect becomes clear as long agglomerates (1/4") walk along the duct.

Agglomerate speed is a function of frequency and agglomerate length. Two steps are taken every cycle, each equal to the agglomerate length. Agglomerate size has a strong dependency on wave structure frequency, there being a gradual decay in agglomerate length between 1 Hz and 40 Hz. Above 40 Hz particle agglomerates are small ($<100\mu$). Inertial effects become even more important above 60 Hz where motion is impeded. Particles are observed to form into very thin (1-4 particle diameters thick) hill-type structures (fig. 8-3,b). All motion at these frequencies occurs by particles skirmishing over the top of such hills; the area between these thin hills remains clean. This particle formation forms to minimize the reluctance in the region below the field structure. The dominant mode of operation at lower frequencies involves walking

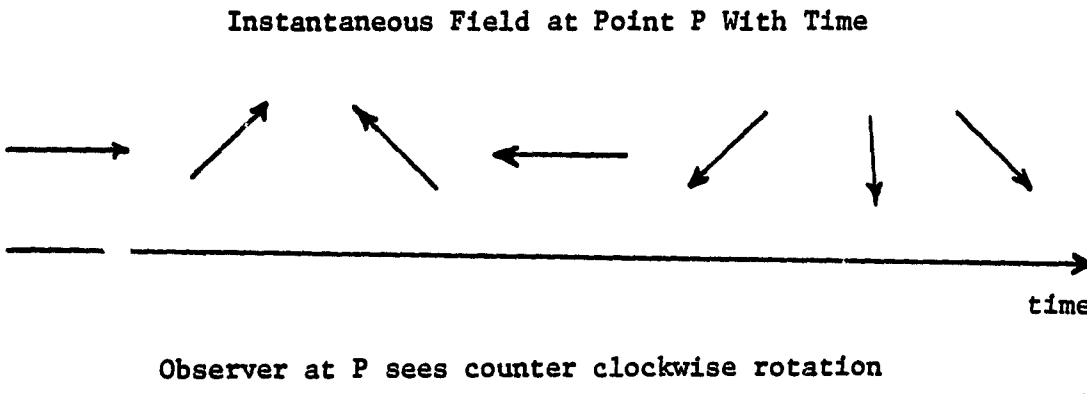
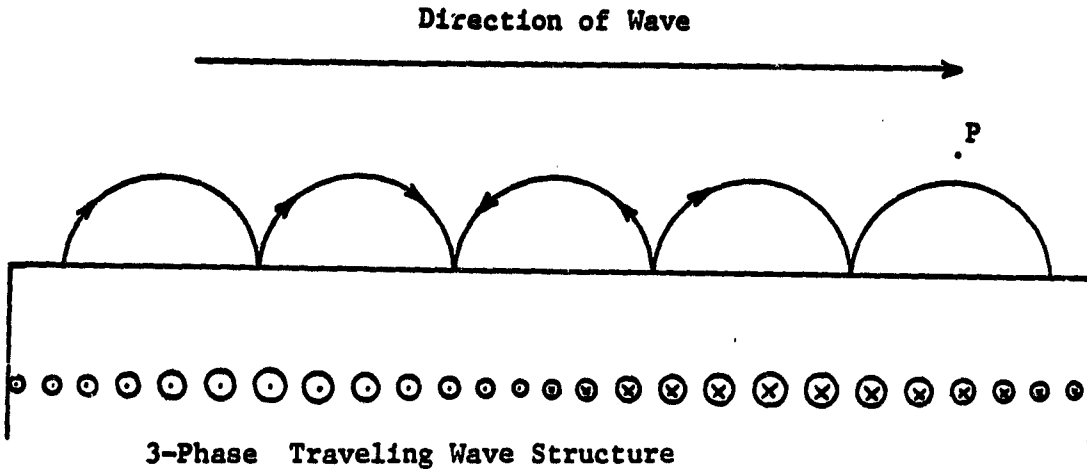


Figure 8-1 Circulating Field above Traveling Wave Structure

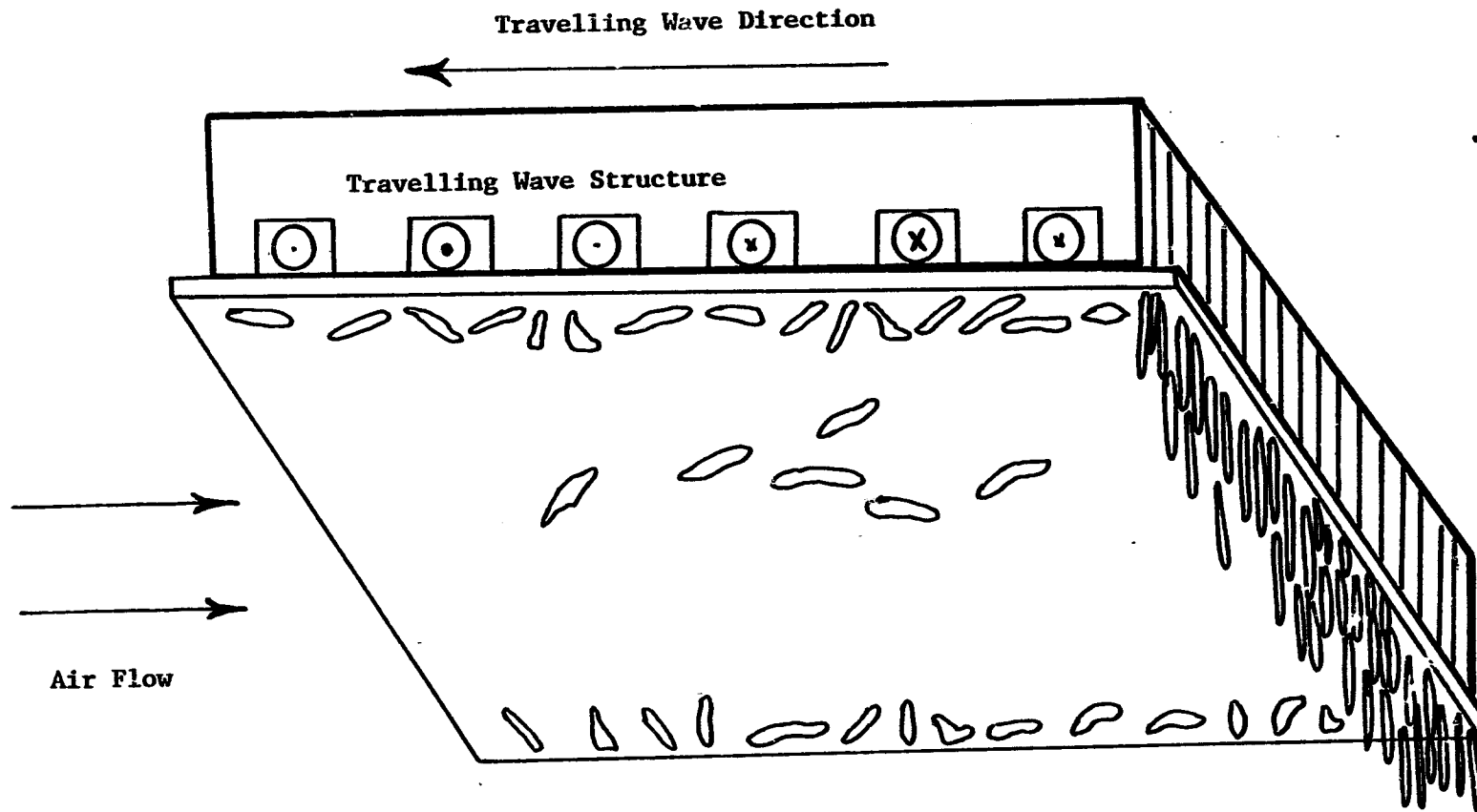
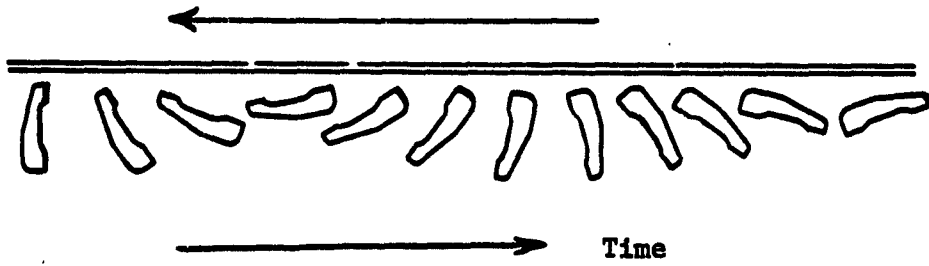
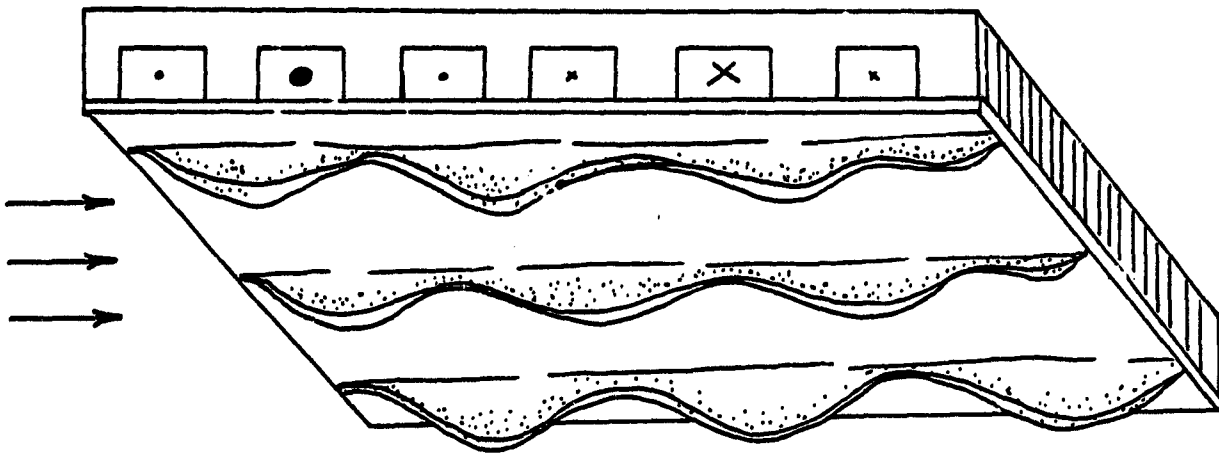


Figure 8-2 Instantaneous Picture of Agglomerates Under the Travelling Wave Structure in the Duct

Direction of Travelling wave



(a) Single Agglomerate Walking Motion ($f < 40$ Hz)



(b) Stationary Particle "hills" Formed above 60 Hz

Figure 8-3 Particle Formations

uniformly on the duct wall with a wave undulation moving opposite to the particle migration in the same direction as the travelling wave.

An alternative step for studying these effects is shown in fig. (8-4)*. A 4-pole, 3 phase synchronous stator now serves as the field structure. A cylindrical chamber with a rectangular plate of plexiglass suspended on pins serves as the secondary member. It is sealed and filled with water and a small amount of iron powder. A clockwise field causes the powder to circulate counter clockwise on the walls of the chamber. The powder drives the water by viscosity which in turn causes a rotation of the paddle. The experiment is especially suited to correlating particle speed with frequency. The speed was found to increase somewhat linearly with frequency up to 20 Hz (indicating that agglomerate length is a nonlinear inverse function of frequency, decreasing sharply after 20 Hz).

These effects indicate particle ducting via a travelling wave structure is feasible. The exact nature of drag reduction benefits obtainable from particles confined and shuffled in this manner is not clear. The particles do bounce and rotate along the surface and provide a mechanism for both transferring momentum from the wall to the flow or vice versa. This transfer can be coherent in the sense of tending to prolong a net circulation, but it appears that it could also function on the scale of the turbulent eddies. A longer interaction in the free stream flow might be obtainable by actually releasing the particles by using a standing, rather than travelling wave field. The consideration of particle loss may cause this mode of operation to be impractical. In any event, operation in either mode must be at a frequency less

*This experimental apparatus was built and studied by Ed Wooten, Massachusetts Institute of Technology.

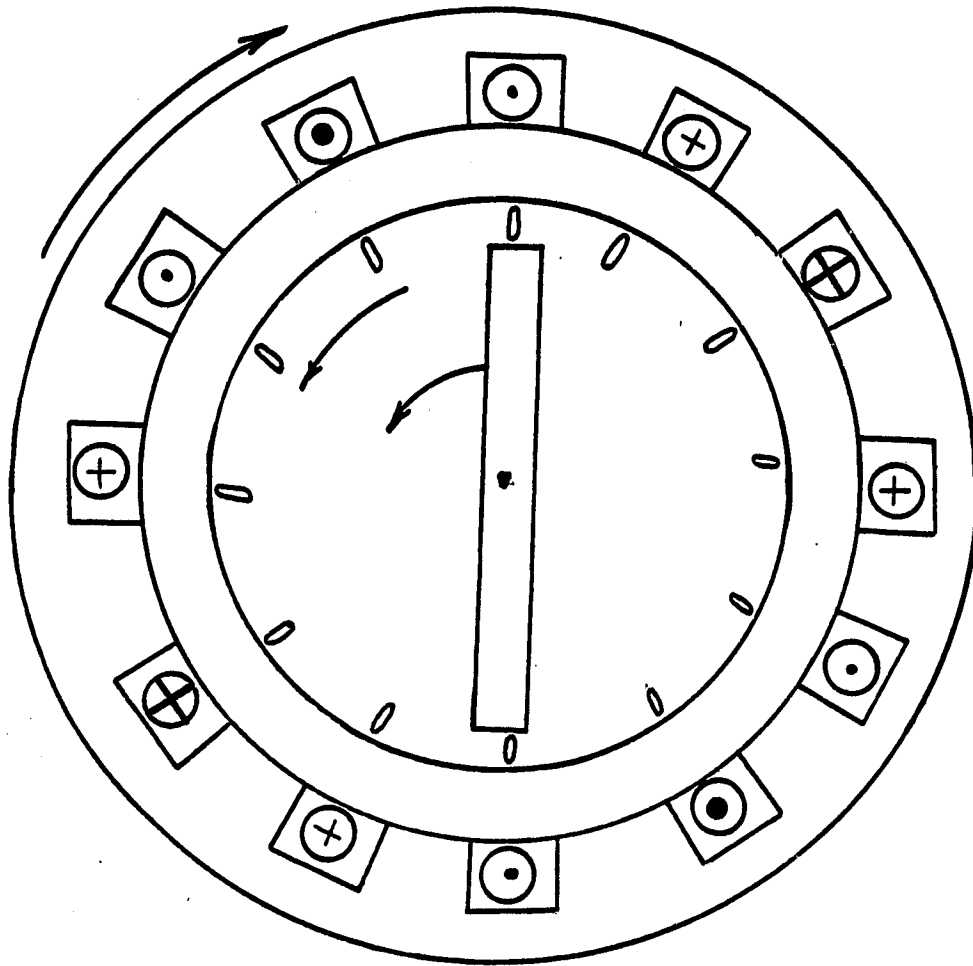


Figure 8-4 Cylindrical Wave Structure for Studying Particle Motions Without End Effects

than 60 Hz. This restriction necessitates the use of a long pole pitch if a travelling wave is used to synchronously (a distance 1/3 of the way into the boundary layer where the speed is roughly half the free stream speed) shuttle particles along the aircraft skin. A 500 MPH jet operating at 40 Hz would require a wave structure pole pitch

$$P = \frac{v}{2f} = \frac{1}{2} \frac{(500)(5280)}{(3600)(.0254)} = 1.4 \text{ m} \quad (8-1)$$

The results of this thesis are directly applicable to the design of a precipitator for capturing the particulate at the aircraft tail and shuttling it to the nose.

As energy needs expand, it may be desirable to apply this process to ships and underwater vessels. The travelling wave interaction could in fact be the basis for propulsion, perhaps with a reduction in hydrodynamic noise associated with conventional propulsion. The restriction on weight would not be as severe. The smaller difference in density between particulate and flow medium will be an advantage in terms of particle loss. The implantation of a travelling wave structure near the skin of the vessel should be an easier task as well.

C. Synopsis and Related Research

The thrust of this thesis centered on the prediction of magnetic particle ducting and precipitation in turbulent air flows. Towards this end two models were developed, one appropriate for light particles ($< 20\mu$) and the other for heavy particles ($> 20\mu$). The light particle model requires the solution of a diffusion equation with appropriate boundary conditions imposed where trajectories enter the duct volume. Inertial effects are unimportant. The heavy particle hybrid inertial-diffusion model represents the particle momentum balance in Lagrangian co-ordinates with an additional diffusion term added in by superposition. In both models, the effects of turbulent diffusion are lumped into a

measurable diffusivity constant. By means of correlation with experiments, both models have been shown to provide a useful degree of accuracy in predicting particle precipitation. Significant improvement over analytical models was shown in correlations with experimental data. This encouraged the application of the hybrid diffusion model to the problem of particle containment in the aerodynamic boundary layer. Results indicated about 4% of the injected particulate would be lost if permanent magnet collection were used in a boundary layer of typical aircraft. The analysis further revealed 90% of the particulate would be precipitated over a 4 to 6 meter length of the aircraft. Thus, unless it were reentrained in some manner of benefit to drag reduction, it also would be lost as a drag reducing agent.

The analysis indicated that to improve correlation of experiment with predictions, the three dimensional nature of the problem must be brought into the model. Specifically either the flow and field structure needed to be made wider, or the three dimensional considerations needed to be added to the model. Incorporation of variations of flow over the width of the channel and viscous effects of the side walls into the model would lead to higher precipitation predictions in both heavy and light particle analyses. Magnetic field edge effects which are a function wavelength should explain some wavelength trends observed. For application to precipitation technology, for example coal desulfurization, the consideration of small gradients around the tips of precipitated dendrite structures may be the most significant area for further study. The dependence of precipitation on loading would give a clue as to the magnitude of this effect.

The precipitation models should be of use to particle ducting studies in which loss of particulate is undesirable. The models developed should aid

researchers in particle augmented drag reduction since precipitation would normally be required simply to conserve particles.

The wind tunnel is quite useful for experimentally studying general drag reduction effects and in this context, the above research is directly applicable in collecting particulate.

Appendix A - Particle Magnetizable Spherical Particle

It is helpful in determining the nature of the magnetic force to consider the analogous polarized particle in an external electric field. The polarization originates from charges separated by a distance d (fig. A-1), and the force can be examined separately on the two charges, i.e.,

$$\vec{F} = 2E(\vec{r} + \vec{d}) = 2E(r) \quad (A-1)$$

Employing Taylor's expansion and assuming d small, (A-1) becomes

$$\vec{F} = 2(E(\vec{r}) + \vec{d} \cdot \nabla E) - 2E(\vec{r}) \quad (A-2)$$

or

$$\vec{F} = \vec{p} \cdot \nabla E \quad (A-3)$$

where \vec{p} is the particle polarization given by $2\vec{d}$. The material can be considered to have a number of dipoles per unit volume n_p . From equation (A-3), the force density \vec{F} is had by multiplying by n_p , i.e.,

$$\vec{F} = n_p \vec{p} \cdot \nabla E = \vec{P} \cdot \nabla E \quad (A-4)$$

The force on a magnetized particle now follows by analogy. No magnetic monopoles exist, but one can certainly examine magnetic dipoles and define \vec{M} as the number of magnetic dipoles \vec{m} per unit volume. Now the electric force of (A-4) can be obtained via energy arguments, i.e., by taking the gradient of energy of electric dipoles in an external electric field. It is legitimate to use the same energy arguments with magnetic dipoles and the result must be the same, i.e.,

$$\vec{F} = \mu_0 \vec{M} \cdot \nabla H \quad (A-5)$$

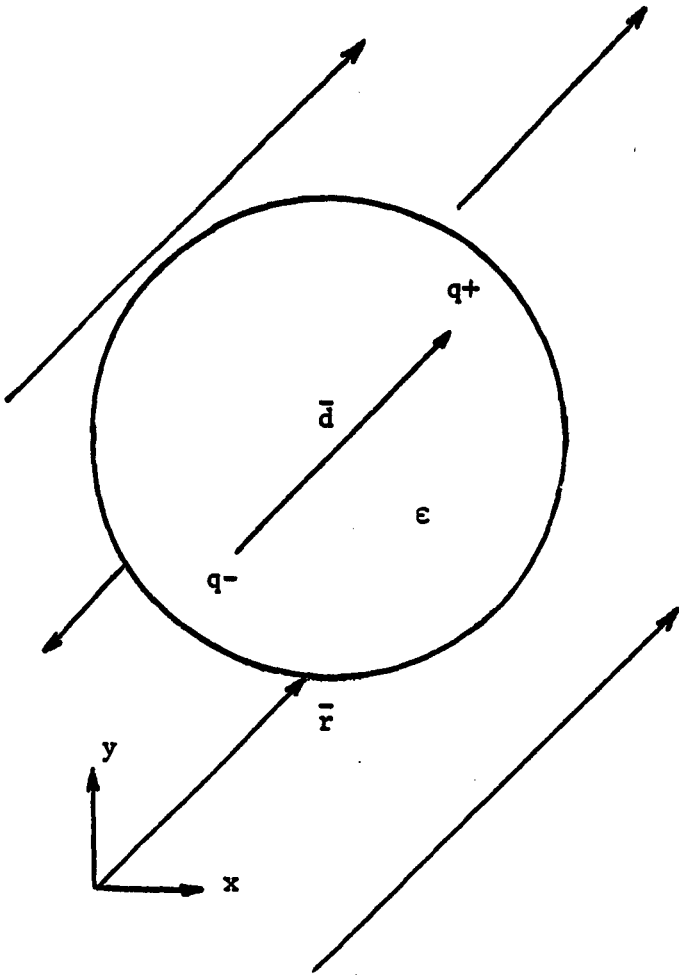
where the μ_0 comes in because of the historical definition of \vec{M}

$$(\nabla \cdot \mu_0 (\vec{M} + \vec{H}) = 0; \nabla \cdot (\epsilon_0 \vec{E} + \vec{P}) = \rho).$$

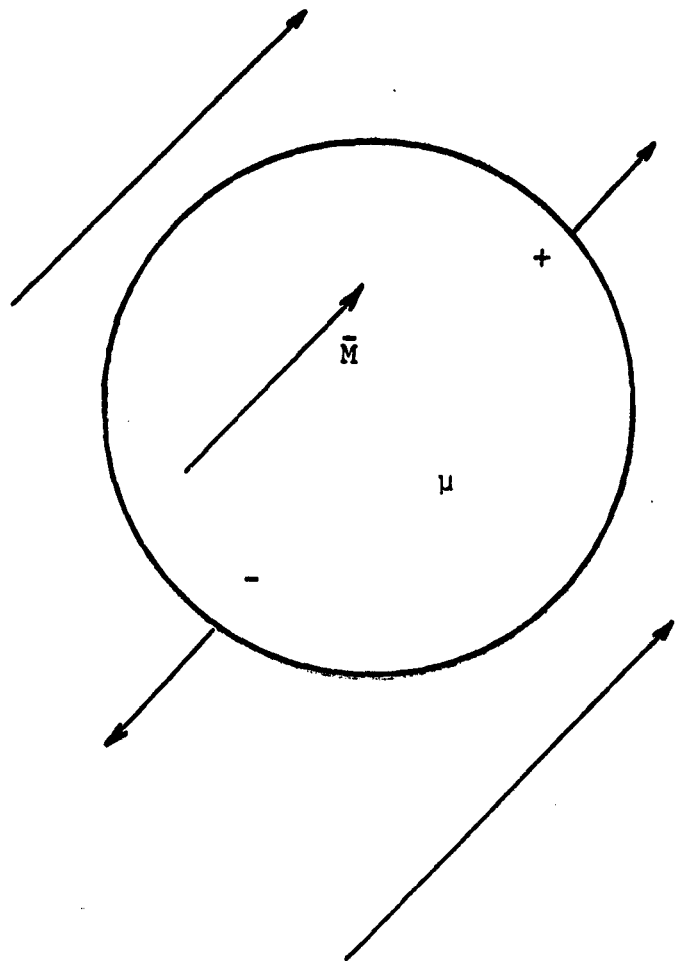
The requirement of a gradient in the external field is intuitively reasonable; there must exist a different field at either end of a particle (acting

$$\vec{F} = \vec{p} \cdot \nabla \vec{E}$$

$$\vec{F} = \mu_0 \vec{M} \cdot \nabla \vec{H}$$



(a) Polarized Particle



(b) Magnetized Particle

Figure A-1 Particle Magnetic Force

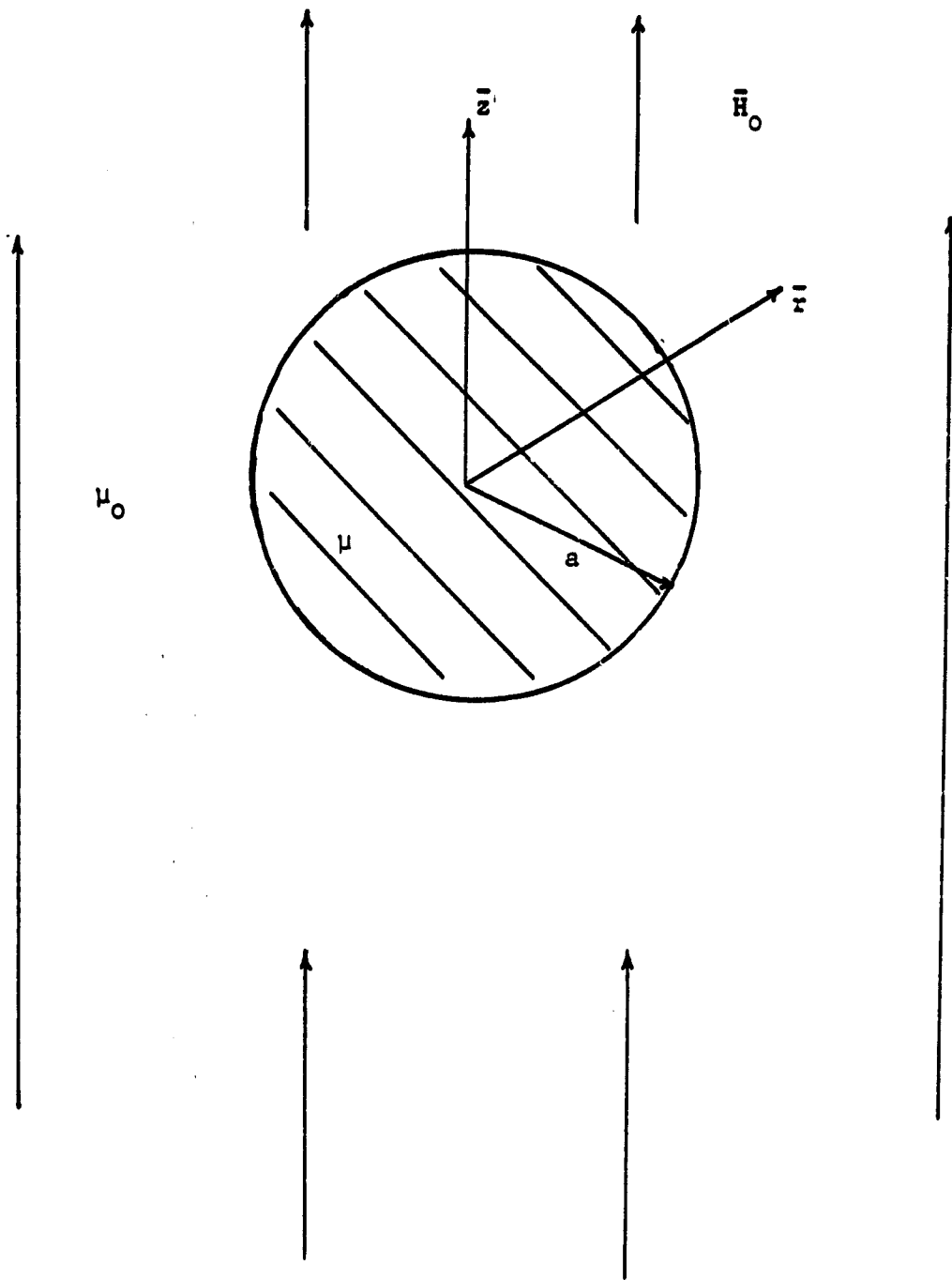


Figure A-2 Permeable Sphere in External Field

differently on the poles) to yield a net force.

To apply (A-5) in determining the force, it is necessary to examine the field internal to a highly permeable sphere in an external field H_0 (fig. A-2). For the external Z directed field H_0 and a particle of radius a, the scalar potential outside the sphere is represented as

$$\psi_o = -H_0 r \cos\theta + \frac{D}{r^2} \cos\theta \quad (A-6)$$

$$\psi_{in} = Ar \cos\theta \quad (A-7)$$

where $H = -\nabla\psi$

Matching tangential H and normal B at $r = a$ gives

$$D = H_0 a^3 \left(\frac{\frac{\mu}{\mu_0} - 1}{2 + \frac{\mu}{\mu_0}} \right)$$

$$A = -H_0 \left(\frac{3}{2 + \frac{\mu}{\mu_0}} \right) \quad (A-8)$$

In a linear permeable material, the magnetization \bar{M} and H are related as

$$\bar{M} = \left(\frac{\mu}{\mu_0} - 1 \right) H \quad (A-9)$$

Using (2-10) then, one finds \bar{M} to be

$$\bar{M} = \left(\frac{3}{2 + \frac{\mu}{\mu_0}} \right) \left(\frac{\mu}{\mu_0} - 1 \right) H_0 \quad (A-10)$$

With (2-5) and the fact that the particle force is obtained by multiplying by the volume, one finds that

$$F = \frac{4}{3} \pi a^3 \left(\frac{3}{2 + \frac{\mu}{\mu_0}} \right) \left(\frac{\mu}{\mu_0} - 1 \right) \mu_0 \frac{1}{2} \nabla (\mathbf{H} \cdot \mathbf{H})$$

or

$$F = \alpha' \nabla (\mathbf{H} \cdot \mathbf{H}) \tag{A-11}$$

Here the \mathbf{H} due to magnetization has been brought inside the gradient. It should be emphasized that the \mathbf{H} in (A-11) is the external field only.

Appendix B - Refinement of Basic Precipitation Models

The refined models and laminar flow test calculation are developed from the results of chapter 2, section C. The easiest model to refine is the Deutch model for a turbulent, fully mixed flow. The model posed thus far incorporated migration due to magnetic force only. Adding gravitational migration for particles with mass m (2-21) to

$$\frac{1}{n} \frac{dn}{dx} = \frac{mg}{(2a)U\beta} - \frac{\alpha k e^{-2ky}}{U\beta(2a)} \quad (B-1)$$

The solution of (C-1) again gives an exponential fall for the density. Since precipitation occurs at $y = 0$, the density becomes

$$\frac{n}{n_0} = \exp - \left(\frac{x-x_0}{2aU \frac{(mg + \alpha k)}{\beta}} \right) \quad (B-2)$$

Two additions to the particle trajectory laminar flow are in order. The first is the inclusion of the gravitational migration. The second deals with the replacement of the assumed uniform air velocity plug flow with the

characteristic turbulent flow profile ($\bar{U} = U_0 \left(\frac{y}{a} \right)^{\frac{1}{9}} \bar{i}_x$). The net particle flux now contains a more accurate convective term along with two migration terms.

$$\bar{\Gamma} = \bar{U} n \bar{i}_x - \frac{mgn \bar{i}_y}{\beta} - \frac{\alpha k e^{-2ky}}{\beta} n \bar{i}_y \quad (B-3)$$

Following the procedure above of taking the divergence of $\bar{\Gamma}$ gives

$$\frac{\partial n}{\partial t} + U_0 \frac{y}{a}^{\frac{1}{9}} \bar{i}_x - \frac{mgn \bar{i}_y}{\beta} + \left(\frac{\alpha \nabla \cdot \nabla (\bar{H} \cdot \bar{H})}{\beta} \right) \cdot \nabla n = - \frac{\alpha \nabla \cdot \nabla (\bar{H} \cdot \bar{H})}{\beta} n \quad (B-4)$$

or in the particle's frame,

$$\frac{dn}{dt} = -\alpha' \frac{\nabla \cdot \nabla (\mathbf{H} \cdot \mathbf{H})}{\beta} n$$

along

$$\frac{d\vec{r}}{dt} = U_0 \left(\frac{\gamma}{a} \right)^{\frac{1}{g}} \vec{i}_x - \frac{mg}{\beta} \vec{i}_y + \alpha' \nabla (\mathbf{H} \cdot \mathbf{H}) \quad (\text{B-5})$$

As in the previous study it is noted that if the force field is not divergence-free, $(\nabla \cdot (\nabla \mathbf{H} \cdot \mathbf{H}) \neq 0)$, the density is not constant along a trajectory line.

For a single harmonic sinusoidal field (C-5) becomes

$$\frac{dn}{dt} = \frac{-2\alpha k^2 e^{-2ky}}{\beta} n$$

$$\text{along } \frac{d\vec{r}}{dt} = U_0 \left(\frac{\gamma}{a} \right)^{\frac{1}{g}} \vec{i}_x - \frac{mg \vec{i}_y}{\beta} - \frac{\alpha k e^{-2ky}}{\beta} \vec{i}_y \quad (\text{B-6})$$

The particle trajectory dependence is (C-5, b) as before. The vertical trajectory's dependence on time can be found by integration immediately as

$$\beta \frac{(y-y_0)}{mg} + \frac{\beta}{2kmg} \ln \left(\frac{mg + \alpha k e^{-2ky}}{mg + \alpha k e^{-2ky_0}} \right) = t \quad (\text{B-7})$$

It is not as fruitful to seek the trajectory and density time dependence in this refined model, but is more convenient to solve for the x - y trajectory character and then to find the density dependence on a space dimension. Towards this end, dt can be eliminated from the two equations in (2-25,b) to give

$$\frac{dx}{dy} = \frac{U_0 \left(\frac{\gamma}{a} \right)^{\frac{1}{g}}}{-\frac{mg}{\beta} - \frac{\alpha k}{\beta} e^{-2ky}} \quad (\text{B-8})$$

The density y dependence is obtained by substituting for dt its equivalent in terms of dy from (2,25,b), i.e.,

$$dt = \frac{dy}{\frac{-mg}{\beta} - \frac{\alpha ke^{-2ky}}{\beta}} \quad (B-9)$$

and thus

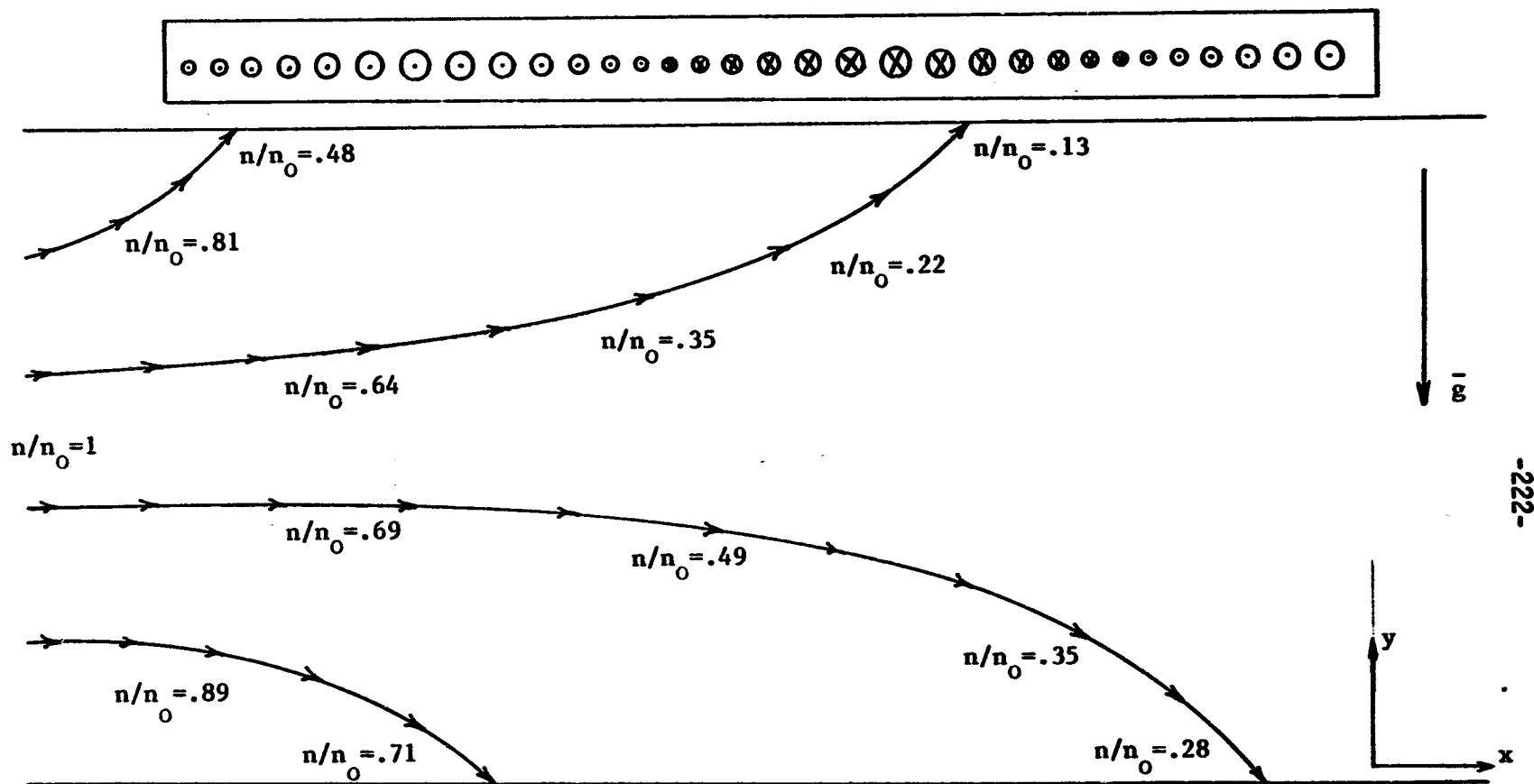
$$\frac{dn}{dy} = \frac{2\alpha k^2 e^{-2ky} n dy}{mg + \alpha ke^{-2ky}} \quad (B-10)$$

It follows from (2-41) that

$$\frac{n}{n_0} = \ln \left(\frac{mg + \alpha ke^{-2ky_0}}{mg + \alpha ke^{-2ky}} \right) \quad (B-11)$$

For any starting position y_0 , the density upon impact at $y=0$ follows directly. The particle's trajectory follows by numerically integrating (C-9). The program KDTRAG (Appendix C) uses a forward Eulerian integration, stepping y from y_0 to the duct wall at $y=0$. Fig. (B-1) shows typical trajectories of iron particles where the magnetic migration is upward. The calculation for these profiles assumed the particle size and magnetic field were such that the magnetic force balanced gravitational force midway up the duct. The increased downward curvature of the gravitationally dominated trajectory lines near $y=0$ reflect the convective $(\frac{y}{a})^{\frac{1}{9}}$ dependence. The magnetically dominated trajectories exhibit an even greater curvature (upward) due to the exponential field dependence.

3 Phase Traveling Wave Structure



-222-

Figure B-1 Particle Trajectories with Upward Magnetic Migration

Appendix C - KDDTRAG

This program calculates particle trajectories according to the refined inertia-free model developed in appendix B. X and Y represent the particle's axial and vertical position respectively, while n represents particle density. The program is in basic.

```
10 DIM YO(3),X0(3),N(3),Y(3,100),X(3,100),J9(3)
12 PRINT 'THIS PROGRAM COMPUTES INERTIAL FLOW TRAJECTORIES'
13 PRINT 'FOR SINGLE HARMONIC B--UO(1/9),B,AND GRAVITY '
14 PRINT 'T-GRAV,T-IN,MAG ,T-RES, K FOLLOW'
15 INPUT G1,M1,R1,K \ PRINT G1,M1,R1,K
20 D2=.1 \ D3=.01
30 FOR I=1 TO 2
35 YO(1)=.4252 \ YO(2)=.315 \ X(I,0)=0
40 FOR J=0 TO 400
50 Y(I,J+1)=YO(I)-J*D3
55 IF Y(I,J+1)<1.00000E-03 GO TO 85
60 U=G1/R1*(2*(1-Y(I,J+1)))^.111111
65 IF Y(I,J+1)<.5 THEN U=G1/R1*(2*Y(I,J+1))^-.111111
70 F=U/(1+G1/M1*EXP(-2*K*Y(I,J+1)))*D3
75 IF J=0 THEN F=F*.5
80 X(I,J+1)=X(I,J)+F \ NEXT J
85 N(I)=(1+G1/M1*EXP(-2*K*YO(I)))/(1+G1/M1)
88 J9(I)=J
90 X0(I)=X(I,J) \ NEXT I
93 PRINT 'THE YO,X0, N FOLLOW'
95 FOR I=1 TO 2
100 PRINT YO(I);X0(I);N(I), \ NEXT I \ PRINT
105 INPUT H1 \ PRINT 'THE X,Y TRAJECTORIES FOLLOW'
110 FOR I=1 TO 2
120 FOR J=1 TO J9(I)
125 PRINT X(I,J);Y(I,J), \ NEXT J \ PRINT
130 INPUT H2 \ NEXT I
135 STOP
```

Appendix D - Analytical Diffusion Analysis

The point of this analysis is to determine the nature of the density gradient at a boundary separating regions at high and low diffusivity. Figure (D-1) shows the problem considered here, two thin layer regions of small diffusivity d and thickness δ separated by a large core region of diffusivity D and thickness $(2a-2\delta)$. Only gravitational migration exists and no x dependence is considered. Injection of particulate occurs at the upper wall and the boundary conditions are $n = n_0$ at $y = 2a$ and $n = 0$ at $y = 0$ (perfectly absorbing lower wall).

The flux in region 1 is

$$\Gamma_y = -d \frac{\partial n}{\partial y} - \frac{mg}{\beta} n \quad (D-1)$$

In the steady state with $\frac{\partial n}{\partial t} = 0$,

$$-d \frac{\partial^2 n}{\partial y^2} - \frac{mg}{\beta} \frac{\partial n}{\partial y} = 0 \quad (D-2)$$

The same equations apply to region 2 with $d \rightarrow D$. Normalizing to the duct width, we have

$$\begin{aligned} \chi &= \frac{y}{2a} \\ \frac{(2a)^2}{d} &= \tau_d \quad (D-3) \\ \frac{(2a)^2}{D} &= \tau_D \\ \frac{2a}{\frac{mg}{\beta}} &= \tau_g \\ \underline{n} &= \frac{n}{n_0} \end{aligned}$$

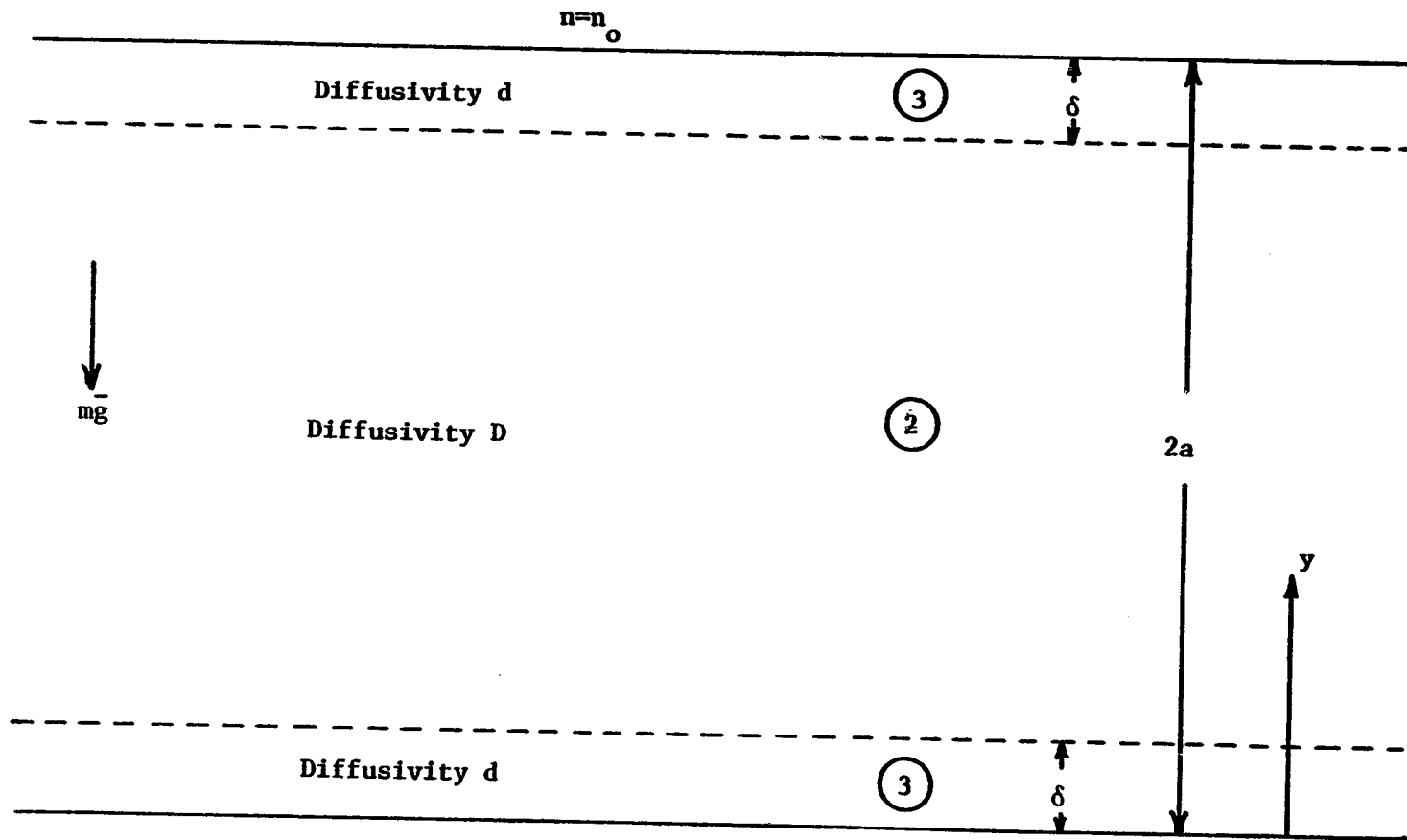


Figure D-1 Analytical Diffusion Study Model

(D-2) becomes

$$\frac{\partial^2 \underline{n}}{\partial y^2} + \frac{\tau_d}{\tau_g} \frac{\partial \underline{n}}{\partial \underline{y}} = 0 \quad (D-4)$$

The general solution of (D-4) is

$$\underline{n} = c_1 + c_2 e^{-\frac{\tau_d}{\tau_g} \underline{y}} \quad (D-5)$$

With the boundary condition $\underline{n} = 0$ at $\underline{y} = 0$, we have

$$\underline{n}_1 = c_1 \left\{ 1 - e^{-\frac{\tau_d}{\tau_g} \underline{y}} \right\} \quad (D-6)$$

Similarly for region 2, the density is

$$n_2 = c_3 + c_4 e^{\left(\frac{\tau_D}{\tau_g} \underline{y} \right)} \quad (D-7)$$

Imposing the condition of continuity of particle density and flux at $\underline{y} = \frac{\delta}{2a} = \underline{\delta}$ determines \underline{n}_2 to be

$$\underline{n}_2 = c_1 \left(1 - e^{\left(\frac{\tau_D - \tau_d}{\tau_g} \underline{\delta} \right)} \right) \left(e^{\frac{\tau_D}{\tau_g} \underline{y}} \right) \quad (D-8)$$

Finally in region 3, we have a characteristic density

$$\underline{n}_3 = c_5 + c_6 e^{-\frac{\tau_d}{\tau_g} \underline{y}} \quad (D-9)$$

and the boundary conditions $n = 1$ at $\underline{y} = 1$ and continuity of density and flux at $\underline{y} = (1-d)$. Combining (D-6), (D-8), and (D-9) with these conditions yields the densities for each region as

$$\begin{aligned} \underline{n}_1 &= n_0 \left(1 - e^{-\frac{\tau_d}{\tau_g} \underline{y}} \right) \\ \underline{n}_2 &= n_0 \left[1 - e^{-\left(\frac{\tau_d}{\tau_g} \underline{\delta}\right)} \right] \left[e^{-\left(\frac{\tau_D}{\tau_g} (\underline{y} - \underline{\delta})\right)} \right] \\ \underline{n}_3 &= n_0 \left[1 - e^{-\left(\frac{\tau_D}{\tau_g} (1-2\underline{\delta})\right)} \right] \left[e^{-\left(\frac{\tau_d}{\tau_g} (\underline{y} - (1-2\underline{\delta}))\right)} \right] \end{aligned}$$

where

$$n_0 = \frac{1}{1 - \left(e^{-\frac{\tau_D}{\tau_g} (1-2\underline{\delta})} \right) \left(e^{-\frac{\tau_d}{\tau_g} \underline{\delta}} \right)} \quad (D-10)$$

Figure (D-2) shows a typical density profile for this problem assuming $D \gg d$. The ratio of density gradient in the core region to the boundary layer region at $\underline{y} = \underline{\delta}$ or $1-\underline{\delta}$ is found straight away from (D-10). The result is

$$\left. \frac{\partial n}{\partial y} \right|_{\text{region 2}} = \frac{\tau_D}{\tau_d} \left. \frac{\partial n}{\partial y} \right|_{\text{region 1, } \underline{y}=\underline{\delta}} \quad \text{or} \quad \left. \frac{\partial n}{\partial y} \right|_{\text{region 3, } \underline{y}=1-\underline{\delta}} \quad (D-11)$$

Thus, for small diffusivity d , the density gradient is nearly zero in the core. This is explicitly shown for the two curves with $\frac{\tau_D}{\tau_g} = \frac{1}{10}$. The dashed curve with $\frac{\tau_D}{\tau_d} = \frac{1}{100}$ displays a sharp vertical slope at $y=\delta$. Also the effect of smaller core diffusivity is seen to squeeze all the particulate into the lower layer.

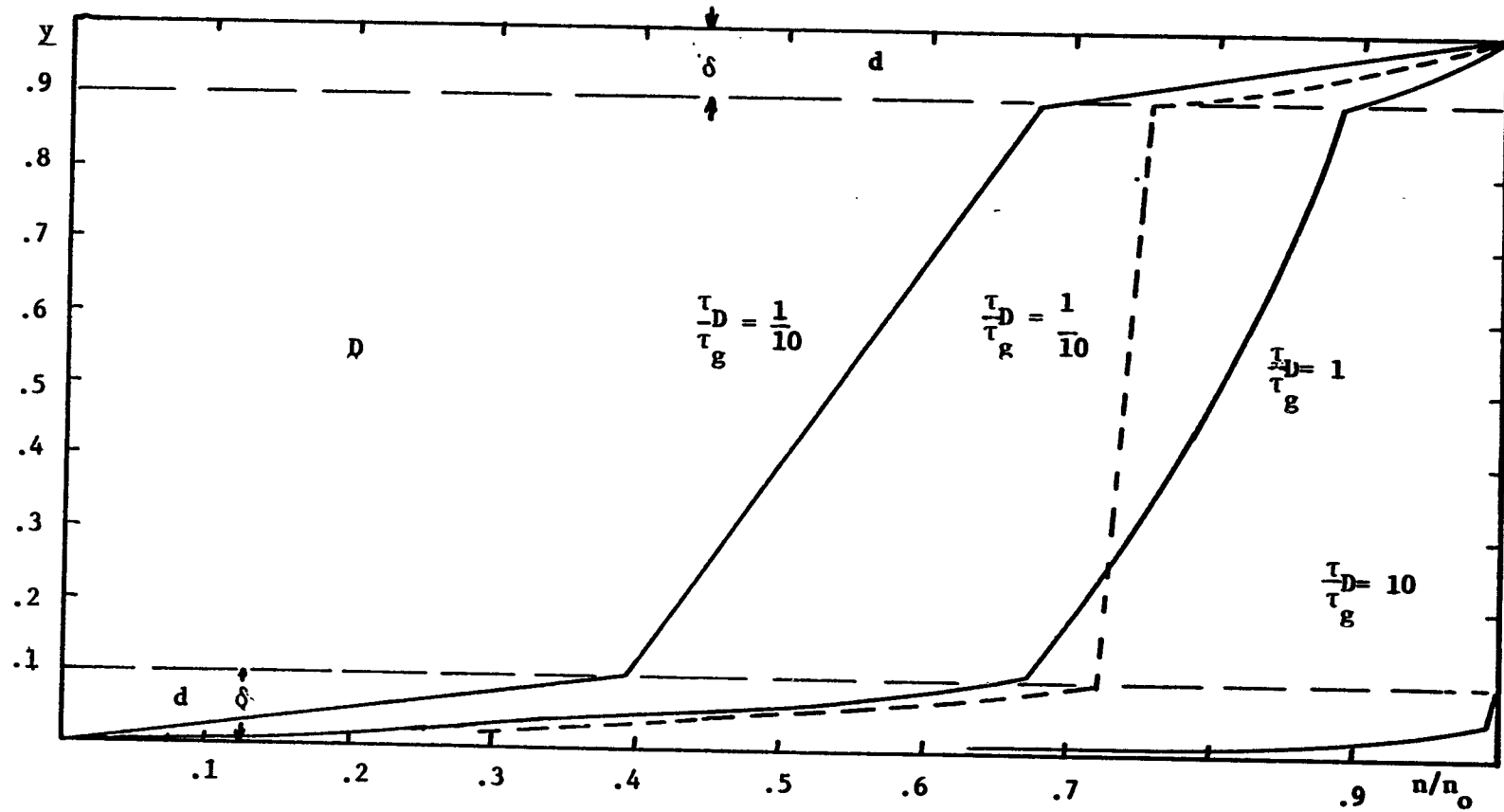


Figure D-2 Typical Density Profiles; solid- $\frac{\tau_d}{\tau_D} = 10$, dash- $\frac{\tau_d}{\tau_D} = 100$

These fortran programs calculate particle density and deposition according to the approximate diffusion model presented in chapter 4-B. KDDI4 imposes the boundary condition $n=0$ on the upper boundary, while KDDI9 uses a zero density gradient condition there.

KDDI4

```
C
C CALCULATION OF DUCT CONCENTRATION PROFILE
C SMALL PARTICLE TURBULENT DIFFUSION CASE
C
      DIMENSION B(10,80),X(80),AN(80),BO(16),AM(10),U(10),AMK(10)
      COMMON AK,BO,U1,AMMU,NHARM,DLTUB
      WRITE(5,5)
      5 FORMAT(' THE NUMBER OF ROWS AND COLUMNS ARE ')
      READ(5,10)IROW,ICOL
      10 FORMAT(2I5)
      WRITE(5,15)IROW,ICOL
      15 FORMAT(2I5,/, ' INPUT VARIABLES G1,AK,XB,AMMU,DLXMS,XMAG,DLTUB ')
      READ(5,20)G1,AK,XB,AMMU,DLXMS,XMAG,DLTUB
      20 FORMAT(F15.2)
      WRITE(5,25)G1,AK,XB,AMMU,DLXMS,XMAG,DLTUB
      25 FORMAT(' THE INPUTS G1,AK,XB,AMMU,DLXMS,XMAG,DLTUB ARE ',/6F10.4)
      READ(5,23)AH1
      23 FORMAT(F10.2)
      WRITE(5,16)
      16 FORMAT(' THE # OF HARMONICS AND THE NORMALIZED B-FIELDS '//
      1 FOLLOW--B(N)=^H**2*Q*K/b/(D/2a)')
      READ(5,10)NHARM
      READ(5,20)(BO(I),I=1,NHARM)
      WRITE(5,17)(BO(I),I=1,NHARM)
      17 FORMAT(8F10.5)
      DLX = 1./(ICOL+1.)
      W=12.7
      DLY = (1.-2.*DLTUB/W)/IROW
      U1=.5968/XB
      YU=1.-DLY-DLTUB/W
      XPOS=XMAG + DLX*XB
      CALL DT2A(XPOS,DT)
      CALL UOAM(YU,U2,AM2,AMK2)
      U(1)=U2
      AM(1)=AM2
      AMK(1)=AMK2
```

```
G2=G1/DT
AM2=AM2/DT
AMK2=AMK2/DT
U2=U2/DT
B(1,1)=1.-DLX/U2*(AMK2+(G2+AM2)/2/DLY+1./DLY**2)
DO 30 I=2,IROW
YU=1.-DLY*I-DLTUB/W
CALL UOAM(YU,U2,AM2,AMK2)
U(I)=U2
AM(I)=AM2
AMK(I)=AMK2
AM2=AM2/DT
AMK2=AMK2/DT
U2=U2/DT
B(I,1)=1.-DLX/U2*AMK2
30 CONTINUE
DO 50 J=2,ICOL
XPOS=XMAG + J*DLX*XB
CALL DT2A(XPOS,DT)
DO 45 I=1,IROW
G2=G1/DT
AM2=AM(I)/DT
AMK2=AMK(I)/DT
U2=U(I)/DT
IF(I.GT.1.AND.I.LT.IROW)B(I,J)=B(I,J-1) + DLX/U2*(
1 -AMK2*B(I,J-1)+(G2+AM2)*(B(I-1,J-1)-B(I+1,J-1))/2/DLY
2 +(B(I-1,J-1)+B(I+1,J-1)-2*B(I,J-1))/DLY**2)
IF(I.EQ.1) B(I,J)=B(I,J-1) +DLX/U2*(-AMK2*B(I,J-1) -
1 (G2+AM2)*B(I+1,J-1)/2/DLY+(B(I+1,J-1)-2*B(I,J-1))/DLY**2)
IF(I.EQ.IROW)B(I,J)=B(I,J-1)+DLX/U2*(-AMK2*B(I,J-1)
1 +(2*B(I-1,J-1) - 2.*B(I,J-1))/DLY**2)
45 CONTINUE
50 CONTINUE
DO 111 J=1,ICOL,10
WRITE(5,90)(I,I=1,10),J
90 FORMAT(' THE DENSITIES ARE AS FOLLOWS',/,3X,I1,9(6X,I2),
1 /,' THE FIRST COLUMN IS',I3)
JJ=J+9
IF(JJ.GT.ICOL)JJ=ICOL
DO 108 I=1,IROW
WRITE(5,100)(B(I,JJJ),JJJ=J,JJ)
100 FORMAT(10F8.4)
108 CONTINUE
READ(5,110)AH3
110 FORMAT(F10.2)
111 CONTINUE
YU = DLTUB/W
DLYO = YU/10.
CALL UOAM(YU,U2,AM2,AMK2)
AMO=AM2
SUM=.5*U2/(G1+AM2)
DO 115 J=1,9
YU=YU-DLYO
CALL UOAM(YU,U2,AM2,AMK2)
```

REPRODUCIBILITY OF THE
ORIGINAL PAGE IS POOR

```
115 SUM=SUM+U2/(G1+AM2)
CONTINUE
SUM=SUM*DLYO
WRITE(5,110)SUM
CALL UOAM(0.,U2,AM2,AMK2)
DO 120 J=1,ICOL
AN(J)=B(IROW,J)*(G1+AM0)/(G1+AM2)*DLXMS
X(J)=(DLX*J+SUM)*XB
120 CONTINUE
WRITE(5,125)(X(I),AN(I),I=1,ICOL,3)
125 FORMAT(4E15.4)
STOP
END
SUBROUTINE UOAM(YU,U,AM,AMK)
DIMENSION BO(16)
COMMON AK,BO,U1,AMMV,NHARM,DLTUB
Y=YU
IF(YU.GT..5)Y=1.-Y
U=U1*(2.*Y)**.1111111
AM=0.
DO 15 I=1,NHARM
P=2.*I*AK*YU
IF(P.GT.20.)GO TO 15
AM=AM+AMMV*BO(I)**2*I*EXP(-P)
15 CONTINUE
IF(YU.LT.DLTUB/12.7)GO TO 30
AMK=0.
DO 25 I=1,NHARM
P=2.*I*AK*YU
IF(P.GT.20.)GO TO 25
AMK=AMK+2.*I**2*AMMV*BO(I)**2*AK*EXP(-P)
25 CONTINUE
30 RETURN
END
SUBROUTINE DT2A(X,DT)
DX=.1524
IF(X.LT.DX)DT=.003625
XE1=2.*DX
IF(X.GE.DX.AND.X.LT.XE1)DT=.003625+.020915*(X-DX)/DX
IF(X.GE.1.33985)DT=.00178
IF(X.LT.XE1.OR.X.GE.1.33985) GO TO 50
DT=.054658-.150851*X+.201784*X**2-.084262*X**3-.07902*
1 X**4+.028938*X**5+.065659*X**6-.033616*X**7
50 DT=DT/.127
RETURN
END
```

KDDI9

C
C CALCULATION OF DUCT CONCENTRATION PROFILE
C SMALL PARTICLE TURBULENT DIFFUSION CASE
C CHANGE UPPER BOUNDARY CONDITION
C

```
      DIMENSION B(10,80),X(80),AN(80),BO(16),AM(10),U(10),AMK(10)
      COMMON AK,BO,U1,AMMU,NHARM
      WRITE(5,5)
      5 FORMAT(' THE NUMBER OF ROWS AND COLUMNS ARE')
      READ(5,10)IROW,ICOL
      10  FORMAT(2I5)
      WRITE(5,15)IROW,ICOL
      15  FORMAT(2I5,/, ' THE INPUT VARIABLES G1,AK,XB,AMMU,DLXMS,XMAG ARE')
      READ(5,20)G1,AK,XB,AMMU,DLXMS,XMAG
      20  FORMAT(F15.2)
      WRITE(5,25)G1,AK,XB,AMMU,DLXMS,XMAG
      25  FORMAT(' THE INPUTS G1,AK,XB,AMMU,DLXMS,XMAG ARE',/6F10.4)
      READ(5,23)AH1
      23  FORMAT(F10.2)
      WRITE(5,16)
      16  FORMAT(' THE # OF HARMONICS AND THE NORMALIZED B-FIELDS'/'
      1  FOLLOW--B(N)='H**2*Q*K/b/(D/2a)')
      READ(5,10)NHARM
      READ(5,20)(BO(I),I=1,NHARM)
      WRITE(5,17)(BO(I),I=1,NHARM)
      17  FORMAT(8F10.5)
      DLX = 1./(ICOL+1.)
      W=12.7
      DLY = (1.-1./W)/(IROW-1.)
      U1=.5968/XB
      YU=1.-.5/W
      XPOS=XMAG + DLX*XB
      CALL DT2A(XPOS,DT)
      CALL UOAM(YU,U2,AM2,AMK2)
      U(1)=U2
      AM(1)=AM2
      AMK(1)=AMK2
      G2=G1/DT
      AM2=AM2/DT
      AMK2=AMK2/DT
      U2=U2/DT
      B(1,1)=1.-DLX/U2*(AMK2)
      DO 30 I=2,IROW
      YU=1.-DLY*(I-1.)-.5/W
      CALL UOAM(YU,U2,AM2,AMK2)
      U(I)=U2
      AM(I)=AM2
      AMK(I)=AMK2
      AM2=AM2/DT
      AMK2=AMK2/DT
```

```
U2=U2/DT
B(I,1)=1.-DLX/U2*AMK2
30 CONTINUE
DO 50 J=2,ICOL
XPOS=XMAG + J*DLX*XB
CALL DT2A(XPOS,DT)
DO 45 I=1,IROW
G2=G1/DT
AM2=AM(I)/DT
AMK2=AMK(I)/DT
U2=U(I)/DT
IF(I.GT.1.AND.I.LT.IROW)B(I,J)=B(I,J-1) + DLX/U2*(
1 -AMK2*B(I,J-1)+(G2+AM2)*(B(I-1,J-1)-B(I+1,J-1))/2/DLY
2 +(B(I-1,J-1)+B(I+1,J-1)-2*B(I,J-1))/DLY**2)
IF(I.EQ.1) B(I,J)=B(I,J-1) +DLX/U2*(-AMK2*B(I,J-1)
1 +(2*B(I+1,J-1)-2.*B(I,J-1))/DLY**2)
IF(I.EQ.IROW)B(I,J)=B(I,J-1)+DLX/U2*(-AMK2*B(I,J-1)
1 +(2*B(I-1,J-1) - 2.*B(I,J-1))/DLY**2)
45 CONTINUE
50 CONTINUE
DO 111 J=1,ICOL,10
WRITE(5,90)(I,I=1,10),J
90 FORMAT(' THE DENSITIES ARE AS FOLLOWS',/,3X,I1,9(6X,I2),
1 /,' THE FIRST COLUMN IS',I3)
JJ=J+9
IF(JJ.GT.ICOL)JJ=ICOL
DO 108 I=1,IROW
WRITE(5,100)(B(I,JJJ),JJJ=J,JJ)
100 FORMAT(10F8.4)
108 CONTINUE
READ(5,110)AH3
110 FORMAT(F10.2)
111 CONTINUE
YU = .5/W
DLYO = YU/10.
CALL UOAM(YU,U2,AM2,AMK2)
AMO=AM2
SUM=.5*U2/(G1+AM2)
DO 115 J=1,9
YU=YU-DLYO
CALL UOAM(YU,U2,AM2,AMK2)
SUM=SUM+U2/(G1+AM2)
115 CONTINUE
SUM=SUM*DLYO
WRITE(5,110)SUM
CALL UOAM(0.,U2,AM2,AMK2)
DO 120 J=1,ICOL
AN(J)=B(IROW,J)*(G1+AMO)/(G1+AM2)*DLXMS
X(J)=(DLX*J+SUM)*XB
120 CONTINUE
WRITE(5,125)(X(I),AN(I),I=1,ICOL,3)
125 FORMAT(4E15.4)
STOP
END
```

REPRODUCIBILITY OF THE
ORIGINAL PAGE IS POOR

```
SUBROUTINE UOAM(YU,U,AM,AMK)
DIMENSION BO(16)
COMMON AK,BO,U1,AMMU,NHARM
Y=Yu
IF(YU.GT..5)Y=1.-Y
U=U1*(2.*Y)**.1111111
AM=0.
DO 15 I=1,NHARM
P=2.*I*AK*YU
IF(P.GT.20.)GO TO 15
AM=AM+AMMU*BO(I)**2*I*EXP(-P)
15 CONTINUE
IF(YU.LT..5/12.7)GO TO 30
AMK=0.
DO 25 I=1,NHARM
P=2.*I*AK*YU
IF(P.GT.20.)GO TO 25
AMK=AMK+2.*I**2*AMMU*BO(I)**2*AK*EXP(-P)
25 CONTINUE
30 RETURN
END
SUBROUTINE DT2A(X,DT)
DX=.1524
IF(X.LT.DX)DT=.003625
XE1=2.*DX
IF(X.GE.DX.AND.X.LT.XE1)DT=.003625+.020915*(X-DX)/DX
IF(X.GE.1.33985)DT=.00178
IF(X.LT.XE1.OR.X.GE.1.33985) GO TO 50
DT=.054658-.150851*X+.201784*X**2-.084262*X**3-.07902*
1 X**4+.028938*X**5+.065659*X**6-.033616*X**7
50 DT=DT/.127
RETURN
END
```

REPRODUCIBILITY OF THE
ORIGINAL PAGE IS POOR

Appendix F- KDDF2

This fortran program calculates particle densities and particulate deposition according to the refined small particle diffusion analysis discussed in chapter 4-B. The exact diffusivity X-Y dependence, vertical densities are solved simultaneously, and space derivatives consistent with causality are used.

REPRODUCIBILITY OF THE ORIGINAL PAGE IS POOR

KDDF2

```
C
C CALCULATION OF DUCT CONCENTRATION PROFILE
C SMALL PARTICLE TURBULENT DIFFUSION CASE
C BOUNDARY CONDITIONS CONSISTANT WITH CAUSALITY
C ZERO DENSITY GRADIENT IMPOSED ON LOWER SURFACE
C
  DIMENSION R(65),X(R0),AN(80),R0(9),R2(65),R2K(65),Y(65),
  IIR(65),ANO(65),RR(65,R0),A(65,3)
  DOUBLE PRECISION A,R
  COMMON AK,R0,W,AMMV,NHARM
  WRITE(6,5)
5  FORMAT(' THE NUMBER OF ROWS AND COLUMNS ARE:')
  READ(5,10)IROW,ICOL
10  FORMAT(2I5)
  WRITE(6,15)IROW,ICOL
15  FORMAT(2I5,/, ' INPUT TG,AMMV,WV,XB,DLXMS ARE:')
  READ(5,20)TG,AMMV,WV,XB,DLXMS
20  FORMAT(5F10.2)
  WRITE(6,25)TG,XB,AMMV,WV,DLXMS
25  FORMAT(' THE INPUTS TG,XB,AMMV,WV,DLXMS ARE',/6F10.4)
  NHARM=9.01
  IF(WV.EQ.8..OR.WV.EQ.12.)GO TO 30
  AK=15.71
  XMAG=.489
  R0(1)=.080356
  R0(2)=.0027
  R0(3)=.00392
  R0(4)=.00151
  R0(5)=.001
  R0(6)=.0000931
  R0(7)=.0007905
  R0(8)=.0005376
  R0(9)=.000352
  GO TO 40
30  IF(WV.EQ.12.)GO TO 35
```

AK=9.975
XMAG=.3175
R0(1)=.099763
R0(2)=.00183
R0(3)=.00457
R0(4)=.0005366
R0(5)=.0015
R0(6)=.000578
R0(7)=.00126
R0(8)=.0005
R0(9)=.00095

REPRODUCIBILITY OF THE
ORIGINAL PAGE IS POOR

GO TO 40
35 AK=6.650
XMAG=.0762
R0(1)=.08993
R0(2)=.00156
R0(3)=.025
R0(4)=.000267
R0(5)=.00128
R0(6)=.0000583
R0(7)=.00354
R0(8)=.000267
R0(9)=.0001064
40 DLX = 1./ (ICOL)
WW=12.7
W=.127
DLY = (1.-.031/WW)/(IROW)
DO 45 I=1,IROW
AN0(I)=1.
Y(I)=1.-DLY*I
45 CONTINUE
DO 50 I=1,IROW
CALL UNAM(Y(I),AM,AMK,U)
B2(I)=AM
B2K(I)=AMK
UR(I)=U/XB

50 CONTINUE
C INPUT FINISHED--SET UP FINITE ELEMENT EQUATIONS
DO 151 NCOL=1,ICOL
XPOS=XMAG + DLX*XB*NCOL
DY=DLY
DO 100 NROW=1,IROW
CALL DT2A(XPOS,DT,Y(NROW),DTMAX)
TID=DT/W**2
C=0.
IF(Y(NROW).LT..125)C=1.
IF(Y(NROW).GT..875)C=-1.
GRDT = C*DTMAX/W**2*TG*12.7/(1.5875-.031)/2./DY
A(NROW,2)=TG*TID**2/DY**2+(1.+TG*B2(NROW)/W)/DY +
1TG*UR(NROW)/DLX+TG*B2K(NROW)
A(NROW,1)=-TG*TID/DY**2-(1.+TG*B2(NROW)/W)/DY-GRDT
A(NROW,3)=-TG*TID/DY**2+GRDT
R(NROW)=TG*UR(NROW)/DLX*AN0(NROW)

100 CONTINUE

A(IROW,2) = A(IROW,2) - (2. + TG * B2(IROW) / W) / DY

A(1,1) = 0.

A(IROW,1) = A(IROW,1) - TG * TD / DY ** 2 - GRDT

A(IROW,3) = 0.

C SINGLE COLUMN OF ELEMENTS NOW READY FOR INVERSION

139 CALL INVRSE(A,R,IROW)

141 AN(NCOL) = AN(IROW) * DLYMS

DO 145 JJ = 1, IROW

AN(JJ) = B(JJ)

RR(JJ, NCOL) = AN(JJ)

145 CONTINUE

X(NCOL) = NCOL * DLX * XR

151 CONTINUE

C DENSITIES ARE NOW KNOWN - OUTPUT FOLLOWS

IF(TG.NE.24.684) GO TO 108

WRITE(6,90) (I, I=11, 71, 20)

90 FORMAT(' THE DENSITIES ARE AS FOLLOWS', /, 10X, I2, 3(6X, I2))

DO 108 I = 1, IROW

WRITE(6, 107) Y(I), (RR(I, J), J=11, 71, 20)

107 FORMAT(F5.3, 4F8.4)

108 CONTINUE

YU = .031 / WW

DLY0 = YU / 5.

CALL UOAM(YU, AM, AMK, U)

AM0 = AM

SUM = .5 * U / (W / TG + AM)

DO 165 J = 1, 4

YU = YU - DLY0

CALL UOAM(YU, AM, AMK, U)

SUM = SUM + U / (W / TG + AM)

165 CONTINUE

CALL UOAM(0., AM, AMK, U)

RAT = (W / TG + AM0) / (W / TG + AM)

SUM = SUM * DLY0 * W

WRITE(6, 187) SUM, RAT

187 FORMAT(' THE X INTEGRATION AND N RATIO ARE', 2E12.5)

DO 170 J = 1, ICOL

AN(J) = AN(J) * RAT

X(J) = X(J) + SUM

170 CONTINUE

WRITE(6, 125) (X(I), AN(I), I=1, ICOL, 3)

125 FORMAT(4E15.4)

STOP

END

SUBROUTINE UOAM(YU, AM, AMK, U)

DIMENSION R0(9)

COMMON AK, R0, W, AMMV, NHARM

Y = YU

IF(YU.GT..5) Y = 1. - Y

U = 4.572 * (2. * Y) * *.11111111

AM = 0.

REPRODUCIBILITY OF THE ORIGINAL PAGE IS POOR

REPRODUCIBILITY OF THE ORIGINAL PAGE IS POOR

```

DO 15 I=1,VHARM
P=2.*I*AK*YU
IF(P.GT.20.)GO TO 15.
AM=AM+AMMV*B0(I)**2*I*EXP(-P)
AMK=AMK+2.*I**2*AMMV*B0(I)**2*AK/W*EXP(-P)
15 CONTINUE
IF(YU.GT..0309/12.7) GO TO 30
U = .242**2*YU*.127/.000015
30 RETURN
END
SUBROUTINE DT2A(X,DT,Y,DTMAX)
DX=.1524
IF(X.LT.DX)DT=.003625
XE1=2.*DX
IF(X.GE.DX.AND.X.LT.XE1)DT=.003625+.020915*(X-DX)/DX
IF(X.GE.1.33985)DT=.00179
IF(X.LT.XE1.OR.X.GE.1.33985) GO TO 50
DT=.054658-.150851*X+.201784*X**2-.084262*X**3-.07902*
1X**4+.028938*X**5+.065659*X**6-.033616*X**7
50 DTMAX = DT
IF(Y.LT..125)DT=DT*Y/.125
IF(Y.LE..030995/12.7) DT = 0.
IF(Y.GT..875)DT=DT*(1.-Y)/.125
RETURN
END
SUBROUTINE INVRSE(A,B,IROW)
DIMENSION A(65,3),B(65),D(65),U(65,2),Y(65)
DOUBLE PRECISION A,B,D,U,Y
U(1,1) = A(1,2)
U(1,2) = A(1,3)
DO 30 I = 2,IROW
U(I,1) = A(I,2)-A(I-1,3)*A(I,1)/U(I-1,1)
U(I,2) = A(I,3)
D(I) = A(I,1)/U(I-1,1)
30 CONTINUE
Y(1) = B(1)
DO 40 I = 2,IROW
Y(I) = B(I)-D(I)*Y(I-1)
40 CONTINUE
B(IROW) = Y(IROW)/U(IROW,1)
DO 50 J=2,IROW
I=IROW+1-J
B(I) = (Y(I)-U(I,2)*B(I+1))/U(I,1)
50 CONTINUE
RETURN
END
//GO.SYSIN DD *
55 80
24.684 14.063 8. 1.5 1.1875
/*
/*EOJ *****

```

This fortran program calculates light particle densities and particulate deposition consistent with causality. Both the x and y diffusivity dependence are included in the model. Diffusivity is allowed to go to zero at the laminar boundary layer and thus, no boundary condition is imposed at the lower core boundary.

KDDF1

```

C
C CALCULATION OF DUCT CONCENTRATION PROFILE
C SMALL PARTICLE TURBULENT DIFFUSION CASE
C BOUNDARY CONDITIONS CONSISTANT WITH CAUSALITY
C NO BOUNDARY CONDITION ON LOWER SURFACE
C
  DIMENSION B(65),X(80),AN(80),R0(9),B2(65),B2K(65),Y(65),
1UR(65),ANO(65),BB(65,R0),A(65,3)
  DOUBLE PRECISION A,B
  COMMON AK,R0,W,AMMV,NHARM
  WRITE(6,5)
5  FORMAT(' THE NUMBER OF ROWS AND COLUMNS ARE ')
  READ(5,10) IROW,ICOL
10  FORMAT(2I5)
  WRITE(6,15) IROW,ICOL
15  FORMAT(2I5,' / ', ' INPUT TG,AMMV,WV,XB,DLXMS ARE ')
  READ(5,20) TG,AMMV,WV,XB,DLXMS
20  FORMAT(5F10.2)
  WRITE(6,25) TG,XB,AMMV,WV,DLXMS
25  FORMAT(' THE INPUTS TG,XB,AMMV,WV,DLXMS ARE ',/6F10.4)
  NHARM=9.01
  IF(WV.EQ.8..OR.WV.EQ.12.)GO TO 30
  AK=15.71
  XMAG=.489
  R0(1)=.080356
  R0(2)=.0027
  R0(3)=.00392
  R0(4)=.00151
  R0(5)=.001
  R0(6)=.0000931
  R0(7)=.0007905
  R0(8)=.0005376
  R0(9)=.000352
  GO TO 40
30  IF(WV.EQ.12.)GO TO 35

```

```
AK=9.975
XMAG=.3175
R0(1)=.099763
31 R0(2)=.00183
R0(3)=.00457
R0(4)=.0005366
R0(5)=.0015
R0(6)=.000578
R0(7)=.00126
R0(8)=.0005
R0(9)=.00095
GO TO 40
35 AK=6.650
XMAG=.0762
R0(1)=.08993
R0(2)=.00156
R0(3)=.025
R0(4)=.000267
R0(5)=.00128
R0(6)=.0000583
R0(7)=.00364
R0(8)=.000267
R0(9)=.0001064
40 DLX = 1./ (ICOL)
WW=12.7
W=.127
DLY = (1.-.031/WW)/(TROW)
DO 45 I=1,TROW
ANO(I)=1.
Y(I)=1.-DLY*I
45 CONTINUE
DO 50 I=1,TROW
CALL UOAM(Y(I),AM,AMK,U)
B2(I)=AM
B2K(I)=AMK
UR(I)=U/XB
50 CONTINUE
C INPUT FINISHED--SET UP FINITE ELEMENT EQUATIONS
C KENT LOVES LANA
DO 151 NCOL=1,ICOL
XPOS=XMAG + DLX*XB*NCOL
DY=DLY
DO 100 NROW=1,TROW
CALL DT2A(XPOS,DT,Y(NROW),DTMAX)
TID=DT/W**2
C=0.
IF(Y(NROW).GT..875)C=-1.
IF(Y(NROW).LT..125)C=1.
GRDT = C*DTMAX/W**2*TG*12.7/(1.5875-.031)/2./DY
A(NROW,2)=TG*TID*2/DY**2+(1.+TG*R2(NROW)/W)/DY +
1TG*UR(NROW)/DLX+TG*R2K(NROW)
A(NROW,1)=-TG*TID/DY**2-(1.+TG*R2(NROW)/W)/DY-GRDT
A(NROW,3)=-TG*TID/DY**2+GRDT
R(NROW)=TG*UR(NROW)/DI X*ANO(NROW)
```

```
100 CONTINUE
    A(IROW,1)=A(IROW,1)+GPDY-DTMAX*(.031/WW+DY)/.125/DY*TG/W**2/DY*10.
    A(IROW,2)=A(IROW,2)+DTMAX*(.031/WW+DY)/.125/DY*TG/W**2/DY*10.
    A(1,1)=0.
    A(IROW,3)=0.
C SINGLE COLUMN OF ELEMENTS NOW READY FOR INVERSION
130 CALL INVRSE(A,R,IROW)
141 AN(NCOL)=AN(IROW)*DLXMS
    DO 145 JJ=1,IROW
        AN(JJ)=B(JJ)
        BR(JJ,NCOL)=AN(JJ)
145 CONTINUE
    X(NCOL)=NCOL*DLX*XR
151 CONTINUE
C DENSITIES ARE NOW KNOWN - OUTPUT FOLLOWS
    IF(TG.NE.24.684) GO TO 108
    WRITE(6,90)(I,I=11,71,20)
90  FORMAT(' THE DENSITIES ARE AS FOLLOWS',/,10X,I2,3(6X,I2))
    DO 108 I=1,IROW
        WRITE(6,107)Y(I),(BR(I,J),J=11,71,20)
107  FORMAT(F5.3,4F8.4)
108 CONTINUE
    YU=.031/WW
    DLY0=YU/5.
    CALL UOAM(YU,AM,AMK,U)
    AM0=AM
    SUM=.5*U/(W/TG+AM)
    DO 165 J=1,4
        YU=YU-DLY0
        CALL UOAM(YU,AM,AMK,U)
        SUM=SUM+U/(W/TG+AM)
165 CONTINUE
    CALL UOAM(0.,AM,AMK,U)
    RAT=(W/TG+AM0)/(W/TG+AM)
    SUM = SUM *DLY0*W
    WRITE(6,187)SUM,RAT
187  FORMAT(' THE X INTEGRATION AND N RATIO ARE',.2E12.5)
    DO 170 J=1,ICOL
        AN(J)=AN(J)*RAT
        X(J)=X(J)+SUM
170 CONTINUE
    WRITE(6,125)(X(I),AN(I),I=1,ICOL,3)
125  FORMAT(4E15.4)
    STOP
    END
    SUBROUTINE UOAM(YU,AM,AMK,U)
    DIMENSION R0(9)
    COMMON AK,R0,W,AMMV,NHARM
    Y=YU
    IF(YU.GT..5)Y=1.-Y
    U=4.572*(2.*Y)**.1111111
    AM=0.
    DO 15 I=1,NHARM
        P=2.*I*AK*YU
```

```

IF(P.GT.20.)GO TO 15
AM=AM+AMMV*RO(I)**2*I*EXP(-P)
AMK=AMK+2.*I**2*AMMV*RO(I)**2*AK/W*EXP(-P)
15 CONTINUE
IF(YU.GT..0300/12.7) GO TO 30
U = .242**2*YU*.127/.000015
30 RETURN
END
SUBROUTINE DT2A(X,DT,Y,DTMAX)
DX=.1524
IF(X.LT.DX)DT=.003625
XE1=2.*DX
IF(X.GE.DX.AND.X.LT.XF1)DT=.003625+.020915*(X-DX)/DX
IF(X.GE.1.33985)DT=.00178
IF(X.LT.XE1.OR.X.GE.1.33985) GO TO 50
DT=.054658-.150851*X+.201784*X**2-.084262*X**3-.07902*
1X**4+.028938*X**5+.065659*X**6-.033616*X**7
50 DTMAX = DT
IF(Y.LT..125)DT=DT*Y/.125
IF(Y.LE..031001/12.7) DT = 0.
IF(Y.GT..875)DT=DT*(1.-Y)/.125
RETURN
END
SUBROUTINE INVPSE(A,R,IROW)
DIMENSION A(65,3),R(65),D(65),U(65,2),Y(65)
DOUBLE PRECISION A,B,D,U,Y
U(1,1) = A(1,2)
U(1,2) = A(1,3)
DO 30 I = 2,IROW
U(I,1) = A(I,2)-A(I-1,3)*A(I,1)/U(I-1,1)
U(I,2) = A(I,3)
D(I) = A(I,1)/U(I-1,1)
30 CONTINUE
Y(1) = B(1)
DO 40 I = 2,IROW
Y(I) = B(I)-D(I)*Y(I-1)
40 CONTINUE
R(IROW) = Y(IROW)/U(IROW,1)
DO 50 J = 2,IROW,1
I = IROW+1-J
B(I) = (Y(I)-U(I,2)*R(I+1))/U(I,1)
50 CONTINUE
RETURN
END

```

//GO.SYSIN DD *

55 80

124.96 1.8519 12. 1.5 .2389

/*

/*EQJ *****

Appendix H - KDIN4

This fortran program calculates heavy particle inertia trajectories and deposition according to the theory of chapter 4-C. No diffusion is considered. Numerical integration is based on a forth order Runge-Cutta method.

```
.TYPE KDIN4.FOR
C
C THIS PROGRAM CALCULATES THE TRAJECTORIES OF HEAVY
C PARTICLES INERTIA DOMINATES--NO DIFFUSION
C
      DIMENSION Y(3,200),YP(3,200),X(3,200),XP(3,200),BO(15),JMAX(3
      COMMON AMMG,NHARM,AK,BO
      WRITE(5,5)
      5  FORMAT(' GIVE ME T-ING,T-INV,T-RES,AMMG,YO,XPO,AK,DLT,DIA')
      READ(5,10)TG,TV,TR,AMMG,YO,XPO,AK,DLT,DIA
      10  FORMAT(F15.5)
      WRITE(5,15)TG,TV,TR,AMMG,YO,XPO,AK,DLT,DIA
      15  FORMAT(' INPUTS TG,TV,TR,AMMG,YO,XPO,AK,DLT,DIA ARE'/8F10.4)
      WRITE(5,20)
      20  FORMAT(' GIVE ME THE #HARMONICS AND THE B"S')
      READ(5,25)NHARM
      25  FORMAT(I5)
      READ(5,10)(BO(I),I=1,NHARM)
      WRITE(5,30)(BO(I),I=1,NHARM)
      30  FORMAT(' THE DENSITIES ARE',/,8F10.6)
      GV=TG/TV
      GVR=TG**2/TR/TV
      Y(2,1)=YO
      Y(1,1)=YO+DIA/2.
      Y(3,1)=YO-DIA/2.
      DO 35 I=1,3
      YP(I,1)=0.
      XP(I,1)=XPO
      X(I,1)=0.
      35  CONTINUE
C INPUT IS FINISHED, VERTICAL INTEGRATION FOLLOWS
      DO 90 I=1,3
      DO 85 J=2,200
      YO=Y(I,J-1)
      YPO=YP(I,J-1)
      CALL AM(YO,AMG)
      DYP1=DLT*(-GV*YPO-1.-AMG)
      YHALF=YO+DLT/2.*YPO
      CALL AM(YHALF,AMG)
      DYP2=DLT*(-GV*(YPO+DYP1/2.)-1.-AMG)
```

```
YHALF=Y0+DLT/2.*(2.*YF0+DYP2)/2.  
CALL AM(YHALF,AMG)  
DYP3=DLT*(-GV*(YF0+DYP2/2.))-1.-AMG)  
Y1=Y0+DLT*(2.*YF0+DYP3)/2.  
CALL AM(Y1,AMG)  
DYP4=DLT*(-GV*(YF0+DYP4))-1.-AMG)  
YF(I,J)=YF0+(DYP1+2.*(DYP2+DYP3)+DYP4)/6.  
Y(I,J)=Y0+(YF0+YF(I,J))/2.*DLT  
YHALF=(Y0 + Y(I,J))/2.
```

C THE Y-INTEGRATION IS FINISHED, X-INTEGRATION FOLLOWS

```
XP0=XP(I,J-1)  
X0=X(I,J-1)  
CALL U1(Y0,U,GVR)  
DXP1=DLT*(-GV*XP0 + U)  
CALL U1(YHALF,U,GVR)  
DXP2=DLT*(-GV*(XP0+DXP1/2.) + U)  
DXP3=DLT*(-GV*(XP0+DXP2/2.)+U)  
CALL U1(Y(I,J),U,GVR)  
DXP4=DLT*(-GV*(XP0+DXP3)+U)  
XF(I,J)=XP0+(DXP1+2.*(DXP2+DXP3)+DXP4)/6.  
X(I,J)=X0+(XP0+XF(I,J))/2.*DLT  
IF(Y(I,J).LE.0.) GO TO 88
```

85 CONTINUE

88 JMAX(I)=J

90 CONTINUE

C X-INTEGRATION FINISHED ,OUTPUT FOLLOWS

```
DO 110 I=1,3  
WRITE(5,93)I,JMAX(I)  
93 FORMAT(' X,Y,UX,VY ARE FOR CASE-',JMAX--,2I5)  
WRITE(5,95)(J,X(I,J),Y(I,J),XF(I,J),YF(I,J),J=1,JMAX(I),10)  
JM=JMAX(I)  
WRITE(5,95)JM,X(I,JM),Y(I,JM),XF(I,JM),YF(I,JM)  
95 FORMAT(I5,4F15.5)  
READ(5,10)AH1
```

110 CONTINUE

STOP

END

SUBROUTINE AM(Y,AMG)

DIMENSION BO(15)

COMMON AMMG,NHARM,AK,BO

AMG=0.

DO 10 I=1,NHARM

F=2.*AK*Y*I

IF(P.LT.0.)F=0.

IF(P.GT.20) GO TO 20

AMG=AMG+AMMG*I*BO(I)**2*EXP(-F)

10 CONTINUE

20 RETURN

END

SUBROUTINE U1(Y,U,GVR)

U=0.

IF(Y.LT.0.)GO TO 5

IF(Y.LT..5)U=GVR*(2.*Y)**.1111111

IF(Y.GE..5)U=GVR*(2.*(1.-Y))**.1111111

5 RETURN

END

Appendix I - KDIN7

REPRODUCIBILITY OF THE ORIGINAL PAGE IS POOR

This fortran program predicts particle densities and deposition according to the hybrid-inertial theory presented in chapter 4-D. Particle trajectories are calculated as in the diffusion-free model, but the diffusion term causes additional trajectory spreading. The analysis is especially tailored to intermediate sized particles where inertia and diffusion are important.

CC

C THIS PROGRAM CALCULATES THE TRAJECTORIES OF HEAVY
C PARTICLES INERTIA DOMINATES--WITH DIFFUSION!!
C

```

      DIMENSION Y(30),YP(30),X(30),XP(30),B0(9),JMAX(30),AN(30),
1     DLN(30),AN00(30),AN0(30),GCLT(30),GCLT2(30),Y00(30),X00(30)
      DOUBLE PRECISION X,Y,XP,YF,AN,Y00,X00,AN00,X0,XF0,Y0,YF0,
1     PCHY,PCHX,YCHAN,XCHAN,X3,Y3,RN3
      COMMON AMMG,NHARM,AK,B0
      WRITE(5,5)
5     FORMAT(' GIVE ME T-ING,T-INV,T-RES,AMMG,Y0,XF0,WV,DLT',/
1     ' DIA,XTUBE ,BND-LAYER(CM), #ROWS,DIF-ON')
      READ(5,10)TG,TU,TR,AMMG,Y0,XF0,WV,DLT,DIA,XTUBE,BL,ROW,DON
10    FORMAT(F15.5)
      WRITE(5,15)TG,TU,TR,AMMG,Y0,XF0,WV,DLT,DIA,XTUBE,BL,ROW,DON
15   FORMAT(' TG,TU,TR,AMMG,Y0,XF0,WV,DLT,DIA,XTUBE,BL,ROW,DON'
1     ',/,6F12.6)
      NROW=ROW+.01
      NHARM=9+.01
      T=.006244
      IF(WV.EQ.8..OR.WV.EQ.12.)GO TO 20
      AK=15.71
      B0(1)=.080356
      B0(2)=.0027
      B0(3)=.00392
      B0(4)=.00151
      B0(5)=.001
      B0(6)=.0000931
      B0(7)=.0007905
      B0(8)=.0005376
      B0(9)=.000352
      GO TO 30
20   IF(WV.EQ.12.)GO TO 25
      AK=9.975
      B0(1)=.099763
      B0(2)=.00183
      B0(3)=.00457
      B0(4)=.0005366

```

```
      B0(5)=.0015
      B0(6)=.000678
      B0(7)=.00126
      B0(8)=.0005
      B0(9)=.00095
      GO TO 30
25     AK=6.649
      B0(1)=.08993
      NHARM=1.+01
      GO TO 30
26     B0(2)=.00156
      B0(3)=.025
      B0(4)=.000267
      B0(5)=.00128
      B0(6)=.0000583
      B0(7)=.00364
      B0(8)=.000267
      B0(9)=.0001064
30     GV=TG/TV
      GVR=GV*TG/TR
      DG=TG**2/.127**2/TV*DON
      DLY=DIA/(NROW+1)
      DO 35 I=1,NROW
      Y(I)=Y0+DIA/2.-I*DLY
      X(I)=0.
      XP(I)=XFO
      YP(I)=0.
      JMAX(I)=1000
      ANO(I)=(1.-ABS(Y(I)-Y0)/(DIA/2.))**.1111111
      AN(I)=ANO(I)
35     CONTINUE
      CALL DT(XTUBE,D)
      DLN(1)=-AN(2)/2./DLY/AN(1)*D
      DLN(NROW)=AN(NROW-1)/2./DLY/AN(NROW)*D
      DO 36 I=3,NROW
      DLN(I-1)=(AN(I-2)-AN(I))/AN(I-1)/2./DLY*D
36     CONTINUE
      DLX0=XFO*DLT
      IMAX=NROW
C      INPUT IS FINISHED, VERTICAL INTEGRATION FOLLOWS
      DO 120 J=1,1000
      DO 40 I=1,IMAX
      Y0=Y(I)
      YP0=YP(I)
      CALL AM(Y0,AMG)
      DYP1=DLT*(-GV*YP0-1.-AMG-DG*DLN(I))
      YHALF=Y0+DLT/2.*YP0
      CALL AM(YHALF,AMG)
      DYP2=DLT*(-GV*(YP0+DYP1/2.)-1.-AMG-DG*DLN(I))
      YHALF=Y0+DLT/2.*(2.*YP0+DYP2)/2.
      CALL AM(YHALF,AMG)
      DYP3=DLT*(-GV*(YP0+DYP2/2.)-1.-AMG-DG*DLN(I))
      Y1=Y0+DLT*(2.*YP0+DYP3)/2.
      CALL AM(Y1,AMG)
```

```
DYP4=DLT*(-GV*(YF0+DYP3)-1.-AMG-DG*DLN(I))
YP(I)=YF0+(DYP1+2.*(DYP2+DYP3)+DYP4)/6.
Y(I)=Y0+ (YF0+YP(I))/2.*DLT
YHALF=(Y0 + Y(I))/2.
C THE Y-INTEGRATION IS FINISHED, X-INTEGRATION FOLLOWS
XPO=XP(I)
X0=X(I)
CALL U1(Y0,U,GVR)
DXP1=DLT*(-GV*XPO + U)
CALL U1(YHALF,U,GVR)
DXP2=DLT*(-GV*(XPO+DXP1/2.) + U)
DXP3=DLT*(-GV*(XPO+DXP2/2.)+U)
CALL U1(Y(I),U,GVR)
DXP4=DLT*(-GV*(XPO+DXP3)+U)
XP(I)=XPO+ (DXP1+2.*(DXP2+DXP3)+DXP4)/6.
X(I)=X0+(XPO+XP(I))/2.*DLT
IF(Y(I).LE.0.) IMAX=IMAX-1
IF(Y(I).LE.0.) JMAX(I)=J
Y00(I)=Y0
X00(I)=X0
40 CONTINUE
C X-INTEGRATION FINISHED ,NOW GET DENSITY
DO 90 I=1,NROW
X0=X00(I)
Y0=Y00(I)
ANO0(I)=AN(I)
IF(I.EQ.1)GO TO 65
IF(Y(I-1).LE.0..AND.JMAX(I).LT.J)GO TO 90
IF(I.EQ.NROW)GO TO 68
YCHAN=(Y(I-1)-Y(I+1))/2./DLY
IF(Y(I+1).LE.0.)YCHAN=(Y(I-1)-Y(I))/DLY
XCHAN=(X(I)-X0)/DLX0
PCHY=(X(I-1)-X(I+1))/2./DLY
PCHX=(Y(I)-Y0)/DLX0
GO TO 70
65 YCHAN=(Y(1)-Y(2))/DLY
XCHAN=(X(1)-X0)/DLX0
PCHY=(X(1)-X(2))/DLY
PCHX=(Y(1)-Y0)/DLX0
GO TO 70
68 YCHAN=(Y(NROW-1)-Y(NROW))/DLY
XCHAN=(X(NROW)-X0)/DLX0
PCHY=(X(NROW-1)-X(NROW))/DLY
PCHX=(Y(NROW)-Y0)/DLX0
70 AN(I)=ANO(I)/(XCHAN*YCHAN-PCHY*PCHX)
90 CONTINUE
C DENSITIES ARE KNOWN-GET D*GRADIENT(N)
95 DO 110 I=1,NROW
DLN(I)=0.
IF(I.GT.IMAX)GO TO 110
IF(Y(I).LE.BL/12.7.OR.Y(I).GE.(1.-BL/12.7))GO TO 110
XPOS=X(I)*.127+XTUBE
CALL DT(XPOS,D)
IF(I.EQ.1) GO TO 100
IF(I.EQ.NROW)GO TO 105
```

```
Y3=Y(I+1)
X3=X(I+1)
RN3=AN(I+1)
106 DLN(I)=((AN(I-1)-RN3)*(X(I)-X00(I))-(AN(I)-AN00(I))*
1 (X(I-1)-X3))/((Y(I-1)-Y3)*(X(I)-X00(I))-(Y(I)-Y00(I))*
2 (X(I-1)-X3)) / AN(I)*D
GO TO 109
100 DLN(1)=-AN(2)*(Y(1)-Y(2))/((X(1)-X(2))*2+(Y(1)-Y(2))
1 **2)/AN(I)*D/2.
GO TO 109
105 DLN(NROW)=AN(NROW-1)*(Y(NROW-1)-Y(NROW))/((X(NROW-1)-
1 X(NROW))*2+(Y(NROW-1)-Y(NROW))*2)/AN(NROW)*D/2.
109 SIGN=1.
IF(DLN(I).LT.0.)SIGN=-1.
W=.127*SQRT(D/T)
IF(SIGN*DLN(I).GT.W)DLN(I)=SIGN*W
110 CONTINUE
IF(Y(1).LE.0.)GO TO 125
114 IF(MOD(J,5).NE.0)GO TO 120
112 WRITE(5,111)J
111 FORMAT(' THE OUTPUTS-X,Y,XP,YF,DENSITY,DLN-CASE=',I5)
DO 115 I=1,NROW
WRITE(5,113)I,X(I),Y(I),XP(I),YP(I),AN(I),DLN(I)
113 FORMAT(I5,6E12.5)
115 CONTINUE
120 CONTINUE
```

C
C NET INTEGRATION FINISHED--OUTPUT FOLLOWS
C

```
125 WRITE(5,126)
126 FORMAT(' THE OUTPUT FOLLOWS',/2X,'I',X,'JMAX',6X,'X',11X,
1 'Y',10X,'XP',12X,'YP',9X,'GCLT',8X,'GCLT2')
DO 135 I=1,NROW
IF(I.NE.1.AND.I.NE.NROW)GDX=(X(I-1)-X(I+1))/2.
IF(I.EQ.1)GDX=X(1)-X(2)
IF(I.EQ.NROW)GDX=X(NROW-1)-X(NROW)
GCLT(I)=100./9/DIA*DLY/GDX*WV/2./12.7*ANO(I)
GCLT2(I)=-100.*WV/2./12.7/.9/DIA/XPO*AN(I)*YP(I)
135 CONTINUE
DO 140 I=1,NROW
X(I)=X(I)*.127
WRITE(5,130)I,JMAX(I),X(I),Y(I),XP(I),YP(I),GCLT(I),GCLT2(I)
130 FORMAT(2I4,6E12.5)
140 CONTINUE
STOP
END
SUBROUTINE AM(Y,AMG)
DIMENSION BO(9)
COMMON AMMG,NHARM,AK,BO
AMG=0.
DO 10 I=1,NHARM
P=2.*AK*Y*I
IF(P.LT.0.)P=0.
```

REPRODUCIBILITY OF THE
ORIGINAL PAGE IS POOR

```
IF(F.GT.20.) GO TO 20
AMG=AMG+AMMG*I*B0(I)**2*EXP(-F)
10 CONTINUE
20 RETURN
END
SUBROUTINE U1(Y,U,GVR)
U=0.
F=1./9.
IF(Y.LE.0.)GO TO 5
IF(Y.GT.(1.-.5/12.7))U=GVR*(2.*.5/12.7)**F
IF(U.NE.0.)GO TO 5
IF(Y.LT..5)U=GVR*(2.*Y)**F
IF(Y.GE..5)U=GVR*(2.*(1.-Y))**F
5 CONTINUE
RETURN
END
SUBROUTINE DT(X,D)
D=.061664-.146418*X+.135854*X**2-.013655*X**3
1 -.03752*X**4-.002257*X**5+.009903*X**6
50 RETURN
END
```

Appendix J - FOURIE

REPRODUCIBILITY OF THE
ORIGINAL PAGE IS POOR

This basic program performs a discrete fourier analysis of the magnetic field density waveform $1/4$ " above the permanent magnet structure.

The analysis follows that described in chapter 5.

```
10 DIM X(31),B(16)
12 PRINT 'N HARMONICS FOLLOW--NEED 2N-1 DATA POINTS'
15 PRINT 'N=' \ INPUT N \ PRINT 'X(I) FOLLOWS'
17 P=2*N-1
20 FOR I=1 TO P \ INPUT X(I) \ NEXT I
23 PRINT 'THE X'S ARE' \ FOR I=1 TO P \ PRINT X(I), \ NEXT I \ PRINT
35 FOR J=1 TO N \ B(J)=0
40 FOR I=1 TO P
45 B(J)=B(J)+X(I)/N*SIN(3.14159/N*J*I)
50 NEXT I \ NEXT J
55 FOR I=1 TO N \ PRINT I,B(I) \ NEXT I
```

Appendix K - KD747G

This fortran program calculates particle density and deposition for intermediate sized particles injected over the skin of an aircraft flying 500 MPH at an altitude of 40,000 ft. The exact normal and axial diffusivity dependence in the boundary layer is used. Only magnetic migration exists normal to the fluid stream flow; gravitational effects are ignored. the analysis follows that described in chapter 7.

CC

C THIS PROGRAM CALCULATES THE TRAJECTORIES OF HEAVY
C PARTICLES- INERTIA DOMINATES--WITH DIFFUSION!!
C CALCULATES FLIGHT OF PARTICLES OVER 747 JET
C ALTITUDE= 40,000 FT., SPEED=500 MPH.

C

```
      DIMENSION Y(30),YF(30),X(30),XP(30),B0(9),JMAX(30),AN(30),
1     DLN(30),AN00(30),AN0(30),GCLT(30),GCLT2(30),Y00(30),X00(30)
      DOUBLE PRECISION X,Y,XP,YF,AN,Y00,X00,AN00,X0,XP0,Y0,YF0,
1     FCHY,FCHX,YCHAN,XCHAN,X3,Y3,RN3
      COMMON AMMG,NHARM,AK,B0
      WRITE(5,5)
5     FORMAT(' GIVE ME T-ING,T-INV,T-RES,AMMG,Y0,XP0,WV,DLT',/
1     ' DIA,XTURB, #ROWS,DIF-ON')
      READ(5,10)TG,TV,TR,AMMG,Y0,XP0,WV,DLT,DIA,XTURB,ROW,DON
10    FORMAT(F15.5)
      WRITE(5,15)TG,TV,TR,AMMG,Y0,XP0,WV,DLT,DIA,XTURB,ROW,DON
15   FORMAT(' TG,TV,TR,AMMG,Y0,XP0,WV,DLT,DIA,XTURB,ROW,DON'
1     ',/,6F12.6)
      NROW=ROW+.01
      NHARM=9+.01
      IF(WV.EQ.8..OR.WV.EQ.12.)GO TO 20
      AK=123.68
      B0(1)=.080356
      B0(2)=.0027
      B0(3)=.00392
      B0(4)=.00151
      B0(5)=.001
      B0(6)=.0000931
      B0(7)=.0007905
      B0(8)=.0005376
      B0(9)=.000352
      GO TO 30
20   IF(WV.EQ.12.)GO TO 25
      AK=78.54
      B0(1)=.099763
```

```
B0(2)=.00183
B0(3)=.00457
B0(4)=.0005366
B0(5)=.0015
B0(6)=.000678
B0(7)=.00126
B0(8)=.0005
B0(9)=.00095
GO TO 30
25 AK=52.36
B0(1)=.08993
B0(2)=.00156
B0(3)=.025
B0(4)=.000267
B0(5)=.00128
B0(6)=.0000583
B0(7)=.00364
B0(8)=.000267
B0(9)=.0001064
30 GV=1.
GVR=TV/TR
DG=TV*DON
DLY=DIA/(NROW+1)
DO 35 I=1,NROW
Y(I)=Y0+DIA/2.-I*DLY
X(I)=0.
XP(I)=XPO
YP(I)=0.
JMAX(I)=850
ANO(I)=(1.-ABS(Y(I)-Y0)/(DIA/2.))**.1111111
AN(I)=ANO(I)
Y00(I)=Y(I)
X00(I)=-XPO*DLT
AN00(I)=AN(I)
35 CONTINUE
DLX0=XPO*DLT
IMAX=NROW
C INPUT IS FINISHED, VERTICAL INTEGRATION FOLLOWS
DO 120 J=1,850
DO 40 I=1,IMAX
Y0=Y(I)
YPO=YP(I)
X0=X(I)
XDT=XTURB+X0
DL=.37*XDT*(XDT/TR/.4701)**(-.2)
GO TO 95
39 CALL AM(Y0,AMG)
DYP1=DLT*(-GV*YPO-AMG-DG*DLN(I))
YHALF=Y0+DLT/2.*YPO
CALL AM(YHALF,AMG)
DYP2=DLT*(-GV*(YPO+DYP1/2.))-AMG-DG*DLN(I))
YHALF=Y0+DLT/2.*(2.*YPO+DYP2)/2.
CALL AM(YHALF,AMG)
```

REPRODUCIBILITY OF THE
ORIGINAL DATA

```
DYP3=DLT*(-GV*(YF0+DYP2/2.)-AMG-DG*DLN(I))
Y1=Y0+DLT*(2.*YF0+DYP3)/2.
CALL AM(Y1,AMG)
DYP4=DLT*(-GV*(YF0+DYP3)-AMG-DG*DLN(I))
YF(I)=YF0+(DYP1+2.*(DYP2+DYP3)+DYP4)/6.
Y(I)=Y0+(YF0+YF(I))/2.*DLT
YHALF=(Y0 + Y(I))/2.
```

C THE Y-INTEGRATION IS FINISHED, X-INTEGRATION FOLLOWS

```
XP0=XP(I)
CALL U1(Y0,U,GVR,DL)
DXP1=DLT*(-GV*XP0 + U)
CALL U1(YHALF,U,GVR,DL)
DXP2=DLT*(-GV*(XP0+DXP1/2.) + U)
DXP3=DLT*(-GV*(XP0+DXP2/2.)+U)
CALL U1(Y(I),U,GVR,DL)
DXP4=DLT*(-GV*(XP0+DXP3)+U)
XP(I)=XP0+(DXP1+2.*(DXP2+DXP3)+DXP4)/6.
X(I)=X0+(XP0+XP(I))/2.*DLT
IF(Y(I).LE.0.) IMAX=IMAX-1
IF(Y(I).LE.0.)JMAX(I)=J
Y00(I)=Y0
X00(I)=X0
```

40 CONTINUE

C X-INTEGRATION FINISHED ,NOW GET DENSITY

```
DO 90 I=1,NROW
X0=X00(I)
Y0=Y00(I)
AN00(I)=AN(I)
IF(I.EQ.1)GO TO 65
IF(Y(I-1).LE.0..AND.JMAX(I).LT.J)GO TO 90
IF(I.EQ.NROW)GO TO 68
YCHAN=(Y(I-1)-Y(I+1))/2./DLY
IF(Y(I+1).LE.0.)YCHAN=(Y(I-1)-Y(I))/DLY
XCHAN=(X(I)-X0)/DLX0
PCHY=(X(I-1)-X(I+1))/2./DLY
PCHX=(Y(I)-Y0)/DLX0
GO TO 70
```

65 YCHAN=(Y(1)-Y(2))/DLY
XCHAN=(X(1)-X0)/DLX0
PCHY=(X(1)-X(2))/DLY
PCHX=(Y(1)-Y0)/DLX0

GO TO 70

68 YCHAN=(Y(NROW-1)-Y(NROW))/DLY
XCHAN=(X(NROW)-X0)/DLX0
PCHY=(X(NROW-1)-X(NROW))/DLY
PCHX=(Y(NROW)-Y0)/DLX0

70 AN(I)=AN0(I)/(XCHAN*YCHAN-PCHY*PCHX)

90 CONTINUE

```
IF(Y(1).LE.0.)GO TO 125
IF(MOD(J,5).NE.0)GO TO 120
WRITE(5,91)J,IMAX
```

```
91  FORMAT(' X,Y,XP,YF,DENSITY,DLN-CASE=',I5,' IMAX=',I5)
    DO 93 I=1,NROW
    WRITE(5,92)I,X(I),Y(I),XP(I),YF(I),AN(I),DLN(I)
92  FORMAT(I5,6D12.5)
93  CONTINUE
120 CONTINUE
C DENSITIES ARE KNOWN-GET D*GRADIENT(N)--THE FOLLOWING STATEMENTS
C ACT AS A SUBROUTINE TO GET THE GRADIENT
95  DLN(I)=0.
    IF(I.GT.IMAX)GO TO 39
    IF(Y(I).GE.DL.OR.Y(I).LE.0.)GO TO 39
    CALL DT(DL,Y(I),D)
    IF(I.EQ.1) GO TO 100
    IF(I.EQ.NROW)GO TO 105
    Y3=Y(I+1)
    X3=X(I+1)
    RN3=AN(I+1)
106 DLN(I)=((AN(I-1)-RN3)*(X(I)-X00(I))-(AN(I)-AN00(I))*
1   (X00(I-1)-X3))/((Y00(I-1)-Y3)*(X(I)-X00(I))-(Y(I)-Y00(I))
2   *(X00(I-1)-X3)) / AN(I)*D
    GO TO 109
100 DLN(1)=-AN(2)*(Y(1)-Y(2))/((X(1)-X(2))*2+(Y(1)-Y(2))
1   **2)/AN(I)*D/2.
    GO TO 109
105 DLN(NROW)=AN(NROW-1)*(Y00(NROW-1)-Y(NROW))/((X00(NROW-1)
1   -X(NROW))*2+(Y00(NROW-1)-Y(NROW))*2)/AN(NROW)*D/2.
109 SIGN=1.
    T=DL/.7/223.5
    IF(DLN(I).LT.0.)SIGN=-1.
    W=SQRT(D/T)
    IF(SIGN*DLN(I).GT.W)DLN(I)=SIGN*W
    GO TO 39
C
C NET INTEGRATION FINISHED--OUTPUT FOLLOWS
C
125 WRITE(5,126)
126 FORMAT(' THE OUTPUT FOLLOWS',/ ,2X,'I',X,' JMAX',6X,'X',11X,
1   'Y',10X,'XP',12X,'YF',9X,'GCLT',8X,'GCLT2')
    DO 135 I=1,NROW
    IF(I.NE.1.AND.I.NE.NROW)GDX=(X(I-1)-X(I+1))/2.
    IF(I.EQ.1)GDX=X(1)-X(2)
    IF(I.EQ.NROW)GDX=X(NROW-1)-X(NROW)
    GCLT(I)=100./ .9/DIA*DLY/GDX*WV/2./12.7*ANO(I)
    GCLT2(I)=-100.*WV/2./12.7/.9/DIA/XFO*AN(I)*YF(I)
135 CONTINUE
    DO 140 I=1,NROW
    WRITE(5,130)I,JMAX(I),X(I),Y(I),XP(I),YF(I),GCLT(I),GCLT2(I)
130 FORMAT(2I4,6E12.5)
140 CONTINUE
    STOP
    END
```

REPRODUCIBILITY OF THE
ORIGINAL PAGE IS POOR

```
SUBROUTINE AM(Y,AMG)
DIMENSION BO(9)
COMMON AMMG,NHARM,AK,BO
AMG=0.
DO 10 I=1,NHARM
P=2.*AK*Y*I
IF(P.LT.0.)P=0.
IF(P.GT.20.) GO TO 20
AMG=AMG+AMMG*I*BO(I)**2*EXP(-P)
10 CONTINUE
20 RETURN
END
SUBROUTINE U1(Y,U,GVR,DL)
U=0.
IF(Y.LE.0.)GO TO 5
IF(Y.LT.DL)GO TO 3
U=GVR
GO TO 5
3 P=1./7.
U=GVR*(Y/DL)**P
5 CONTINUE
RETURN
END
SUBROUTINE DT(DL,Y,D)
D=0.
IF(Y.LE.0..OR.Y.GT.DL)GO TO 50
YN=Y/DL
D=-.01031+2.91226*YN+.070557*YN**2-13.614712*YN**3
+4.179703*YN**4+21.233276*YN**5-2.772369*YN**6-
15.559235*YN**7-8.465072*YN**8+12.027271*YN**9
D=D*.0037*223.5*DL
IF(D.LT.0.)D=-D
50 RETURN
END
```

Appendix L - Refinement of Causal Fundamental Light Particle Model

The density profiles predicted by the fundamental causal model are integrated to give mass deposition per half wavelength on the lower duct surface. This technique integrates out numerical difficulties in the lower duct region caused by diffusivity gradients and a steep exponential magnetic variation. The integration forces the model predictions to be consistent with causality.

Figure (L-1) shows a representative flux balance at position x in the duct. Mass conservation demands that

$$\int_{x-\lambda/2}^{x+\lambda/2} \Gamma_y w dx = \int_0^{2a} (\Gamma_{x \text{ in}}(x=x-\lambda/2) - \Gamma_{x \text{ out}}(x=x+\lambda/2)) w dy \quad (L-1)$$

REPRODUCIBILITY OF THE ORIGINAL PAPER IS GOOD

Assuming steady state operation over an interval t_0 seconds, the amount of particulate collected on the lower duct surface is

$$\begin{aligned} \frac{(\text{mass collected})}{\lambda/2} &= \int_0^{t_0} \int_{x-\lambda/2}^{x+\lambda/2} \Gamma_y dx dt \\ &= w t_0 \int_{x-\lambda/2}^{x+\lambda/2} \Gamma_y dx \end{aligned} \quad (L-2)$$

With an average axial duct velocity, U_{avg} in the duct, the net mass injected is

$$\begin{aligned} (\text{mass injected}) &= \int_0^{2a} \int_0^{t_0} n_0 U w dt dy \\ &= n_0 U_{\text{avg}} w t_0 \end{aligned} \quad (L-3)$$

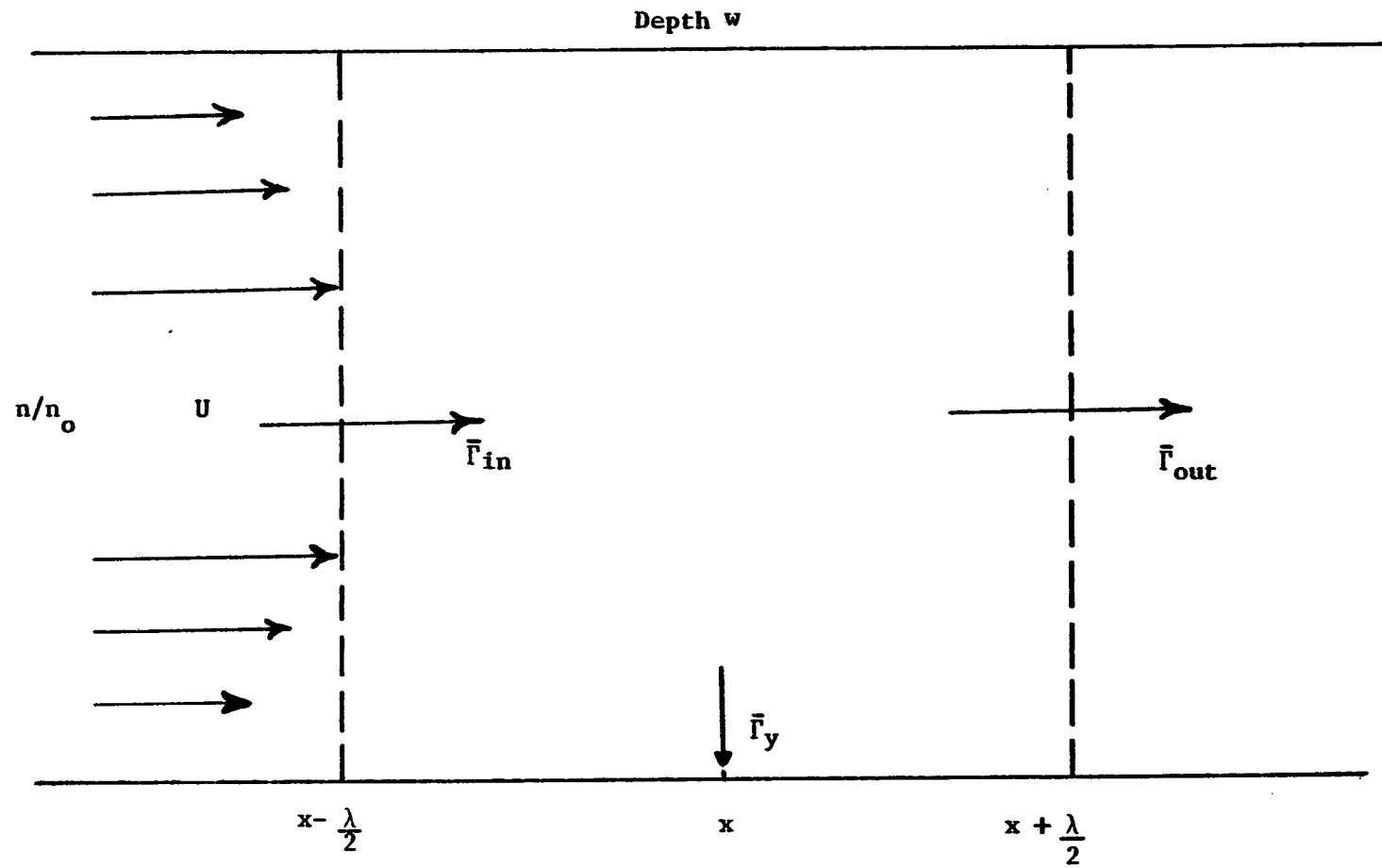


Figure (L-1) Flux Balance in Duct

combining (L-1), (L-3) with (L-2) gives

$$\frac{(\text{mass collected})}{\lambda/2} = \frac{(\text{mass injected})^*}{n_o U_{\text{avg}}} \tag{L-4}$$
$$\int_0^{2a} [\Gamma_{x \text{ in}}(x=x-\lambda/2) - \Gamma_{x \text{ out}}(x=x+\lambda/2)] dy$$

The program predicts n/n_o and since $\Gamma_y = n u$, the mass collected can be calculated. The FORTRAN program KDFF1 incorporating these changes is listed in Appendix M. Simpson's rule is used to perform the transverse flux integration.

Appendix M - KDF1

This FORTRAN program computes densities and half wavelength deposition for light particles. Particle deposition is computed using mass conservation arguments; integration of the entire transverse profile is involved in predicting deposition. The analysis occurs in Appendix L.

```
C  CALCULATION OF DUCT CONCENTRATION PROFILE
C  SMALL PARTICLE TURBULENT DIFFUSION CASE
C  BOUNDARY CONDITIONS CONSISTENT WITH CAUSALITY
C  NO BOUNDARY CONDITIONS ON LOWER SURFACE
C
```

```
dimension b(100),x(1000),an(1000),b0(9),b2(100),b2k(100),y(100)
dimension ur(100),an0(100),bb(100,4),a(100,3),ans(2,100),ncs(40),
ncf(140)
double precision a,b
common ak,b0,w,ammv,nharm
write(6,5)
5 format(' THE NUMBER OF ROWS AND COLUMNS ARE ')
read(5,10)irow,icol
10 format(2i5)
write(6,15)irow,icol
15 format(2i5,/, ' INPUT TG,AMMV,WV,XB,DLXMS ARE ')
read(5,20)tg,ammv,wv,xb,dlxms
20 format(f15,5)
write(6,25)tg,xb,ammv,wv,dlxms
25 format(' THE INPUTS TG,XB,AMMV,WV,DLXMS ARE ',/6f10.4)
nharm=9.01
nu=0
no=icol/25
ncoll=0
if(wv.eq.8..or.wv.eq.12.)go to 30
ak=15.71
xmag=.489
b0(1)=.080356
b0(2)=.0027
b0(3)=.00392
b0(4)=.00151
b0(5)=.001
b0(6)=.0000931
b0(7)=.0007905
b0(8)=.0005376
b0(9)=.000352
go to 40
30 if(wv.eq.12.)go to 35
ak=9.975
xmag=.3175
b0(1)=.099763
31 b0(2)=.00183
b0(3)=.00457
b0(4)=.0005366
```

```

b0(5)=.0015
b0(6)=.000678
b0(7)=.00126
b0(8)=.0005
b0(9)=.00095
35  go to 40
    ak=6.650
    xmas=.40005
38  b0(1)=.08993
    b0(2)=.00156
    b0(3)=.025
    b0(4)=.000267
    b0(5)=.00128
    b0(6)=.0000583
    b0(7)=.00364
    b0(8)=.000267
    b0(9)=.0001064
40  dlx = 1./(icol)
    ww=12.7
    w=.127
    ndlf=ww/2.*.01/dlx/xb
    kes=0
    kc=0
    nend=icol-no
    do 43 J=no,nend,no
42  kc=kc+1
    if((xb*J*dlx-ww/4*.01).gt.(kc*xb*dlx)) go to 42
    kes=kes+1
    ncs(kes)=kc
    ncf(kes)= kc+ndlf
43  continue
    kesend=kes
    write(6,44)kesend,(ncs(J),ncf(J),J=1,kesend)
44  format(' kesend,ncs,and ncf are'i3/14i5)
    kc=1
    dly=(1-.031/ww)/irow
    do 45 i=1,irow
    y(i)=1.-dly*i
    an0(i)=1.
45  continue
    do 50 i=1,irow
    call u0am(y(i),am,amk,u)
    b2(i)=am
    b2k(i)=amk
    ur(i)=u/xb
50  continue
c INPUT FINISHED--SET UP FINITE ELEMENT EQUATIONS
c KENT LOVES LANA
    do 151 ncol=1,icol
    xpos=xmas + dlx*xb*ncol
    dy=dly
    do 100 nrow=1,irow
    call dt2a(xpos,dt,y(nrow),dtmax)
    tid=dt/w**2
```

REPRODUCIBILITY OF THE
ORIGINAL PAGE IS POOR

```
d3=1/w**2/dy*10.
c=0.
if(y(nrow).gt..875)c=-1.
if(y(nrow).lt..125)c=1.
grdt = c*dtmax/w**2*tg*12.7/(1.5875-.031)/2./dy
a(nrow,2)=tg*tid*2/dy**2+(1.+ts*b2(nrow)/w)/dy+ts*ur(nrow)/
\c(nrow) l dlx+tg*b2k(nrow)
a(nrow,1)=-tg*tid/dy**2-(1.+ts*b2(nrow)/w)/dy-grdt
a(nrow,3)=-tg*tid/dy**2+grdt
b(nrow)=ts*ur(nrow)/dlx*an0(nrow)
100 continue
a(irow,1)=a(irow,1)+grdt-dtmax*(.031/ww+dy)/.125/dy*tg *d3
a(irow,2) =a(irow,2)+dtmax*(.031/ww+dy) /.125/dy*tg *d3
a(1,1)=0.
a(irow,3)=0.
c SINGLE COLUMN OF ELEMENTS NOW READY FOR INVERSION
139 call invrse(a,b,irow)
do 145 JJ=1,irow
  an0(JJ) = b(JJ)
  nco = icol/4
  if(ncol.ne.nco.and.ncol.ne.2*nco.and.ncol.ne.3*nco.and.ncol
  .ne.(4*nco-1)) go to 145
  if(ncol1.eq.ncol)go to 903
  nu=nu+1
903 ncol1=ncol
  bb(JJ,nu)=an0(JJ)
145 continue
  ndum=1
  if(ncol.ne.ncs(kc).and.ncol.ne.ncs(kc+1)) go to 185
  if(ncol.ge.ncs(kc+1)) ndum=2
  do 180 i=1,irow
  ans(ndum,i)=an0(i)
  180 continue
  185 if(ncf(kc).eq.ncol)call fluxin(ans,an0,irow,ur,dlx,difa)
  if(ncf(kc).ne.ncol) go to 151
  if(ncol.lt.ncs(kc+1)) go to 170
  do 187 i=1,irow
  ans(1,i)=ans(2,i)
  187 continue
  170 kc=kc+1
  an(ncol)=100.*difa*xb/.9/4.572
151 continue
c DENSITIES ARE NOW KNOWN - OUTPUT FOLLOWS
  nco=icol/4
  write(6,90)(i,i=nco,icol,nco)
90 format(" THE DENSITIES ARE AS FOLLOWS",/,10x,i4,3(6x,i4))
  do 108 i=1,irow,3
  write(6,107)s(i),(bb(i,J),J=1,4)
107 format(f5.3,4f8.4)
108 continue
  do 190 J=1,kcsend
  x(i)=ncs(i)*dlx*xb+ww/4.*.01
  190 continue
  write(6,125)(x(i),an(i),i=1,kcsend)
125 format(4e15.4)
  stop
end
```

REPRODUCIBILITY OF THE ORIGINAL PAGE IS POOR

```
subroutine u0am(u,am,amk,u)
dimension b0(9)
common ak,b0,w,ammv,nharm
u=yu
if(yu,st,.5)u=1.-u
u=4.572*(2.*u)**.1111111
am=0.
do 15 i=1,nharm
r=2.*i*ak*u
if(r,st,20.)go to 15
am=am+ammv*b0(i)**2*i*exp(-r)
amk=amk+2.*i**2*ammv*b0(i)**2*ak/w*exp(-r)
15 continue
if(yu,st,.0309/12.7) go to 30
u = .242**2*u*.127/.000015
30 return
end
subroutine dt2a(x,dt,w,dtmax)
dx=.1524
if(x.lt.dx)dt=.003625
xel=2.*dx
if(x.ge.dx.and.x.lt.xel)dt=.003625+.020915*(x-dx)/dx
if(x.ge.1.33985)dt=.00178
if(x.lt.xel.or.x.ge.1.33985) go to 50
dt=.054658-.150851*x+.201784*x**2-.084262*x**3-.07902*x**4
50 dtmax = dt
dt=dt*w/.125
if(w.le..031001/12.7) dt = 0.
if(w.st..875)dt=dt*(1.-w)/.125
return
end
subroutine invrse(a,b,irow)
dimension a(135,3),b(135),d(135),u(135,2),v(135)
double precision a,b
u(1,1) = a(1,2)
u(1,2) = a(1,3)
do 30 i = 2,irow
u(i,1) = a(i,2)-a(i-1,3)*a(i,1)/u(i-1,1)
u(i,2) = a(i,3)
d(i) = a(i,1)/u(i-1,1)
30 continue
v(1) = b(1)
do 40 i = 2,irow
v(i) = b(i)-d(i)*v(i-1)
40 continue
b(irow)= v(irow)/u(irow,1)
do 50 j = 2,irow,1
i = irow+1-j
b(i) = (v(i)-u(i,2)*b(i+1))/u(i,1)
50 continue
return
end
```

```
subroutine fluxin(ans,an0,irow,ur,dly,difa)
dimension ans(2,100),an0(100),ur(100)
f1=dly/3.*ans(irow)*ur(irow)
f2=dly/3.*an0(irow)*ur(irow)
iro=irow-1
iroe=irow-2
do 10 i=1,iro,2
f1=f1+ur(i)*4.*dly/3.*ans(i)
f2=f2+ ur(i)*4.*dly/3*an0(i)
10 continue
do 20 i=2,iroe,2
f1=f1+ur(i)*2.*dly/3.*ans(i)
f2=f2+ur(i)*2.*dly/3.*an0(i)
20 continue
difa=f1-f2
return
end
```

BIOGRAPHICAL NOTE

The author was born in [REDACTED] on [REDACTED]. He was awarded the Rensselaer Science Award in May, 1970 and graduated from Martin Behrman High School in June 1970. In the fall of that year he began undergraduate study in Electrical Engineering at Tulane University and graduated in June, 1974. He was elected to Tau Beta Pi in 1973 and Eta Kappa Nu in 1974.

In June 1974 the author began work with Westinghouse Electric Corporation as a development engineer in electric machinery. He remained with Westinghouse for $2\frac{1}{3}$ years until August 1976, and in this time he was awarded three patent awards in electric machinery. Also during this time he acquired an M.S. in Power Engineering at Carnegie Mellon University and an M.S. in Physics at the University of Pittsburgh. In September, 1976 he began his doctoral program in electrical engineering at MIT.

On July 24, 1977 he married the former Lana Patricia Gatian of Morgantown, West Virginia.

The author has avid interest in sports and holds awards in cycling, badminton, track, and chess.

REPRODUCIBILITY OF THE
ORIGINAL PAGE IS POOR